

TUNING THE ELECTRON BEAM EVAPORATION PARAMETERS FOR THE  
PRODUCTION OF HOLE AND ELECTRON TRANSPORT LAYERS FOR  
PEROVSKITE SOLAR CELLS

A THESIS SUBMITTED TO  
THE GRADUATE SCHOOL OF NATURAL AND APPLIED SCIENCES  
OF  
MIDDLE EAST TECHNICAL UNIVERSITY

BY

MUSTAFA BURAK COŞAR

IN PARTIAL FULFILLMENT OF THE REQUIREMENTS  
FOR  
THE DEGREE OF DOCTOR OF PHILOSOPHY  
IN  
METALLURGICAL AND MATERIALS ENGINEERING

JUNE 2019



Approval of the thesis:

**TUNING THE ELECTRON BEAM EVAPORATION PARAMETERS FOR  
THE PRODUCTION OF HOLE AND ELECTRON TRANSPORT LAYERS  
FOR PEROVSKITE SOLAR CELLS**

submitted by **MUSTAFA BURAK COŞAR** in partial fulfillment of the requirements  
for the degree of **Doctor of Philosophy in Metallurgical and Materials Engineering**  
**Department, Middle East Technical University** by,

Prof. Dr. Halil Kalıpçılar  
Dean, Graduate School of **Natural and Applied Sciences**

\_\_\_\_\_

Prof. Dr. Cemil Hakan Gür  
Head of Department, **Met. and Mat. Eng.**

\_\_\_\_\_

Prof. Dr. Ahmet Macit Özenbaş  
Supervisor, **Met. and Mat. Eng., METU**

\_\_\_\_\_

**Examining Committee Members:**

Prof. Dr. Mehmet Parlak  
Physics, METU

\_\_\_\_\_

Prof. Dr. Ahmet Macit Özenbaş  
Met. and Mat. Eng., METU

\_\_\_\_\_

Prof. Dr. M. Kadri Aydınol  
Met. and Mat. Eng., METU

\_\_\_\_\_

Assoc. Prof. Dr. Z. Göknur Büke  
Mat. Science and Nanotechnology Eng., TOBB ETU

\_\_\_\_\_

Assist. Prof. Dr. Şahin Coşkun  
Met. And Mat. Eng., Eskişehir Osmangazi University

\_\_\_\_\_

Date: 28.06.2019

**I hereby declare that all information in this document has been obtained and presented in accordance with academic rules and ethical conduct. I also declare that, as required by these rules and conduct, I have fully cited and referenced all material and results that are not original to this work.**

Name, Surname: Mustafa Burak Coşar

Signature:

## ABSTRACT

### **TUNING THE ELECTRON BEAM EVAPORATION PARAMETERS FOR THE PRODUCTION OF HOLE AND ELECTRON TRANSPORT LAYERS FOR PEROVSKITE SOLAR CELLS**

Coşar, Mustafa Burak  
Doctor of Philosophy, Metallurgical and Materials Engineering  
Supervisor: Prof. Dr. Ahmet Macit Özenbaş

June 2019, 210 pages

This study evaluates the use of electron beam evaporation technique for the deposition of electron and hole transport layers for perovskite solar cells where cell productions were performed in n-i-p structure. NiO and TiO layers were studied for hole transport layer and TiO<sub>2</sub> and Nb<sub>2</sub>O<sub>5</sub> layers were deposited for electron transport purposes. To optimize the suitable evaporation parameters for efficient perovskite cell production, single layers of each material were deposited at different conditions of oxygen flow rate, deposition temperature, deposition rate and plasma assistance. The structural, optical, and electrical properties of each layer were associated with the produced perovskite cells. Oxygen addition provides better cell performances in the case of both NiO and TiO hole transport layers; however, oxygen requirement of the TiO thin films were optimized at a lower value than NiO layers. When hole transport layer thicknesses were obtained at 75 nm and 50 nm for NiO and TiO, conversion efficiencies for these cells were recorded as best performances of 6.13 % and 5.72 %. Nb<sub>2</sub>O<sub>5</sub> compact electron transport layers were used in the production of the perovskite solar cells at planar, heat treated planar and Nb<sub>2</sub>O<sub>5</sub>- mesoporous TiO<sub>2</sub> bilayer architectures. Although, oxygen addition is crucial for the plasma assisted condition, it is detrimental for the unassisted condition for all types of architectures. It is detected

that plasma assistance yields better performance compared to unassisted deposition. The use of Nb<sub>2</sub>O<sub>5</sub>-mesoporous TiO<sub>2</sub> bilayer provides sharp enhancement in the cell performance and 13.87 % conversion efficiency was sustained.

Keywords: Electron Beam Evaporation, Perovskite Solar Cell, Compact Electron Transport Layer, Hole Transport Layer.

## ÖZ

### **PEROVSKİT GÜNEŞ HÜCRELERİNDE ELEKTRON VE BOŞLUK TAŞIYICI KATMANLARIN ÜRETİLMESİ İÇİN ELEKTRON IŞINI BUHARLAŞTIRMA PARAMETRELERİNİN OPTİMİZASYONU**

Coşar, Mustafa Burak  
Doktora, Metalurji ve Malzeme Mühendisliği  
Tez Danışmanı: Prof. Dr. Ahmet Macit Özenbaş

Haziran 2019, 210 sayfa

Bu çalışmada, n-i-p konfigürasyonundaki perovskit güneş hücrelerinin oluşturulmasında kullanılan elektron taşıyıcı ve boşluk taşıyıcı katmanların elektron ışını buharlaştırma tekniği kullanılarak üretilmesi değerlendirilmektedir. NiO ve TiO katmanları boşluk taşıyıcı katman olarak çalışılmıştır ve TiO<sub>2</sub> ile Nb<sub>2</sub>O<sub>5</sub> katmanları elektron taşıyıcı olarak kullanılmıştır. Uygun ince film büyütme parametrelerinin elde edilmesi için, bütün malzemeler tek katman olarak elektron ışını buharlaştırma tekniği ile farklı oksijen akış miktarlarında, kaplama sıcaklıklarında, kaplama hızlarında ve plazma desteği koşullarında oluşturulmuştur. Yapısal, optik ve elektriksel özellikler her bir katman için analiz edilmiştir ve sonuçlar üretilen perovskit hücreler üzerindeki kaplama parametrelerinin etkilerinin açıklanmasında kullanılmıştır. NiO ve TiO ince filmlerin büyütülmesinde oksijen katkısının hücre verimliliğini iyileştirdiği tespit edilmiştir. Bununla birlikte optimize edilen oksijen miktarının TiO boşluk taşıyıcı katmanı için NiO boşluk taşıyıcı katmanına göre daha az olduğu belirlenmiştir. NiO ve TiO boşluk taşıyıcı katman kalınlıkları olarak 75 nm ve 50 nm kalınlıkları uygulandığında, hücrelerden elde edilen verim değerleri sırası ile 6.13 % and 5.72 % olarak elde edilmiştir. Nb<sub>2</sub>O<sub>5</sub> kompakt elektron taşıyıcı katmanı perovskit güneş hücresi üretiminde düzlemsel, ısıtılmış düzlemsel ve Nb<sub>2</sub>O<sub>5</sub>-gözenekli TiO<sub>2</sub>

ikilisi hücre şekillerinde olmak üzere üç farklı mimaride kullanılmıştır. Plazma desteđi ile yapılan Nb<sub>2</sub>O<sub>5</sub> ince film kaplamalarında oksijen katkısı performansı iyileştirirken, plazma desteđi olmayan filmlerde ise oksijen katkısı verimlerde düşüşe neden olmuştur. Plazma desteđinin, tüm yapılarda plazma desteksiz kaplamalara göre daha verimli hücreler oluşturduđu tespit edilmiştir. Nb<sub>2</sub>O<sub>5</sub>-gözenekli TiO<sub>2</sub> ikili hücre yapısı verimlerde keskin bir artış sağlayarak 13.87 % çevrim verimi elde edilmiştir.

Anahtar Kelimeler: Elektron Işını İle Buharlaştırma, Perovskit Güneş Pili, Kompakt Elektron Taşıyıcı Katman, Boşluk Taşıyıcı Katman.

I would like to dedicate this thesis to my wife Kübra, my daughter Defne and my family for their loves and supports.

## ACKNOWLEDGEMENTS

First of all, I am very grateful to my supervisor Prof. Dr. A. Macit Özenbaş for his guidance, support during this work, and his great attention and patience on me from beginning until the end of my graduation.

It has been my pleasure and honor to work and share with my colleague Kerem Çağatay İçli. I am very grateful to my laboratory colleagues Çağrı Özdilek, Başar Süer, Utku Er, Merve Ertuğrul, Burak Yurdakul, and Bahadır Can Kocaoğlu for their support and friendship at every stage of this study and my graduation. I am also very grateful to all the staff of the Department of Metallurgical and Materials Engineering.

I gratefully acknowledge Alp Eren Sinan Özhan for the guidance and support in the experimental work. I would like to thank to Melih Kaldırım from ASELSAN for his assistance through XRD and Hall Effect measurements. Many thanks also to co-workers Hacı Batman, Gülgün Hamide Aydoğdu Kuru, Tolga Yelboğa, Levent Yaka, Emrah Atmaca, Serhat Soylu, Recep Uçar and Ahmet Çobanbaşı from ASELSAN for their help and supports.

I want to acknowledge Enver Kahveci from National Nanotechnology Research center (UNAM) for his assistance in XPS measurements. I want to thank you Central Laboratory of Middle East Technical University for their attention during UPS measurements. I would like to thank to all the staff of the GUNAM.

Finally, I would like to express my deepest gratitude to my family for sharing my hard times with me and their love, support and patience during my life.

## TABLE OF CONTENTS

ABSTRACT .....	v
ÖZ .....	vii
ACKNOWLEDGEMENTS .....	x
TABLE OF CONTENTS .....	xi
LIST OF TABLES .....	xvi
LIST OF FIGURES .....	xviii
LIST OF ABBREVIATIONS .....	xxiii
CHAPTERS	
1. INTRODUCTION .....	1
REFERENCES.....	5
2. LITERATURE REVIEW .....	7
2.1. Photovoltaic Energy Conversion.....	7
2.1.1. Main Properties and Definitions for Sunlight.....	8
2.1.2. Semiconductors.....	11
2.1.3. The p-n Junction .....	13
2.1.4. Absorption of the Light by Semiconductor .....	14
2.1.5. Recombination Losses in Solar Cells .....	16
2.1.6. Carrier Transport in Solar Cells.....	17
2.1.7. Output Parameters for Solar Cells .....	18
2.2. Types of Solar Cells and Main Materials in Production .....	21
2.2.1. Crystalline Silicon Solar Cells.....	21
2.2.2. Thin Film Solar Cells.....	23

2.2.2.1. Amorphous Silicon Solar Cells .....	23
2.2.2.2. Gallium Arsenide Solar Cells .....	24
2.2.2.3. Copper Indium Diselenide Solar Cells and Copper Indium Gallium Diselenide Solar Cells.....	25
2.2.2.4. Cadmium Telluride Solar Cells .....	26
2.2.3. Dye Sensitized Solar Cells .....	26
2.3. Perovskite Solar Cells .....	28
2.3.1. Working Principle of Perovskite Solar Cells .....	30
2.3.2. Device Architectures of Perovskite Solar Cells .....	31
2.3.3. Perovskite Sensitizer .....	35
2.3.3.1. Crystal Structure of Perovskite.....	35
2.3.3.2. Compositional Analysis of Perovskite.....	37
2.3.4. Deposition Techniques for Perovskite Sensitizer Layer .....	39
2.3.4.1. Solution Based Depositions.....	40
2.3.4.2. Vapor Based Deposition .....	44
2.3.5. Electron Transport Layer (ETL).....	45
2.3.5.1. Compact Layer.....	46
2.3.5.2. Scaffold Layer .....	48
2.3.6. Hole Transport Layer .....	49
2.3.7. Electrodes .....	52
REFERENCES .....	55
3. EXPERIMENTAL METHODS .....	59
3.1. Thin Film Deposition .....	60
3.1.1. Vacuum Based Thin Film Deposition .....	61

3.1.1.1.	Some of the Parameters of the Vacuum Based Thin Film Deposition .....	61
3.1.1.2.	Physical Vapor Deposition .....	63
3.1.1.3.	Evaporation Processes .....	64
3.1.1.4.	Electron Beam Evaporation .....	65
3.1.1.5.	Sputtering.....	66
3.1.1.6.	Film Formation in PVD Coatings .....	66
3.1.2.	Sol-Gel Coatings .....	68
3.1.2.1.	Spin Coating.....	69
3.2.	Construction of Hybrid Mesoporous and Planar Perovskite Solar Cells .....	70
3.2.1.	Etching of the Substrate .....	71
3.2.2.	Substrate Cleaning .....	72
3.2.3.	Preparation of Compact Layer .....	72
3.2.4.	Preparation of Mesoporous Layer.....	76
3.2.5.	TiCl <sub>4</sub> Treatment for Mesoporous Layer.....	77
3.2.6.	Preparation of Perovskite Layer .....	78
3.2.7.	Preparation of Hole Transport Layer .....	79
3.2.8.	Deposition of Back Electrode Layer.....	80
3.3.	Characterization Techniques .....	82
3.3.1.	Characterization of Single Layers.....	83
3.3.1.1.	Determination of Coating Thickness and Refractive Index Dispersion .....	83
3.3.2.	Characterization of Perovskite Solar Cells .....	89
3.3.2.1.	Electrochemical Impedance Spectroscopy (EIS).....	90

REFERENCES .....	93
4. PLASMA ASSISTED LOW TEMPERATURE ELECTRON BEAM DEPOSITED NiO THIN FILMS FOR ELECTRO-OPTIC APPLICATIONS .....	95
4.1. Experimental Studies .....	96
4.2. Results and Discussions .....	98
4.2.1. Structural Properties .....	98
4.2.2. Optical Properties .....	105
4.2.3. Electrical Properties .....	109
4.3. Conclusion .....	115
REFERENCES .....	117
5. EFFECT OF OXYGEN FLOW RATE ON THE LOW TEMPERATURE DEPOSITION OF TITANIUM MONOXIDE THIN FILMS VIA ELECTRON BEAM EVAPORATION .....	121
5.1. Experimental Procedure .....	123
5.2. Results and Discussions .....	125
5.3. Conclusion .....	139
REFERENCES .....	141
6. ELECTRON BEAM EVAPORATED NiO AND TiO HOLE TRANSPORT LAYERS IN n-i-p CONFIGURED PEROVSKITE SOLAR CELL .....	147
6.1. Experimental Studies .....	148
6.2. Results and Discussions .....	151
6.2.1. Characterization of Single Layer TiO <sub>2</sub> Thin Films.....	151
6.2.2. Characterization of Perovskite Thin Films.....	157
6.2.3. Characterization of Perovskite Solar Cells.....	158
6.3. Conclusion .....	166

REFERENCES.....	169
7. TUNING THE ELECTRON BEAM EVAPORATION PARAMETERS FOR THE PRODUCTION OF NIOBIUM PENTOXIDE COMPACT LAYERS FOR PEROVSKITE SOLAR CELLS .....	171
7.1. Experimental Studies.....	173
7.1.1. Deposition of Single Nb <sub>2</sub> O <sub>5</sub> Thin Films and Their Characterizations ....	173
7.1.2. Perovskite Solar Cell Production and Their Characterizations .....	174
7.2. Results and Discussions .....	177
7.2.1. Optical Characterization of Single Layer Nb <sub>2</sub> O <sub>5</sub> Thin Films .....	177
7.2.2. Structural Characterization of Single Layer Nb <sub>2</sub> O <sub>5</sub> Thin Films .....	182
7.2.3. Characterization of Perovskite Solar Cells .....	186
7.1. Conclusion.....	195
REFERENCES.....	197
8. SUMMARY, CONCLUSIONS AND SUGGESTIONS.....	201
CURRICULUM VITAE .....	209

## LIST OF TABLES

### TABLES

Table 3.1. Pressure level and evaporated molecule relation.....	61
Table 4.1. Deposition parameters for NiO thin films. ....	98
Table 4.2. Grain size and lattice parameter of NiO thin films.....	100
Table 4.3. Amounts of Ni and O atoms. ....	104
Table 4.4. Thicknesses and band gaps of NiO thin films. ....	109
Table 4.5. Hall effect measurements of NiO thin films for different deposition parameters.....	111
Table 5.1. Band gap values of titanium monoxide thin films.....	133
Table 5.2. Hall Effect measurements of titanium oxide thin films for different oxygen flow rates. ....	136
Table 6.1. Deposition conditions for NiO and TiO HTLs in the perovskite solar cell production.....	151
Table 6.2. Cell parameters of the devices produced with NiO HTL deposited at different oxygen flow rates of 0, 10, 25 and 50 sccm.....	160
Table 6.3. Cell parameters of the devices produced with NiO HTL deposited at different deposition temperatures: 30, 80, and 170 °C. ....	161
Table 6.4. Cell parameters of the devices produced with NiO HTL deposited at different layer thicknesses: 10, 25, 50, 75 and 100 nm. ....	162
Table 6.5. Cell parameters of the devices produced with TiO HTL deposited at different layer thicknesses: 10, 25, 50, 75 and 100 nm. ....	164
Table 6.6. Cell parameters of the devices produced with TiO HTL deposited at different oxygen flow rates of 0, 1, 2, 5 and 10 sccm.....	165
Table 7.1. Deposition parameters for single layer Nb <sub>2</sub> O <sub>5</sub> thin films and cell configuration for these deposition conditions.....	175

Table 7.2. Actual thickness and band gap values for single layer Nb<sub>2</sub>O<sub>5</sub> thin films for as deposited and heat treated conditions. ....179

Table 7.3. Measured photovoltaic parameters for all cell configurations.....191

Table 7.4. Charge transfer (R<sub>ct</sub>) and recombination (R<sub>rec</sub>) resistances of the cells. ....194

## LIST OF FIGURES

### FIGURES

Figure 2.1. Radiation distribution from perfect blackbody sources at three different temperatures.....	9
Figure 2.2. Simplified schematic of sun. ....	9
Figure 2.3. Schematic demonstration of air mass.....	10
Figure 2.4. Energy band diagram of semiconductor materials.....	11
Figure 2.5. Energy levels for donor (n-type doping) and acceptor (p-type doping) states. ....	13
Figure 2.6. Band diagram and band bending after the formation of p-n junction. ....	14
Figure 2.7. Absorption phenomena in both direct and indirect band gap materials..	15
Figure 2.8. Recombination mechanisms.....	16
Figure 2.9. Current-Voltage curves for a solar cell. ....	19
Figure 2.10. Series and shunt resistances on an I-V curve. ....	20
Figure 2.11. Architecture of the conventional silicon solar cell.....	22
Figure 2.12. Main components and working steps for DSSC's. ....	27
Figure 2.13. Working principle of perovskite solar cells. ....	31
Figure 2.14. Formal and inverted mesoporous PSC architectures.....	33
Figure 2.15. Formal and inverted planar PSC architectures.....	34
Figure 2.16. Crystal structure of perovskite materials.....	36
Figure 2.17. Demonstration of one step deposition process.....	41
Figure 2.18. Demonstration of anti-solvent dripping method. ....	42
Figure 2.19. Two step deposition of perovskite layer. ....	44
Figure 2.20. Vapor assisted deposition of perovskite layer.....	44
Figure 2.21. Conduction band edge positions of alternative compact ETLs.....	46
Figure 2.22. Valence band edge positions of alternative HTLs. ....	49

Figure 3.1. Vacuum pumps: a) Mechanical pump, b) Diffusion pump, c) Turbomolecular pump, and d) Cryo pump.....	62
Figure 3.2. Components of electron beam source.....	65
Figure 3.3. Thornton zone model.....	67
Figure 3.4. Four steps of the spin coating process. ....	70
Figure 3.5. Etching procedure of the FTO coated glass.....	71
Figure 3.6. Tecport deposition system. ....	73
Figure 3.7. Components and working principle of the plasma source.....	74
Figure 3.8. Pre-melted material for e-beam evaporation. ....	75
Figure 3.9. Demonstration of Adduct Method.....	79
Figure 3.10. Sputtering system. ....	81
Figure 3.11. Mask used for gold back contact coating. ....	82
Figure 3.12. Final perovskite solar cell used for the measurements. ....	82
Figure 3.13. a) Young double slit experiment, b) constructive and destructive interference.....	84
Figure 3.14. Reflection from thin film/air and thin film/substrate interfaces.....	85
Figure 3.15. Formation of interference fringes when thin films with different refractive indices are deposited on glass which has a refractive index of 1.52.....	86
Figure 3.16. Refractive index dispersion of SiO <sub>2</sub> . ....	87
Figure 3.17. Optilayer characterization software fitting algorithms.....	88
Figure 3.18. Optilayer characterization software fitting process and calculated refractive index-coating thickness values. ....	89
Figure 3.19. Nyquist plot of a cell with modelled equivalent circuit.....	91
Figure 4.1. X-Ray diffraction of NiO thin films for different deposition parameters: a) oxygen flow rate, b) deposition temperature, c) deposition rate, d) oxygen flow rate with plasma assistance. ....	99
Figure 4.2. SEM images of NiO thin films deposited at different oxygen flow rates. ....	101
Figure 4.3. SEM images of NiO thin films deposited at different temperatures. ....	101
Figure 4.4. SEM images of NiO thin films at different deposition rates. ....	102

Figure 4.5. SEM images of NiO thin films deposited at different oxygen flow rates with plasma assistance.....	102
Figure 4.6. XPS graph of nickel for NiO thin film.....	103
Figure 4.7. XPS graphs of oxygen for NiO thin films for different deposition parameters: a) oxygen flow rate, b) deposition temperature, c) deposition rate, d) oxygen flow rate with plasma assistance.....	104
Figure 4.8. Transmission spectrum of NiO thin films for different deposition parameters: a) oxygen flow rate, b) deposition temperature, c) deposition rate, d) oxygen flow rate with plasma assistance.....	106
Figure 4.9. Reflection spectrum of NiO thin films for different deposition parameters: a) oxygen flow rate, b) deposition temperature, c) deposition rate, d) oxygen flow rate with plasma assistance.....	107
Figure 4.10. Refractive index dispersion of NiO thin films for different deposition parameters: a) oxygen flow rate, b) deposition temperature, c) deposition rate, d) oxygen flow rate with plasma assistance.....	108
Figure 4.11. UPS spectrum of NiO deposited films for different deposition parameters: a) oxygen flow rate, b) deposition temperature, c) deposition rate, d) oxygen flow rate with plasma assistance (1:onset and 2:cutoff positions).....	112
Figure 4.12. Band positions of NiO thin films for different deposition parameters: a) oxygen flow rate, b) deposition temperature, c) deposition rate, d) oxygen flow rate with plasma assistance.....	114
Figure 5.1. X-ray diffraction patterns of titanium monoxide thin films a) as deposited, and b) vacuum heat treated (A and R denote anatase and rutile phases of titanium dioxide, respectively).....	126
Figure 5.2. Cross sectional SEM images of titanium monoxide thin films deposited using different oxygen flow rates.....	128
Figure 5.3. XPS analysis of TiO thin films for a) titanium and b) oxygen.....	130
Figure 5.4. Transmission measurements of thin films deposited a) at 0, 1, 2, 5 and 10 and b) at 25 and 50 sccm oxygen flow rates.....	131

Figure 5.5. The variation of $(h\nu\alpha)^2$ as a function of $h\nu$ for titanium monoxide thin films deposited at 2, 5, 10, 25 and 50 sccm oxygen flow rates. ....	133
Figure 5.6. Reflectance and Kubelka-Munk function analysis (in the inset) of TiO thin films deposited at 0 and 1 sccm oxygen flow rates.....	135
Figure 5.7. UPS spectra of titanium monoxide thin films deposited at 0, 1, and 10 sccm oxygen flow rates a) onset b) cut-off. ....	138
Figure 5.8. Energy band levels of titanium monoxide thin films deposited at 0, 1, and 10 sccm oxygen flow rates.....	138
Figure 6.1. a) Cross-sectional image of TiO <sub>2</sub> compact layer b) Surface of the compact layer.....	152
Figure 6.2. XRD patterns of TiO <sub>2</sub> compact layer for as deposited condition (0 sccm oxygen flow) and heat treated conditions using different oxygen flow rates as 0 sccm, 5 sccm, 15 sccm and 25 sccm. ....	153
Figure 6.3. XPS spectra of a) Ti <sup>+4</sup> 2p level and b) O 1s level.....	154
Figure 6.4. Optical transmittance spectrum of TiO <sub>2</sub> thin films which were deposited at 0, 5, 15, and 25 sccm oxygen flow rates. ....	156
Figure 6.5. Refractive index dispersion for TiO <sub>2</sub> thin films which were deposited at 0, 5, 15, and 25 sccm oxygen flow rates. ....	156
Figure 6.6. SEM images of perovskite thin film a) surface and b) cross-section. ...	157
Figure 6.7. XRD pattern of CH <sub>3</sub> NH <sub>3</sub> PbI <sub>3</sub> perovskite thin film. ....	158
Figure 6.8. J-V curves for perovskite solar cells produced with NiO HTL deposited at different oxygen flow rates of 0, 10, 25 and 50 sccm. ....	160
Figure 6.9. J-V curves for perovskite solar cells produced with NiO HTL deposited at different deposition temperatures: 30, 80, and 170 °C. ....	161
Figure 6.10. J-V curves for perovskite solar cells produced with NiO HTL deposited at different layer thicknesses: 10, 25, 50, 75 and 100 nm. ....	163
Figure 6.11. J-V curves for perovskite solar cells produced with TiO HTL deposited at different layer thicknesses: 10, 25, 50, 75 and 100 nm. ....	164
Figure 6.12. J-V curves for perovskite solar cells produced with TiO HTL deposited at different oxygen flow rates of 0, 1, 2, 5 and 10 sccm. ....	166

Figure 7.1. Transmission spectrum of Nb <sub>2</sub> O <sub>5</sub> thin films a) Plasma assisted deposition b) Non-plasma assisted deposition, c) After the heat treatment process. ....	178
Figure 7.2. Refractive index spectrum of Nb <sub>2</sub> O <sub>5</sub> thin films a) Plasma assisted deposition, b) Non-plasma assisted deposition, c) Plasma assisted deposited samples after heat treatment, and d) Non-plasma assisted deposited samples after heat treatment. ....	180
Figure 7.3. The variation of $(h\nu\alpha)^{1/2}$ as a function of $h\nu$ for Nb <sub>2</sub> O <sub>5</sub> thin films a) Plasma assisted depositions, and b) Non-plasma assisted depositions. ....	181
Figure 7.4. X-ray diffraction pattern of Nb <sub>2</sub> O <sub>5</sub> thin films. ....	182
Figure 7.5. SEM images of Nb <sub>2</sub> O <sub>5</sub> thin films. ....	183
Figure 7.6. XPS analyses of Nb <sub>2</sub> O <sub>5</sub> thin films; a) Plasma assisted deposition condition for niobium, b) Non-plasma assisted deposition for niobium, c) Plasma assisted deposition condition for oxygen, d) Non-plasma assisted deposition for oxygen, e) Plasma assisted deposition condition for niobium (heat treated) and f) Non-plasma assisted deposition for niobium (heat treated). ....	185
Figure 7.7. Cross sectional images of a) planar and b) mesoporous perovskite solar cells. ....	187
Figure 7.8. J-V graphs of as deposited Nb <sub>2</sub> O <sub>5</sub> compact layer used for perovskite solar cells of planar configuration. ....	188
Figure 7.9. J-V graphs of heat treated Nb <sub>2</sub> O <sub>5</sub> compact layer used for the production of planar perovskite solar cells. ....	190
Figure 7.10. J-V graphs of perovskite cells produced using mesoporous TiO <sub>2</sub> layer and Nb <sub>2</sub> O <sub>5</sub> compact layer. ....	191
Figure 7.11. Nyquist plots of the cells produced using a) Planar Nb <sub>2</sub> O <sub>5</sub> , b) Planar heat treated Nb <sub>2</sub> O <sub>5</sub> , c) Nb <sub>2</sub> O <sub>5</sub> compact layer and mesoporous TiO <sub>2</sub> and d) Equivalent circuit model used to fit the impedance data. ....	194

## LIST OF ABBREVIATIONS

### ABBREVIATIONS

ALD	: Atomic Layer Deposition
AM	: Air Mass
CBM	: Conduction Band Minimum
CVD	: Chemical Vapor Deposition
DC	: Direct Current
DSSC	: Dye Sensitized Solar Cell
EIS	: Electrochemical Impedance Spectroscopy
ETL	: Electron Transport Layer
HOMO	: Highest Occupied Molecular Orbital
HTL	: Hole Transport Layer
HWOT	: Half Wave Optical Thickness
LED	: Light Emitting Diodes
LPE	: Liquid Phase Epitaxy
LUMO	: Lowest Unoccupied Molecular Orbital
MA	: Methylammonium
MAI	: Methylammonium Iodide
MBE	: Molecular Beam Epitaxy
MOCVD	: Metal-Organic Chemical Vapor Deposition
MOSFET	: Metal Oxide Semiconductor Field Effect Transistor

MP	: Maximum Power
NREL	: National Research Energy Laboratory
OC	: Open Circuit
PAPVD	: Plasma Assisted Physical Vapor Deposition
PLD	: Pulsed Laser Deposition
PSC	: Perovskite Solar Cell
PVD	: Physical Vapor Deposition
QWOT	: Quarter Wave Optical Thickness
RF	: Radio Frequency
SC	: Short Circuit
SEM	: Scanning Electron Microscope
TCO	: Transparent Conductive Oxide
TFT	: Thin Film Transistor
UPS	: Ultraviolet Electron Spectroscopy
XPS	: X-Ray Photoelectron Spectroscopy
XRD	: X-Ray Diffraction
VBM	: Valence Band Maximum

## **CHAPTER 1**

### **INTRODUCTION**

Solar power has great potential to take in place of fossil fuels. Solar energy is never ending and environmentally friendly source. The photovoltaic market has been dominated since many years by the crystalline silicon solar cells. To become an important candidate in photovoltaic industry, high stability, high conversion efficiency and low production cost should be maintained. Potential of third generation solar cells was understood about twenty years ago. Dye sensitized solar cells, organic solar cells and quantum dot sensitized solar cells belong to this generation. Main advantages of the third generation solar cells are low cost production, easy application, suitability to flexible substrates and processing from readily available materials. However, efficiency gap with crystalline silicon solar cells was not reduced up to the evolution of perovskite solar cells from dye sensitized solar cells. First attempt was performed in 2009, and potential of perovskite solar cells was determined at 2012. In a short period of time, cell efficiencies became higher than 20 %. Addition to high energy conversion potential, perovskite solar cells offer high stability in outside usage. Scalability is the major drawback of the perovskite solar cells like all third generation solar cells [1-3].

Perovskite absorber and small molecule organic hole transport layer are the two main components which are the reasons of efficiency boosting of the perovskite solar cells. Spiro-OMeTAD hole conductor plays an important role in the evolution of perovskite solar cells, because it replaced the liquid electrolyte used in dye sensitized solar cells. Therefore, it provides the high efficiency together with high outdoor stability. Despite the advantages of spiro-OMeTAD, there are many efforts to replace it with some alternative materials or the possibility of hole conductor free cell production. High

cost and long-term stability problem of spiro-OMeTAD are the main barriers to the commercialization of the perovskite solar cells. Inorganic oxide hole conductors are widely studied and potential use of them was observed. Although there are some studies using of CuO, VO<sub>x</sub>, and MoO<sub>x</sub>, as hole transport layer, NiO<sub>x</sub> is the most promoting material in this group due to its suitable band gap edges, wide band gap nature, easy processing and low cost. Their main disadvantage is the inability of low temperature processing of inorganic oxide materials on top of perovskite absorber layer. Therefore, studies mostly focus on the inverted p-i-n cell design for these hole conductors [4-6].

Compact layer is another critical component for the production of efficient perovskite solar cells. Due to the charge transport nature of the perovskite absorber, it is required to use hole blocking layer to minimize the recombination reactions. For efficient hole blocking, this layer should have enough thickness and provide effective electron transfer. For this reason, compact layer is mostly chosen from n-type conductor alternatives. TiO<sub>2</sub> is well known and mostly used compact layer material which has advantages such as environmentally friendly nature, wide band gap, high electron mobility, and good stability. However, alternative materials have been studied widely to produce better electron transfer and reduce the interfacial resistances between transparent conducting oxide and compact layer. ZnO, Cs<sub>2</sub>CO<sub>3</sub>, SnO<sub>2</sub>, WO<sub>3</sub>, Nb<sub>2</sub>O<sub>5</sub> and doped TiO<sub>2</sub> are some of the candidates for compact layer. Perovskite solar cells can be produced in mesoporous or planar architectures whether a mesoporous layer is involved or not. Mesoporous layers are directly deposited on top of the compact layer and they can be used just for scaffold to perovskite absorber and increase the electron transfer process [4, 7].

Both hole transport and compact electron transport layers can be deposited by solution processing or vacuum coating techniques. Solution based production is cost effective and easily applicable method; however, quality of thin films depends on many factors such as humidity, environment, solution chemistry. Therefore, repeatability is always

questionable in these solution-based processes. Also, in most of the cases, oxide inorganic layers should be heat treated for the removal of organics or additives to enhance the crystallization together with interconnection. Drawbacks in solution processing make vacuum deposition critical in the production of perovskite solar cells, although, vacuum depositions provide higher cost compared to solution-based processing. Vacuum depositions are reliable, industrial and highly reproducible techniques. In addition, upon modifying the process parameters, stoichiometry and band gap modification can be applicable in vacuum deposition. In addition, dense, uniform, high quality, and good coverage films can easily be obtained in vacuum evaporation techniques [8, 9].

The objective of this work is to develop mesoporous and planar perovskite solar cells using electron beam evaporation technique for the production of compact electron transport and hole transport layers. NiO and TiO layers were studied as suitable p-type conductors for hole transportation. Although, there are some studies using NiO in inverted p-i-n cell configuration, there is no previous study using TiO for hole conducting purpose [10, 11]. Both materials were firstly studied in single layer forms. While NiO single layers were deposited at different oxygen flow rates, deposition temperatures, deposition rates and plasma assistance, TiO single layers were studied just depending on different oxygen flow rate conditions. Structural, optical and electrical properties of single layers were determined using different characterization tools. The studies performed about the characterization of NiO and TiO single layers were published in Journal of Vacuum Science & Technology A in the form of two separate manuscripts [12, 13]. After that, these deposition conditions were used to develop NiO and TiO hole conductor containing perovskite solar cells. Also, layer thickness optimization was performed for both hole conductor materials. Nb<sub>2</sub>O<sub>5</sub> layers were studied for the electron transfer purposes as a final study. Nb<sub>2</sub>O<sub>5</sub> is a very promising alternative compact layer material due to its high carrier mobility, low hysteresis and suitable conduction band edge position. Also, Nb<sub>2</sub>O<sub>5</sub> is transparent, air

and water stable and band position can easily be tuned by changing its stoichiometry or crystalline structure. Spiro-OMeTAD was used for hole conductor material for the cell production in this case. Similar to NiO and TiO, Nb<sub>2</sub>O<sub>5</sub> layers were studied in single layers and after that this knowledge was transferred to the production of perovskite solar cells. Oxygen flow rate and effect of plasma assistance for the deposition were the analyzing parameters for the production of Nb<sub>2</sub>O<sub>5</sub> electron transport layer. This study is currently under review in the journal of Solar Energy.

## REFERENCES

- [1] A. B. Djurišić, F. Z. Liu, H. W. Tam, M. K. Wong, A. Ng, C. Surya, W. Chen, Z. B. He, Perovskite solar cells - an overview of critical issues, *Progress in Quantum Electronics*, 53 (2017) 1-37.
- [2] M. I. H. Ansari, A. Qurashi, M. K. Nazeeruddin, Frontiers, opportunities, and challenges in perovskite solar cells: A critical review, *Journal of Photochemistry and Photobiology C-Photochemistry Reviews*, 35 (2018) 1-24.
- [3] T. T. Xu, L. X. Chen, Z. H. Guo, T. L. Ma, Strategic improvement of the long-term stability of perovskite materials and perovskite solar cells, *Physical Chemistry Chemical Physics*, 18 (2016) 27026-27050.
- [4] A. R. B. Mohd Yusoff, P. Gao, M. K. Nazeeruddin, Recent progress in organohalide lead perovskites for photovoltaic and optoelectronic applications, *Coordination Chemistry Reviews*, 373 (2018) 258-294.
- [5] Z. H. Bakr, Q. Wali, A. Fakharuddin, L. Schmidt-Mende, T. M. Brown, R. Jose, Advances in hole transport materials engineering for stable and efficient perovskite solar cells, *Nano Energy*, 34 (2017) 271-305.
- [6] Z. Liu, A. Zhu, F. Cai, L. Tao, Y. Zhou, Z. Zhao, Q. Chen, Y.-B. Cheng, H. Zhou, Nickel oxide nanoparticles for efficient hole transport in p-i-n and n-i-p perovskite solar cells, *Journal of Materials Chemistry A*, 5 (2017) 6597-6605.
- [7] M. Habibi, F. Zabihi, M. R. Ahmadian-Yazdi, M. Eslamian, Progress in emerging solution-processed thin film solar cells – part ii: Perovskite solar cells, *Renewable and Sustainable Energy Reviews*, 62 (2016) 1012-1031.
- [8] J. Feng, Z. Yang, D. Yang, X. Ren, X. Zhu, Z. Jin, W. Zi, Q. Wei, S. F. Liu, E-beam evaporated Nb<sub>2</sub>O<sub>5</sub> as an effective electron transport layer for large flexible perovskite solar cells, *Nano Energy*, 36 (2017) 1-8.
- [9] B. Abdollahi Nejand, V. Ahmadi, H. R. Shahverdi, New physical deposition approach for low cost inorganic hole transport layer in normal architecture of durable perovskite solar cells, *ACS Applied Materials & Interfaces*, 7 (2015) 21807-21818.
- [10] Z. Zhu, Y. Bai, T. Zhang, Z. Liu, X. Long, Z. Wei, Z. Wang, L. Zhang, J. Wang, F. Yan, S. Yang, High-performance hole-extraction layer of sol-gel-processed NiO nanocrystals for inverted planar perovskite solar cells, *Angewandte Chemie*, 126 (2014) 12779-12783.

- [11] S. Seo, I. J. Park, M. Kim, S. Lee, C. Bae, H. S. Jung, N.-G. Park, J. Y. Kim, H. Shin, An ultra-thin, un-doped NiO hole transporting layer of highly efficient (16.4%) organic–inorganic hybrid perovskite solar cells, *Nanoscale*, 8 (2016) 11403-11412.
- [12] M. B. Cosar, K. C. Icli, M. Ozenbas, Effect of oxygen flow rate on the low temperature deposition of titanium monoxide thin films via electron beam evaporation, *Journal of Vacuum Science & Technology A*, 37 (2019) 031505.
- [13] M. B. Cosar, K. C. Icli, M. Ozenbas, Plasma assisted low temperature electron beam deposited NiO thin films for electro-optic applications, *Journal of Vacuum Science & Technology A*, 36 (2018) 031501.

## CHAPTER 2

### LITERATURE REVIEW

#### 2.1. Photovoltaic Energy Conversion

Photo electrochemical effect was discovered by Becquerel in 1839 using halide coated platinum electrodes immersed in an electrolyte while exposing light in the study. This experiment is accepted as the origin of photovoltaic studies. Followed by Becquerel, Smith had shown that selenium bars have photoconducting properties in 1873 which is the first study regarding all solid materials. In 1940s, p-n junction was discovered by Ohl, who used silicon material with trace amount of impurities. Present technology for solar cells was reported firstly by Chapman and Fuller at 1954 using semiconductor junctions. After the understanding of the potential of silicon solar cells, their first market became space satellites. However, developments in the technology reduce the cost/energy ratio and also increase the cell performance. Also, the decrease in the amount of fossil fuels together with increase in the demand for energy opened an era for the use of solar cells in commercial applications [1-4].

Photovoltaic cells are also remarkable in many studies due to their clean and infinite nature. Fuel sources will become scarce in the near future and they are always debatable as a pollutant energy source. Other advantages of photovoltaic cells can be given as low operating costs, no moving parts, high reliability, silence, quick installation and applicability to any area. Solar cells can be found in many application areas in daily life. Studies in photovoltaic area are conducted under many branches. In some of them, while the main idea is the lowering of cost, others focus to advance photo conversion efficiency [2, 3].

Solar cells have a growing industry, their ratio in total energy production increases year by year. However, fuel sources continue to be the dominant energy. Because, sunlight is relatively low density energy compared to fuel energy. Also, initial costs of solar cells are more expensive which create longer amortization periods. Unclearness continues in the storage of electricity produced from solar cells. Final drawback is the useful life time and photo conversion efficiency of solar cells which are not sufficient for some of the applications [2, 5].

### **2.1.1. Main Properties and Definitions for Sunlight**

Light was a mystical topic starting from earliest times. Many studies were realized to understand the nature of light. Firstly, light was accepted as small particles in late 1600s from the view of Newton's mechanic laws. At 1800s, Young and Fresnel show interference effect which is the result of wave motion. Electromagnetic radiation theory of Maxwell was accepted at 1860s which presents the light as a portion of electromagnetic spectrum. Today, accepted theory is the particle-wave duality of light which is summarized by the equation 2.1. In this equation, light has a specific frequency ( $\nu$ ) or wavelength ( $\lambda$ ), and energy ( $E$ ) of light is dependent on the Planck's constant ( $h$ ) and velocity of light ( $c$ ) in addition to wavelength [6].

$$E = h\nu = \frac{hc}{\lambda} \quad \text{Eq. [2.1]}$$

Blackbody is an ideal absorber and emitter. When a blackbody is heated, it starts to glow and emits electromagnetic radiation. When the heating temperature is increased, emissivity shifts to lower wavelength and higher emissivity power is obtained [6]. Figure 2.1 demonstrates the emittance from blackbody object at different temperatures.

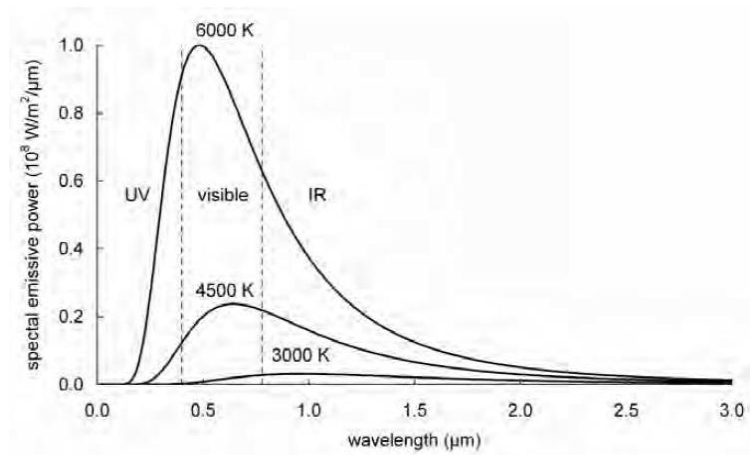


Figure 2.1. Radiation distribution from perfect blackbody sources at three different temperatures [3].

Internal temperature of sun is above 20 million K, nuclear fusion reactions are the reason of these high temperatures. Heat transfer in the sun is explained in Figure 2.2. Heat is radiated to the surface regions of sun where hydrogen ions absorb most of the energy. Remaining energy is transferred by convective way to reach photosphere and after that re-radiation happens at the surface of sun. This radiation is approximately same with the blackbody radiation which is around 6000 K [3, 5, 6].

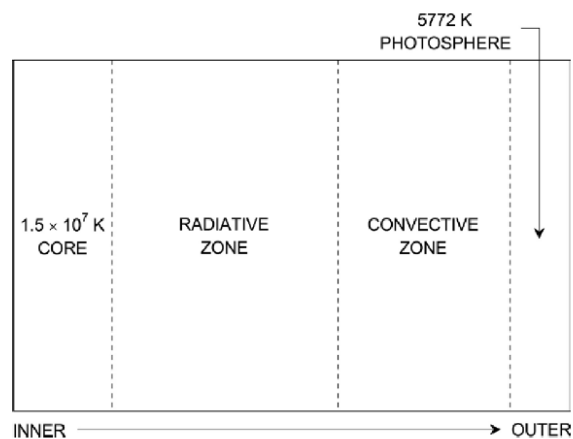


Figure 2.2. Simplified schematic of sun [1].

Radiation from the sun is mostly constant; however, amount of photon reaches to the surface of earth is variable. Maximum radiation reaches to earth surface when the sky is clear and sun is located at directly overhead. Shortest path length is obtained at overhead position. Position of sun according to earth surface is defined using Air Mass (AM) term which is defined in equation 2.2. For the overhead position, angle is zero which is the AM1 condition. For the photovoltaic studies, AM1.5 position is used which corresponds to 48.2°. AM0 is the spectral distribution of sunlight at outside of the atmosphere. Figure 2.3 explains the air mass term. Sun can reach to earth surface directly or diffusing from any object into the sky. Total of direct and diffuse radiation is known as global radiation which is shown as AM1.5G. 30 % energy of the sun does not reach to the surface of earth. Main reasons of this reduction are Rayleigh scattering, scattering by aerosols and dust particles and absorption from atmospheric gases [6, 7].

$$AirMass = \frac{1}{\cos(\theta)} \quad \text{Eq. [2.2]}$$

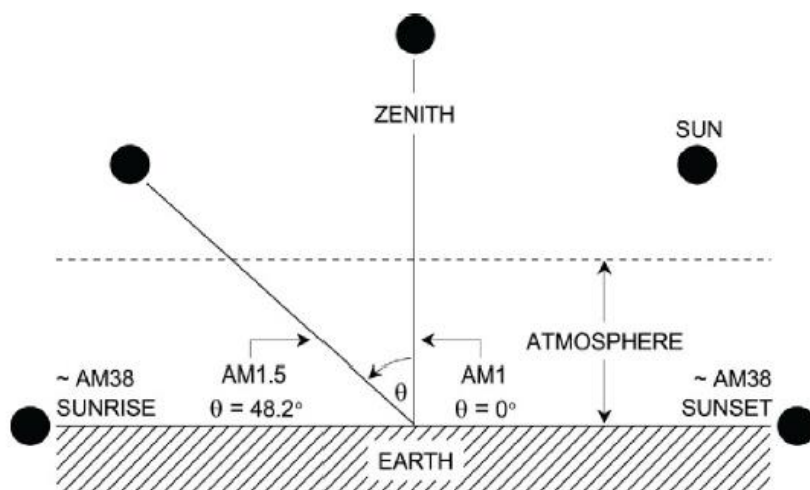


Figure 2.3. Schematic demonstration of air mass [1].

### 2.1.2. Semiconductors

Semiconductor materials are used for the production of photovoltaic cells. Electrical properties of semiconductors were explained in two different models: bond and band models. In the bond model, covalent bonds are present between the semiconductor atoms. Covalent bonds are stable without stimulant and electrons cannot move outside bond area. When any kind of energy is subjected, bonds are broken and electrons become free to move. For band model, energy levels are used to explain conductive nature of semiconductors under any stimulation. In the band model, materials are formed from two energy bands; they are valence and conduction bands. Valence band is the same with electrons inside the area of covalent bonds. Conduction band corresponds to free electrons. There is a gap between the valence and conduction band which is called as forbidden gap. To make any semiconductor conductive, it requires that higher stimulation energy is required to overcome this forbidden band barrier [2, 3, 8]. Electrons in valence band jump to conduction band, holes are formed inside in valence band which is shown in Figure 2.4.

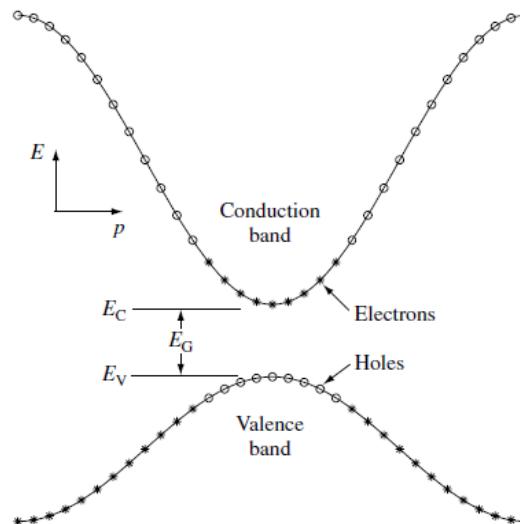


Figure 2.4. Energy band diagram of semiconductor materials [2].

Most commonly used semiconductor is silicon which can be in the form of single crystal, polycrystalline and amorphous. GaAs, GaInP, Cu(InGa)Se<sub>2</sub>, and CdTe are some of the other semiconductor materials used in the production of solar cells. Compound semiconductors are formed from group III-V or Group II-VI elements. There are two main parameters while choosing the semiconductor materials; the ease in production and absorption character. Silicon becomes the first choice from the beginning of the solar cell technology due to well matched absorption band with the solar spectrum and therefore, its fabrication technology is developed with time. Change of balance between electrons and holes is realized by doping of impurity elements. Doping of semiconductors with one more electron supplies n-type material, whereas one less electron creates a p-type material. For the silicon solar cells, doping is realized with substitutional impurities in which impurity atom is located at the exact position of host atom. To create n-type material, silicon atoms are substituted by group V elements (such as phosphorus), whereas, group III elements (such as boron) are used in doping to form a p-type material [2, 3, 8].

When group V dopants replace with silicon atoms, four electrons of group V element make covalent bond with silicon host atoms. One electron is remained, and this electron is located neither in valence band nor in conduction band. However, this electron can be free with lower energy compared to the undoped condition. At this situation, an energy level is formed in forbidden gap and near to the conduction band (Figure 2.5). For the other case, there are not enough valence electrons to satisfy four covalent bonds when doped with group III atoms. In this case, holes are formed and again, lower energy is required to release the holes. Therefore, an energy level is formed above the valence band and inside the forbidden gap. In doped semiconductors, there are excess carriers in terms of electrons and holes, they are also mobile. However, the mobility of these carriers is random, and net current is not generated in one direction. p-n junction is required to create a driving force which is supplied by the contact of p and n type semiconductors [2, 3, 8].

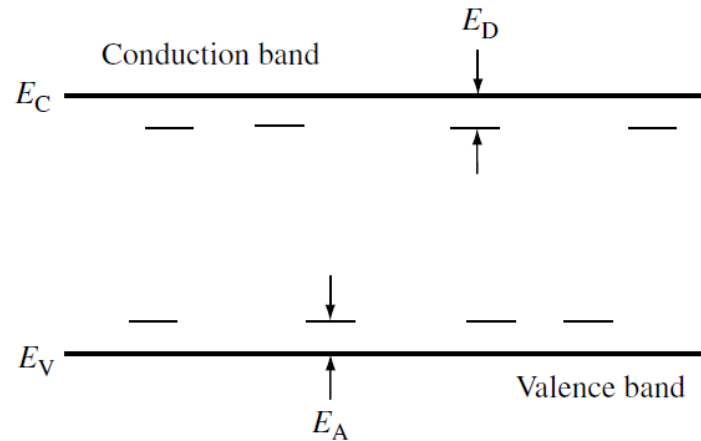


Figure 2.5. Energy levels for donor (n-type doping) and acceptor (p-type doping) states [2].

### 2.1.3. The p-n Junction

p-n junction is the fundamental of solar cells which is formed when a p-type and an n-type semiconductor materials come into contact. There is a concentration gradient at the junction. While excess electrons are found in n-type semiconductors, p-type material has too much holes inside. When the contact happens, excess electrons have tendency to go to lower concentration region which means they move from n-type material to p-type material. Also, reverse case is happened for the holes, they diffuse from p-type to n-type material. After this movement happens, a space charge region is formed at both side of the junction. In the region inside the p-type material, electrons expose the holes and create negatively charged region. At the other side of the junction, holes expose the electrons and create positively charged region inside the n-type material. Exposed charges create an electric field against the natural diffusion path which creates the drift current. Negative charges in space charge region of p-type materials move to n-type materials and also vice versa. This lasts until the charge balance occurs. Therefore, space charge region is also called as depletion region. Because both electrons and holes are depleted at this region [2, 3, 8, 9]

At balance condition, fermi energy levels of the donor and acceptor materials become the same. This happens with rearrangement of conduction and valence band of the materials. This phenomenon is known as band bending. Figure 2.6 illustrates the p-n junction, depletion region and band bending. The electrostatic potential difference creates the built in voltage which is the result of exposed positive and negative charges in the depletion region [2, 3, 8, 9].

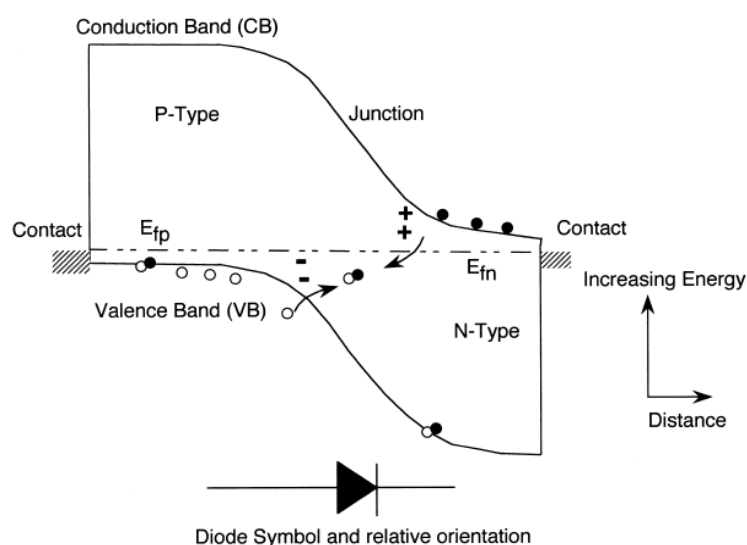


Figure 2.6. Band diagram and band bending after the formation of p-n junction [9].

#### 2.1.4. Absorption of the Light by Semiconductor

Light and materials can be interacted at three different mechanisms. Light can be passing inside the material or it can be reflected from the surface of materials. Both events are occurring when the energy of light is lower than the band gap of material. On the other hand, third process, absorption of incident light generates separated electron-hole pairs in the semiconductor which is the principle of working mechanism of solar cells. Photons have the larger energy than the band gap of material, ejects one electron from valence band to conduction band. Excited electron leaves a hole in the

valence band state. Carrier generation is created by band to band transitions which can be realized in two ways according to the crystal momentum position of the band levels. First one is the direct band gap in which crystal momentum position is the same for valence and conduction bands. Higher photon energy with respect to the band gap is sufficient for the absorption. The other one is indirect band gap which has different crystal momentum positions for conduction and valence bands. Therefore, not only the photon energy but also lattice momentum is required for the absorption. This condition results in higher absorption coefficient values for direct band gap materials compared to the indirect band gap materials. Therefore thicker structures must be used in indirect band gap semiconductors, like Si, compared to direct band gap materials, like GaAs. For indirect band gaps, a second mechanism which is referred as phonon is involved in two step processes required for electrons to reach the conduction band. Phonons have small energy and large momentum which is contrary to the properties of photons. After the excitation of electrons to the energy level of conduction band, phonon emission or absorption occurs to move the wave vector to the position of conduction band [2, 5, 6, 10]. Figure 2.7 explains the absorption phenomena in both direct and indirect band gap structures.

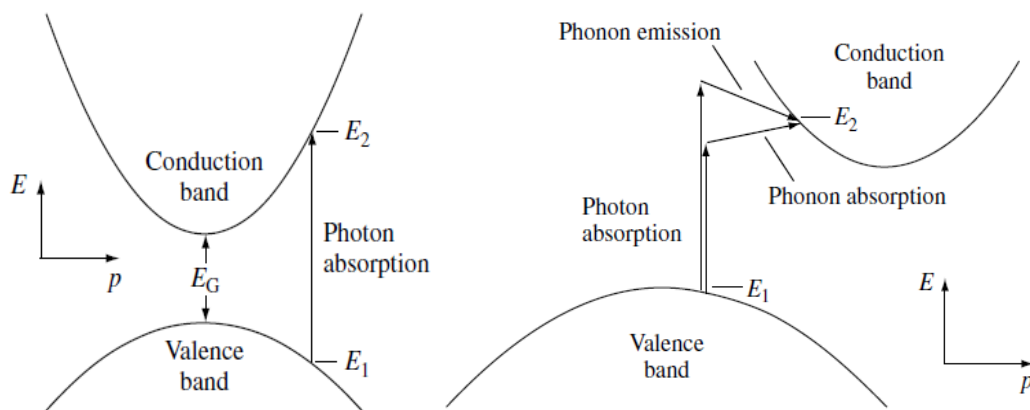


Figure 2.7. Absorption phenomena in both direct and indirect band gap materials [2].

### 2.1.5. Recombination Losses in Solar Cells

Recombination process is the reverse case of the electron-hole pair generation. It is an undesirable phenomenon; however, it is inevitable. There are great efforts to minimize the recombination in all kind of solar cells. There are four main recombination processes which are shown in Figure 2.8.

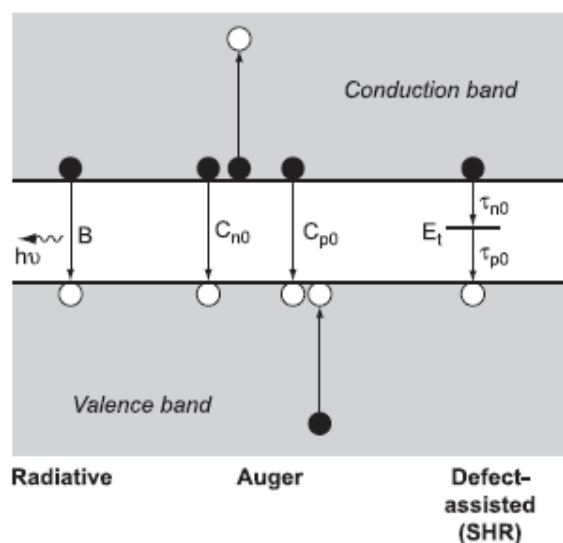


Figure 2.8. Recombination mechanisms [6].

First one is the band to band transition in which the reverse case of photon absorption occurs. This is widely observed in solar cells, after the recombination, photon emission occurs. When the photon emission happens, recombination is called as radiative. If the emitted matter is phonon, then it is non-radiative recombination. It is quite similar with absorption, an additional momentum is required for indirect band gap materials, and therefore it is mostly observed in direct band gap semiconductors [3].

Secondly, when the band to band transition recombination happens, excess energy of photons is produced. These photons excite another electron to higher energy level.

When this electron relaxes to its original position with phonon emission (non-radiative), this type of recombination is called as Auger recombination which is observed mostly in highly doped semiconductors [3].

Third recombination is the result of traps and therefore it is known as defect level recombination. Impurities in the semiconductor create additional energy levels in forbidden band gap. These levels do not supply a positive effect in charge generation and also, recombination will be easier from these trap levels. Excited electrons firstly relax to this position and later they move to the valence band. This recombination is also non-radiative, which produces phonon emission. It is clear that purity is critical for an efficient solar cell [3].

Surface recombination is the final loss mechanism. Surfaces are different from the bulk region and these surface areas include much more defects than the bulk. Vacancies, unbonded and dangled atoms are the main defects at the surface. These defects create additional energy levels and increase the probability of recombination. Surface passivation is applied in thin film solar cells where it is more critical due to the aspect ratio [3].

#### **2.1.6. Carrier Transport in Solar Cells**

Electrons and holes are the free particles at p-n junctions. However, there is no current flow. When the light absorption occurs, electron and hole pairs are created. Electron and holes make their movement with the help of two driving forces, the first one is the concentration gradient (diffusion current) and the second one is the difference in electrostatic potential energy (drift current). These current terms form the transport equations (Eq [2.3]) which govern the electron ( $J_n$ ) and hole ( $J_p$ ) current densities [2, 5, 8].

$$\begin{aligned}
J_n &= q\mu_n n\varepsilon + qD_n \nabla_n \\
J_p &= q\mu_p p\varepsilon - qD_p \nabla_p
\end{aligned}
\tag{Eq. [2.3]}$$

$\mu$  defines the mobility of the carriers,  $D$  is the diffusion coefficient of the electron and holes,  $\varepsilon$  is the electric field and  $q$  is the elementary charge in these equations. First equation is written for the electrons and the second one is for the holes. First term in the equations explains the drift current and the second term is for the diffusion current. Main component of the drift current is mobility, which depends on temperature, doping concentration and impurity content. Also scattering event in solar cells have a strong effect on transport due to the lowering of the mobility, carrier scattering and ionized impurity scattering which are two common scattering types in solar cells. Also, high temperature and electric field decrease the time for the collision, hence the mobility decreases [2, 5, 8].

### 2.1.7. Output Parameters for Solar Cells

Working principle of solar cells depends on the conversion of the sunlight directly to the electricity. The basic characterization of the solar cells depends on the current (I) – voltage (V) measurements. Because, this measurement supplies many important information about the cell performance such as short circuit current, open circuit voltage, fill factor and especially efficiency (Figure 2.9). After measurement is performed, current-voltage curve is drawn and power values are calculated using each voltage and corresponding current values. For the maximum power point, current and voltage are defined with  $I_{mp}$  and  $V_{mp}$  [2, 3].

At short circuit condition where zero voltage passes through the cell, obtained current value is called as short circuit current ( $I_{sc}$ ). This value is also exactly the same with the light generated current which is the largest current which can be obtained from the cell. Short circuit current is directly related to the photon collection ability of the cell.

It is maximized with increase in the number of photons trapped. It is also dependent on the cell area and therefore current density ( $J_{sc}$ ) term is used instead of short circuit current to n the effect of area. Current density is calculated by dividing the value of current to active cell area. Other important term is open circuit voltage ( $V_{oc}$ ) which is the voltage value when the net current equals to zero. This term is affected by the recombination processes. Therefore, defect free cell production is important to maximize the open circuit voltage. Fill factor is another term which can be obtained from I-V measurements. Fill factor is the measure of how close is the I-V curve to the square shape. This gives information about the ratio of obtained maximum power to maximum obtainable power from the cell [2, 3]. It is calculated using the equation 2.4.

$$FF = \frac{V_{mp} * I_{mp}}{V_{oc} * I_{sc}} \quad \text{Eq. [2.4]}$$

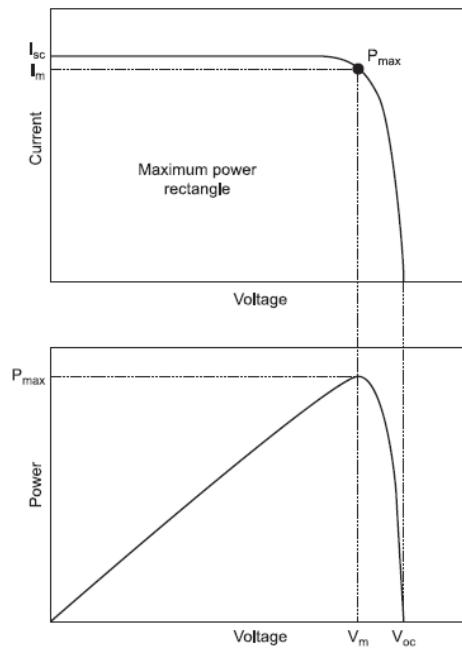


Figure 2.9. Current-Voltage curves for a solar cell [6].

I-V curve deviates from the square shape due to the resistance sources in the solar cell. These resistance sources divide into two types: series and shunt. These resistances decrease the fill factor and cell efficiencies. Series resistances are due to the contact and bulky resistances and shunt resistance is due to the manufacturing defects. These defects create alternative ways for the flow of current and this decreases the shunt resistance of the cell (Figure 2.10). To reach the square shape,  $R_s$  slope should go to zero and  $R_{sh}$  slope should go to infinity [2, 3].

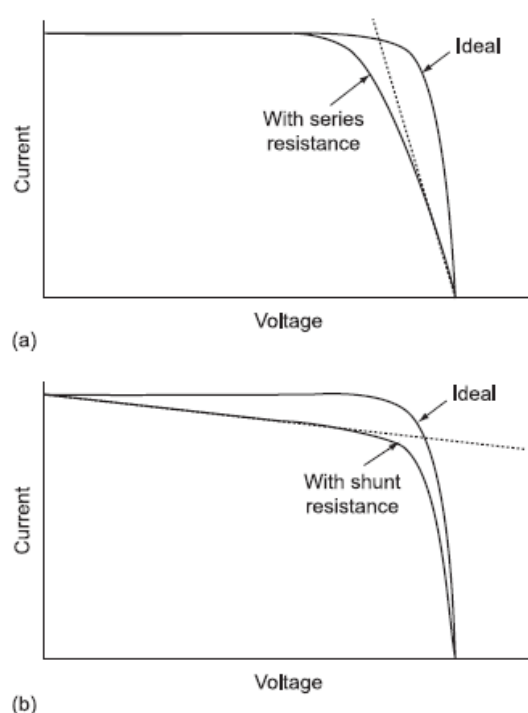


Figure 2.10. Series and shunt resistances on an I-V curve [6].

Efficiency is the last and most important parameter obtained from the I-V curve. Efficiency is used to compare all of the solar cell devices. It is the value of how much input energy is converted into the electricity. Equation 2.5 gives explanation about the calculation of efficiency. I-V analyses are conducted under AM1.5 condition as a standard [2, 3].

$$\eta = \frac{P_{\max}}{P_{in}} = \frac{V_{mp} * I_{mp}}{P_{in}} \quad \text{Eq. [2.5]}$$

## 2.2. Types of Solar Cells and Main Materials in Production

### 2.2.1. Crystalline Silicon Solar Cells

Silicon has been the dominant semiconductor material in solar cells from the beginning of technology. In the periodic table, silicon is located in the group IV A. It mostly occurs as silicon oxide and silicates in nature. Silicon is the second abundant element in Earth's crust as 26 %. Crystalline silicon has diamond cubic crystal structure and it has 1.12 eV band gap. Compared to the alternative semiconductors, silicon possesses high stability, advance chemical, optical and electronic properties. Due to these advantages, silicon has become the first choice in the industry for not only silicon solar cells but also in all microelectronic applications. Also, studies using of silicon in microelectronic industry make the production technology mature and decrease the cost of the production in time. Silicon solar cells have been commercialized for 20 years. These conditions present 80 % of the photovoltaic industry market occupied by crystalline silicon. Crystalline silicon solar cells are used in the market at two different crystal structures as polycrystalline and single crystalline.

Production techniques are different for both single and poly crystals. Single crystal silicon solar cells were fabricated by Czochralski crystal growth, in which, a direction known seed is dipped into the silicon melt and followed by the upward pull of the seed and rotated and molten silicon is cooled down at the known single direction. Oppositely, polycrystalline silicon is produced by direct casting of molten silicon. Minority carrier life time, which is the elapsed time for a free electron recombining

with a hole, is a good indicator for the solar cells. For the silicon solar cells; Fe, Cr and Ni are detrimental elements for the cells and they decrease the minority carrier life time. Therefore, purity is so critical for the cell performance. After these processes, production continues the same for both types. Ingots are produced by p-type doping; boron is the mostly used dopant material. Then, ingots are sliced in the order of 300-500  $\mu\text{m}$  thickness, this level is mainly known as wafer. This thickness is a must for the silicon solar cells, because silicon has indirect band gap nature and therefore it has low absorption coefficient. To increase the absorption, thickness should be increased. However, there is a limiting thickness due to the carrier diffusion length. Then these wafers are etched from smooth surface to a rough surface. Phosphorus, as n-type emitter, is diffused on p-type silicon wafer as a very thin layer (0.5  $\mu\text{m}$ ) for high light passing. After the diffusion process, a p-n junction is formed. Then, remaining phosphorous is cleaned from the back and front side of the wafer. Front side is coated with a single layer anti-reflective coating which can be tantalum oxide, titanium oxide or silicon nitride followed by the screen printing of metal contacts (silver) on front and rear sides. Finally, fire process is applied to the cell. Figure 2.11 represents the final architecture of the Si solar cell.

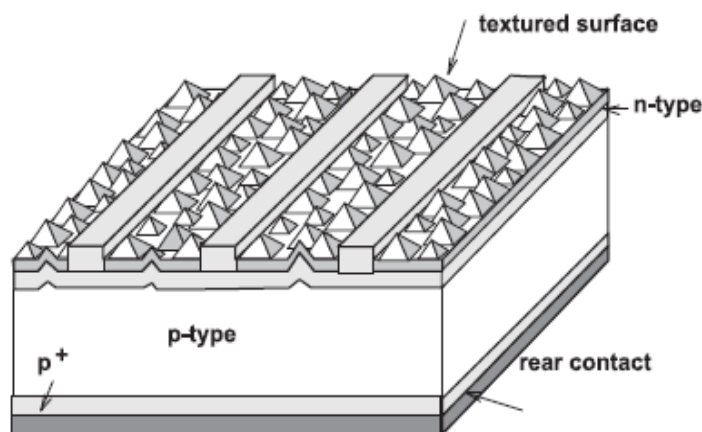


Figure 2.11. Architecture of the conventional silicon solar cell [6].

Silicon solar cells have been shown a marked improvement in the efficiency and cost per watt values since their first use in the market. Also, laboratory studies continue to improve the cell performance regarding their efficiency and stability. Another aim is to decrease the cost/watt price. Up to now, best cell efficiency was obtained as 27.6 % from a single crystalline silicon solar cell. Stability of silicon solar cell reaches to 20 years. Despite these impressive factors, panel prices are still very high compared to other solar cell technologies and companies have not reached to laboratory efficiencies in outdoor usage conditions, because of the fact that silicon solar cells should take sunlight at high light intensities and specific angles depending on the position [5, 11, 12].

### **2.2.2. Thin Film Solar Cells**

Thin film solar cells compose the second generation of solar cells. Low cost, robustness and stability are the main advantages of thin film solar cells. They are mostly deposited using vacuum techniques. They have high absorption coefficients; therefore, they can be applicable in thin films.

#### **2.2.2.1. Amorphous Silicon Solar Cells**

Amorphous silicon ( $\alpha$ -Si) has been located in our lives as used in calculators for 40 years.  $\alpha$ -Si can be produced easily and cost efficiently. Also, its good performance and flexibility make it attractive in the applications. At the beginning of the studies for the use  $\alpha$ -Si thin films for solar cells, problem was understood easily. Due to the amorphous structure, long range order is not observed. In other words, there is not a constant distance between the atoms. This situation creates many undangled bonds. These bonds can be positively charged, negatively charged or can be neutral. Charged bonds create many levels inside in the forbidden gap and these levels behave as recombination centers and directly decrease the efficiency of the cells. Therefore, number of defects is so critical for  $\alpha$ -Si thin films. This gives a result that doping is

not possible and also a p-n junction. Also, hydrogen passivation is performed to unbonded atoms to decrease the defect concentration in amorphous Si. This process also works like doping. Therefore, cell architecture was changed, intrinsic silicon layer is inserted between p and n-type structures. In other words, p-i-n structure is used for amorphous silicon instead of p-n junction. Intrinsic silicon layer works like an absorption layer. Undoped silicon layer increases the thickness of the cell, therefore it supplies an increase in photon absorption, and also it helps the charge separation with a drift mechanism creating an electric field. Cells are produced by sequential deposition of p-type, intrinsic and n-type  $\alpha$ -Si layers. They are deposited using chemical vapour deposition of  $\text{SiH}_4$  gas. Record efficiency is about 13 %, however, they suffer from Staebler-Wronski effect which is about the destruction of  $\alpha$ -Si:H with induced light [6, 12, 13].

#### **2.2.2.2. Gallium Arsenide Solar Cells**

Compound semiconductors are widely used in solar cells which can be group III-V and group II-VI compounds. Gallium arsenide (GaAs) is the most common semiconductor material in III-V group for solar cell energy. GaAs has a 1.42 eV band gap energy, which is very close for the optimum solar spectrum. Also, GaAs is a direct band gap material which means a thinner film can supply high absorption. Therefore, it can be useful in thin film solar cells. Also, they have high resistance to radiation and temperature effects; therefore, it is more proper to use in space applications compared to silicon.

p-n junction formation in GaAs solar cells is realized by doping with silicon to create n-type structure and carbon to create p-type structure. Also, it is possible to tune the band gap by the optimization of alloying and doping. This makes GaAs thin films suitable for tandem solar cells. GaAs thin films can be deposited using liquid phase epitaxy (LPE), molecular beam epitaxy (MPE) and metal-organic chemical vapour deposition (MOCVD) techniques where these methods supply accurate composition

and thickness control. All of these deposition techniques suffer from high initial cost. Also, both gallium and arsenic are toxic materials. These two drawbacks limit the usage of GaAs only in solar cells for space applications, although, the efficiencies for GaAs solar cells reach to 26 % [6, 12, 14].

### **2.2.2.3. Copper Indium Diselenide Solar Cells and Copper Indium Gallium Diselenide Solar Cells**

Copper Indium Diselenide (CIS) and Copper Indium Gallium Diselenide (CIGS) both possess chalcopyrite structure with tetrahedrally bonded in nature. They belong to the compound of I-III-V group in the periodic table. Both of these materials have semiconductor nature with direct band gap. They are suitable for thin film solar cell applications. Thin films are mostly deposited using vacuum evaporation techniques. Also, there are studies about the use of electrodeposition, printing and spray pyrolysis methods in fabrication. Both of the materials are deposited on metal coated glass substrates where metal layer is used for back contact purposes. Deposited CIS or CIGS layers have copper deficiency which possesses p-type structure. They are fabricated using co-evaporation of the elements in the order of 2  $\mu\text{m}$  coating thicknesses. p-n junction is not suitable for these types of thin films due to the high surface recombination and series resistance. Therefore, cells are fabricated at heterojunction structure which is realized using CdS as n-type material and finally ZnO layer is deposited as front contact. CIS and CIGS can be produced between 1.0 to 1.7 eV band gap which is sustained with composition of the elements. Therefore, band gap can be tuned for better cell performance. CIGS cells are reached to 20 % efficiency for cells and 16 % for modules in research studies and nowadays, many companies work on commercialization of the CIS and CIGS thin film solar cells [6, 12, 14].

#### **2.2.2.4. Cadmium Telluride Solar Cells**

Another member of II-VI compounds which is used in solar cells is CdTe. CdTe has 1.45 eV direct band gap. CdTe has intrinsically p-type in nature. Again, CdS is used for n-type heterojunction like in CIGS. CdTe layer is deposited using vacuum evaporation techniques, mostly sputtering is used. Also, spray pyrolysis and chemical vapor deposition are studied in the literature. 18.3 % photovoltaic efficiency has been reached in laboratory conditions; however, their theoretical limit is about 29 %. This makes CdTe solar cells an attractive topic both in research and commercial applications. CdTe also has superior stability due to the strong ionic bonds and therefore they are most suitable solar cells for outdoor usage. Main problems are the tellurium supply and cadmium toxicity, which limit the studies [6, 12, 14].

#### **2.2.3. Dye Sensitized Solar Cells**

The research background for dye sensitized solar cells stands to 50 years ago; however, its conversion efficiency was limited to 1 % up to 1990s due to weak absorption of sunlight. Then, the study of Gratzel and O'Regan which is the increase in the surface area of photoanode makes a big jump in this technology and conversion efficiency. High surface area directly supplies higher dye molecule absorption and increases the number of excited electrons. This improvement makes the efficiency of DSSC firstly 7 % and then 10 %. After this pioneering study, many studies have been worked to increase the efficiency using larger active areas and stability of the cells. According to NREL values, world record is 13.6 % in DSSC's.

DSSC is built between two transparent conductive oxide (TCO) coated glasses. One TCO layer is coated with highly porous wide band gap n-type semiconductor oxide. Photoanode coated TCO is dipped into the sensitizer and almost one day is required for the sensitizer absorption into photoanode. Then, platinum is deposited onto other TCO and these two TCO structured glasses are sealed with the hot melt polymers to

prevent the leaking of liquid electrolyte outside the cell. Finally, electrolyte is filled between two TCO structures (Figure 2.12).

Working principle of DSSC starts with photon absorption of sensitizer. Electrons jump from Highest Occupied Molecular Orbital (HOMO) state to Lowest Unoccupied Molecular Orbital (LUMO) state and holes remain at HOMO state. Excited electrons are pushed from the conduction band of photoanode, because, conduction band of photoanode is located a bit lower state than LUMO level. Electrons follow the 3-dimensional photoanode network to reach the electrode. By this way, oxidized dye molecules come back to their original states by the electron donation from electrolyte species.  $I^-$  anions become  $I_3^-$  with electron donation. After that, second reaction is realized and  $I_3^-$  returns back to  $I^-$  form by receiving electrons from the counter electrode. Electrolyte mediator provides this cycle by giving and receiving electrons while the process is lasted. All reactions are completed in nanosecond time ranges, thus; limited time does not permit any other reactions different than the ones mentioned.

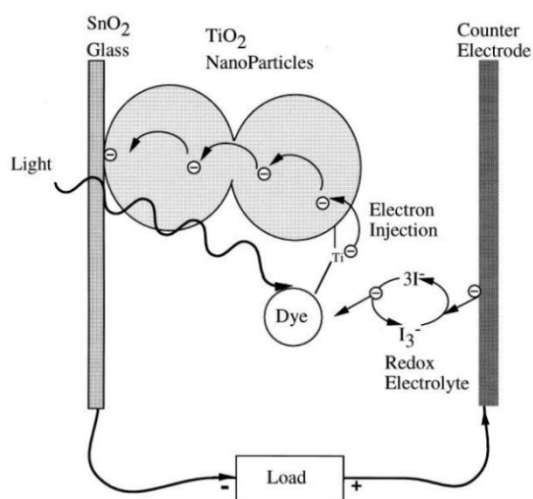


Figure 2.12. Main components and working steps for DSSC's [9].

Dye sensitized solar cells have been an attractive topic for 20 years. In this time period, many studies have been conducted to evolve the cell performance. These studies both include the use of alternative materials and deposition methods. Record performance of DSSC reaches to 14 % efficiency. However, sealing problem of DSSC is the biggest obstacle behind the commercialization of them. To overcome this problem, main approach is the use of solid-state electrolyte instead of liquid counterpart. Studies for these purposes open a new solar cell technology area, which is known as Perovskite Solar Cells (PSC). The large potential of PSC converts most of the studies from DSSC to PSC in the last 6 years [9, 15-17].

### **2.3. Perovskite Solar Cells**

In 1830's, German mineralogist Gustav Rose found a gray color and shiny mineral at Ural Mountains. Mineral takes its name from a Russian mineralogist L.A. Perovski as perovskite [18]. Perovskite was defined as the same crystal structure with  $ABX_3$  structure. The first studied perovskite semiconductor was  $CsPbCl_3$ , which was performed by Moller in 1957. In that study, main aim was the use high photoconductive property of perovskite material. Following this work, the use of methylammonium (MA) cations instead of cesium was offered by Weber in 1978 [19]. By using MA, obtained structure was called as hybrid organic-inorganic perovskite structure. In the last few years, application of these perovskite structures into photovoltaic field takes the attraction of all scientific people due to their enhanced photo conversion efficiency compared to organic solar cells and dye sensitized solar cells. Nowadays, application areas of perovskite are well analyzed, and it is shown that their potential is not restricted to solar cells. They have great potential in LED, photo detectors and laser products [20].

From the first study, which was performed in 2009, cell performance dramatically and swiftly increases and nowadays best effort is higher than 23 %. Addition to cell performance, they can be fabricated by wet chemistry methods which present low cost

production. This condition also increases the number of studies for perovskite solar cells. Perovskite possesses many advantages in the applications; they are their versatility in composition, optimal band gap, high absorption condition, long carrier diffusion length, ambipolar carrier transport property and tolerance in defect amounts [21].

Perovskite material was firstly used in liquid electrolyte included DSSCs to enhance the light absorption; this study was performed by Miyasaka and coworkers in 2009. In this study,  $\text{CH}_3\text{NH}_3\text{PbBr}_3$  and  $\text{CH}_3\text{NH}_3\text{PbI}_3$  perovskite absorbers show 3.1 % and 3.8 % efficiency [22]. Following study includes the use of perovskite quantum dots as sensitizers in DSSC's. Quantum dot perovskites hop to conversion efficiency from 3.8 to 6.2 %. Although more photo-injected electrons were generated using quantum dot perovskites, electron recombination increases due to the interaction of photo anode and electrolyte [23]. Big breakthrough is generated by the use of perovskite material in 2012 by Gratzel et al. [24] and Snaith et al [25], independently. In both studies, perovskite nanocrystals were used as light harvesters and submicron thick mesoporous  $\text{TiO}_2$  film and spiro-MeOTAD are used as an electron and hole-transporting layer, sequentially. Photo conversion efficiencies were reached to 9.7 % (Gratzel work). Snaith report investigates  $\text{Al}_2\text{O}_3$  insulator layer on top of thick mesoporous  $\text{TiO}_2$  layer. This combination enhances the electron transport which creates 10.9 % efficiency. After the breakthrough, first healing was realized in the deposition method and 14.1 % conversion efficiency was obtained at 2013 [26]. 16.2 % efficiency was obtained when the use of hybrid halogen perovskite layer is employed in the late of 2014 [27]. After that, there have been many studies for the purpose of the cell performance improvement. Composition of the perovskite layer, change in components, change in the deposition techniques and optimization of the interfaces are some of the topics studied. Best effort in perovskite solar cells yielded 23.3 % efficiency. All of these values were taken from the very small areas around  $10 \text{ mm}^2$ , therefore, scale up in the production is an important issue to commercialize these perovskite solar cells. Another challenge is the increase in the life time of these devices by enhancing their stability.

### 2.3.1. Working Principle of Perovskite Solar Cells

PSC is evolved from the DSSC. In the basic, PSC has two different media compared to DSSC: a sensitizer and a hole transport layer. Like DSSC, bottom electrode is mostly TCO coated glass and upper electrode is a kind of metal. On top of the bottom electrode, an n-type wide band gap semiconductor is used for efficient electron transfer. There is no requirement for mesoporous structure due to the electron transport character of perovskite sensitizer which is directly coated on the electron transport layer (ETL). Following layer is the solid hole transport layer (HTL) and finally upper metal electrode. Each layer has a lower thickness than sub-micron values. Figure 2.13 demonstrates classical PSC and carrier motions.

Incoming photons pass from TCO and n-type semiconductor and they are absorbed by the perovskite layer. Absorbed energy creates excitons which separate holes and electrons. Electrons move to excited lowest unoccupied molecular orbital (LUMO) and holes are found in highest occupied molecular orbital (HOMO). Thus, charge separation process is concluded. Then, the excited electrons are taken by the ETL and holes go to HTL. ETL has the ability to transport the electrons and at the same time they can block the hole motion and vice versa is valid for HTL. Then both carriers easily flow to the electrodes due to the suitable Fermi levels. Fermi level difference between the electrons and holes creates external voltage and carrier extraction happens with photocurrent formation in the external circuit. There are four possible reactions in a PSC. Two of them are in positive ways; they are the electron injection into ETL and hole injection into HTL reactions. Others affect the cells negatively; recombination and photoluminescence reactions [28].

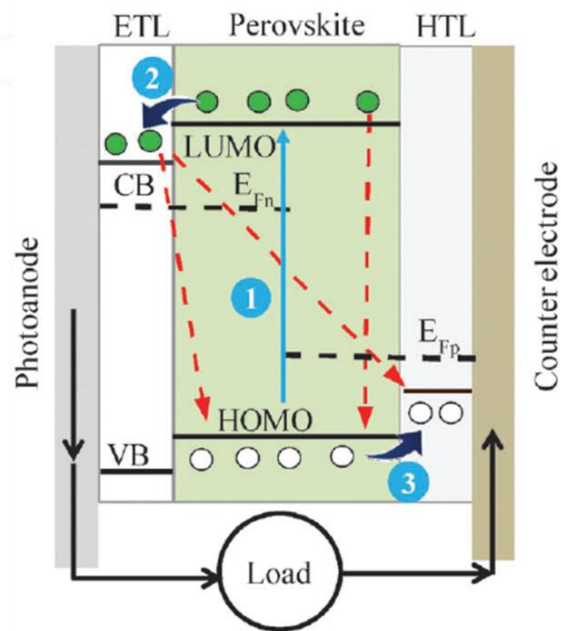


Figure 2.13. Working principle of perovskite solar cells [28].

### 2.3.2. Device Architectures of Perovskite Solar Cells

Dye sensitized solar cells are formed between two electrodes; which are FTO coated glass and platinum. Mesoscopic titania, dye molecules and electrolyte layers are located sequentially on the top of FTO coated glass. With the idea of using semiconductor material instead of dye absorber layer initiates the perovskite solar cells. Perovskite absorber layer takes the place of dye molecules and solid hole transport materials are used instead of liquid electrolyte in perovskite solar cells. Perovskite absorber has great advantage over dye molecules which is its higher absorption coefficient. Due to the low absorption coefficient of dye molecules, thickness of the mesoporous layer is about 5  $\mu\text{m}$  in DSSC to increase the photocurrent. However, thicker film suffers from recombination due to the long diffusion length requirement. Sub-micron thick mesoporous layer is enough in PSC due to the high absorption nature. This first configured perovskite solar cell is called as mesoporous perovskite solar cell because of the use of mesoporous layer. Due to the electron

transport property of perovskite material, it is not possible to use just mesoporous ETL. Therefore, bottom electrode and perovskite layers must be separated from each other. With this knowledge, ETL was healed using two different layers. Firstly, compact electron transport layer is deposited on TCO coated glass substrate and after that mesoporous layer is deposited. First used mesoporous material was  $\text{TiO}_2$  like in DSSC.  $\text{TiO}_2$  has the property of being both electron transport and template for perovskite deposition. Therefore, mesoporous  $\text{TiO}_2$  layer is known as active scaffold. Perovskite, HTL and back electrode complete the cell (Figure 2.14). Addition to the use of nanoparticles, mesoporous layer can also be grown in nanotubes, nanorods, nanocones, and nanowires. These structures provide higher charge separation rate and decreased recombination which conclude with improved conversion efficiencies. These structures suggest higher surface to volume ratio. Mesoporous cells can be also configured at inverted design, which stands to the use of mesoporous p-type material.

Following studies focus on the use alternative mesoporous layers. Due to the electron transport nature of perovskite layer, mesoporous layer can be an insulator material.  $\text{Al}_2\text{O}_3$  mesoporous layer shows a promising performance. Although its band gap is too high to use for electron transport purpose, it is directly used as a scaffold for perovskite layer. Therefore, these types of mesoporous layers are called as passive scaffold. This bottom layer plays an important role while in the deposition of perovskite layer. Scaffold layer affects both crystal growth and morphology of the perovskite layer. Drawbacks of the mesoporous layer are the high temperature annealing requirement and incomplete filling of the pores. These drawbacks are the main reason of the formation of planar architecture.

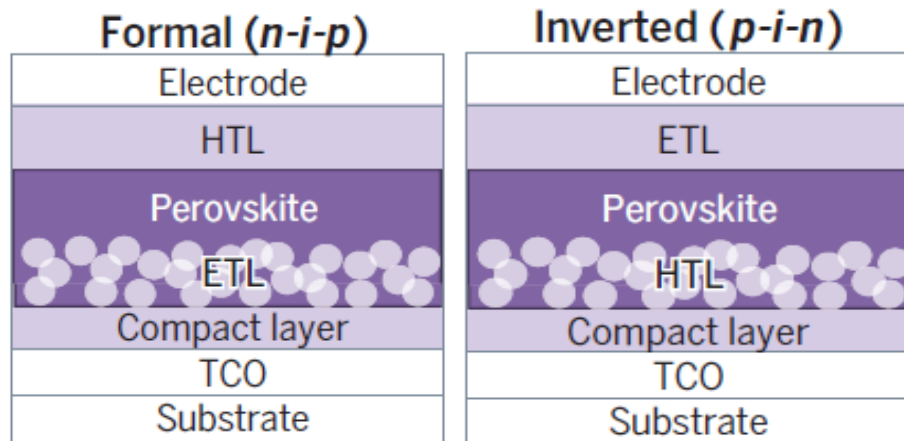


Figure 2.14. Formal and inverted mesoporous PSC architectures [29].

Mesoporous layer is removed from the perovskite solar cells in planar cell configuration which is shown in Figure 2.15. Planar cells have already been shown having lower cell efficiencies compared to mesoporous cells. While required diffusion length for the carriers is about 10 nm in mesoporous cell, 250 nm is the value for the diffusion length in planar cells. This long distance increases the recombination process. To minimize the diffusion length, perovskite layer should be minimized. It is difficult to fabricate too thin perovskite layers and also, too thin films suffer from the low surface coverage. Undeposited areas become transparent to incident light and these points behave as parallel diode due to the contact between electron transport and hole transport layers which results in decreasing cell performances. Also scaffold layer acts as template for the perovskite layer and therefore it is easy to create thin perovskite layers in mesoporous configuration. However, there are some studies to increase the diffusion length of carriers evaluating alternative perovskite absorber materials. It was found that diffusion length reaches to 1  $\mu\text{m}$  range for  $\text{MAPbI}_{3-x}\text{Cl}_x$  for perovskite absorber; however, diffusion length is just 100 nm for  $\text{MAPbI}_3$ .

Both mesoporous and planar perovskite solar cells can be fabricated in both formal (n-i-p) and inverted (p-i-n) designs. Inverted cells are produced by the deposition of

the p-type material previous to perovskite layer. These cells are shortly defined as p-i-n configuration. Also inverted design takes attraction of the use of organic photovoltaic materials in perovskite solar cells. Organic materials have advantages in easy fabrication, high throughput and material diversity. Similar to planar configuration, higher carrier diffusion lengths and thicker perovskite absorbers should be applied for inverted PSC. Larger grain size also decreases the recombination which yields better cell efficiency. Opposite to common n-i-p configuration, electrons and holes are collected by back metal contact and front transparent conductive oxide contact layers, sequentially.

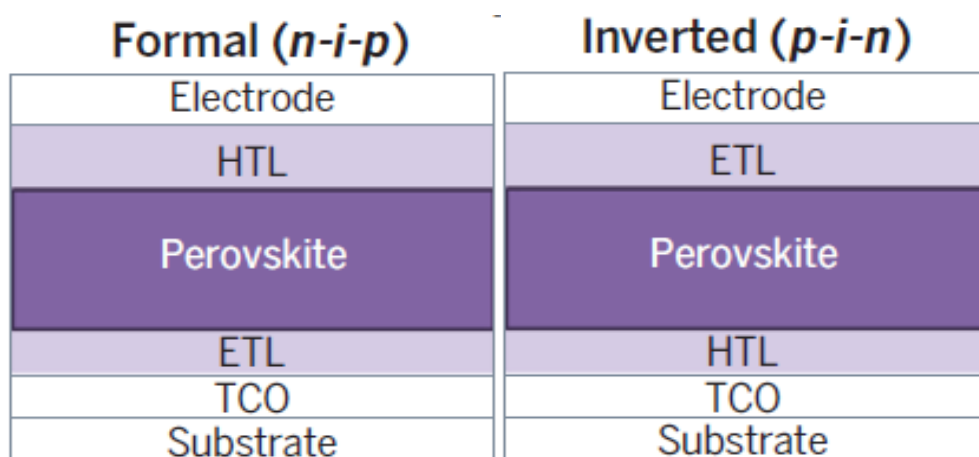


Figure 2.15. Formal and inverted planar PSC architectures [29].

After learning of the potential use of perovskite material as an absorber, it was detected that perovskite absorbers have ambipolar charge transport characteristics. Perovskite materials have ability to transport both electrons and holes. Although there is a dependence on the perovskite type, it is known that they have better charge transport character for holes compared to electrons. Therefore, it provides to fabricate perovskite cells without either electron transport layer or hole transport layer. Although these types of cells suffer from charge recombination, their photo conversion efficiencies are above the promising limits. When hole transport layer is

not used in the device, PSC should be produced with thick perovskite layer with smooth surface and good back contact. This is critical for avoiding from the shunt pathways [30-32]. Perovskite solar cells are constructed using 4 main components: perovskite sensitizer, electron transport layer, hole transport layer and electrode.

### **2.3.3. Perovskite Sensitizer**

Perovskite sensitizer has suitable band gap to create electron and hole pairs by the effect of incident light.  $\text{MAPbI}_3$  has about 1.1 eV band gap which covers the visible and near infrared light. Perovskite absorbers have ambipolar conductivity which is the transportation of both electrons and holes. Perovskite materials have high absorption coefficient and therefore very thin film is enough to absorb all incident light. Therefore, PSCs provide high conversion efficiency with high stability. However, many researches have been carried out related to composition and deposition techniques of perovskite layer.

#### **2.3.3.1. Crystal Structure of Perovskite**

Crystal structure of perovskite material is defined as  $\text{ABX}_3$  (Figure 2.16). Perovskites have unit cells composed of five atoms in a cubic structure where cation B has six nearest neighbor anions X and cation A has twelve nearest neighbor anions X. A cation is occupied in a cubooctahedral site and B cation is occupied in an octahedral site. X can be oxygen, carbon or any kind of halogen like chlorine, bromine or iodine and they are at the face centers of the cubic unit cell. These halide perovskites are used in perovskite solar cells. Main material is lead (Pb) as B metal cations due to its high efficiency and stabilization. Tin (Sn) can also be an alternative material in the same group of the periodic table and it also has a similar band gap. However, Sn suffers from ease of oxidation and lack of stability. Compositional variability of the perovskite material creates different opto-electronic properties in each case. Therefore, it is crucial to understand the effect of composition on the crystal structure.

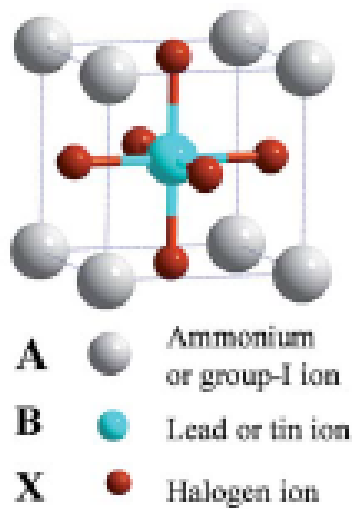


Figure 2.16. Crystal structure of perovskite materials [33].

Tolerance factor ( $t$ ) is an important definition to understand the crystallographic stability and perovskite structures which is given in equation 2.6. In this equation,  $R_A$ ,  $R_B$  and  $R_X$  define ionic radii of ions. Cubic structure corresponds to the tolerance factor as 1. When the tolerance factor is bigger or smaller than unity, deviation from the cubic structure is observed. It is found that from the equation 2.6, ionic radii of A cations should be larger than the ionic radii of B cations. Pb has already a large radius and therefore, A cation should be extremely large. Cs has the largest value for ionic radius in the group I as an alternative material for A cations. However, its radius is not sufficient to create the required symmetry. Therefore, organic molecules became the first choice for A sites. At room temperature conditions, acceptable value for the tolerance factor varies between 0.813 and 1.107. When this value is lower than 0.813, tetragonal and rhombohedral structures are favorable. When it becomes higher than the upper limit, 2-D structures become dominant. 2-D structures have lower absorption and they are not preferred in solar cells. Cr, Br and I are used materials as halogens. When their radii are used to calculate the tolerance factor, it is found that

ionic radius of A cation should be between 1.6-2.5 Å. Methyammonium (MA) is the most promising element as the organic cation for A site which has 1.8 Å ionic radius [19, 34].

$$t = \frac{R_A + R_X}{\sqrt{2}(R_B + R_X)} \quad \text{Eq. [2.6]}$$

It is calculated that the most stable phase is orthorhombic at 0 K and the least is the cubic phase. Also, it is detected that there are two phase change temperatures, where these values depend on the composition of perovskite material. For MAPbI<sub>3</sub>, stable phase becomes tetragonal above 160 K and it is cubic when temperature is over than 330 K [33].

### 2.3.3.2. Compositional Analysis of Perovskite

A site of the perovskite material is occupied by cations. The selection of the A cations depends on the tolerance factor which is explained under the crystal structure discussion. Alternative materials are cesium (Cs), rubidium (Rb), methylammonium (MA), formamidinium (FA) and ethylammonium (EA). MA was the first studied material, it showed over than 15 % efficiency. However, its tolerance factor is at the lowest limit. This situation causes the formation of tetragonal structure. Band gap of MAPbI<sub>3</sub> is obtained between 1.51-1.55 eV which is at a bit higher value than optimum Shockley-Queisser limit of 1.34 eV. For these two reasons, studies are focused to change MA with higher ionic radii cations. When the radii of candidate materials are compared, it is seen that ionic radii increase starting from Cs, MA, FA and EA. From this point, first alternative becomes EA. However, EA dissolves the 3D structure and therefore decreases the absorption which results with low efficiency in the final cell. FA provides a better symmetry compared to MA and also FA shows a lower band gap as 1.43-1.48 eV which is closer to optimum band gap. In the application of FA, it is

detected that some yellowish hexagonal one-dimensional structure is formed. These structures limit the cell performance due to the adverse band coordination with  $\text{TiO}_2$ . When this problem is solved, cells produced using FA can yield a higher efficiency than MA containing cells. Cs is also another alternative material for A sites. Cs was used in the form of  $\text{CsSnI}_3$  which shows good photoluminescence properties in near infrared range. However, it has a lower radius which causes a higher band gap and lower cell performance. Mixing of the cations is also evaluated. Mixing of MA and FA supplies the tuning of the band gap. In a study which uses such a mixture, 14.9 % efficiency was sustained with higher absorption compared to MA. Also, a mixture of MA and 5-aminovaleric acid (5-AVA) was studied which results in a better contact between perovskite layer and titania [35].

Group IV metals are the optimum material family for B sites. They have +2 oxidation states and Pb, Sn and Ge are the alternative materials. Pb is the most widely used material; it has a higher cell performance and better stability compared to its alternatives. Germanium has a changeable character at +2 states and therefore, its use in perovskite materials is limited. Lower atomic number possesses lower band gap;  $\text{MASnI}_3$  and  $\text{MAPbI}_3$  have 1.3 and 1.7 eV band gaps. Band gap of Sn containing perovskite material is closer to the optimum value. However, Sn has detrimental effects on the perovskite material such as rapid oxidation of  $\text{Sn}^{4+}$  occurs. Due to the stability problems, the use of Sn is also limited.

X site is the most critical part of the perovskite material which has a direct effect on the performance of the perovskite material. Single and mixed halides are used for this site. Halides are the materials at VIIA group of the periodic table. Band gap of the perovskite materials increases when the halogen material is changed from I to Br and Br to Cl. This is accompanied by a shift in the absorption band from lower to higher wavelengths. Iodide is the most preferred halide between the alternative materials. Electronegativity of the iodide is so close to lead metal and this causes the bond structure between these molecules be a mixture of ionic and covalent bonds. This

condition supplies a better stability compared to other candidates. Chloride is an alternative halide material for perovskites. When chloride is incorporated in the structure, the diffusion length and life time of the carriers are increased. Therefore, they are more suitable for use in planar architectures. Bromide is also another material which can be suitable for X site. Both I-Br and I-Cl mixtures were also studied. Iodide creates tetragonal structure and Br and Cl form cubic structures. Main aims are to create cubic structure and tuning of the band gap in these I-Br and I-Cl mixture studies [36].

#### **2.3.4. Deposition Techniques for Perovskite Sensitizer Layer**

Perovskite absorber can be fabricated using different approaches. Basically, wet chemistry approaches and vapor deposition techniques are the two main methods of perovskite production. Wet chemistry methods of perovskite layer deposition are realized using solution-based depositions. One step and two step deposition processes are the generally accepted methods in this solution-based deposition. Perovskite layer can also be produced using the vapors of the precursors which can be under vacuum or atmospheric conditions. Solution based depositions are preferable due to their low cost, easy application and suitability on large area depositions. Vapor based depositions are promoted due to their controllability and repeatability. However, vapor-based depositions are performed under vacuum which requires highly expensive systems. Also, in some applications, solution-based depositions are done under inert atmosphere conditions which also increase the process costs. Formation of the perovskite layer is directly sensitive to deposition conditions. To obtain high quality perovskite layers; nucleation kinetics, intermediates, transformation pathways and structure-property relationships of perovskite films should be well understood. Production of the perovskite thin films is extremely sensitive to very fine details; therefore, it creates a large difference in the experimental conditions which vary from laboratory to laboratory. This is the reason why same approaches can fail or be successful in different laboratories [31, 32, 37, 38].

### **2.3.4.1. Solution Based Depositions**

Both one step and two step deposition methods show similar performances in the devices; therefore, studies in both methods presently continue in the literature. In these techniques, precursor materials are mixed with solvent and then they are coated on the substrate. Firstly, solvent is evaporated and perovskite crystals are formed. Solvent is the major factor which determines the performance of the cell and it directly affects the orientation and grain size of the crystals. Evaporation rate of the solvents are also an important factor on both reproducibility and efficiency of the cell. Finally, deposition atmosphere has a strong effect on the final performance of the cell [31, 32, 37, 38].

#### **a) One Step Deposition**

This type of production technique was used in the first perovskite solar cell study by mixing the chemicals: organic halides ( $\text{CH}_3\text{NH}_3\text{X}$ ) and lead halides ( $\text{PbX}_2$ ). These chemicals are dissolved in a solution  $\gamma$ -butyrolactone (GBL), dimethylformamide (DMF), or dimethylsulphoxide (DMSO). Solution preparation and deposition can be performed under inert atmosphere or at a determined humidity level. Spin coating technique was used for the deposition of the prepared solution. It starts with small spin rates and then the rate is increased gradually for the formation of dense layers. Finally, films were annealed for solvent evaporation. One step deposition is the easiest deposition way, which supplies slow crystallization. It is demonstrated in Figure 2.17. High defect density formation was obtained due to slow crystallization. Also, it is detected that one step deposition strictly depends on annealing temperature, atmosphere environment, substrate materials, and film thickness. All of these parameters directly affect the film thickness and morphology which are the main parameters to obtain high quality films. Main drawback of one step deposition is the creation of pinholes [31, 32, 37, 38].

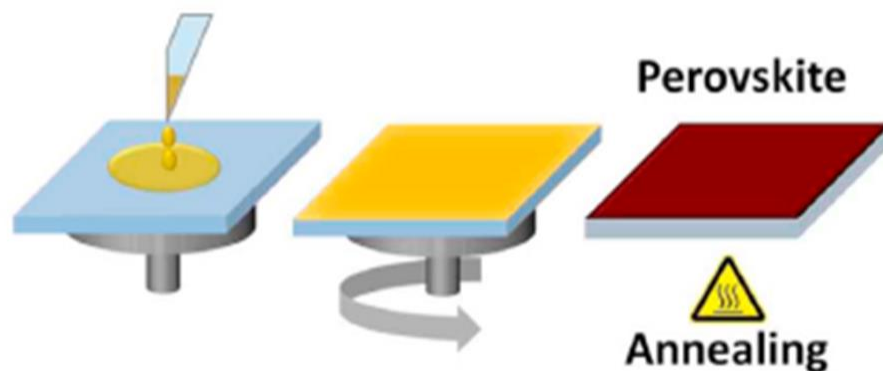


Figure 2.17. Demonstration of one step deposition process [39].

To minimize number of pinholes and to obtain high quality films, anti-solvent dripping technique was studied (Figure 2.18). Main aim in this process is to regulate the growth kinetics which promotes fast nucleation. This is supplied by reducing the solubility of  $\text{CH}_3\text{NH}_3\text{PbX}_3$  by mixing it with DMF and DMSO as solvents. In this technique,  $\text{CH}_3\text{NH}_3\text{PbX}_3$  is mixed with DMSO and DMF or GBL and DMSO. Then, the solution is spin coated and after a period of time anti-solvent is dripped on the substrate. Finally, annealing is applied about  $100^\circ\text{C}$ . In this technique, a better film and larger grain formation are observed. Toluene, chlorobenzene, chloroform, diethyl ether, and diisopropyl ether are the studied anti-solvent chemicals. When one step deposition and anti-solvent dripping methods are compared, in the anti-solvent dripping technique voids and pinholes are significantly removed and better-quality reproducible films and entire surface coverage are obtained for perovskite thin films [31, 32, 37, 38].

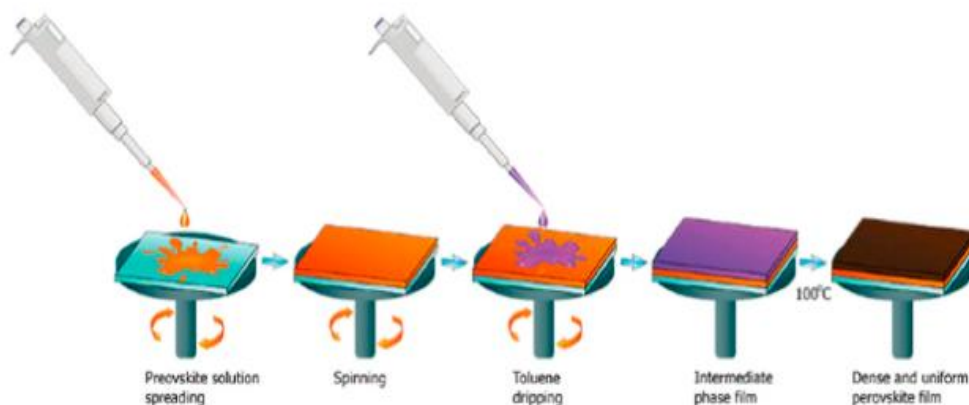


Figure 2.18. Demonstration of anti-solvent dripping method [38].

Another attempt to improve the film quality is using the additives which can be metal halide salts, organic halide salts, polymers, fullerene, nanoparticles, and inorganic acids. Polymers supply uniform crystallization and enhanced properties. Polyethylene glycol (PEG), amine-polymer poly[(9,9-bis(3'-(N,N-dimethylamino) propyl)-2,7-fluorene)-alt-2,7-(9,9-dioctylfluorene)], polyvinylpyrrolidone, and polyacrylonitrile are the most commonly used polymer additives for perovskites. Polymeric additives enhance the morphology and surface coverage. NaI, CuI, CuBr and, AgI are the commonly used alkali metal halide salts which increase the homogenous nucleation. Therefore, larger crystal formation is obtained [31, 32, 37, 38].

### b) Two Step Deposition

Two step deposition stands to sequential deposition of  $\text{PbI}_2$  and methylammonium iodide (MAI) solutions. Demonstration of two step deposition is given in Figure 2.19. The first studies using this technique involve the deposition of  $\text{PbI}_2$  by spin coating method and drying of the film. Then, coated substrate was dipped into MAI containing solution (MAI+2-propanol) which changes the color of the film from yellow to dark brown. Change in the color shows the formation of perovskite layer.

Main advantage of this method is the creation of  $\text{PbI}_2$  at small size which directly enhances the post reaction in dipping process. Also, produced films have lower defect amounts and decreased surface roughness compared one step process. However, there are some shortcomings in two-step deposition of perovskite layer. When the surface roughness decreases, larger grain formation is obtained. Secondly, MAI can form dense layers by reacting small  $\text{PbI}_2$  crystals and some unreacted  $\text{PbI}_2$  crystals remain under this dense layer. Dipping process has great influence on the cell performance and therefore, concentration and dipping time should be optimized for better cell performance. High MAI concentrations increase the amount of iodine ions in the solution which reduce hole density. Therefore, carrier density and charge transport nature are affected negatively. In reverse, higher concentrations provide an advantage to react more nuclei. Therefore, lower size grains are produced at high MAI concentrations which are the main reasons of better surface coverage. In other words, low MAI concentrations form large cuboids and high MAI concentrations create small cuboids. Small cuboids provide better packing and better charge transport, therefore higher open circuit voltage is obtained. On the other hand, larger cuboids enhance the internal light scattering which results in a higher short current density. Two step method is also applied by spin coating of MAI instead of dip coating. Main aim in this modification is to solve the problems related to dip coating. In this method, MAI solution is deposited by spin coating on top of  $\text{PbI}_2$  layer. It was detected that the use of two step spin coating deposition supplies an advantage to determine the morphology of perovskite crystals which is not possible in one step deposition process [31, 32, 37, 38].

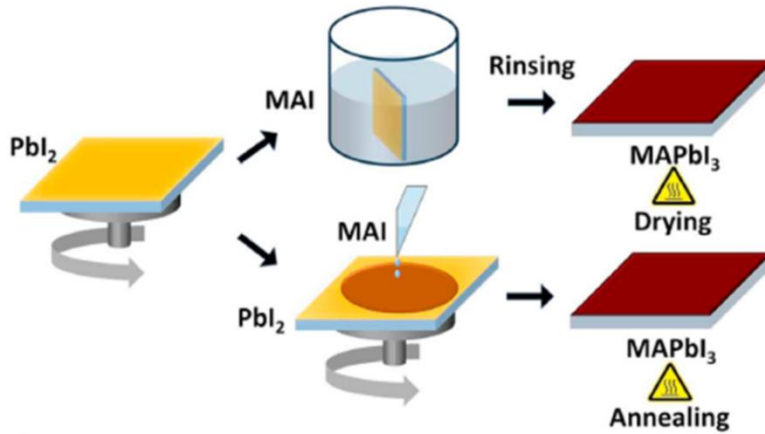


Figure 2.19. Two step deposition of perovskite layer [39].

#### 2.3.4.2. Vapor Based Deposition

Vapor assisted deposition can be performed using different methods. The simplest one is vapor assisted deposition which is realized by the modification of two step deposition technique (Figure 2.20).  $\text{PbI}_2$  layer is again deposited using spin coating. Then, coated substrate is exposed to MAI vapor. Produced films with this method have a good surface coverage, low surface roughness and large crystal size. Also, morphology and grain size modification can be supplied using gas-solid crystallization. It was resulted that, vapor assisted deposition provides better exciton formation with increased life time compared to two step deposition process.

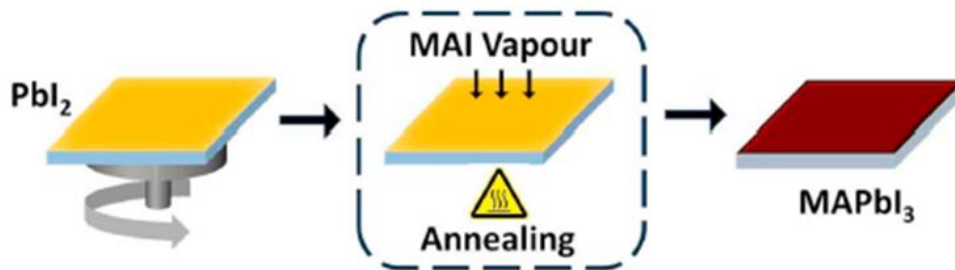


Figure 2.20. Vapor assisted deposition of perovskite layer [39].

Other vaporization techniques stand to vacuum deposition concept. Co-deposition of  $\text{PbX}_2$  and MAX is realized under high vacuum. With vacuum deposition techniques, exact thickness, good surface coverage and uniform coating can be supplied. After deposition, annealing process is additionally applied under nitrogen atmosphere. Following the annealing, perovskite layer is fully crystallized which supplies uniform distribution of perovskite in a crystalline and homogeneous morphology.

Perovskite layer can also be deposited by chemical vapor deposition (CVD) method. CVD technology has been used mostly in the fabrication of perovskite layer. Hybrid CVD and low-pressure CVD (LPCVD) are the main sub-CVD applications in the production of perovskite films.  $\text{PbX}_2$  and MAX are deposited sequentially in CVD techniques. Firstly,  $\text{PbX}_2$  layer is formed using thermal evaporation and the post MAX layer is formed by heating of the solution to about  $180^\circ\text{C}$ . Heated solution is transported using inert gas on top of  $\text{PbX}_2$  layer. Growth temperature, gas pressure, gas diffusion rate are the main parameters which affect the performance of perovskite layer. CVD coated perovskite layers show good crystallization, strong absorption, long carrier diffusion length and good humidity stability. These improved performances are obtained due to the minimized reaction rates [31, 32, 37, 38].

### **2.3.5. Electron Transport Layer (ETL)**

Electron transport layer is chosen according to two main criteria. First one is the charge extraction and mobility and position of energy levels is the second criteria. Organic and inorganic alternatives of electron transport layer can be used in perovskite solar cells. n-type metal oxide materials are widely used as inorganic ETL for charge transport purposes. They can be used in both mesoporous and planar configurations. In planar configuration, ETL is just formed using a compact layer. There is an additional mesoporous layer used on top of compact layer in mesoporous cells. Mesoporous layer can be used for template purposes and also it has charge transport

ability. Also, some types of nanoarrays have been studied to improve the charge collection as mesoporous layer [31, 32, 40, 41].

### 2.3.5.1. Compact Layer

Main responsibility of the compact layer is gathering of the excited electrons in perovskite layer and transferring to bottom electrode. Additionally, they should be barrier to holes to prevent recombination. Conduction band of compact layer should be so close to lowest unoccupied molecular orbital (LUMO) level of perovskite to accept the excited electrons efficiently. Open circuit voltage is directly affected from energy levels of the layers. When closer band energies are supplied, higher  $V_{oc}$  can be obtained. Also, this condition directly minimizes the possible interfacial recombinations. Figure 2.21 shows the band positions of alternative compact layers compared to perovskite layer. Inorganic and organic alternative materials can be used for compact layer.

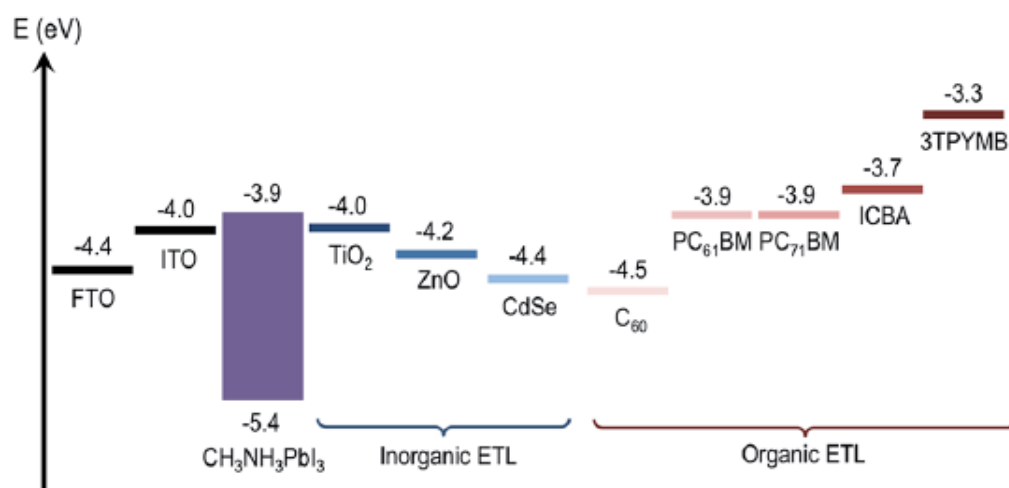


Figure 2.21. Conduction band edge positions of alternative compact ETLs [31].

TiO<sub>2</sub> is the most widely studied material in ETL alternatives because of its suitable band edge positions, low cost, variable deposition methods, and long electron life time. Opposite to popularity of TiO<sub>2</sub>, their stability is always debatable. Main problems are the degradation of sensitizer and inefficient electron extraction. Also, low electron mobility, high density trap states in the conduction band and high process temperature requirement should be improved. To improve the stability issues, studies are mostly focused on the composition, morphology, thickness, surface modifications and deposition techniques of these ETLs. To supply fast carrier injection and extraction, band position is optimized by doping of the compact layer. Yttrium is one of the common dopants for TiO<sub>2</sub>. Another improvement is performed by surface preparation of compact TiO<sub>2</sub> layers using UV/O<sub>3</sub> and TiCl<sub>4</sub> treatments. UV/O<sub>3</sub> treatment removes any organic contaminants left on the compact layer and supplies better adhesion of perovskite layer. TiCl<sub>4</sub> treatment fills the pin holes and creates uniform films. Also, TiCl<sub>4</sub> treatment supplies a better band matching of TiO<sub>2</sub> and perovskite.

Drawbacks of TiO<sub>2</sub> direct the studies to alternative materials such as SnO<sub>2</sub>, ZnO, CdS, and Zn<sub>2</sub>SnO<sub>4</sub>. SnO<sub>2</sub> is a suitable material which offers high electron mobility, good anti-reflection property and deep conduction band. These properties enhance the charge transfer rate. Also, they provide better stability because it does not have photocatalytic properties like TiO<sub>2</sub>. Up to now, obtained cell performances are at competing levels with TiO<sub>2</sub> compact layer. Another candidate material is ZnO which has good transport properties, high conductivity and suitable energy levels. ZnO has been used in both planar and mesoporous configurations. However, they have a big disadvantage which is the thermal decomposition of the perovskite layer due to the presence of ZnO. TiO<sub>2</sub> shows better thermal stability compared to ZnO. Enhancing the stability is realized using an interfacial layer between ZnO and perovskite sensitizer.

Organic counterparts of the metal oxides are also studied in the production of perovskite cells. Alternative materials are P3HT, PCBM, C60, and P3HT: PCBM. They are produced using solution chemistry and they can easily be applied to flexible substrates. Also, they can be used together with metal oxides as hybrid ETL [31, 32, 40, 41].

### **2.3.5.2. Scaffold Layer**

Mesoporous structures are used to create templates for the perovskite layer and charge transport purposes. They control the growth, size and distribution of the perovskite layer. TiO<sub>2</sub> was the first mesoporous layer material while the technology was evolved from DSSC to PSC. Both particle and pore sizes of the TiO<sub>2</sub> mesoporous layer have strong influence on the cell performance which directly affect the short circuit current density. To increase the flux of the carriers or channeling the excited electrons, alternative TiO<sub>2</sub> nanoarrays like nanowires and nanocones were studied instead of nanoparticles in mesoporous layer. Also, doping with metals was tried to increase the conductivity of mesoporous TiO<sub>2</sub>. Lithium is one of the important dopants in mesoporous TiO<sub>2</sub> layers. Doping enhances the mobility and conductivity of the electrons by reducing charge trap sites and recombination centers. Mesoporous layers are mostly fabricated using sol-gel techniques. They have to be annealed around 500°C to create mesoporous structures.

Passive scaffold layers are used as base for perovskite layer. Passive scaffolds layers have deep conduction band and high valence band. This creates a large bandgap and therefore passive scaffolds are mostly insulator in nature. Their energy band levels are far from the perovskite layer. Therefore, it is not possible to extract electrons from the LUMO level of perovskite layer. SiO<sub>2</sub>, Al<sub>2</sub>O<sub>3</sub> and ZrO<sub>2</sub> are the main materials used for passive scaffold layer. Passive scaffold materials do not contribute to charge transport. Al<sub>2</sub>O<sub>3</sub> also supplies an advantage by removing H<sub>2</sub>O from the perovskite layer which yields humidity resistant cell fabrication [31, 32, 40, 41].

### 2.3.6. Hole Transport Layer

HTL is responsible for both positive charge extraction and efficient hole transport process in perovskite solar cells (PSC). Therefore, HTL should have suitable band position with HOMO level of perovskite material, good hole mobility, good interaction with perovskite layer and good film forming properties. Band positions of alternative materials are given in Figure 2.22. Also, HTL should act as electron barrier to minimize the recombination. High thermal stability and resistance to external degradation factors are also primary requirements expected from HTL. Hole transport layers should be deposited in pin hole free condition; because, O<sub>2</sub> and moisture can penetrate from any defective region and degrade the perovskite layer. In addition to stability issue, pin hole free HTL is crucial to supply high mobility. Finally, cost of hole transport material is an important parameter to commercialize the PSCs. HTL can be evaluated under two material classifications which are the organic and inorganic. Organic HTLs can be evaluated under three types: small molecules, polymers and oligomers.

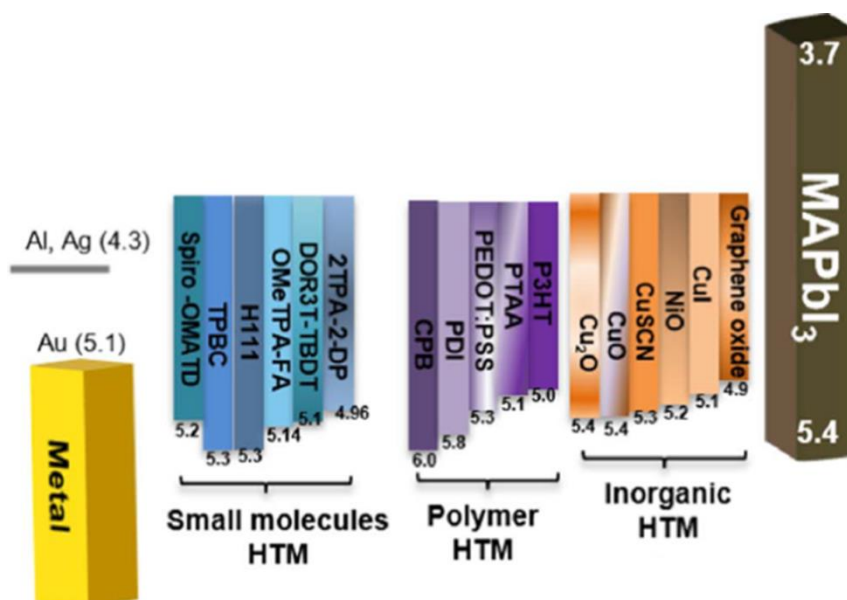


Figure 2.22. Valence band edge positions of alternative HTLs [42].

Small molecule based HTMs are popular material group in PSCs. Spiro-OMeTAD which belongs to the small molecule organic group, has been the first choice in the alternatives since the technology evolution is due to its high-performance nature. Spiro-OMeTAD was firstly tried in the production of solid state DSSCs. However, its performance was not higher than its liquid counterpart. The reason of the low efficiency is the low hole mobility and incomplete pore filling in thick mesoporous layers. When perovskite materials are in use, spiro-OMeTAD takes the position of liquid electrolyte in this technology. Pure spiro-OMeTAD has triangular pyramidal configuration, which causes large intermolecular distances. Therefore, it has low charge mobility and poor conductivity which yield high series resistance and low recombination resistance. For this reason, pure spiro-OMeTAD should be doped to enhance the conductivity. Bis(trifluoromethane)sulfonimide lithium salt (Li-TFSI) and 4-tert-butylpyridine (t-BP) are the main additives which suppress charge recombination and improve interface contact. High cost and difficult production of spiro-OMeTAD are the main disadvantages. Studies are focused on doping and using derivatives of spiro-OMeTAD.

Although the success of the spiro-OMeTAD is accepted, researches on alternative materials still continue. Polymeric HTL shows promising cell performances and they have higher hole mobility without doping and shows better stability. P3HT, PTAA and PEDOT: PSS are the main polymeric HTLs. P3HT is a widely used conducting polymer in organic solar cell applications, it can be produced relatively at a lower cost. Many studies are found in the literature about the application of P3HT as HTL in perovskite solar cells. Its performance is at promising levels; however, its flat molecular structure increases the charge recombination which lowers the cell efficiency. PTAA is also an important polymer for HTL production due to its high hole mobility. PTAA has high molecular weight which provides partial penetration to the TiO<sub>2</sub>/perovskite interface. Therefore, PTAA can be used as capping layer which offers low series resistance and high fill factor. PTAA HTL cells reach over 20 % efficiency. PEDOT: PSS is one of the promising HTL which is used together with

PCBM ETL due to suitable band positions. These cells are mostly constructed in inverted planar architecture due to transparent nature of PEDOT: PSS. It can be deposited at low temperatures which makes it suitable to flexible substrates. Acidity nature of PEDOT: PSS makes the usage limited.

Oligomers are the last organic HTL group. They possess intermediate relative molecular mass with small plurality. Oligomers have absorption nature which contributes to light harvesting. Their hole mobility is between the small molecules and polymeric HTLs. Also, their low molecular weight supplies good electron blocking.

Using of inorganic HTL is observed in limited studies due to low amount of material possibility. However, inorganic HTL provides low cost, wide band gap, easy processing and higher stability. CuI, CuSCN, NiO<sub>x</sub>, VO<sub>x</sub>, and MoO<sub>x</sub> are the main inorganic layers used in perovskite solar cells. Main problem is the low deposition temperature requirement of HTL on top of the perovskite layer in regular cell design. Therefore, the use of inorganic HTL was carried out mostly in inverted design.

Using CuI HTL was tried in both DSSC and PSC due to its high hole mobility. However, cells are suffered from high recombination due to improper band edge positions. Another drawback is that solvent for CuI can also dissolve the perovskite material; therefore, many efforts were carried out to find alternative deposition techniques. CuSCN has good transparency, high mobility and good stability which make it another candidate HTL. Optimization of CuSCN layer thickness is crucial for better cell performance. While thinner CuSCN suffers from low shunt resistance, thicker CuSCN creates higher series resistance. Possible usage of NiO as p-type material was detected in Irwing's work [43] who researches the possible healing in DSSCs. Addition to p-type nature, NiO has large band gap, good conductivity, and well-matched band position with perovskite layer. However, first report did not create a good impact due to low coverage of perovskite layer. Quality of NiO film and surface treatments are dramatically enhance the cell performance. Therefore, deposition

technique of NiO is an important factor for PSCs. Healing in device performance was observed when the deposition was performed by sputtering technique which provides uniform and homogenous layer. Another attempt of NiO is the use of it in both planar and mesoporous configuration which can supply the use of a thicker perovskite layer. There is limited study in which NiO was used in n-i-p configuration. Due to high temperature annealing requirement, cell was constructed in inverted design.  $\text{Cu}_2\text{O}$ , graphene oxide,  $\text{MoO}_3$ ,  $\text{VO}_x$  and  $\text{WO}_x$  are the possible inorganic materials for HTL.  $\text{Cu}_2\text{O}$  was studied due to its high hole mobility, long carrier diffusion length and direct band gap. Graphene oxide and  $\text{MoO}_3$  are the promising materials for organic solar cells due to their high charge mobility and electrical conductivity and therefore there are some studies using them in PSCs. Low temperature deposition is the main advantages of  $\text{VO}_x$  and  $\text{WO}_x$  [31, 32, 40, 42].

### **2.3.7. Electrodes**

Perovskite solar cells are built up between two electrodes. One of the electrodes should be transparent to incoming photons and these two electrodes should be conductive for charge pick up. Transparent and conductive oxides (TCO) are the main materials for the bottom side electrode. They have long wavelength transparency, metal like conductivity, and suitable work function. Metal-semiconductor junction is formed between TCO and n-type semiconductor material. This interface behaves as barrier and reduces output power. To maximize the power, work function of the TCO should be lower than fermi energy of semiconductor. In this case, electrons can easily be collected by TCO electrode. They are deposited on top of glass or flexible polymer substrates. If the cell is designed on top of metal sheet, TCO should be deposited on the top electrode. Two common materials in TCO family are fluorine doped tin oxide (FTO) and indium doped tin oxide (ITO). FTO is chosen when a high temperature process is required for the production of the cells. Conductivity of ITO decreases when it is exposed to high temperatures. ITO is the common electrode material when cells are produced at low temperatures. Also, it is found that FTO is deposited at higher

roughness values compared to ITO; this causes better wettability of n-type semiconductor on top of FTO.

If the bottom layer is transparent, the use of metals is favorable for the top electrode. Top electrode should make ohmic contact with the layer underneath the electrode, which is mostly hole transport layer. Opposite to bottom electrode, top electrode should have higher work function than the fermi energy level of HTL. With higher work function, formation of Schottky junction is avoided. Gold, aluminum and silver are the main metal electrodes. Gold has the highest work function; however, its visible reflection is not good. Silver has better reflectivity and lower work function. Metallic films are deposited using vacuum evaporation or sputtering techniques. Carbon electrode is also an important alternative electrode. Although their cell performances are not at competing levels with metals, they have advantage in stability, easy processing and low cost. Carbon electrodes can be coated using screen printing methods which are suitable for large area deposition and flexible substrates [39, 44].



## REFERENCES

- [1] A. P. Kirk, Solar photovoltaic cells: Photons to electricity, Academic Press, 2014.
- [2] A. Luque, S. Hegedus, Handbook of photovoltaic science and engineering, John Wiley & Sons, 2011.
- [3] S. R. Wenham, M. A. Green, M. E. Watt, R. Corkish, A. Sproul, Applied photovoltaics, Routledge, 2013.
- [4] R. R. Willey, Field guide to optical thin films, Society of Photo Optical, 2006.
- [5] M. A. Green, Solar cells: Operating principles, technology, and system applications, Englewood Cliffs, NJ, Prentice-Hall, Inc., 1982.
- [6] A. J. McEvoy, L. Castaner, T. Markvart, Solar cells: Materials, manufacture and operation, Academic Press, 2012.
- [7] P. Würfel, U. Würfel, Physics of solar cells: From basic principles to advanced concepts, John Wiley & Sons, 2009.
- [8] T. Dittrich, Materials concepts for solar cells, World Scientific Publishing Company, 2014.
- [9] G. P. Smestad, Optoelectronics of solar cells, SPIE press, 2002.
- [10] A. Fahrenbruch, R. Bube, Fundamentals of solar cells: Photovoltaic solar energy conversion, Elsevier, 2012.
- [11] A. Goetzberger, J. Knobloch, B. Voss, Crystalline silicon solar cells, John Wiley & Sons Ltd, 1998.
- [12] J. Nelson, The physics of solar cells, World Scientific Publishing Company, 2003.
- [13] B. Sørensen, Renewable energy: Its physics, engineering, environmental impacts, economics & planning, 2000.
- [14] F. Kreith, D. Y. Goswami, Handbook of energy efficiency and renewable energy, Crc Press, 2007.
- [15] M. Grätzel, Dye-sensitized solar cells, Journal of Photochemistry and Photobiology C: Photochemistry Reviews, 4 (2003) 145-153.

- [16] K. Kalyanasundaram, Dye-sensitized solar cells, EPFL press, 2010.
- [17] J.-K. Lee, M. Yang, Progress in light harvesting and charge injection of dye-sensitized solar cells, *Materials Science and Engineering: B*, 176 (2011) 1142-1160.
- [18] A. R. B. Mohd Yusoff, P. Gao, M. K. Nazeeruddin, Recent progress in organohalide lead perovskites for photovoltaic and optoelectronic applications, *Coordination Chemistry Reviews*, 373 (2018) 258-294.
- [19] M. Habibi, F. Zabihi, M. R. Ahmadian-Yazdi, M. Eslamian, Progress in emerging solution-processed thin film solar cells-part ii: Perovskite solar cells, *Renewable and Sustainable Energy Reviews*, 62 (2016) 1012-1031.
- [20] N. Elumalai, M. Mahmud, D. Wang, A. Uddin, Perovskite solar cells: Progress and advancements, *Energies*, 9 (2016) 861.
- [21] R. Fan, Y. Huang, L. Wang, L. Li, G. Zheng, H. Zhou, The progress of interface design in perovskite-based solar cells, *Advanced Energy Materials*, 6 (2016) 1600460.
- [22] A. Kojima, K. Teshima, Y. Shirai, T. Miyasaka, Organometal halide perovskites as visible-light sensitizers for photovoltaic cells, *Journal of the American Chemical Society*, 131 (2009) 6050-6051.
- [23] J. H. Im, C. R. Lee, J. W. Lee, S. W. Park, N. G. Park, 6.5% efficient perovskite quantum-dot-sensitized solar cell, *Nanoscale*, 3 (2011) 4088-4093.
- [24] H. S. Kim, C. R. Lee, J. H. Im, K. B. Lee, T. Moehl, A. Marchioro, S. J. Moon, R. Humphry-Baker, J. H. Yum, J. E. Moser, M. Grätzel, N. G. Park, Lead iodide perovskite sensitized all-solid-state submicron thin film mesoscopic solar cell with efficiency exceeding 9%, *Scientific Reports*, 2 (2012) 591.
- [25] M. M. Lee, J. Teuscher, T. Miyasaka, T. N. Murakami, H. J. Snaith, Efficient hybrid solar cells based on meso-superstructured organometal halide perovskites, *Science*, 338 (2012) 643.
- [26] J. Burschka, N. Pellet, S. J. Moon, R. Humphry-Baker, P. Gao, M. K. Nazeeruddin, M. Grätzel, Sequential deposition as a route to high-performance perovskite-sensitized solar cells, *Nature*, 499 (2013) 316.
- [27] N. J. Jeon, J. H. Noh, Y. C. Kim, W. S. Yang, S. Ryu, S. I. Seok, Solvent engineering for high-performance inorganic-organic hybrid perovskite solar cells, *Nature Materials*, 13 (2014) 897.

- [28] T. A. Berhe, W. N. Su, C. H. Chen, C. J. Pan, J. H. Cheng, H. M. Chen, M. C. Tsai, L. Y. Chen, A. A. Dubale, B. J. Hwang, Organometal halide perovskite solar cells: Degradation and stability, *Energy & Environmental Science*, 9 (2016) 323-356.
- [29] Y. Rong, Y. Hu, A. Mei, H. Tan, M. I. Saidaminov, S. I. Seok, M. D. McGehee, E. H. Sargent, H. Han, Challenges for commercializing perovskite solar cells, *Science*, 361 (2018).
- [30] C. T. Zuo, H. J. Bolink, H. W. Han, J. S. Huang, D. Cahen, L. M. Ding, Advances in perovskite solar cells, *Advanced Science*, 3 (2016) 16.
- [31] T. Salim, S. Sun, Y. Abe, A. Krishna, A. C. Grimsdale, Y. M. Lam, Perovskite-based solar cells: Impact of morphology and device architecture on device performance, *Journal of Materials Chemistry A*, 3 (2015) 8943-8969.
- [32] T. H. Liu, K. Chen, Q. Hu, R. Zhu, Q. H. Gong, Inverted perovskite solar cells: Progresses and perspectives, *Advanced Energy Materials*, 6 (2016) 17.
- [33] W. J. Yin, J. H. Yang, J. Kang, Y. Yan, S. H. Wei, Halide perovskite materials for solar cells: A theoretical review, *Journal of Materials Chemistry A*, 3 (2015) 8926-8942.
- [34] N. G. Park, Perovskite solar cells: An emerging photovoltaic technology, *Materials Today*, 18 (2015) 65-72.
- [35] G. Grancini, C. Roldán-Carmona, I. Zimmermann, E. Mosconi, X. Lee, D. Martineau, S. Narbey, F. Oswald, F. De Angelis, M. Graetzel, M. K. Nazeeruddin, One-year stable perovskite solar cells by 2d/3d interface engineering, *Nature Communications*, 8 (2017) 15684.
- [36] M. I. H. Ansari, A. Qurashi, M. K. Nazeeruddin, Frontiers, opportunities, and challenges in perovskite solar cells: A critical review, *Journal of Photochemistry and Photobiology C-Photochemistry Reviews*, 35 (2018) 1-24.
- [37] H. S. Jung, N. G. Park, Perovskite solar cells: From materials to devices, *Small*, 11 (2015) 10-25.
- [38] M. S. Jamal, M. S. Bashar, A. K. M. Hasan, Z. A. Almutairi, H. F. Alharbi, N. H. Alharthi, M. R. Karim, H. Misran, N. Amin, K. B. Sopian, M. Akhtaruzzaman, Fabrication techniques and morphological analysis of perovskite absorber layer for high-efficiency perovskite solar cell: A review, *Renewable and Sustainable Energy Reviews*, 98 (2018) 469-488.

- [39] A. B. Djurišić, F. Z. Liu, H. W. Tam, M. K. Wong, A. Ng, C. Surya, W. Chen, Z. B. He, Perovskite solar cells - an overview of critical issues, *Progress in Quantum Electronics*, 53 (2017) 1-37.
- [40] X. Tong, F. Lin, J. Wu, Z. M. M. Wang, High performance perovskite solar cells, *Advanced Science*, 3 (2016) 18.
- [41] T. Singh, J. Singh, T. Miyasaka, Role of metal oxide electron-transport layer modification on the stability of high performing perovskite solar cells, *Chemsuschem*, 9 (2016) 2559-2566.
- [42] Z. H. Bakr, Q. Wali, A. Fakharuddin, L. Schmidt-Mende, T. M. Brown, R. Jose, Advances in hole transport materials engineering for stable and efficient perovskite solar cells, *Nano Energy*, 34 (2017) 271-305.
- [43] M. D. Irwin, D. B. Buchholz, A. W. Hains, R. P. H. Chang, T. J. Marks, p-type semiconducting nickel oxide as an efficiency-enhancing anode interfacial layer in polymer bulk-heterojunction solar cells, *Proceedings of the National Academy of Sciences*, 105 (2008) 2783.
- [44] T. T. Xu, L. X. Chen, Z. H. Guo, T. L. Ma, Strategic improvement of the long-term stability of perovskite materials and perovskite solar cells, *Physical Chemistry Chemical Physics*, 18 (2016) 27026-27050.

## CHAPTER 3

### EXPERIMENTAL METHODS

This work investigates the use of electron beam evaporation technique for the deposition of hole transport and electron transport layers of perovskite solar cells. Titanium dioxide ( $\text{TiO}_2$ ) and niobium pentoxide ( $\text{Nb}_2\text{O}_5$ ) materials were deposited for electron transport layer and nickel oxide ( $\text{NiO}$ ) and titanium monoxide ( $\text{TiO}$ ) were used for hole transport layer. These materials were investigated in single layer form. Deposition temperature, oxygen addition, deposition rate and plasma source were taken as the affecting parameters for the thin films related to the structural, optical and electrical properties. During the production of perovskite cells, hole transport and electron transport layers were deposited by electron beam evaporation technique. Mesoporous layers, perovskite layers and organic hole transport layers were formed using wet chemistry and deposited using spin coating technique. Back electrode was coated using the sputtering technique. When hole transport and electron transport layers were deposited, the same deposition conditions used for the single layer deposition of the materials were employed. Cell performances were explained using the results of structural, optical and electrical analyses of single layer films.

Morphological and structural characterizations of single layers were performed using scanning electron microscope (SEM), X-ray diffraction (XRD) and X-ray photoelectron spectroscopy (XPS). Optical measurements were realized using ultraviolet and visible photospectroscopy in which reflectance and transmittance measurements were carried out. Thicknesses of the single layers and refractive index dispersions were calculated using fitting algorithms. Band gap values were also calculated using the optical measurements. Hall effect measurements and ultraviolet photoelectron spectroscopy techniques were used to investigate the electrical

properties of single layers. Current density-voltage measurements of cells were carried out under simulated solar light conditions. Cells were also characterized using the electrochemical impedance spectroscopy (EIS) to understand the performance of the charge transfer properties of each layer. In the following parts; firstly, fundamentals of the thin film deposition will be explained. Production of the perovskite solar cells will be discussed in the second part of this chapter.

### **3.1. Thin Film Deposition**

Many of the optical, electrical, magnetic, chemical, mechanical and thermal properties can be obtained by the use of thin films. Some of the applications of thin films are given below:

- Anti-reflective coatings
- Memory disks
- Gas/liquid sensors
- Heat sinks
- Semiconductor devices
- Piezo electric devices

There are many deposition techniques for the production of thin films. These methods can be evaluated under two main branches: vacuum based depositions and solution based depositions. Vacuum based physical and chemical deposition approaches are performed under vacuum conditions. While deposition is made using solid materials in physical techniques, gas precursors are used in chemical techniques. Solution based deposition always starts with the production of the suitable chemical precursor. Then, these chemicals are applied on substrates using the methods of spin coating, dip coating, spray coating and screen printing methods. Following parts explain some of the critical points related to thin film depositions [1, 2].

### 3.1.1. Vacuum Based Thin Film Deposition

#### 3.1.1.1. Some of the Parameters of the Vacuum Based Thin Film Deposition

##### a) Vacuum

Vacuum environment is the major tool for the formation of thin films. Vacuum is defined as the lower pressure form of the atmosphere from rough to ultra-high vacuum. Vacuum condition supplies long mean free path of the vaporized molecules and therefore, it is easier to supply line of sight deposition. Vacuum regimes are classified as rough vacuum, medium vacuum, high vacuum and ultrahigh vacuum. Better vacuum atmosphere supplies lower gas density and longer mean free path. However, low deposition rate is yielded for high vacuum atmosphere. These relations are given in Table 3.1.

Table 3.1. Pressure level and evaporated molecule relation [3].

Degree of vacuum	Pressure (Torr)	Gas Density (molecules/m <sup>3</sup> )	Mean Free Path (m)	Time for monolayer deposition (s)
Atmosphere	760	$2 \times 10^{19}$	$10^{-7}$	$10^{-9}$
Low	1	$3 \times 10^{16}$	$10^{-4}$	$10^{-6}$
Medium	$10^{-3}$	$3 \times 10^{13}$	$10^{-1}$	$10^{-3}$
High	$10^{-6}$	$3 \times 10^{10}$	$10^2$	1
Ultra-High	$10^{-10}$	$3 \times 10^6$	$10^6$	$10^4$

Vacuum atmosphere formation starts with low vacuum which is sustained with mechanical pumps. Mechanical pumps operate by the compression and throw of a

specific volume of gas at high pressure. Working principle of mechanical pump can be seen in Figure 3.1a. At high pressure, viscous flow is obtained due to molecule to molecule collision. When the pressure is lowered, main transport mechanism returns to molecular flow in which collision occurs at the wall of the containers. When a specific vacuum level (mainly  $10^{-3}$  torr) is reached by mechanical pump, high vacuum pumps start to work. Different types of high vacuum pumps can be used such as diffusion pumps, turbomolecular pumps and cryo pumps. Figure 3.1 demonstrates all high vacuum pumps. Diffusion pump operates by holding of gas molecules using directed jet of oil molecules. Turbomolecular pump has a high velocity rotating turbine for the strike of gas molecules. Cryo pumps operate by freezing or condensation of gas molecules on the colder surfaces [4-6].

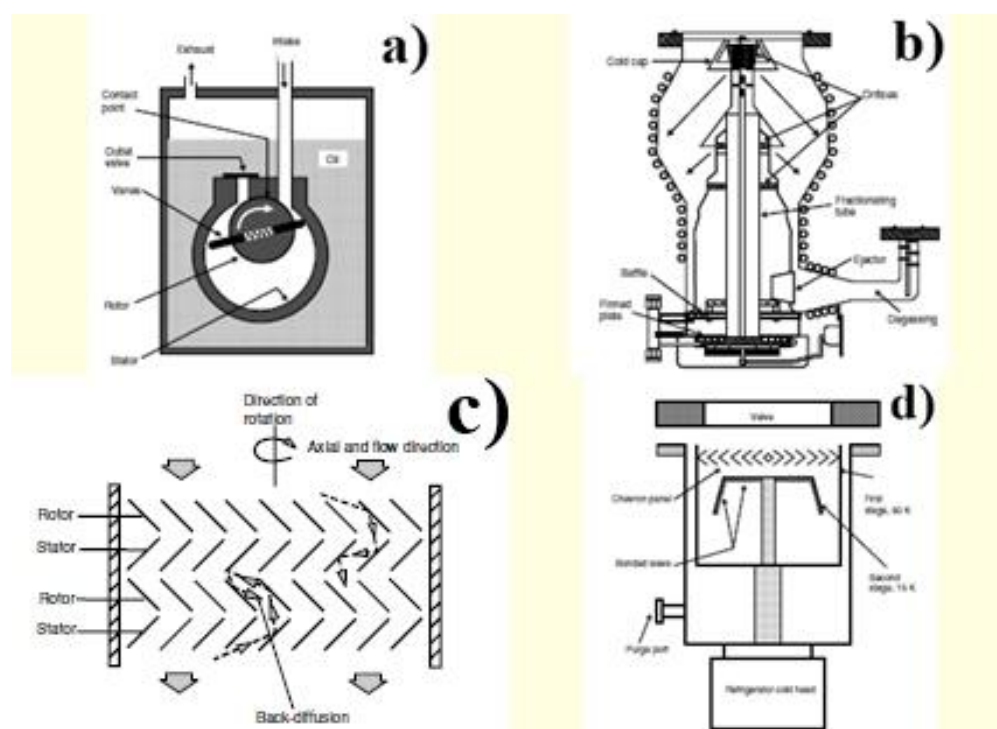


Figure 3.1. Vacuum pumps: a) Mechanical pump, b) Diffusion pump, c) Turbomolecular pump, and d) Cryo pump [6].

## **b) Plasma**

Plasma, which includes ions, electrons and atomic species, is weakly ionized quasi neutral gas. Plasma sources are mostly used in deposition systems; they can be used for etching, assisting and enhancing the evaporation and sputtering properties. In each case, plasma has a different density ranging from  $10^8$  to  $10^{18}$  ions per  $\text{cm}^3$ . Plasma formation is based on the discharging process. In a cathode box, an electron source is used to generate the electrons. At the same time inert gas (mostly argon) is sent to the cathode box and a small voltage is applied. Free ions and electrons firstly move to the opposite electrodes. When the voltage increases, gas molecules and electrons collide and some ionization is produced which is called as discharge. Plasma is generated at specific pressure according to the gas type. Enough collision is not supplied at low pressure and enough acceleration is not sustained for collision at high pressure [2, 4, 5].

## **c) Uniformity**

Thickness uniformity of thin films on the substrate is an important parameter. To supply higher uniformity, main approaches are using large area sources, substrate rotation and increasing distance between the source and the substrate. Distance between the source and substrates can be between 5-100 cm in which required vacuum should be better than  $10^{-5}$  torr to avoid collision [5, 7].

### **3.1.1.2. Physical Vapor Deposition**

Physical vapor deposition (PVD) is realized in three sequential steps. Firstly atoms or molecules are vaporized from a solid or liquid surface, followed by the transport of vaporized atoms or molecules to the deposition surface and finally, these atoms or molecules are condensed on the substrate. PVD is based on two different technologies

with respect to vaporization type. One technology is the thermal heating of the material at a temperature for its vaporization which is commonly called as thermal evaporation or sublimation. Secondly, vaporization can be performed by momentum transfer by the ion bombardment of the solid surface which is named as physical sputtering. Thin films produced by PVD can be used for many discrete areas such as electrically conductive, transparent electrical conductors, electrically insulating, optical, thermal control, and decorative coatings.

Evaporation of materials can occur due to different reactions. Common reactions are evaporation without dissociation, decomposition and evaporation with dissociation. Evaporation without dissociation is observed in SiO and GeO, in which species are vaporized and condensed on the substrate directly. Ag<sub>2</sub>S and GaAs are the examples of the decomposed evaporated materials. These types of materials are deposited using separate sources. Some of the oxides like SiO<sub>2</sub> and TiO<sub>2</sub> dissociate during the evaporation and therefore, additional oxygen atmosphere is required during evaporation [2, 8].

### **3.1.1.3. Evaporation Processes**

Evaporation processes can be carried out using different processes. Some of the important evaporation processes are resistive (thermal), electron beam, pulsed laser, ion assisted and cathodic arc evaporations. Resistive evaporation occurs by joule heating of refractory metal crucible like tungsten and tantalum in which evaporating material is placed. Resistive evaporation is suitable for the low melting or sublimation temperature materials. Most of the metals and some fluorides and sulfides can be deposited using resistive heating. Ultraviolet or visible laser is used for the ablation of the materials in pulsed laser deposition (PLD) technique. Ablated materials are deposited on a substrate opposite to the target. High deposition rate, cleaning and high stoichiometric film formation are the advantages. Non uniformity and small area coatings are the basic disadvantages of PLD. Another common process is cathodic arc

evaporation. In this process, metal vapor plasma, which is produced using electric arc, is employed to vaporize solid cathode material. This process is widely used for the deposition of TiN for hard coating purposes [2, 8].

#### 3.1.1.4. Electron Beam Evaporation

Electron beam evaporation is a proper method for the deposition of high melting or sublimation temperature materials. Electron beam can create temperature up to  $3500^{\circ}\text{C}$ . Electrons are produced using hot tungsten filament. Produced electron beam is focused magnetically and the beam is deflected  $270^{\circ}$  using permanent magnet to focus the electron beam on top of the material. Vaporized material is placed inside a crucible, which are water-cooled to decrease the effect of heating. Produced beam has 3 mm diameter which creates around  $25\text{ kW/cm}^2$  of intensity. Electron beam can be swept on the material using magnets. Sweeping of the electron beam yields a better rate of control and better quality films. Components of electron beam source are given in Figure 3.2 [2, 8].

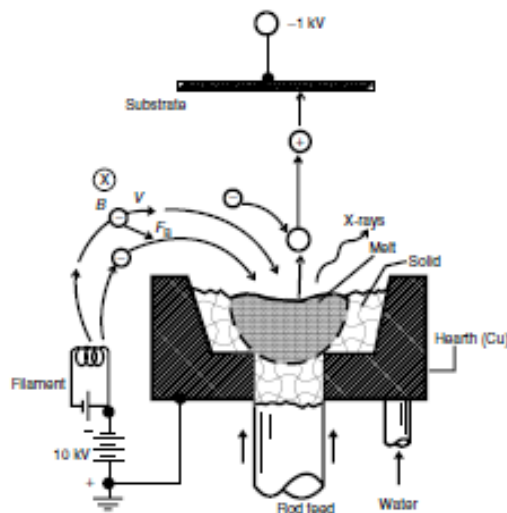


Figure 3.2. Components of electron beam source [2].

### **3.1.1.5. Sputtering**

Sputtering process occurs by the bombardment of the target material using accelerated ions. Accelerated ions crash to the target and eject atoms from the target. Ejected atoms transport and condense on the substrate. Argon ions are mostly used for sputtering. Different types of sputtering techniques are available such as DC sputtering, RF sputtering, magnetron sputtering, and reactive sputtering. DC sputtering is mostly used for the deposition of metallic films. However, it is not possible to deposit insulators at reasonable rates in DC sputtering technique. For the insulators, RF sputtering is used. RF sputtering is performed at 13.56 MHz in which ions are relatively immobile. Difference in the mobilities of ions and electrons creates negative self-bias which allows for sputtering of the insulators. Magnetron sputtering can be applicable to both RF and DC sputtering. Without magnets, there is a possible recombination loss at the chamber walls. The use of magnetic field enhances the electron path length by decreasing recombination. Reactive sputtering is another process for the formation of oxides and nitrides. Metallic or insulator targets are deposited under extra oxygen or nitrogen [8].

### **3.1.1.6. Film Formation in PVD Coatings**

Reactive or electron beam evaporating vapors have around 0.1 eV energy. The vaporized molecules transport to the substrate surface and condense there. If the substrate is cold, atoms give up their energies whenever they are in contact with the surface. Therefore atoms do not have any time to provide a granular structure and thin films are formed in columnar structure. When the substrate temperature increases, atoms do not give their energies quickly. Energetic atoms can migrate and they can go to lower energetic states. This creates a denser film formation. Structural evaluation of thin films was explained by structure zone models which was firstly studied by Movchan and Demchishin for resistive and electron beam evaporation. Then, Thornton expands the study for the sputtering process. In the first study, structures of

thin films were correlated with deposition temperature ( $T_s$ ) to melting temperature ( $T_m$ ) ratio. Three zones are separated from each other using  $T_s/T_m$  ratio. Zone 1, zone 2 and zone 3 correspond to  $T_s/T_m$  ratio smaller than 0.3, between 0.3 and 0.45 and higher than 0.45, sequentially. Zone 1 is the region of columnar growth with significant voids. Zone 2 is the densely packed columns and zone 3 is the region of polycrystalline structure. Additionally Zone T was defined to represent the transition zone from zone 1 microstructure to zone 2 microstructure. Zone T consists of poorly defined fibrous grains without void boundaries. Thornton study investigates the argon pressure together with  $T_s/T_m$  ratio on the nucleation and growth kinetics of thin films [9, 10]. Figure 3.3 shows structural zones for Thornton zone model. The other variables which affect the nucleation and growth kinetics in other words all the properties of thin films are:

- Film material
- Deposition rate (Flux of film material)
- Kinetic energy of the film materials (Plasma assistance)
- Substrate material
- Surface cleanliness

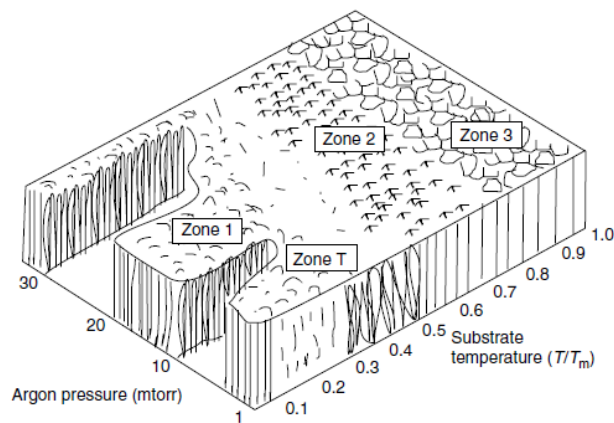
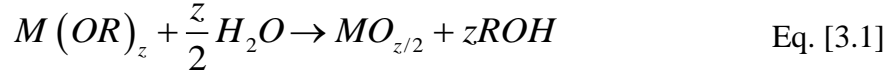


Figure 3.3. Thornton zone model [9].

### 3.1.2. Sol-Gel Coatings

Sol-gel coatings have gained importance in the last 25 years. Also, they replace some vacuum coatings in many applications due to their easy development and low cost. These applications start with the preparation of the chemical solutions which are obtained by mixing of precursors and solvents. In sol-gel chemistry, metal alkoxides possess the general chemical formula  $[M(OR)_z]_n$  (M=metal, R=organic residue, n=degree of molecular association) and they are the main class to prepare the precursor solution. Metal alkoxides supply high purity, solubility in organic solvents, chemical reactivity and options for chemical modifications, however, they are known as expensive materials compared to their alternatives; such as metal nitrates, oxides, hydroxides, carbonates or carboxylates. Metal alkoxides are produced by replacing the proton of the hydroxyl group of an alcohol molecule (R-OH) with a metal cation. Their preparation is realized by the reaction of metal chlorides with anhydrous alcohols. Chemical solutions are prepared from the metal precursors using the two following reactions: hydrolysis (Eq. [3.1]) and condensation (Eq. [3.2]). The alkoxy groups are replaced by hydroxoligands in the hydrolysis reaction. In these reactions, water is acting as a Lewis base which attacks the metal atom and then proton transfer occurs from the water molecule to the structure, and finally, alcohol molecule is released. Condensation reactions start when the hydroxogroups are formed. Condensation reactions occur in three different steps: formation of 'ol' bridges, formation of 'oxo' bridges and leaving groups by proton transfer to hydroxyl groups and formation of metal-oxygen-metal bonds water or alcohol removing. After condensation of the solution, metal-oxide coating solution is formed. These coating solutions can form films on the substrate by spin, dip or spray coating methods. Coating solution is dropped on the substrate and then, substrate is rotated, a thin coating is formed on the substrate surface in the spin coating method. In dip coating, substrate is dipped into the coating solution and then substrate is removed from the solution at a controlled rate. In spray coating, coating solution is sprayed on the substrate [11].



### 3.1.2.1. Spin Coating

Spin coating is a simple and fast process to deposit thin films. Spin coating is mostly deposited on flat surfaces. Spin coating is a relatively cheap method and it is suitable to batch process. Spin coating is used in a variety of areas from experimental to industrial. Spin coating process starts with the dissolving of the coating material into the suitable solvent. Substrates are placed on the rotating disk and prepared solution is poured onto the substrate. Solution dispensing can be performed using manual or automatic means. Disk is rotated and majority of solution is flung off the side. Rotation can be carried out between 1000 to 10000 rpm which supplies uniform covering of the substrate. High rotation speed provides centrifugal forces combined with surface tension of the solution. In this way, majority of the solvent is dried by air flow and plasticized film is formed. Then, solvent evaporates from the top of the solution and thin film is formed. Spin coating deposition occurs in four sequential steps: fluid dispensing, spin-up, spin-off and evaporation. Stages of spin coating are demonstrated in Figure 3.4. In spin coating method, deposition thickness can be varied between few nm to few  $\mu\text{m}$ . Film thickness and quality strictly depend on the viscosity, drying rate, amount of solids and surface tension of the solutions. When solution is not wetted to the substrate, some pre-process should be applied to decrease the contact angle. Wetting of the solution to the substrate is crucial to yield better films. Also, edge effect formation possibility increases when the solution has a high surface tension. For this reason, low surface tension solutions yield the elimination of the edge irregularities. In addition, process parameters like rotational speed, acceleration, and time strongly affect the film properties [12, 13].

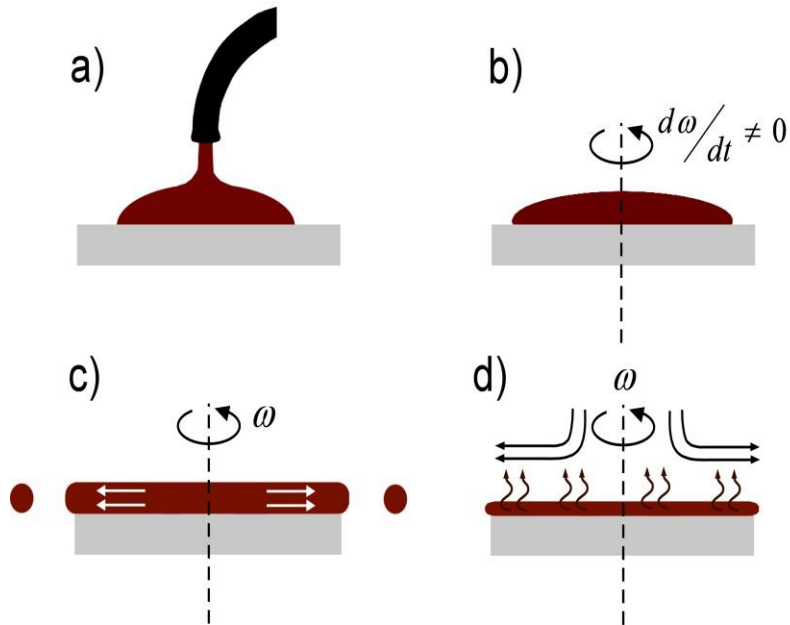


Figure 3.4. Four steps of the spin coating process [12].

### 3.2. Construction of Hybrid Mesoporous and Planar Perovskite Solar Cells

In this study, electron beam deposited electron transport (ETL) and hole transport layers (HTL) were investigated. For this reason, perovskite solar cells were constructed using these layers and they are characterized. Performances of perovskite solar cells are highly dependent on the production routes in the construction of perovskite solar cells. In this study, all the cells were fabricated in n-i-p configuration. Cells are formed on top of FTO coated glass layer. While some of the cells include mesoporous layer, some of them were produced in planar configuration. For the studies of alternative hole transport layers, TiO<sub>2</sub> compact and mesoporous layers were used as electron transport layer. Also, while investigating the alternative ETL's, spiro-OMeTAD was used for HTL. Finally back gold contact was deposited to produce perovskite cells. Following section explains the production routes for the perovskite solar cells.

### 3.2.1. Etching of the Substrate

FTO deposited glass substrates were firstly cut to the dimensions of 15 mm width and 20 mm length. Then, these substrates were patterned by etching FTO coatings on the glass substrates. For the production of perovskite solar cells, all layers are deposited on each other. For the current density and voltage measurements, contacts are used as front and back electrodes. During the measurements, there is a strong possibility that interfacial layers between the electrodes can be damaged. This situation increases the short circuit pathways between the electrodes in the perovskite solar cell. For this reason, contact positions of the front and back electrodes were separated from each other by etching of the FTO layer. Firstly, tape type masking is performed for the regions which will not be etched. Then, zinc powder is poured on top of the FTO coated substrates followed by placing diluted HCl on zinc powder. Zinc powder and HCl undergo into a reaction and hydrogen gas is formed. Hydrogen gas reduces the tin oxide which is washed by the acid. Finally, cells were cleaned by plenty of water. Figure 3.5 schematizes the patterning of the FTO coated substrates.

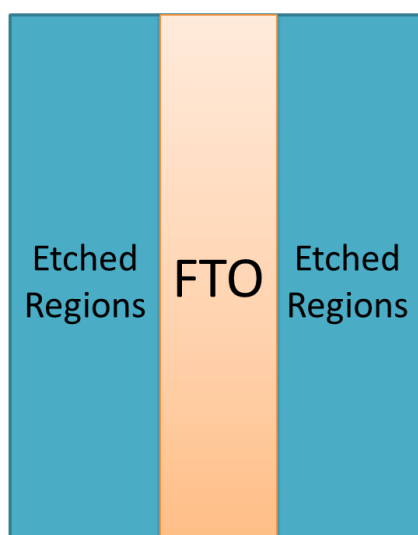


*Figure 3.5.* Etching procedure of the FTO coated glass.

### **3.2.2. Substrate Cleaning**

Substrate cleaning is the following step in the production of perovskite solar cells. FTO coated glass should be cleaned to create defect free surface which is critical for better adherence of the following layer. Any dust or dirty regions are resulted with pinholes on the following layer or the peeling of the film. For these reasons, etched FTO substrates were subjected to following cleaning steps. Substrates were dipped and cleaned ultrasonically in a detergent solution, deionized water, acetone, deionized water, and isopropanol, sequentially for 10 min. Cleaned substrates were stored in isopropanol solution until the deposition of compact layer. When the substrates were taken off from the isopropanol, they were dried using nitrogen flow. Then, UV-Ozone treatment was applied for 15 min to the substrates previous to the deposition of compact layer. UV-Ozone treatment removes most of the organic contaminants and directly enhances the carrier transport between FTO and compact layer [14].

### **3.2.3. Preparation of Compact Layer**

In this study, compact layers were deposited using electron beam evaporation technique. Depositions were performed using Tecport thin film coating system which has 1200 mm diameter and is 1350 mm in height. The coating system can be seen in Figure 3.6. System has two rough pumps which are mechanical and booster pumps. Mechanical pump starts firstly before the booster pump becomes active. When the pressure level decreases to  $10^{-3}$  torr, valve which is in front of the diffusion pump is opened. Then, system transfers from rough vacuum to high vacuum regime. This system has two 24 inch diffusion pumps. Diffusion pump oil is heated to  $230^{\circ}\text{C}$  before the vacuum process starts. It means that diffusion pump is kept at ready position for pumping. High vacuum is measured using ion gauge and convectron gauge is used to measure low vacuum in chamber. Polycold unit is used to fasten the pumping rate. Polycold, which works as cold trap for water based molecules, is a closed loop of  $-120^{\circ}\text{C}$  liquid inside the chamber. Substrates are placed above the four planetary

rotation holders. Holders are connected to the main rotation body. Rotation was performed at 10 rpm during the deposition process. Planetary movement supplies better thickness uniformity along the diameter of holders. Substrate temperature can be increased up to 300°C. Heating is realized using halogen lamps. System has 3 electron beam sources and 2 resistive heating sources. Also, one plasma source is located into the system to assist deposition. Coating thickness is determined using a quartz crystal which measures the change in the natural frequency by added mass.



*Figure 3.6.* Tecport deposition system.

Compact layers were deposited on top of FTO layer. Firstly, etching process in vacuum was applied to create better surface for deposition. Etching process was started when the base pressure of the system reaches to  $10^{-5}$  torr vacuum level. Etching was carried out using the plasma source for 2 min at 70 V bias voltage. Discharging was created using argon gas at 10 A current and 100 V voltage values. Working principle of plasma source which was used in Tecport system is given in Figure 3.7.

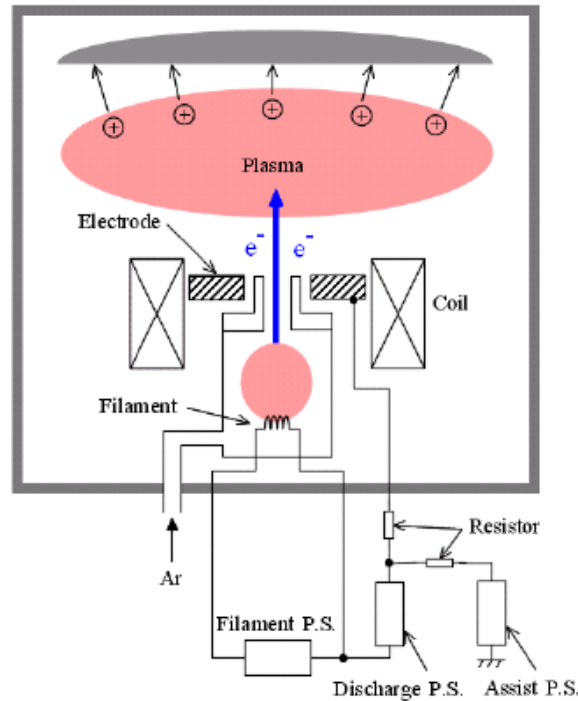
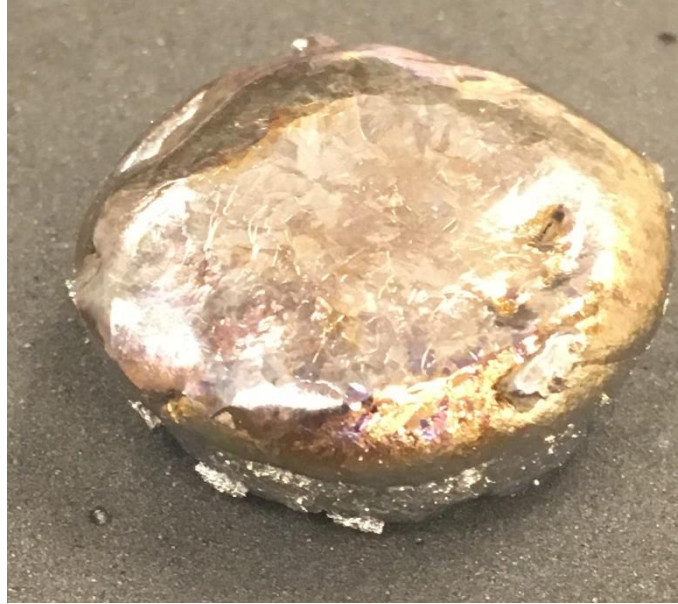


Figure 3.7. Components and working principle of the plasma source.

When surface etching is completed, deposition starts when the base pressure reaches to  $8 \times 10^{-6}$  torr.  $\text{TiO}_2$  and  $\text{Nb}_2\text{O}_5$  compact layers were used in the production of perovskite solar cells. Both materials were deposited using electron beam evaporation technique. Electron beam source has direct cooling using closed loop water flow. Both materials were prepared using pre-melting process previous to deposition. In pre-melting process, powder, chunk or granule materials are melted in a crucible using low electron beam energy. When this process is applied, small particles are melted and cooled as a single bulk material. Figure 3.8 shows a pre-melted material. Without pre-melting, electron beam energy can disperse the powder or granules, for this reason pre-melting supplies a better deposition condition. In the production of  $\text{TiO}_2$  and  $\text{Nb}_2\text{O}_5$  compact layers,  $\text{Ti}_3\text{O}_5$  and  $\text{Nb}_2\text{O}_5$  materials were used as starting materials. Most of the oxide materials are evaporated using dissociation reactions. Oxygen can be separated from metal part and therefore, oxygen deficient growth is produced. For

this reason, most of the oxides are produced using reactive evaporation, which is realized by additional oxygen supply to the vacuum chamber.



*Figure 3.8.* Pre-melted material for e-beam evaporation.

A shutter is located on top of the electron beam source. Shutter does not allow the vaporized molecules to reach to the substrate. The use of shutter supplies an advantage in the preparation of the evaporating material. When the material is ready, deposition starts with opening the shutter. Electron beam power is controlled using rising and soaking time parameters. Rising and soaking time parameters are determined as not to damage the material and to obtain a constant rate. For this reason, firstly materials are studied to determine their electron beam power, rising and soaking times. Then, these values are used during the deposition of thin films. Materials become ready to be coated when the rising and soaking times are determined. Also, deposition rate depends on the power of the electron beam. When electron beam power increases, higher deposition rates can be obtained. Higher rates supply an advantage to lower the

deposition time. However, high rates can suffer from low film quality. When the required thickness is reached, shutter is closed.

Optimized values for electron beam power, rising and soaking times were firstly obtained for the  $\text{TiO}_2$  and  $\text{Nb}_2\text{O}_5$  thin films. For both of the thin films, materials become ready for the deposition after 4 pre-steps. As the first step, current of the electron beam was increased to 0.3 A in 1 min, followed by keeping e-beam current at the same value for 30 s for both of the materials. In the following step, current was increased to 0.42 A for  $\text{TiO}_2$  and 0.39 A for  $\text{Nb}_2\text{O}_5$  in 30 s and kept at that value for 30 s. Finally, shutter was opened for the constant rate deposition. During deposition of the materials, some of the parameters were changed to tune the thin film characteristics. Both of the materials were deposited under different oxygen flow rates.  $\text{TiO}_2$  thin films were deposited using plasma assistance; however, both plasma assisted and non-assisted conditions were employed for  $\text{Nb}_2\text{O}_5$  thin films. Plasma bias voltage was applied at 115 V for  $\text{TiO}_2$  thin films and at 90 V for  $\text{Nb}_2\text{O}_5$  thin films.

#### **3.2.4. Preparation of Mesoporous Layer**

Opposite to DSSC's, thinner mesoporous layer can work effectively in perovskite solar cells due to the highly absorbing nature of perovskite layer. Because of the thicker layer (5 to 10  $\mu\text{m}$ ) requirements, mesoporous layers are mostly deposited using screen printing method in DSSC's. However, preferred method is spin coating for the mesoporous layer in perovskite solar cells. To create mesoporous layer, first procedure is the production of the paste. In this study,  $\text{TiO}_2$  is used for the mesoporous electron transport layer.  $\text{TiO}_2$  pastes were used in both as prepared and commercially supplied forms.

$\text{TiO}_2$  paste production starts with the grinding process of  $\text{TiO}_2$  nanopowders using ethanol inside titanium mortar followed by the application of ultrasonic treatment to the solution to break the agglomerated nanoparticles. Then, ethyl cellulose and

terpineol were mixed with nanopowder solution. Ratios of the mixing components were 2:1:7 by weight for TiO<sub>2</sub> nanopowder, ethyl cellulose and terpineol, respectively. Finally, ethanol was evaporated using rotary evaporator under vacuum at 40°C.

As prepared and commercially supplied (Dyesol NRT-18) titania pastes were mixed with ethanol in 1:3 weight ratio to supply fluidity. Due to the spin coating deposition technique, spreading of the solution is critical to supply pin hole free deposition. After the mixing with ethanol, solution was stirred for a long time to create good dispersion of the paste. Compact layer deposited substrates were subjected to UV-Ozone treatment for 15 min which provides better homogeneity for mesoporous layer addition to remove the organic contaminants. Then, mesoporous layers were deposited immediately using spin coating technique. Rotation speed and time were optimized to obtain good film quality as 2000 rpm and 5 s. The applied procedure provides enough viscosity to yield a 250 nm thick mesoporous titania layer. After the deposition, films were dried at 125 °C for 5 min. If thicker films are required, deposition and drying steps can be repeated. Finally, annealing was applied to the films at 500 °C for 2 h using a belt furnace.

### **3.2.5. TiCl<sub>4</sub> Treatment for Mesoporous Layer**

Titanium tetrachloride treatment was applied previous to the deposition of perovskite active layer. In this treatment, mesoporous TiO<sub>2</sub> coated substrates were dipped into the TiCl<sub>4</sub> aqueous solution which is prepared using 0.2 mmol TiCl<sub>4</sub>. Solution was heated to 90°C and dipping was ended after 15 min. Hydrolyzation reaction of TiCl<sub>4</sub> occurs and ultrafine TiO<sub>2</sub> nanoparticles are produced in a film form on top of the mesoporous layer. There are many explanations about the healing performance of perovskite solar cells due to this treatment. Ultrafine TiO<sub>2</sub> layer increases the density of states near TiO<sub>2</sub> and therefore higher charge mobility is provided. Also, treatment supplies better adhesion of perovskite layer to the mesoporous layer which causes decreased recombination processes. When the treatment was ended, samples were cleaned using

deionized water. Finally, they were subjected to second heat treatment process again at 500°C for 2 h [15, 16].

### 3.2.6. Preparation of Perovskite Layer

In literature, there are several studies for the deposition of perovskite layer. Methods can be evaluated under two main classes. These are vacuum coating and solution based coating of perovskite layer. Due to the simplicity of solution based coatings, number of studies for these types of depositions is higher than that of vacuum coating of perovskite layer. There are three approaches for the solution based deposition of perovskite layer. First approach is one step deposition technique in which the solution is prepared directly by mixing CH<sub>3</sub>NH<sub>3</sub>I (MAI), PbI<sub>2</sub> and N,N-dimethylformamide (DMF) followed by the application of the solution using spin coating method. Second approach is the two step deposition technique, which is performed in two sequential steps. PbI<sub>2</sub> and DMF are mixed and then deposited by spin coating. Coated substrates are then immersed into the MAI solution. Final and the approach used in this work is the adduct method.

Adduct method is based on the Lewis acid-base concept. Base is described as electron pair donor and acid as electron pair acceptor. Lewis acid-base, where reactions are nonaqueous, yields redox reaction or adduct formation. When adduct formation occurs, adduct is linked by shared electrons which are originated from the Lewis base. Adduct of PbI<sub>2</sub> and N,N-dimethyl sulfoxide (DMSO) is used in this approach due to Lewis acid nature of PbI<sub>2</sub> and O-donor nature of DMSO. Adduct structure produces an intermediate layer which plays a critical role on the morphology of perovskite layer. Also, adduct approach decreases the rate constant for the formation of perovskite layer and therefore crystal growth control becomes easier. As a result, this method offers larger and continuous crystal formation.

In this study, 1:1:1 molar ratio of  $\text{PbI}_2$ , MAI and DMSO were dispersed into DMF which is 40% in weight. This solution was poured on the substrates and spin coating process was applied at 4000 rpm for 30 s. Diethyl ether was dropped on the spinning substrate at the fifth second of the rotation. Diethyl ether treatment was applied to wash out the DMF solvent. This treatment provides better solvent evaporation which yields good surface coverage of perovskite layer. When the spin coating was finished, produced transparent film includes adduct of  $\text{PbI}_2 \cdot \text{DMSO}$ . Finally, deposited films were applied to heat treatment for 5 min at  $100^\circ\text{C}$ . Figure 3.9 demonstrates process of adduct method. Heat treatment process evaporates DMSO and creates completely crystallized  $\text{MAPbI}_3$ . Obtained film is formed at good coverage without pin hole formation. Films have shiny black appearance after the heat treatment [17, 18].

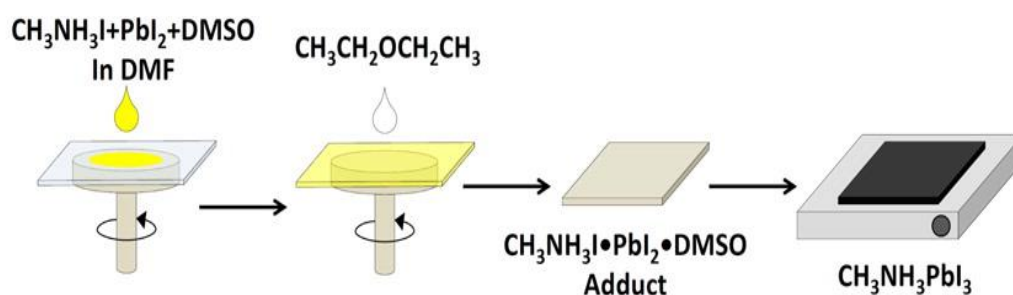


Figure 3.9. Demonstration of Adduct Method [18].

### 3.2.7. Preparation of Hole Transport Layer

In this study, two different approaches were used to deposit hole transport layer. NiO and TiO hole transport layers were deposited by electron beam evaporation technique as the first approach. These materials were used together with  $\text{TiO}_2$  electron transport layer. However, spiro-OMeOTAD was used as HTL when  $\text{Nb}_2\text{O}_5$  ETL was employed. NiO and TiO precursors were used in the evaporation process. While, TiO was evaporated after the pre-melting process, NiO was deposited directly from the chunky form due to the sublimation of NiO. Same deposition system and approach with ETL

was used for the deposition of TiO and NiO HTL thin films. These materials were deposited on glass substrates for single layer characterizations. Plasma etching was applied to glass substrates previous to the deposition of single layers. However, etching was not applied during the production of perovskite solar cell not to damage the perovskite layer. Both of these materials were studied using different deposition parameters: deposition temperature, deposition rate, plasma assistance and oxygen flow rate. Spiro-OMeOTAD thin films were deposited using spin coating method as the second approach. Solution was prepared by dissolving of spiro-OMeOTAD, 4-tert-butyl pyridine and lithium bis(trifluoromethanesulfonyl)imide (Li-TFSI) in chlorobenzene. Prepared solution is poured onto the perovskite layer and rotated at 3000 rpm for 30 s. Solvent can be evaporated at room temperature and a rigid film is formed on top of the perovskite layer.

### **3.2.8. Deposition of Back Electrode Layer**

Back electrode deposition is the final process for the production of perovskite solar cells. Metallic coatings are the promising back side electrodes. Gold, silver and aluminum coatings can be used for this purpose. In this study, gold coating was employed. Gold has very low work function which is around 5.2 eV, which is critical for efficient hole collection from both perovskite and hole transport layer. Deposition processes were conducted in Nanovak sputtering system which can be seen in Figure 3.10 where a gold target was subjected to DC sputtering. Sputtering process was started when the base pressure is lower than  $5 \times 10^{-6}$  mbar. For sputtering process, chamber pressure was kept as constant at 15  $\mu$ bar with corresponding argon flow. DC voltage is then firstly increased to 300 V in 1 min and waited there for 5 min for target cleaning, followed by an increase in voltage to 320 V in 20 s and the shutter in front of the cells was opened. The deposition rate was around 1  $\text{\AA}/\text{s}$  and deposition ended when the film thickness reached to 120 nm. This thickness is enough to collect and transport the charges. Deposition of gold was conducted using a mechanical mask which can be seen in Figure 3.11 and it provides the formation of 8 different cells

which has  $0.05 \text{ cm}^2$  active area. Finally, silver paste was applied to form the contacts to provide a better contact for the measurements. Figure 3.12 shows how the final cell looks like. Back contacts are taken from the gold contacts and the front contact was taken from FTO regions formed by scratching the films on top of FTO layer.

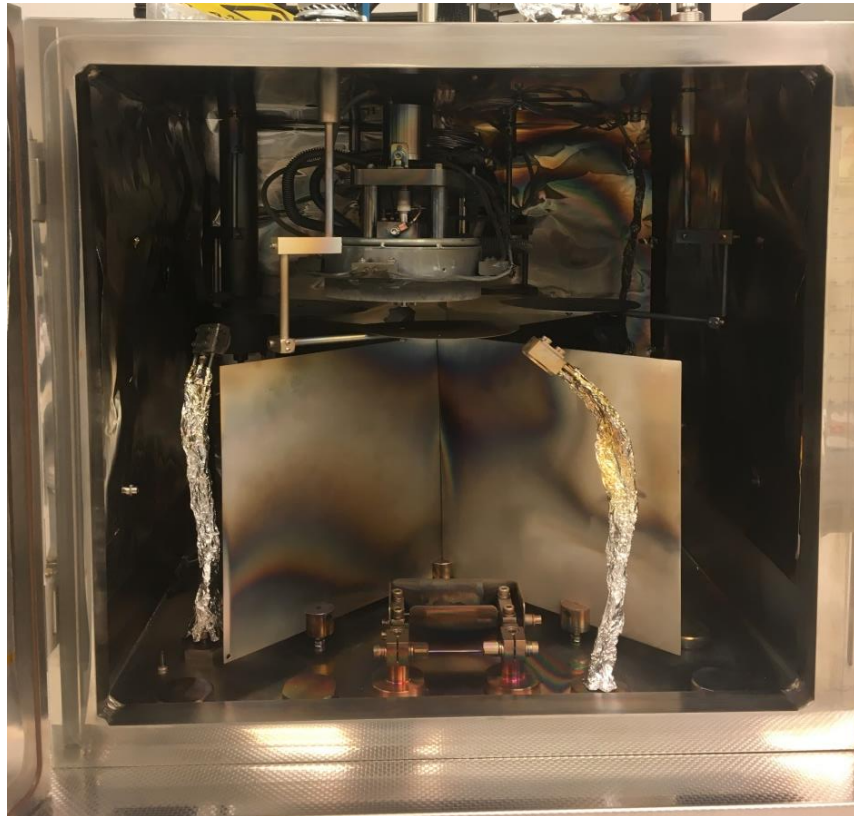


*Figure 3.10.* Sputtering system.



*Figure 3.11.* Mask used for gold back contact coating.

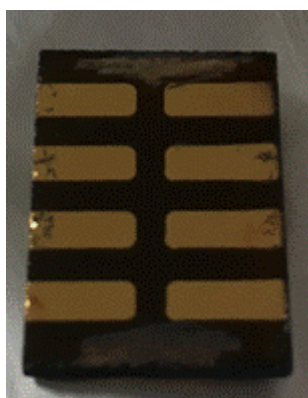


*Figure 3.12.* Final perovskite solar cell used for the measurements.

### **3.3. Characterization Techniques**

In this study, two separate characterizations were performed. First one is the evaluation of the single layers which were deposited by electron beam for their potential use in perovskite solar cells as electron transport or hole transport purposes. Secondly, characterization of the perovskite solar cells which were produced using the alternative ETL and HTL materials.

### **3.3.1. Characterization of Single Layers**

To evaluate the structural, optical and electrical properties of thin films, they were directly deposited on glass substrates at approximately 300 nm thickness. Morphological and structural characterizations of thin films were evaluated using SEM, XRD and XPS techniques. These films then were conducted to transmittance and reflectance measurements to explain their optical properties. Finally, Hall effect and UPS measurements were performed to understand the electrical properties of thin films. Measurement techniques will be explained in detail in the following chapters. In this chapter, only the calculation of refractive index and thickness of thin films will be given.

#### **3.3.1.1. Determination of Coating Thickness and Refractive Index Dispersion**

##### **a) Background of the Approach**

Interference of light was firstly examined in Young double-slit experiment in 1801 by Thomas Young. According to this experiment, the incoming wave splits into two separate waves upon hitting the slit part and later they combine in a single wave. Change in the path lengths of the separate waves forms the phase-shift and interference path. A coherent light source is sent on the two parallel slits. Light passes the slits and an image forms at the back side. Bright and dark areas at the backsides explain the constructive and destructive interference (Figure 3.13). If there are  $(n/2)\pi$  degree phase shifts, two waves form a destructive interference. However, when phase shift equals  $n\pi$ , waves form a constructive interference.

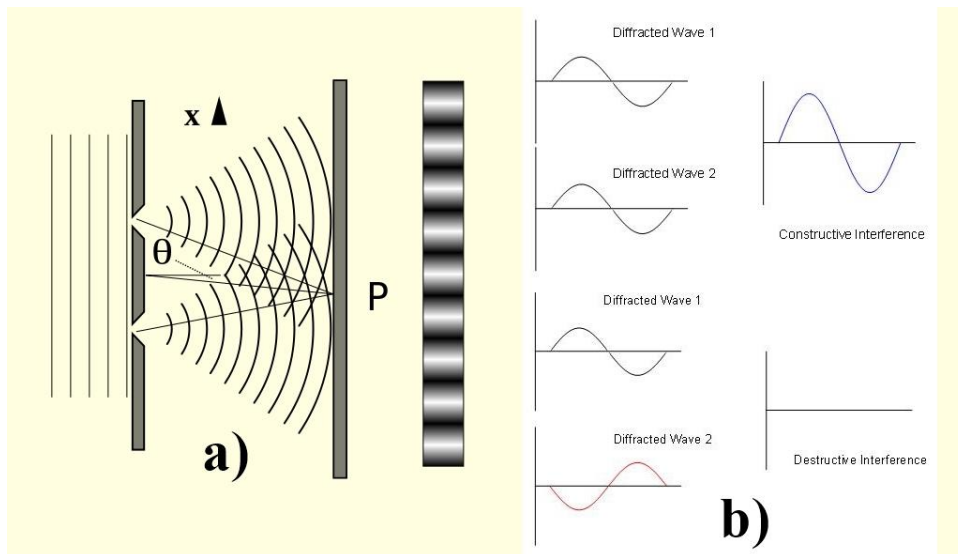


Figure 3.13. a) Young double slit experiment, b) constructive and destructive interference [5].

Light and objects can be interacted in 4 different ways where light can be transmitted, reflected, absorbed or scattered. Since thin films are mostly deposited on flat surfaces, scattering is ignored. If films are accepted to show no absorption, then the sum of the transmitted and reflected ways should be equal to 1. Transmittance and reflectance values are mainly given as a percentage; because, their values are given as the ratio of transmitted/reflected energy to the incoming light energy.

Without any coating on the substrate (without any absorption), reflection can be calculated using Fresnel equation (Eq. [3.3]).  $R$  defines the amplitude of reflection, and  $n_0$  and  $n_1$  define the refractive index of air and substrate, respectively. Refractive index is defined as the ratio of the velocity of light inside the medium to the velocity of light in air. Incoming light is reflected from both front and back surfaces. Reflection amplitude equals to the sum of front and back side reflections. Uncoated substrates (in other words thick media) form a very dense interference; therefore, it is not manipulated. They create continuous transmittance or reflectance spectra corresponding to the wavelength.

$$R = \left( \frac{n_0 - n_1}{n_0 + n_1} \right)^2 \quad \text{Eq. [3.3]}$$

When substrates are coated using a thin film which has a different refractive index than the substrate, interference in transmittance or reflectance measurement is observed. Coated thin film creates two reflection interfaces on one surface which can be seen in Figure 3.14. R1 and R2 define the reflection at interfaces of thin film to air and thin film to substrate. Reflection amplitude is defined in the equation 3.4, after the formation of single layer thin film.  $\beta$ , which is formulated in equation 3.5, corresponds to the phase difference between two reflected light waves. Phase shift between the reflected lights is produced due to the path difference created by the thickness of the thin film. If the phase shift equals to  $\pi/2$ , destructive or constructive interference of R1 and R2 waves are maximized. When the coated thin film has a higher refractive index than the substrate material, reflection is maximized. Also, oppositely, minimum reflection is observed when thin film has a lower refractive index (Figure 3.15). In this condition, optical thickness ( $nd$ ) is equal to  $\lambda/4$  which is also known as quarter wave optical thickness (QWOT). If the phase shift between R1 and R2 equals to  $\pi$ , thin film does not create a change in reflection. These films are called as absentee layer and in this case optical thickness equals to half wave optical thickness (HWOT).

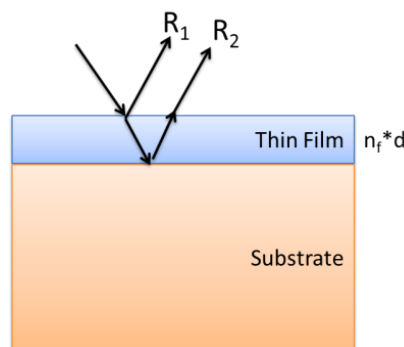


Figure 3.14. Reflection from thin film/air and thin film/substrate interfaces.

$$R = \frac{R_1 + R_2 \exp(-2i\beta)}{1 + R_1 R_2 \exp(-2i\beta)} \quad \text{Eq. [3.4]}$$

$$\beta = \frac{2\pi}{\lambda} nd \quad \text{Eq. [3.5]}$$

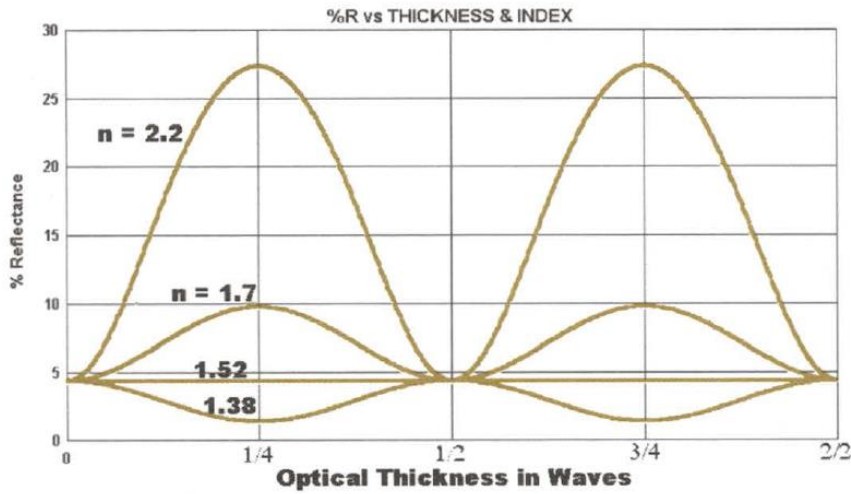


Figure 3.15. Formation of interference fringes when thin films with different refractive indices are deposited on glass which has a refractive index of 1.52 [4].

Absorption is another important optical parameter. If the medium absorbs the light, refractive index of this medium is defined in complex ways (equation 3.6).  $k$  is the extinction coefficient and defines the absorbing nature of the substrate or thin film. Absorption coefficient ( $\alpha$ ) is calculated using the formula given in equation 3.7.

$$N = n_1 - ik_1 \quad \text{Eq. [3.6]}$$

$$\alpha = \frac{4\pi k}{\lambda} \quad \text{Eq. [3.7]}$$

Changes in refractive index depending on the wavelength are called as refractive index dispersion. Dispersion is explained using electromagnetic theory of the molecular structure. When the electromagnetic wave impinges to an atom or molecule, the bound charges vibrate in the same frequency of the incident wave. Refractive index of materials increases when the wavelength decreases. Change in refractive index is very large at lower wavelengths; however, it is nearly constant at longer wavelengths [4, 5, 19] (Figure 3.16).

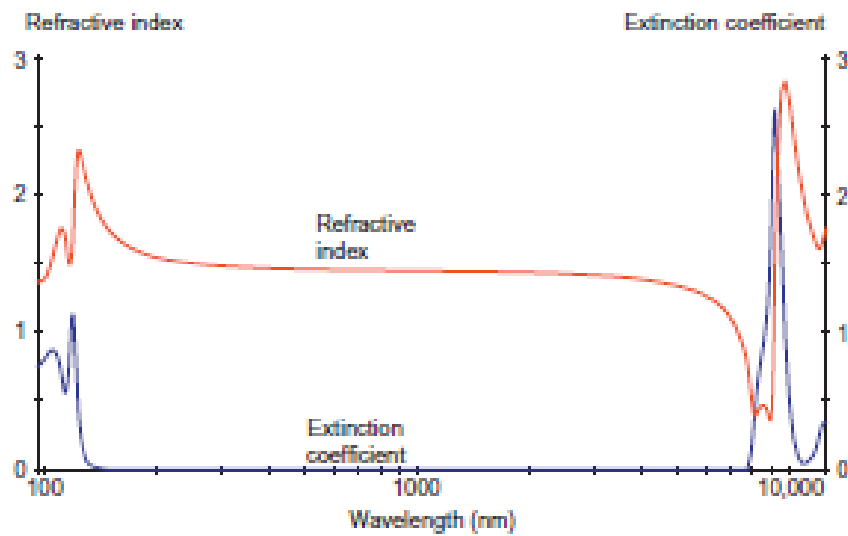


Figure 3.16. Refractive index dispersion of SiO<sub>2</sub> [20].

## b) Application of the Fitting Process

In this study, physical thickness and refractive index dispersion of thin films were calculated using Optilayer Characterization thin film coating software. The main screen of the software can be seen in Figure 3.17. For the characterization, transmittance or reflectance measurements are carried out for uncoated substrate and thin film coated substrates. These measurements were then supplied as input data to the software. Thickness, refractive index and extinction coefficient values were given

as estimated values in the program to select a range for a better starting point. Then, optimum fitting approach was chosen from the options and fitting process was applied. Also, surface and bulk inhomogeneity terms can be added during the fitting process. For low figure of merit, which means a good fitting, refractive dispersion and thickness values are produced by the software. Figure 3.18 shows the fitting and refractive index dispersion as an example.

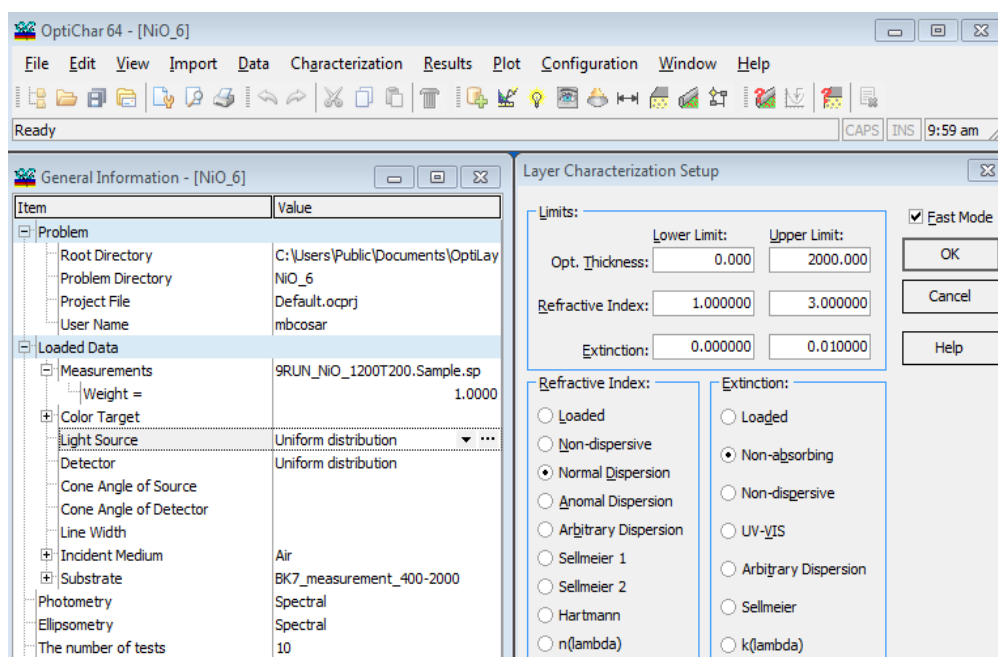


Figure 3.17. Optilayer characterization software fitting algorithms.

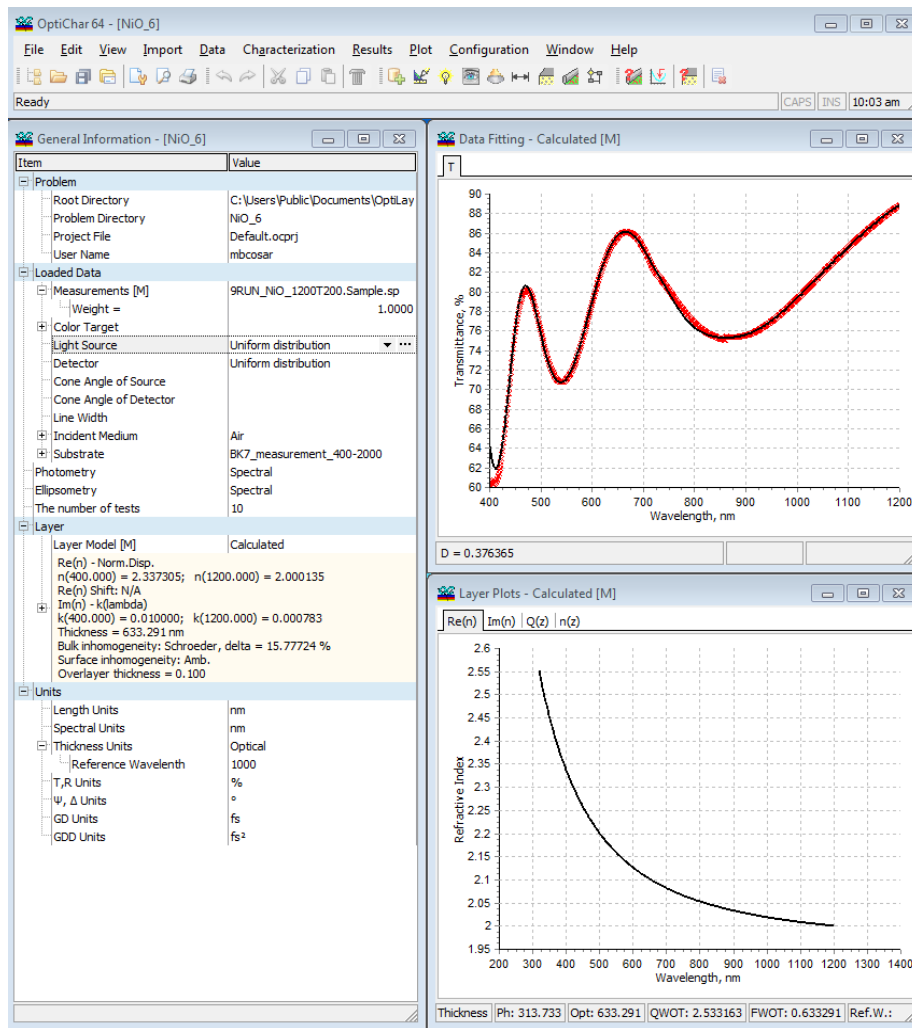


Figure 3.18. Optilayer characterization software fitting process and calculated refractive index-coating thickness values.

### 3.3.2. Characterization of Perovskite Solar Cells

After the production of the perovskite solar cells, current-voltage measurements were carried out under simulated solar light. This measurement provides information about the cell efficiency and internal resistances of the cells. Detailed explanation of the current voltage measurement was given in literature review chapter (Chapter 2). Also, electrochemical impedance spectroscopy (EIS) measurement was carried out to

examine the charge transfer processes and resistance of each layer. In the following part, EIS technique will be explained shortly.

### 3.3.2.1. Electrochemical Impedance Spectroscopy (EIS)

Electrochemical impedance spectroscopy (EIS) measures the response of an electrochemical unit to the small AC signal which is given as a function of the frequency. This technique is widely used in the characterization of the electrochemical or photo electrochemical devices in which ionic or electron transfer processes occur. AC voltage is conducted at specified angular frequency ( $\omega$ ) and produced current is detected. Impedance is the ratio of voltage to the current which is given in equation 3.8. Used frequency is in the range of millihertz to kilohertz. When frequency is equal to zero, applied voltage becomes DC where impedance equals to the resistance of the components in this condition. Impedance shows the difference depending on the angular frequency. When angular frequency is zero, phase difference is also zero. For the case of non-zero phase difference, there will be a phase difference between current and voltage. Main components of the phase difference are capacitor (C) and inductor (L).

$$Z(\omega, t) = \frac{V(\omega, t)}{I(\omega, t)} \quad \text{Eq. [3.8]}$$

Impedance measurements have real and imaginary parts and they are often presented by Nyquist and Cole-Cole plots. Equivalent circuit model is used to explain the results of EIS measurements. Series or parallel circuits are used and resistor, capacitor, inductor and constant phase element components are used in the modelling. Figure 3.19 demonstrates a Nyquist plot for typical Randles with modelled equivalent circuit. High frequency regions are kinetically controlled and low frequency region is

controlled by diffusional processes. Series resistance, capacitance of the kinetic and diffusional processes can be defined using a plot and equivalent circuit [21].

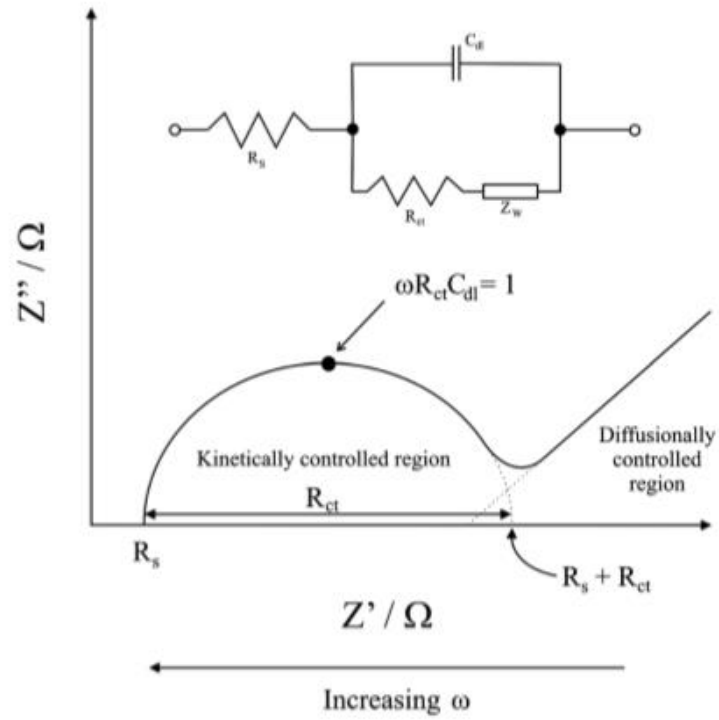


Figure 3.19. Nyquist plot of a cell with modelled equivalent circuit [21].



## REFERENCES

- [1] D. L. Smith, Thin film deposition: Principles and practice, McGraw-Hill Education, 1995.
- [2] K. S. Sree Harsha, Chapter 5-Thermal evaporation sources, Principles of vapor deposition of thin films, Elsevier, Oxford, 2006.
- [3] A. Chambers, Basic vacuum technology, 2nd edition, CRC Press, 1998.
- [4] R. R. Willey, Field guide to optical thin films, Society of Photo Optical, 2006.
- [5] J. D. Rancourt, Optical thin films: User handbook, SPIE Optical Engineering Press, 1996.
- [6] K. S. Sree Harsha, Chapter 6-Gas flow in thin film processing systems, Principles of vapor deposition of thin films, Elsevier, Oxford, 2006.
- [7] R. R. Willey, Practical design and production of optical thin films, Taylor & Francis, 2002.
- [8] L.B. Freund, S. Suresh, Introduction and overview, Thin film materials: Stress, defect formation and surface evolution, Cambridge University Press, Cambridge, 2004.
- [9] K. S. Sree Harsha, Chapter 9-Nucleation and growth of films, Principles of vapor deposition of thin films, Elsevier, Oxford, 2006.
- [10] J. E. Greene, Physics of film growth from the vapor phase, Multicomponent and multilayered thin films for advanced microtechnologies: Techniques, fundamentals and devices, Springer Netherlands, Dordrecht, 1993.
- [11] T. Schneller, R. Waser, M. Kosec, D. Payne, Chemical solution deposition of functional oxide thin films, Springer Vienna, 2014.
- [12] M. D. Tyona, A theoretical study on spin coating technique, Advances in materials Research, 2 (2013) 195-208.
- [13] S. F. Kistler, P. M. Schweizer, Liquid film coating: Scientific principles and their technological implications, Chapman & Hall, 1997.

- [14] Z. Wang, J. Fang, Y. Mi, X. Zhu, H. Ren, X. Liu, Y. Yan, Enhanced performance of perovskite solar cells by ultraviolet-ozone treatment of mesoporous TiO<sub>2</sub>, *Applied Surface Science*, 436 (2018) 596-602.
- [15] G. Choe, J. Kang, I. Ryu, S. W. Song, H. M. Kim, S. Yim, Influence of the concentration of TiCl<sub>4</sub> solution used for post-treatment on mesoporous TiO<sub>2</sub> layers in hybrid lead halide perovskite solar cells, Elsevier, 2017.
- [16] H. K. Adli, T. Harada, S. Nakanishi, S. Ikeda, Effects of TiCl<sub>4</sub> treatment on the structural and electrochemical properties of a porous TiO<sub>2</sub> layer in CH<sub>3</sub>NH<sub>3</sub>PbI<sub>3</sub> perovskite solar cells, *Physical Chemistry Chemical Physics*, 19 (2017) 26898-26905.
- [17] J.-W. Lee, H.-S. Kim, N.-G. Park, Lewis acid–base adduct approach for high efficiency perovskite solar cells, *Accounts of Chemical Research*, 49 (2016) 311-319.
- [18] N. Ahn, D.-Y. Son, I.-H. Jang, S. M. Kang, M. Choi, N.-G. Park, Highly reproducible perovskite solar cells with average efficiency of 18.3% and best efficiency of 19.7% fabricated via lewis base adduct of lead(ii) iodide, *Journal of the American Chemical Society*, 137 (2015) 8696-8699.
- [19] H. A. Macleod, *Thin-film optical filters*, Adam Hilger Limited, 1969.
- [20] H. A. Macleod, Chapter 9-Optical thin films, *Handbook of thin film deposition*. Third edition, William Andrew Publishing, Oxford, 2012.
- [21] E. P. Randviir, C. E. Banks, Electrochemical impedance spectroscopy: An overview of bioanalytical applications, *Analytical Methods*, 5 (2013) 1098-1115.

## CHAPTER 4

### PLASMA ASSISTED LOW TEMPERATURE ELECTRON BEAM DEPOSITED NiO THIN FILMS FOR ELECTRO-OPTIC APPLICATIONS

Nickel oxide (NiO) is a popular ceramic material due to its excellent chemical stability, low-cost, and wide application areas. Application of NiO thin films has been investigated in many popular applications such as catalysts, transparent conducting oxides, photodetectors, electrochromic devices, gas sensors, photovoltaic devices, supercapacitors, and fuel cells [1-3].

Stoichiometric NiO, which has cubic NaCl structure, shows insulating character; therefore, it is mandatory to enhance the electrical conductivity for applications. This can be achieved by increasing the concentration of Ni<sup>2+</sup> vacancies, oxygen interstitials, and monovalent ion doping. NiO thin films mainly show p-type conductivity upon defect introduction into the crystal structure and possess wide band gap ranging between 3.6 and 4.0 eV. Electrical, optical, and magnetic properties of NiO thin films can be tuned by the modification of the stoichiometry [2-4].

There are many studies in literature investigating the effect of the deposition techniques and parameters for NiO thin films. NiO thin films can be produced by spray pyrolysis [5], high temperature oxidation [6], sol-gel process [7], electrochemical deposition [8], and vacuum deposition [9, 10] methods. Recently, vacuum deposited NiO thin films gained importance due to ease of tunability of stoichiometry, by modifying the process parameters. Although pulsed laser atomic layer deposition [11], atomic layer deposition [12] and plasma enhanced chemical vapor deposition [13] are alternative methods, most of the studies are focused on rf

and reactive dc magnetron sputtering of NiO [3, 14-16] due to large area applicability, suitability to doping, and high deposition rate. However, rf or dc magnetron sputtered NiO thin films should be annealed after deposition to obtain NiO crystallinity.

Another important vacuum deposition method, electron beam evaporation, was also used to deposit NiO thin films [17-19]. However, these studies are limited to optical characterizations. Also, these evaporations were conducted from powder or loosely stick form, which are not preferred in e-beam evaporation. In our study, NiO films were produced at different oxygen flow rates, deposition temperatures, deposition rates, and plasma assistance using chunk NiO particles. The effects of process parameters on the morphology, structural, optical, and electrical properties were investigated. All of the films were obtained with high crystallinity and dense structure. Highly conductive films were obtained when films are deposited using plasma assistance.

#### **4.1. Experimental Studies**

NiO thin films were deposited using Tecport plasma assisted physical vapor deposition (PVD) system. NiO chunks between 1 and 5mm, purchased from Materion, were evaporated using electron beam in the PVD system. Main chamber pressure is reduced below  $8 \times 10^{-6}$  mbar before deposition. Thin films were obtained at different process parameters which are given in Table 4.1. The parameters and base values were chosen for effective comparison of thin films such that only one parameter was changed while the other parameters were kept constant. Electron beam power for evaporation of NiO chunks was optimized at a constant rate during deposition. Although the desired thickness is 250 nm, actual thicknesses of the layers change from sample to sample due to the fact that the actual thickness is directly affected by the process parameters. It was observed that the thickness of the NiO layer increases with increasing oxygen flow rate, deposition temperature, and decreasing deposition rate.

Also, the lower layer thickness was obtained when films were deposited under plasma assistance. NiO films were deposited on Schott Bk7 borosilicate glasses, which were cleaned by wiping in acetone and etching in argon in the deposition system. Jeol cold plasma source was used for plasma assistance and substrate etching. Biases of 90V and 130V discharge voltages were applied to obtain denser NiO layers.

NiO thin films were investigated using UV-vis spectrophotometer, x-ray diffractometer, x-ray photoelectron spectroscopy, Hall effect, ultraviolet photoelectron spectroscopy (UPS), and scanning electron microscopy (SEM). A Perkin Elmer Lambda 950 UV-vis near-infrared spectrophotometer was used for transmission and reflection measurements. The refractive index and approximate layer thicknesses were calculated from the “Optilayer” optical thin film calculation software via mathematical approximation. Crystallographic analyses were done by using an x-ray diffractometer, Rigaku (SmartLab) using Cu K $\alpha$  radiation (1.54Å), at a grazing incidence angle of 3° to minimize the substrate effect. X-ray photoelectron spectroscopy (XPS) (Thermo K-Alpha) was used to determine elemental composition of the films. Films were cleaned by argon etching before characterization to remove carbon layers. Hall Effect measurements were made using Lakeshore 7700A system with van der Pauw geometry between 1 and 1.8T. Due to the low conductivity of films, gold contacts were evaporated on the corners of the samples. Electronic band positions of the thin films were calculated from the results of UPS (PHI 5000 Versaprobe) and UV-vis spectrophotometer measurements. NiO thin films were deposited on indium tin oxide coated glass for UPS characterizations. Surface morphologies of the films were investigated using field emission (FESEM, FEI–Nova NanoSEM 430) SEM.

Table 4.1. *Deposition parameters for NiO thin films.*

Sample No:	Deposition temperature (°C)	Deposition rate (Å/s)	Oxygen flow rate (sccm)	Plasma assistance
SN 1	80	2	0	No
SN 2	80	2	10	No
SN 3	80	2	25	No
SN 4	80	2	50	No
SN 5	80	2	100	No
SN 6	30	2	25	No
SN 7	170	2	25	No
SN 8	80	1	25	No
SN 9	80	3	25	No
SN 10	80	2	0	Yes
SN 11	80	2	10	Yes
SN 12	80	2	50	Yes

## 4.2. Results and Discussions

### 4.2.1. Structural Properties

X-ray diffraction patterns of NiO thin films were recorded between 35 and 80° at 3° grazing incidence angle (Figure 4.1.). Five characteristic peaks of NiO were observed, and also no peaks related to metallic Ni were seen in the XRD patterns. Peaks are assigned to NiO face centered cubic rock salt structure with Fm-3m space group. (111), (200), (220), (311), and (222) planes were observed at 37.2°, 43.3°, 62.8°, 75.4°, and 79.4° 2-theta values. A dominant peak is found at 37.2°, showing preferential orientation of (111) plane, except for films deposited at low temperatures. Although (111) plane becomes stronger at high oxygen flow rates, (200) and (222) planes are tending to disappear under these conditions. At higher temperatures, (111)

and (220) plane intensities increase, while (200) plane gives the strongest peak at room temperature deposition. The deposition rate does not affect the crystallographic orientation. A shift in the position of (111) plane to lower 2-theta values is observed when deposition is conducted using plasma assistance.

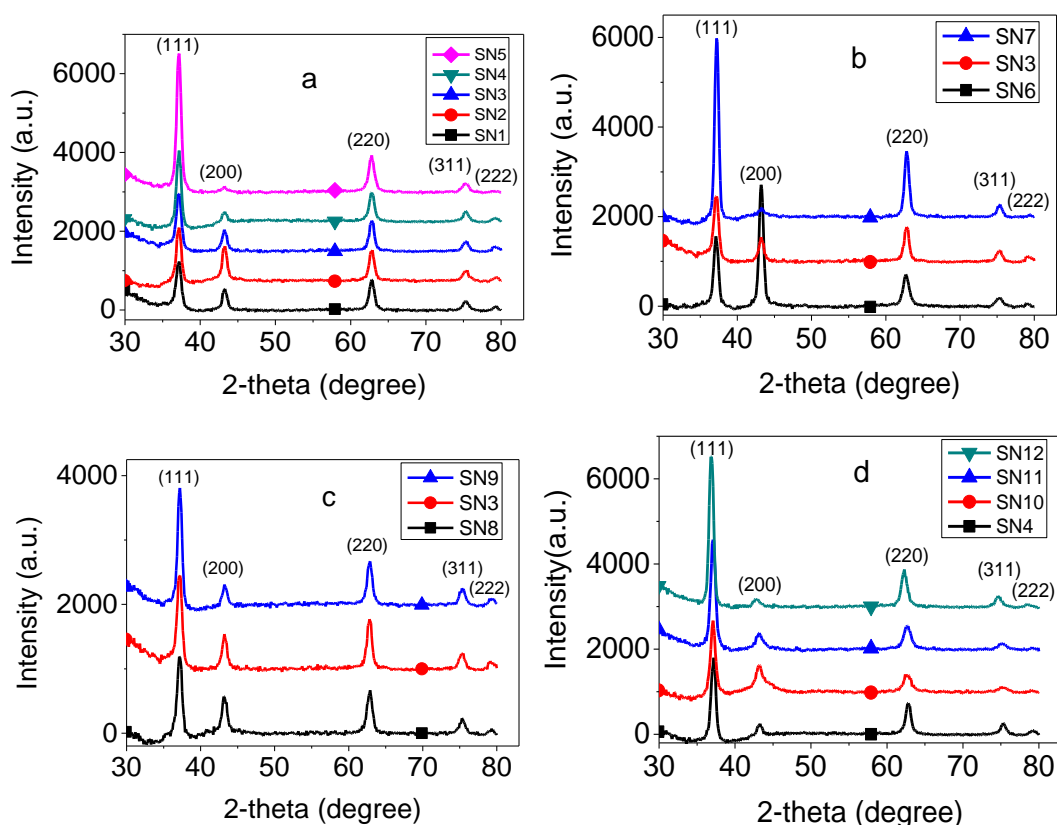


Figure 4.1. X-Ray diffraction of NiO thin films for different deposition parameters: a) oxygen flow rate, b) deposition temperature, c) deposition rate, d) oxygen flow rate with plasma assistance.

Table 4.2. shows the average grain sizes and lattice parameters of the NiO thin films. The grain size was calculated from Scherrer's equation using the strongest peak belonging to (111) plane [14]. It is seen from Table 4.2 that the average grain size of NiO thin films increases with the oxygen flow rate. Higher deposition temperature enhances grain growth and results in larger grain sizes. Also, the deposition rate increases with increasing e-beam power due to vaporization of more atoms at a shorter

time, leading to larger grain sizes. Plasma assistance supplies a relatively high kinetic energy to NiO molecules in the vapor and introduction of higher amounts of energy to NiO vapor results in larger grain sizes. An increased lattice parameter is observed under high oxygen flow rates, high deposition temperatures, low deposition rates, and plasma assisted deposition conditions which we relate to Ni vacancies and interstitial oxygen atoms introduced into the NiO lattice.

Table 4.2. Grain size and lattice parameter of NiO thin films.

Sample No:	Grain size (nm)	Lattice parameter (Å)
SN 1	95.5	4.177
SN 2	95.7	4.179
SN 3	99.7	4.181
SN 4	108.3	4.181
SN 5	120.1	4.185
SN 6	98.1	4.179
SN 7	113.2	4.186
SN 8	97.7	4.186
SN 9	110.1	4.181
SN 10	105.4	4.189
SN 11	108.6	4.195
SN 12	108.8	4.211

Figures 4.2 to 4.5 show the surface SEM images of NiO thin films at the same magnification for different deposition parameters. When NiO thin films are deposited at 80°C without plasma source, the structure is composed of a combination of needle and spherical shaped particles. The ratio of the needle to spherical particles decreases, and the size of needles become smaller with increasing oxygen flow rates. Also, the size of needles reduces under high oxygen flow rate conditions. When NiO thin films are deposited at different deposition rates, the needle to spherical particle ratio remains almost the same. However, the size of needles increases with the deposition rate. Upon

decreasing the deposition temperature, dominant morphology turns to spherical particles, and in addition, cuboidal structures are formed at high deposition temperatures. When plasma assistance is used, the whole surface is covered with spherical particles.

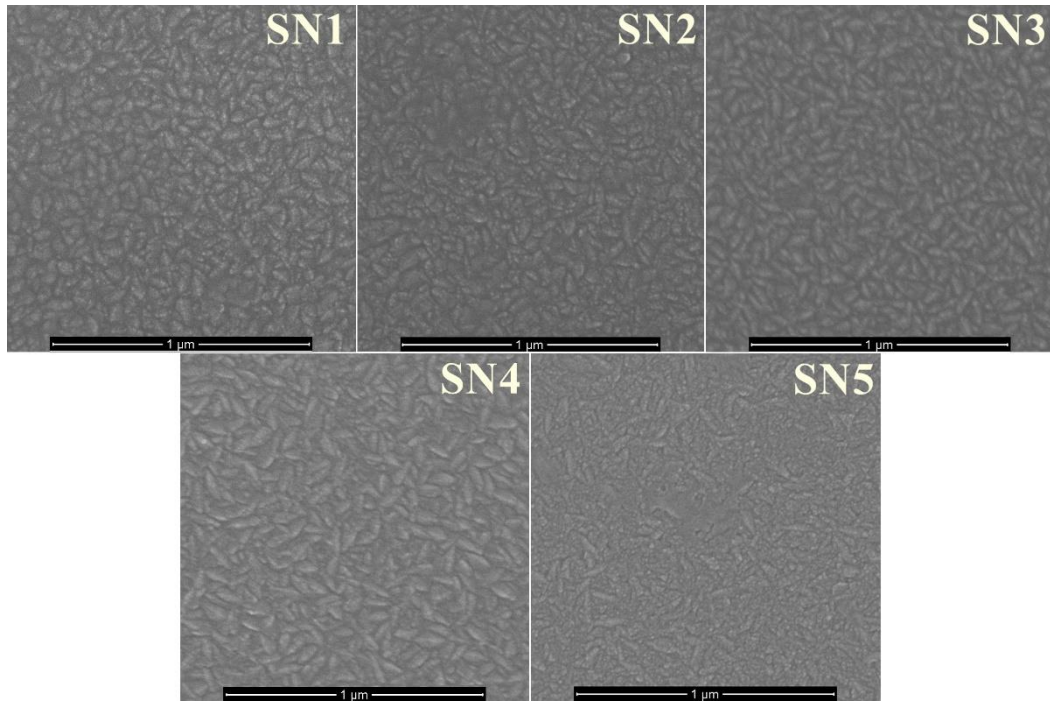


Figure 4.2. SEM images of NiO thin films deposited at different oxygen flow rates.

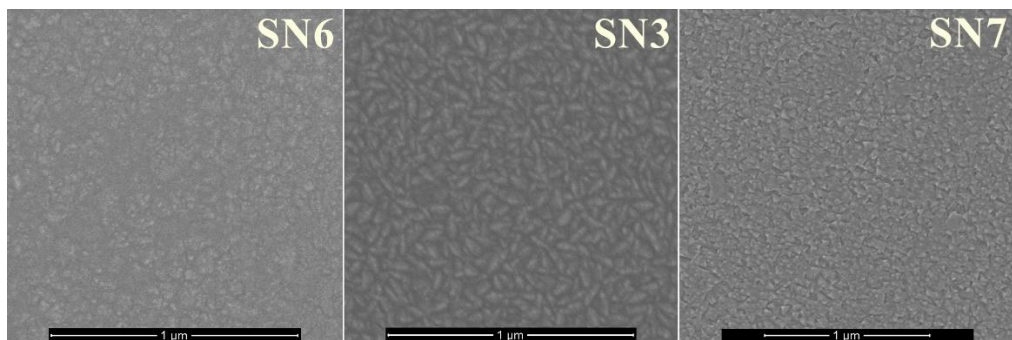


Figure 4.3. SEM images of NiO thin films deposited at different temperatures.

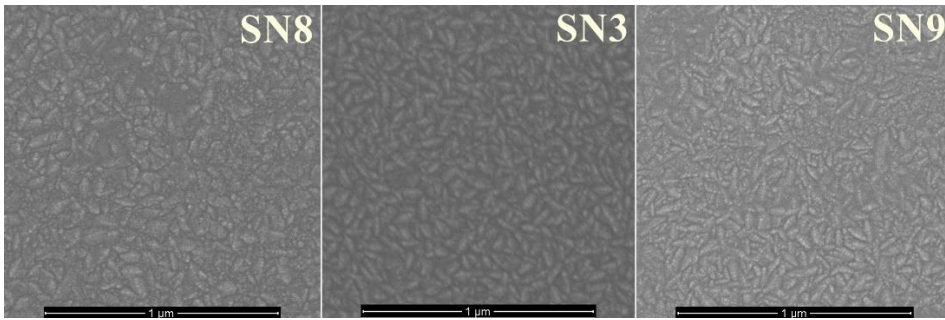


Figure 4.4. SEM images of NiO thin films at different deposition rates.

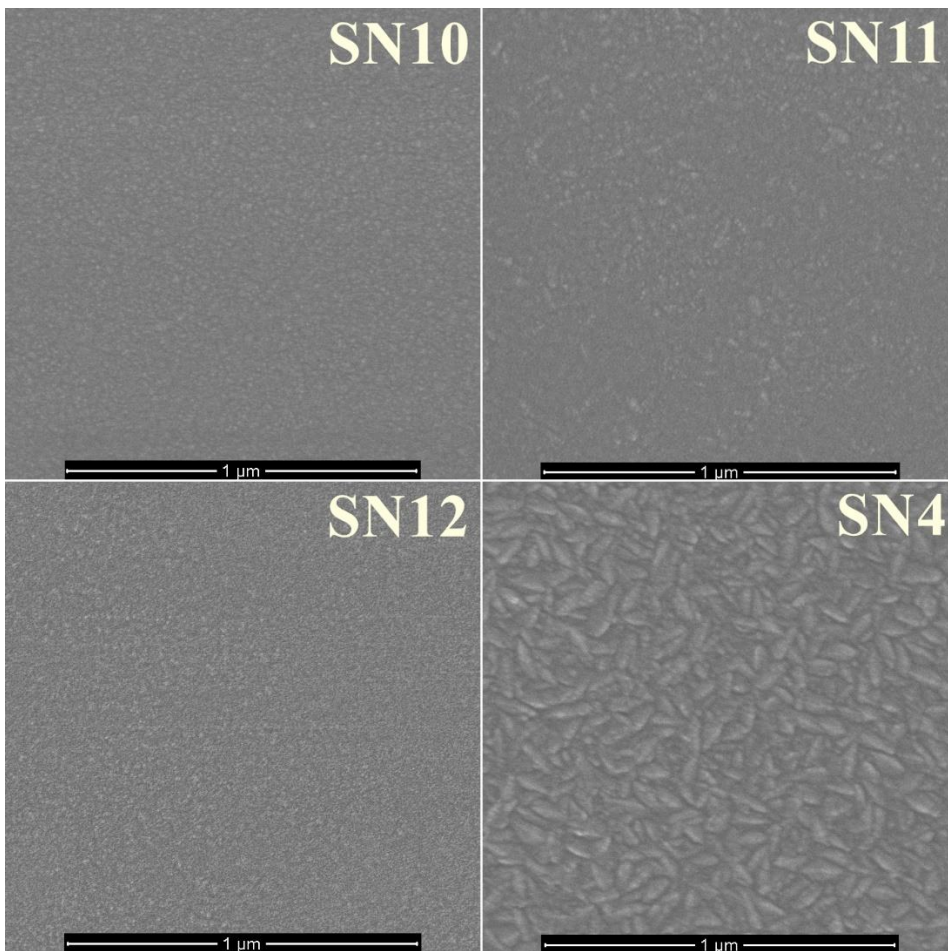


Figure 4.5. SEM images of NiO thin films deposited at different oxygen flow rates with plasma assistance.

XPS measurements were performed to obtain stoichiometry and structure of NiO films, and the results can be seen in Figure 4.6 and Figure 4.7 for nickel and oxygen, respectively. Metallic Ni and Ni(OH)<sub>2</sub> show strong single peaks at 852.6 and 855.6 eV, and due to the absence of these peaks, we conclude that thin films deposited in this study possess only NiO structure at all deposition conditions. NiO has multiplet-split [20] and this characteristic can be seen in Figure 4.6. as an example of specimen SN 3. NiO has four characteristic peaks at 854, 861, 877, and 879 eV, which correspond to Ni2P3/2 multiplet-split, Ni2P3/2 satellite, Ni2P3/2 multiplet-split, and Ni2P1/2 satellite positions, respectively. These four peaks can be seen in all samples and the position of peaks is the same for all films. Oxygen peak appears at 529–530 eV, and this peak shifts to higher binding energies at low oxygen flow rates and high deposition temperatures. Plasma assistance shifts the oxygen peak to a lower binding energy. Table 4.3 shows the atomic concentrations of Ni and O atoms in NiO thin films calculated using XPS measurements. As an expected result, the oxygen content in NiO films increases at high oxygen flow rates. Ni amount in thin films increases with increasing deposition temperature and deposition rate. Plasma assisted and oxygen free deposition conditions result in the most stoichiometric form of NiO films deposited in this study.

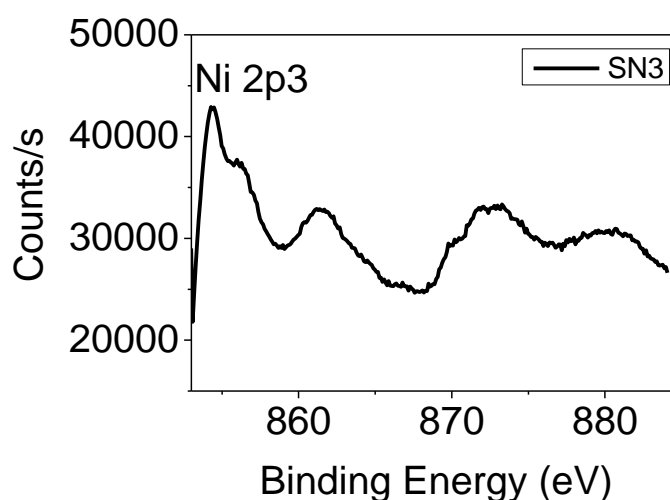


Figure 4.6. XPS graph of nickel for NiO thin film.

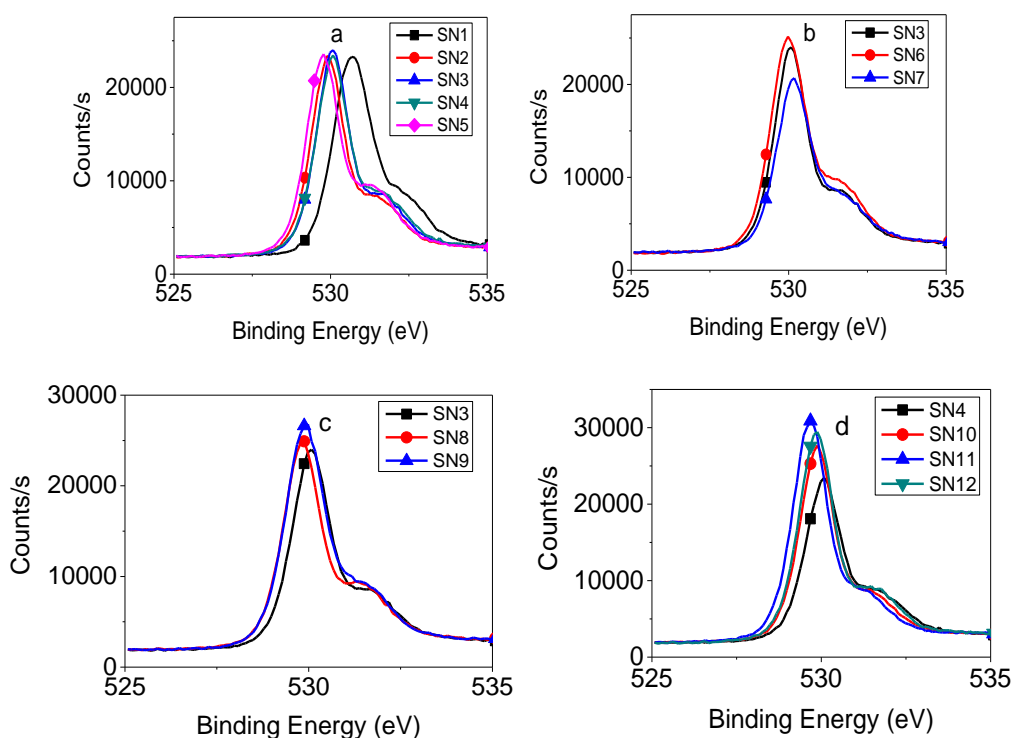


Figure 4.7. XPS graphs of oxygen for NiO thin films for different deposition parameters: a) oxygen flow rate, b) deposition temperature, c) deposition rate, d) oxygen flow rate with plasma assistance.

Table 4.3. Amounts of Ni and O atoms.

Sample No:	Ni (2p3) (at. %)	O (1s) (at. %)
SN 1	48.1	51.9
SN 2	47.9	52.1
SN 3	47.3	52.7
SN 4	46.6	53.4
SN 5	45.4	54.6
SN 6	47.3	52.7
SN 7	47.8	52.2
SN 8	46.7	53.3
SN 9	47.5	52.5
SN 10	49.4	50.6
SN 11	48.0	52.0
SN 12	47.0	53.0

#### 4.2.2. Optical Properties

Transmittance and reflectance measurements were conducted on NiO thin films deposited on glass substrates. Figure 4.8 shows the variation of transmittance with wavelength for different deposition parameters. The thickness values of the films are close to each other, and therefore, it is possible to assume that the samples are identical and convenient comparisons can be made. All of the films show some degree of absorption compared to base 92% transmittance of Bk7 glass. The amount of absorption also increases at shorter wavelengths. It is seen that the main effective parameter affecting the transmission values of the films is the oxygen flow rate. The increase in the oxygen flow rate minimizes the absorption at shorter wavelengths, and sample SN 5 shows the minimum absorption. Absorption decreases at high deposition temperatures and low deposition rates when deposition is performed at a constant oxygen flow rate. It is clear that higher transmittance at longer wavelengths is obtained when the oxygen flow rate is reduced. Upon increasing the amount of oxygen in the deposition chamber, the introduction of defects and porosity into the films resulted in optical scattering and decreased optical transmission. Strong absorption is observed when deposition is conducted by plasma assistance without oxygen. The formation of Ni<sup>3+</sup> ions and increase in the hole concentration are expected in the valence band. Enhanced carrier concentration is known to induce free carrier absorption and decreased transmission for whole spectrum including visible spectrum wavelengths at plasma assisted depositions [21]. A minimum of 50 sccm oxygen flow is required to obtain films with higher optical transmission values when plasma assistance is used.

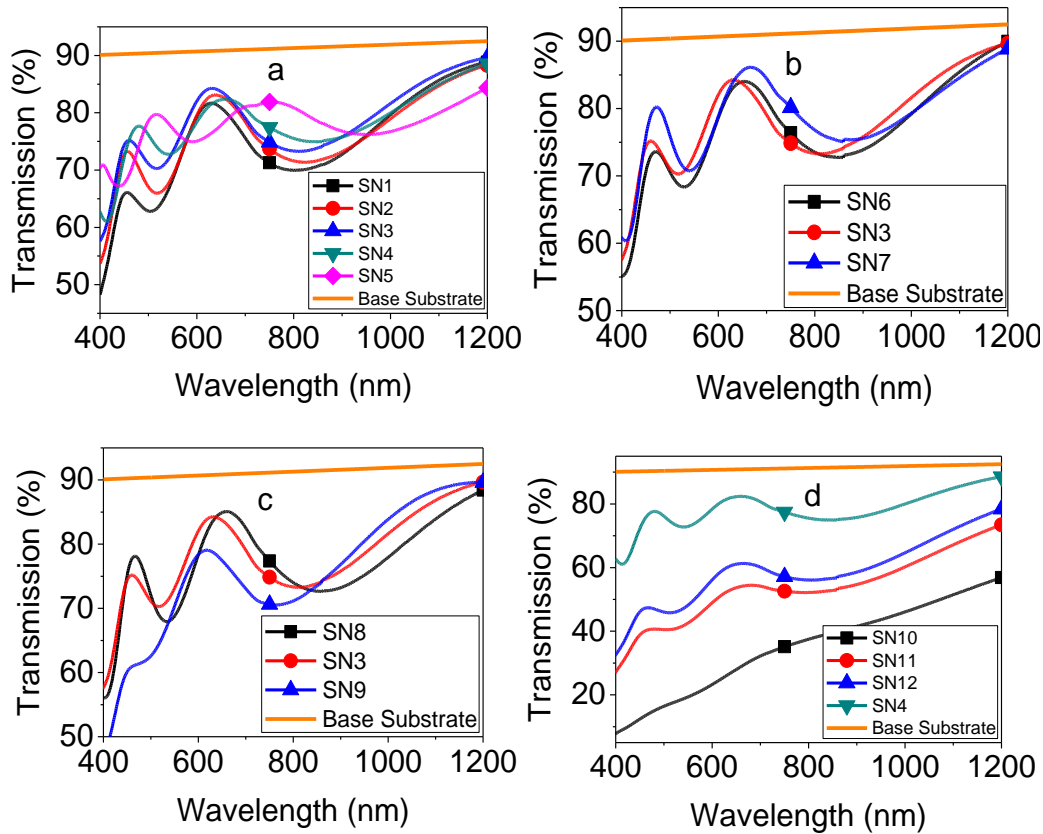


Figure 4.8. Transmission spectrum of NiO thin films for different deposition parameters: a) oxygen flow rate, b) deposition temperature, c) deposition rate, d) oxygen flow rate with plasma assistance.

The change of reflectance behavior of NiO thin films deposited under different deposition conditions can be seen in Figure 4.9. The maximum value of reflection and reflection amplitude are minimized when the oxygen flow rate increases [22, 23]. The amplitudes of reflection shown in Figure 4.9 give important information related to refractive index values of the films and lower amplitude values mean that the refractive index is decreased. The effect of plasma assistance on the optical properties cannot be predicted from transmission measurements due to high amount of absorption. However, reflectance measurements are not affected from absorption and they can be evaluated using the spectra given in Figure 4.9. Refractive index inhomogeneity, which is observed in the films deposited at high temperature and low

deposition rate conditions, can be inferred using reflection measurements. These samples have lower reflectance than the base substrate value, which is around 8%.

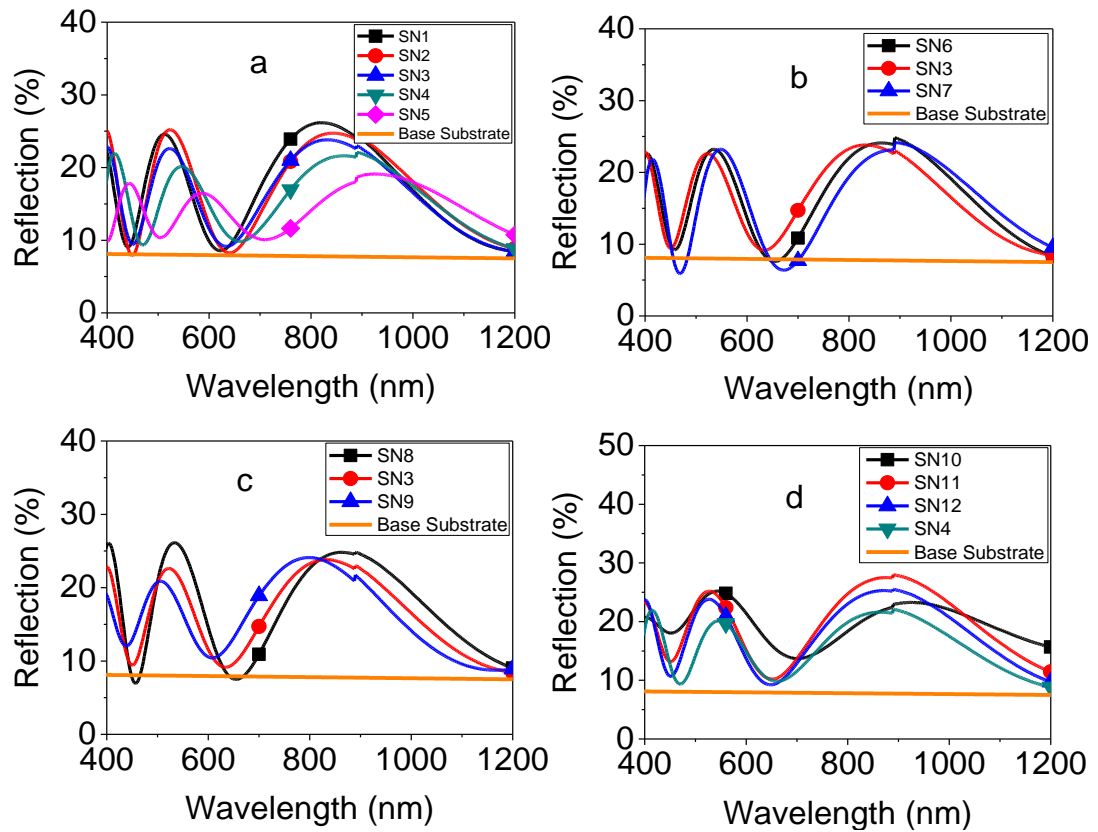


Figure 4.9. Reflection spectrum of NiO thin films for different deposition parameters: a) oxygen flow rate, b) deposition temperature, c) deposition rate, d) oxygen flow rate with plasma assistance.

Optilayer characterization tool was used to calculate refractive indexes, which can be seen in Figure 4.10. Also, thicknesses of thin films given in Table 4.4 were calculated by mathematical fitting of reflectance measurements. Denser films can be obtained at low oxygen flow rates, high deposition temperatures, and low deposition rates, since the presence of air or humidity in the structure of NiO thin films are reduced under these deposition conditions. Refractive index graphs give a good indication of the density of the films which show that the low oxygen flow rate, high deposition

temperature, and low deposition rate conditions yield denser films. Also, plasma assisted film deposition leads to denser films which results in reduced porosity inside the films. The thickness values of the films increase with oxygen pressure inside the chamber and we relate this situation as follows: although the mean free path of the vaporized atoms inside the chamber decreases with additional oxygen species, the porous nature of these films is the major reason for increased coating thicknesses.

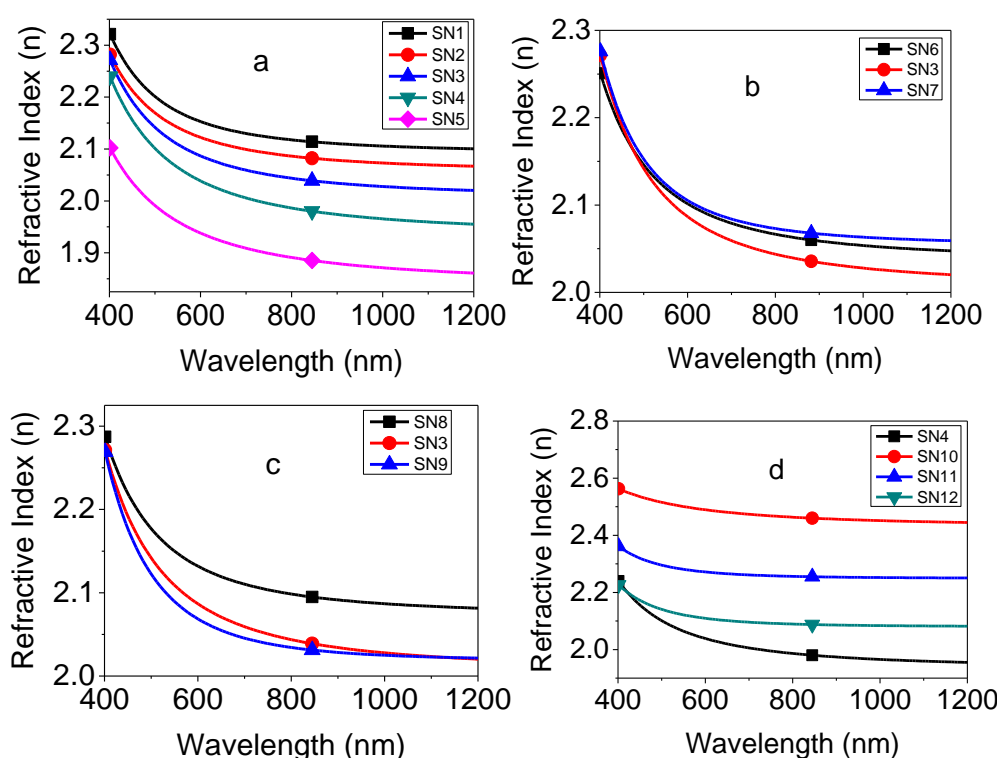


Figure 4.10. Refractive index dispersion of NiO thin films for different deposition parameters: a) oxygen flow rate, b) deposition temperature, c) deposition rate, d) oxygen flow rate with plasma assistance.

Optical band gaps of the deposited thin films were calculated by Tauc plot method. In this method, band gap is found from  $(\alpha h\nu)^2$  versus  $h\nu$  graph for direct band gap materials.  $\alpha$  is calculated from  $1/d \cdot \ln(1/T)$  equation, where  $d$  is the film thickness and  $T$  is optical transmittance [24]. A tangent line from the curve intersects the x-axis and

this value is taken as the band gap of the thin film. Table 4.4 summarizes the calculated band gap values of thin films. Small variations in band gap values, which are between 3.65 and 3.80 eV, are observed for different deposition parameters. Basically, the band gap of the films increases with higher oxygen flow rates, higher deposition temperatures, and higher deposition rates. Plasma assisted deposition yields the minimum band gap values among all deposition conditions. Variation in the band gap values is directly related to the crystallinity of the films and Ni/O ratio. Smaller band gaps are obtained when both Ni concentration and lattice parameter increase.

Table 4.4. *Thicknesses and band gaps of NiO thin films.*

Sample No:	Layer thickness (nm)	Band gap (eV)
SN 1	308.2	3.77
SN 2	319.5	3.77
SN 3	323.9	3.78
SN 4	348.8	3.79
SN 5	398.8	3.8
SN 6	331.3	3.69
SN 7	342.9	3.78
SN 8	324.4	3.76
SN 9	311.6	3.8
SN 10	270.6	3.65
SN 11	276.9	3.69
SN 12	286.3	3.72

#### **4.2.3. Electrical Properties**

The electrical properties of NiO thin films were investigated using Hall effect and UPS measurements. Table 4.5 summarizes the results of Hall effect measurements for thin films deposited at different deposition conditions comparatively. p-type semiconducting behavior is observed for NiO films deposited under each deposition

condition. The stoichiometric form of NiO possesses high resistivity which is around  $10^{13}\Omega\text{cm}$ .  $\text{Ni}^{2+}$  vacancies are the main reason for increased conductivity for NiO films and excess oxygen in NiO thin films forms  $\text{Ni}^{2+}$  vacancy sites which are replaced by two  $\text{Ni}^{3+}$  ions, which in turn results in donation of one hole to the valence band. This defect mechanism is explained by Kroger–Vink notation [5]. The sheet Hall coefficient, sheet carrier density, and mobility values of the thin films were extracted from Hall effect measurements where the resistivity is calculated from the equation 4.1 [25]:

$$\text{Conductivity} = \frac{\text{SheetCarrierDensity} * 1.6 \times 10^{-19} * \text{Mobility}}{\text{FilmThickness}} = \frac{1}{\text{Resistivity}} \text{ Eq. [4.1]}$$

The resistivity of thin films decreases with increased oxygen flow rate, increased deposition temperature, and low deposition rate. XPS results reveal that the decrease in the resistivity is due to the increase in the oxygen content for higher oxygen flow rates and deposition rates. However, the resistivity of sample SN 7 has a lower value than the other oxygen rich samples. As the deposition temperature increases, enlargement in the lattice size leads to the formation of a large number of carriers in the lattice and it results in a lower resistivity. The resistivity of the films dramatically decreases with plasma assisted deposition, although Ni amount in these films increases with plasma assistance. Sheet carrier densities of plasma assisted films are 2 orders of magnitude higher than nonassisted samples although they have lower mobility than nonassisted samples. The mobility of holes is affected by the deposition condition which can be related to the grain size of deposited films. The grain size of NiO films increases with a high oxygen flow rate. A large grain size minimizes the grain boundary area which results in decreased grain boundary scattering and amount of point defects[14]. Therefore, decreased mobility is observed for samples having smaller grain sizes. Plasma assisted deposition yields denser film structures which results in lower mobility even if these films have similar grain sizes compared to nonassisted deposited films. The main reason for the lower mobility values upon

oxygen doping of NiO films is the fact that although oxygen doping enhances the carrier concentration by creating defect sites, these defect sites cause scattering during transport and result in low mobility. However, the overall conductivity of the films increases. Such high conductivity is desirable for devices where lots of stacking layers lead to excessive overall resistance of the device, especially in solar cell applications [26, 27].

Table 4.5. Hall effect measurements of NiO thin films for different deposition parameters.

Sample No:	Sheet hall coefficient (cm <sup>2</sup> /C)	Sheet carrier density (1/cm <sup>2</sup> )	Mobility (cm <sup>2</sup> /(VS))	Resistivity (ohm.cm)	Conductivity (1/ohm.cm)
a)Oxygen flow rate					
SN 1	2.6x10 <sup>12</sup>	7.2x10 <sup>6</sup>	152.1	5.1x10 <sup>5</sup>	2.0x10 <sup>-6</sup>
SN 2	1.4x10 <sup>12</sup>	1.5x10 <sup>7</sup>	207.6	2.0x10 <sup>5</sup>	5.1x10 <sup>-6</sup>
SN 3	1.8x10 <sup>12</sup>	6.9x10 <sup>6</sup>	315.8	1.7x10 <sup>5</sup>	6.0x10 <sup>-6</sup>
SN 4	1.4x10 <sup>12</sup>	1.6x10 <sup>8</sup>	724.6	5.7x10 <sup>4</sup>	1.8x10 <sup>-5</sup>
SN 5	9.6x10 <sup>11</sup>	4.2x10 <sup>7</sup>	1740.9	1.7x10 <sup>4</sup>	6.0x10 <sup>-5</sup>
b)Deposition temperature					
SN 6	5.1x10 <sup>11</sup>	2.0x10 <sup>7</sup>	46.2	3.3x10 <sup>5</sup>	3.0x10 <sup>-6</sup>
SN 3	1.8x10 <sup>12</sup>	6.9x10 <sup>6</sup>	315.8	1.7x10 <sup>5</sup>	6.0x10 <sup>-6</sup>
SN 7	2.5x10 <sup>10</sup>	2.6x10 <sup>8</sup>	93.2	8.0x10 <sup>3</sup>	1.3x10 <sup>-4</sup>
c)Deposition rate					
SN 8	4.4x10 <sup>9</sup>	2.0x10 <sup>9</sup>	5.9	2.3x10 <sup>4</sup>	4.4x10 <sup>-5</sup>
SN 3	1.8x10 <sup>12</sup>	6.9x10 <sup>6</sup>	315.8	1.7x10 <sup>5</sup>	6.0x10 <sup>-6</sup>
SN 9	6.5x10 <sup>11</sup>	3.4x10 <sup>7</sup>	71	2.8x10 <sup>5</sup>	3.6x10 <sup>-6</sup>
d)Oxygen flow rate with plasma assistance					
SN 4	1.4x10 <sup>12</sup>	1.6x10 <sup>8</sup>	724.6	5.7x10 <sup>4</sup>	1.8x10 <sup>-5</sup>
SN 10	9.4x10 <sup>5</sup>	1.1x10 <sup>13</sup>	0.2	1.5x10 <sup>2</sup>	6.6x10 <sup>-3</sup>
SN 11	1.8x10 <sup>7</sup>	3.5x10 <sup>11</sup>	0.2	3.1x10 <sup>3</sup>	3.3x10 <sup>-4</sup>
SN 12	9.6x10 <sup>7</sup>	1.7x10 <sup>11</sup>	0.4	7.6x10 <sup>3</sup>	1.3x10 <sup>-4</sup>

The Fermi energy level and valence band maximum of thin films were obtained from UPS measurements. Figure 4.11 gives the UPS spectra of NiO thin films. First, the Fermi level is calculated from the extraction of work function of NiO from the cut-off energy position. The difference between the fermi energy level and valence band maximum is found from the onset energy which can be seen in Figure 4.11 [28]. Band positions of NiO thin films are represented in Figure 4.12 for different deposition conditions. Minima of conduction band edge positions are found by adding the optical band gap values to the valence band minima energies, where optical band gaps are calculated from Tauc plots. The valence band maximum (VBM) and Fermi energy values shift to more negative values with additional oxygen which can also be seen in plasma assisted deposition. Low and high temperature depositions compared to base 80°C deposition shift the valence band maximum positions to more positive values. The deposition rate does not affect the bands' position critically.

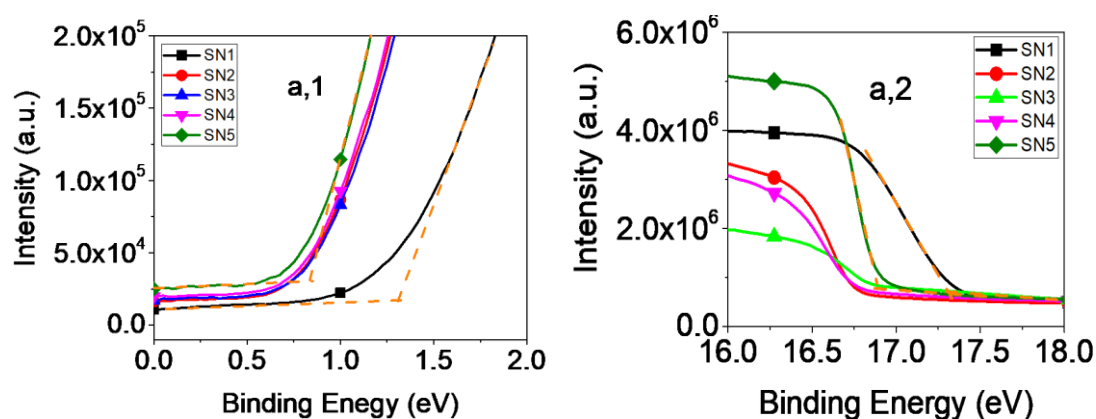


Figure 4.11. UPS spectrum of NiO deposited films for different deposition parameters: a) oxygen flow rate, b) deposition temperature, c) deposition rate, d) oxygen flow rate with plasma assistance (1:onset and 2:cutoff positions)

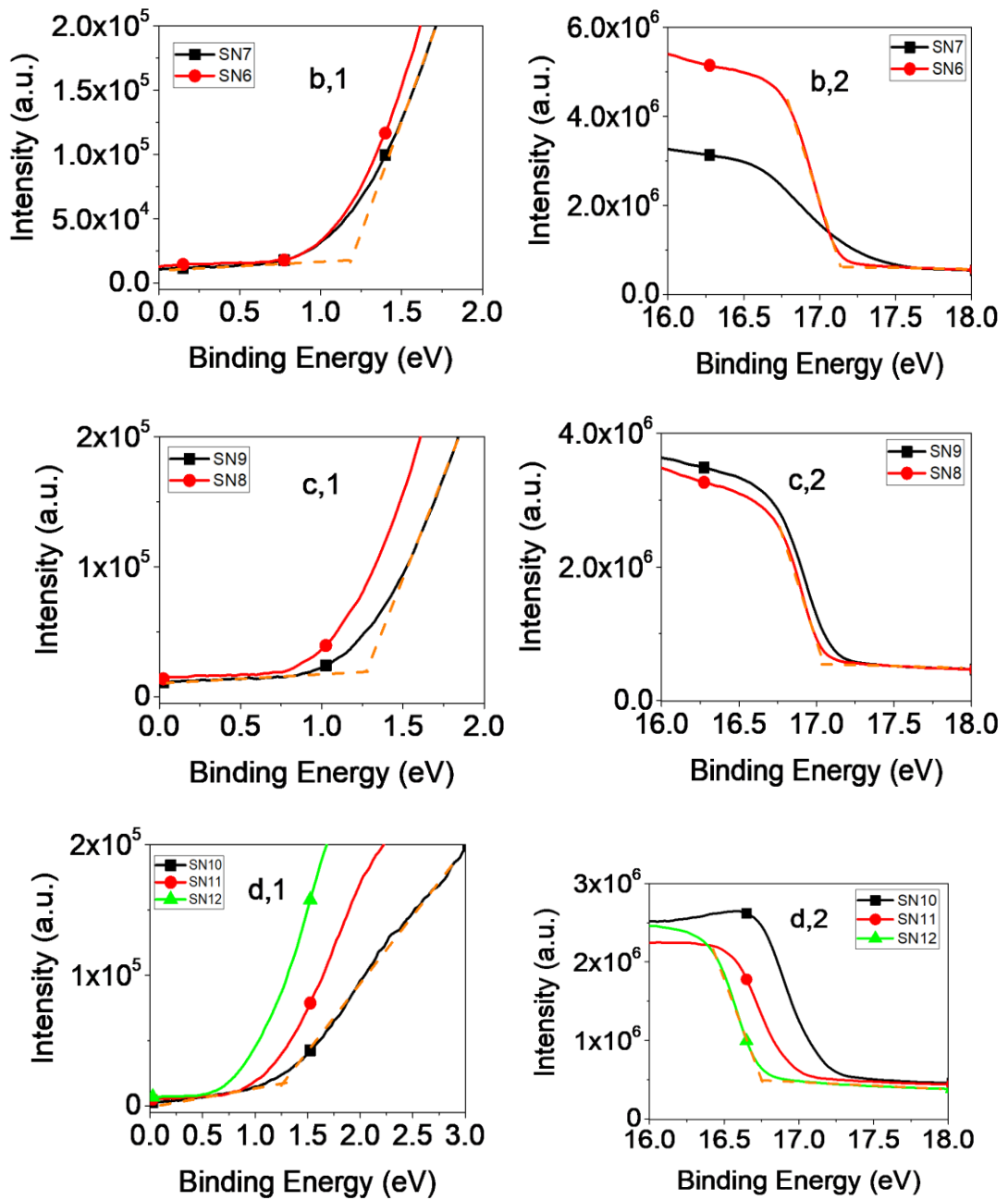


Figure 4.11 (Continued)

From Hall effect measurements and UPS measurements, it is notable that the movement of VBM and hole conductivity of the samples highly depend on oxygen flow rate of the deposition. For both plasma assisted and nonassisted films, as a

general trend, VBM of the films can be tuned to lower energy levels via increasing the oxygen content of the films or in this case oxygen doping. This situation is similar to n-type conducting oxide materials in which the Fermi level and work function can be arranged by doping and electrical conductivity can be enhanced by orders of magnitudes. Oxygen doping in this work resulted in deeper Fermi levels and reduced work function of the films, which is quite favorable for electron blocking ability in optoelectronic devices. The valence band edge of NiO films varies between -5.12 and -5.50 eV, which is quite suitable for most organic and metalorganic perovskite based solar devices. These films can also be deposited on flexible substrates due to low temperature deposition conditions.

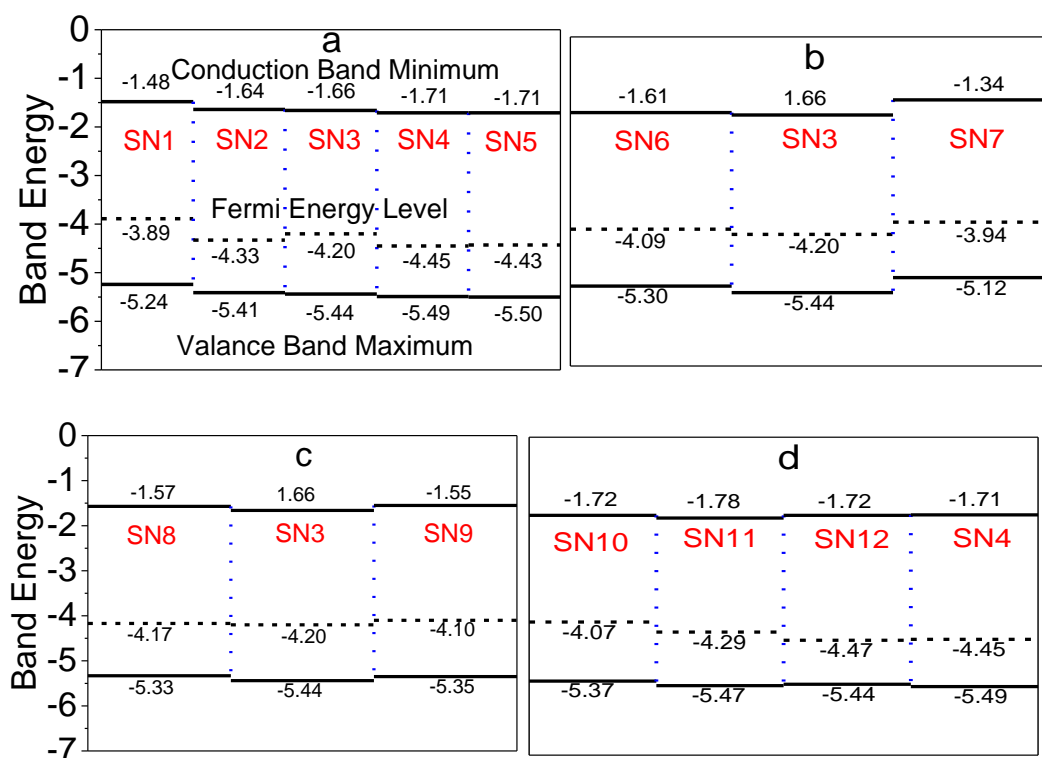


Figure 4.12. Band positions of NiO thin films for different deposition parameters: a) oxygen flow rate, b) deposition temperature, c) deposition rate, d) oxygen flow rate with plasma assistance.

### 4.3. Conclusion

In this work, NiO thin films were deposited on Bk7 glass with electron beam evaporation method under different oxygen flow rates, deposition temperatures, deposition rates, and plasma assistance conditions. The effect of deposition parameters on the film's performance was explained with the help of structural, optical, and electronic characterizations. All the films are produced with good adherence to substrate with dense nature. It was seen that e-beam deposited NiO films tend to grow with a preferential orientation of (111) plane; however, orientation of planes is strongly affected by deposition conditions. SEM investigations revealed that films possess needlelike, spherical, and cuboidal surface morphologies. The nonstoichiometry of NiO thin films is determined from XPS measurements and the oxygen concentration of the films was found to be higher than nickel for all deposition conditions. Both XPS and XRD analyses revealed that the structure is a pure cubic NiO without any secondary phases. The optical absorption behavior of the films was analyzed between 400 and 600 nm wavelengths and it was detected that the increased oxygen flow rate, increased deposition temperature, and low deposition rate minimize the absorption. Although low oxygen containing samples suffered from high absorption, they have a higher transmittance at longer wavelengths due to the nature of low optical scattering. Optical band gaps of the films were found to increase with oxygen amount, temperature and deposition rate. From Hall effect measurements, lowest resistivity was observed in the sample containing the maximum amount of nickel which is deposited by plasma assistance. Although plasma assistance results in lower mobility, conductivity can be enhanced due to the increased carrier concentration. This condition is directly related to denser films with higher crystallinity. The tunability of the band positions of the NiO layer by oxygen doping and low temperature deposition conditions is quite advantageous for most optoelectronic applications where proper band alignment is crucial, in conjunction with polymeric and heat sensitive conductors



## REFERENCES

- [1] M. Ghougali, O. Belahssen, A. Chala, Structural, optical and electrical properties of nio nanostructure thin film, *Journal of Nano and Electronic Physics*, 8 (2016) 04059-04054.
- [2] W. Guo, K. N. Hui, K. S. Hui, High conductivity nickel oxide thin films by a facile sol-gel method, *Materials Letters*, 92 (2013) 291-295.
- [3] S. C. Chen, T. Y. Kuo, T. H. Sun, Microstructures, electrical and optical properties of non-stoichiometric p-type nickel oxide films by radio frequency reactive sputtering, *Surface and Coatings Technology*, 205 (2010) S236-S240.
- [4] G. H. Aydogdu, D. Ruzmetov, S. Ramanathan, Metastable oxygen incorporation into thin film NiO by low temperature active oxidation: Influence on hole conduction, *Journal of Applied Physics*, 108 (2010) 113702.
- [5] B. A. Reguig, A. Khelil, L. Cattin, M. Morsli, J. C. Bernède, Properties of NiO thin films deposited by intermittent spray pyrolysis process, *Applied Surface Science*, 253 (2007) 4330-4334.
- [6] S. A. Makhlof, Electrical properties of NiO films obtained by high-temperature oxidation of nickel, *Thin Solid Films*, 516 (2008) 3112-3116.
- [7] A. M. Soleimanpour, Y. Hou, A. H. Jayatissa, Evolution of hydrogen gas sensing properties of sol-gel derived nickel oxide thin film, *Sensors and Actuators B: Chemical*, 182 (2013) 125-133.
- [8] E. Azaceta, S. Chavhan, P. Rossi, M. Paderi, S. Fantini, M. Ungureanu, O. Miguel, H. J. Grande, R. Tena-Zaera, Nio cathodic electrochemical deposition from an aprotic ionic liquid: Building metal oxide n-p heterojunctions, *Electrochimica Acta*, 71 (2012) 39-43.
- [9] H.-Q. Dai, Y.-N. Zhou, Q. Sun, F. Lu, Z.-W. Fu, Enhanced electrochemical properties of nio-nis nanocomposite thin film, *Electrochimica Acta*, 76 (2012) 145-151.
- [10] Y. Zhao, H. Wang, C. Wu, Z. F. Shi, F. B. Gao, W. C. Li, G. G. Wu, B. L. Zhang, G. T. Du, Structures, electrical and optical properties of nickel oxide films by radio frequency magnetron sputtering, *Vacuum*, 103 (2014) 14-16.

- [11] T. Minoru, H. Takeshi, K. Takeshi, Room-temperature heteroepitaxial growth of n NiO thin films using pulsed laser deposition, *Japanese Journal of Applied Physics*, 39 (2000) 1817.
- [12] T. S. Yang, W. Cho, M. Kim, K.-S. An, T.-M. Chung, C. G. Kim, Y. Kim, Atomic layer deposition of nickel oxide films using  $\text{Ni}(\text{DMAP})_2$  and water, *Journal of Vacuum Science & Technology A: Vacuum, Surfaces, and Films*, 23 (2005) 1238-1243.
- [13] F. Eiji, T. Atsushi, F. Satoru, T. Hideo, H. Masumi, T. Ryoichi, NaCl-type oxide films prepared by plasma-enhanced metalorganic chemical vapor deposition, *Japanese Journal of Applied Physics*, 32 (1993) L1448.
- [14] S. C. Chen, C. K. Wen, T. Y. Kuo, W. C. Peng, and H. C. Lin, Characterization and properties of NiO films produced by rf magnetron sputtering with oxygen ion source assistance, *Thin Solid Films* 572, (2014) 51-55.
- [15] Y. Chen, Y. Sun, X. Dai, B. Zhang, Z. Ye, M. Wang, H. Wu, Tunable electrical properties of NiO thin films and p-type thin-film transistors, *Thin Solid Films*, 592 (2015) 195-199.
- [16] R. Ishikawa, Y. Furuya, R. Araki, T. Nomoto, Y. Ogawa, A. Hosono, T. Okamoto, N. Tsuboi, Preparation of p-type NiO films by reactive sputtering and their application to CdTe solar cells, *Japanese Journal of Applied Physics*, 55 (2016) 02BF04.
- [17] D. Y. Jiang, J. M. Qin, X. Wang, S. Gao, Q. C. Liang, J. X. Zhao, Optical properties of NiO thin films fabricated by electron beam evaporation, *Vacuum*, 86 (2012) 1083-1086.
- [18] M. M. El-Nahass, M. Emam-Ismail, M. El-Hagary, Structural, optical and dispersion energy parameters of nickel oxide nanocrystalline thin films prepared by electron beam deposition technique, *Journal of Alloys and Compounds*, 646 (2015) 937-945.
- [19] B. Subramanian, M. Mohammed Ibrahim, K. R. Murali, V. S. Vidhya, C. Sanjeeviraja, M. Jayachandran, Structural, optoelectronic and electrochemical properties of nickel oxide films, *Journal of Materials Science: Materials in Electronics*, 20 (2008) 953-957.
- [20] I. Hotovy, J. Huran, P. Siciliano, S. Capone, L. Spiess, V. Rehacek, The influences of preparation parameters on NiO thin film properties for gas-sensing application, *Sensors and Actuators B: Chemical*, 78 (2001) 126-132.

- [21] S. Visvanathan, Free carrier absorption arising from impurities in semiconductors, *Physical Review*, 120 (1960) 379.
- [22] M. J. Rand, Spectrophotometric thickness measurement for very thin SiO<sub>2</sub> films on Si, *Journal of Applied Physics*, 41 (1970) 787-790.
- [23] R. Swanepoel, Determination of the thickness and optical constants of amorphous silicon, *Journal of Physics E: Scientific Instruments*, 16 (1983) 1214.
- [24] A. Karpinski, N. Ouldhamadouche, A. Ferrec, L. Cattin, M. Richard-Plouet, L. Brohan, M. A. Djouadi, P. Y. Jouan, Optical characterization of transparent nickel oxide films deposited by dc current reactive sputtering, *Thin Solid Films*, 519 (2011) 5767-5770.
- [25] L. J. van der Pauw, A method of measuring specific resistivity and hall effect of discs of arbitrary shapes, *Philips research reports*, 13 (1958) 1-9.
- [26] H. L. Z. Kelvin, X. Kai, G. B. Mark, G. E. Russell, P-type transparent conducting oxides, *Journal of Physics: Condensed Matter*, 28 (2016) 383002.
- [27] W. Chen, Y. Wu, Y. Yue, J. Liu, W. Zhang, X. Yang, H. Chen, E. Bi, I. Ashraful, M. Grätzel, L. Han, Efficient and stable large-area perovskite solar cells with inorganic charge extraction layers, *Science*, 350 (2015) 944-948.
- [28] D. Cahen, A. Kahn, Electron energetics at surfaces and interfaces: Concepts and experiments, *Advanced Materials*, 15 (2003) 271-277.



## CHAPTER 5

### EFFECT OF OXYGEN FLOW RATE ON THE LOW TEMPERATURE DEPOSITION OF TITANIUM MONOXIDE THIN FILMS VIA ELECTRON BEAM EVAPORATION

Titanium monoxide (TiO) is an attractive ceramic material for many applications. It belongs to the same family with nitride or carbide based hard refractory metals, therefore it has around 20 GPa Vicker's hardness. Also, TiO thin films exhibit a golden yellow color and as a result it is a good alternative for both protective and decorative coating applications [1-3]. Due to the unique thermoelectric properties, it can be used in thermoelectric generators [4]. Surface of TiO suddenly oxidizes to TiO<sub>2</sub> by reacting with oxygen upon exposure to air, therefore TiO thin films can be used for anticorrosive purposes [5]. TiO thin films are also used in microelectronic and piezoelectric applications for metallization and they act as a barrier layer for inter diffusion of Cu, Si and Al due to their low electrical resistivity [3, 5, 6]. Stoichiometric TiO exhibits p-type semiconducting character, so it can be used as an amorphous oxide semiconductor [7]. Also tungsten doped TiO for the detection of nitrogen dioxide gas has been reported for gas sensing applications [8]. In addition, it was reported that optical absorption threshold of TiO is around 1.2 eV and it fully covers the visible spectrum [3, 6, 9]. Due to the high optical absorption and hole transport characteristics, it is a promising material for p-type absorber for photovoltaic applications [3, 7]. Stoichiometric TiO can be formed in cubic, triclinic and hexagonal crystal structures; however, low temperature phases are only cubic  $\beta$ -TiO and monoclinic  $\alpha$ -TiO [10]. Both structures can possess up to 15 percent vacancy concentration for both titanium and oxygen atoms. However, high concentration of point defects can be filled by titanium and oxygen sub-lattice which causes the change of x between 0.7 and 1.3 for

TiO<sub>x</sub>. Unique features of optical, electrical, magnetic and thermal properties arise due to the structural vacancy and stoichiometry exhibited in TiO [1, 3, 7, 11].

In contrast to its n-type fully oxidized form TiO<sub>2</sub>, TiO exhibits p-type electronic conduction. Intrinsic n-type conductivity observed in TiO<sub>2</sub> films due to internal defects like vacancies, tends to convert to p-type conductivity in highly degenerated vacancy formation conditions [12]. This ability of oxides of titanium paves the way for construction of many optical and electronic elements like detectors [13], thin film transistors (TFT) and metal oxide semiconductor field effect transistors (MOSFET) [14]. Electronic structure highly depends on the oxygen content of the films and fine-tuning of the opto-electronic properties is feasible [15]. This tunability is important for proper charge transfer processes in many photoelectronic devices [16-18]. There is a high demand especially in photovoltaic industry for stable and environmentally friendly p-type oxide based semiconductors as a replacement for unstable organic or polymeric counter parts, for deposition of inorganic p-n heterojunctions [19, 20]. In addition, low temperature deposition of these oxide layers is also subject to great interest due to the enormously growing flexible devices [21, 22] or wearable technologies market. E-beam evaporation is a widely used film growth technique for deposition of homogeneous epitaxial layers in vacuum environment similar to ALD technique without damaging the underneath layers [23].

Production of TiO thin films have been reported by several methods. Suitable deposition method is selected according to the application area and coating thickness. Most of the coating methods demand high temperature post processes to achieve crystallinity and structure formation [8]. TiO thin films can be deposited by rough methods like reduction of TiO<sub>2</sub> by sintering [24], ion bombardment [25] or co-evaporation together with metallic titanium [12], DC arc fusion [26], and ink-jet printing methods[3], however it can also deposited using vacuum deposition methods like chemical vapor deposition (CVD) [27], pulsed laser deposition (PLD) [28], sputtering [1, 2, 7, 8, 29, 30], ion beam deposition [30], thermal evaporation [31-33]

and electron beam evaporation [5, 6, 34]. Depositions are mostly performed using reactive sputtering in the presence of oxygen [1, 2, 8, 28-30] or using post oxidation of metallic titanium [6, 30]. Some of the studies also investigate plasma and ion assisted deposition of titanium monoxide [7, 8, 29].

In this study, titanium monoxide thin films were deposited under vacuum using electron beam evaporation technique. Depositions were performed at different oxygen flow rates to investigate the effect of deposition conditions on structural, electrical and optical performances of the films. Depositions were carried out at low temperatures in order to obtain TiO thin films on temperature sensitive substrates, which is important for extending the suitability of TiO thin films for a wide range of application areas. We have demonstrated that crystalline TiO thin films can be deposited at low temperatures without assistance of a post annealing treatment due to highly energetic and powerful deposition characteristic of electron beam evaporation technique.

### **5.1. Experimental Procedure**

TiO thin films were deposited on Schott BK7 glasses. Depositions were performed in Tecport physical vapor deposition system. Titanium monoxide pellets were purchased from Materion with 99.9% purity. Pellets were firstly premelted in a copper crucible to obtain better quality thin films. Premelted TiO was prepared for the deposition in 4 sequential steps using 7.2 kV DC high voltage energy source. As a first step, current of the electron beam was increased to 0.3 A in 1 min, after that e-beam current was kept at the same value for 30 s. In the following step, current was increased to 0.4 A in 30 s and kept at that value for 30 s. After the last step, shutter was opened and deposition was started by preventing the splitting of the material. Substrates were cleaned with acetone wiping before loading them into the system and also they were cleaned in vacuum chamber by argon-oxygen mixture etching without damaging the surface. Depositions were started when vacuum level inside the chamber reached to  $8 \times 10^{-6}$  mbar. Substrate temperature was set to no more than 80°C in order to prevent

any damage to temperature sensitive substrates. Stable deposition rate was obtained at 2 Å/s which is accepted as optimized value for proper oxidization of evaporated Ti atoms and deposition of the stoichiometric TiO films. Coating thickness was measured by a natural quartz crystal and films were grown until the value of 300 nm thickness was reached. Natural Oxygen gas was introduced from the top of the electron beam source at 1, 2, 5, 10, 25 and 50 sccm flow rates. Also, one of the thin film samples was deposited without any oxygen flow.

TiO thin films were analyzed by spectrophotometer, X-ray diffractometer (XRD), X-ray photoelectron spectroscopy (XPS), Hall Effect, ultraviolet photoelectron spectroscopy (UPS) and scanning electron microscopy (SEM). Perkin Elmer Lambda 950 spectrophotometer was used for optical transmission and reflection measurements. Crystallographic analyses were conducted by a thin film X-ray diffractometer, PANalytical using Cu K $\alpha$  radiation (1.54 Å) at 3° grazing incidence to minimize the substrate effect. X-ray photoelectron spectroscopy (Thermo K-Alpha) was used to differentiate Ti<sup>2+</sup> from the other oxidation states. Photoelectrons were collected by charge compensation at 9 V. Films were etched by argon before characterization about 5 minutes at 500 eV to remove thin titanium dioxide layer, which unavoidably forms on TiO films upon exposure to atmosphere. Etching process was optimized not to create any preferential sputtering of either titanium or oxygen atoms. Hall Effect measurements were made using Lakeshore 7700A system with van der Pauw geometry between 1 and 1.8 T. Gold film was deposited on the corner of the samples for contacts. Electronic band positions of the thin films were calculated using the results of UPS (PHI 5000 Versaprobe). TiO<sub>x</sub> thin films were deposited on indium:tin oxide (ITO) coated glass for UPS characterizations. Surface morphologies and cross-sections of the films were investigated by scanning electron microscopy (FEI, Nova NanoSEM 430).

## 5.2. Results and Discussions

Titanium monoxide thin films were characterized firstly using XRD for crystal structure analysis. XRD pattern of as deposited thin films were recorded between  $20^\circ$  to  $70^\circ$  and measurements were performed at  $3^\circ$  grazing angle in order to eliminate the contribution of the substrate. Crystallization is not observed in the samples deposited using 25 and 50 sccm oxygen flow rate, where they do not yield any reflection associated with a peak in XRD pattern. However, crystallization is observed when depositions are performed up to 10 sccm oxygen flow rates. Figure 5.1a shows the XRD pattern of as deposited titanium monoxide thin films. Peaks are observed at  $37.5^\circ$ ,  $43.4^\circ$  and  $63.1^\circ$  which correspond to (111), (200) and (220) planes. They are well matched to TiO with 08-0117 JSPDS card number and they are shown in Figure 5.1a. Later that, all samples were heat treated at  $350^\circ\text{C}$  for 2 h under vacuum to increase the crystallization of the thin films (Figure 5.1b) in order to clearly indicate the difference between the as deposited and heat treated films. It is seen from XRD patterns that as deposited films possess TiO structure with crystallinity showing that TiO films can be successfully formed at reduced temperatures without any heat treatment assistance. However, preferred orientation of the crystallites changes upon heat treatment. (111) plane is dominant in as deposited films, whereas (200) plane starts to be dominant in heat treated samples for lower oxygen flow rate samples. The property of successful formation of crystalline low temperature deposited TiO films with e-beam deposition is important for heat sensitive substrate applications. Additionally, it is given in the study of Pazidis et.al., TiO structure can be formed in both cases where substrate temperature is held at  $240^\circ\text{C}$  and at room temperature [35]. Increase in oxygen flow rate minimizes the peak intensities which result in removal of (111) and (220) planes. When flow rate reaches to 25 sccm, all the peaks disappear. As the oxygen flow rates reach 50 sccm, anatase (A) and rutile (R) phases of titanium dioxide are formed together with titanium monoxide and structure is a mixture of these phases. For both as deposited and heat treated samples, measurements show that peak broadening occurs when oxygen flow rate increases. This means that grain sizes

decrease with increase in oxygen flow rates. It is also seen that peak intensities are minimized with increase in oxygen flow rates upon heat treatment. Changes in color of thin films are correlated with the atomic orientation as seen in the work of Li et al [8]. In that study, it was emphasized that TiO films have metallic appearance when (200) plane is not observed. This phenomenon is also observed in our study. Also, with increase in oxygen flow rate, color of the film firstly returns to a golden color, then the films appear as bluish and finally they become clear [36].

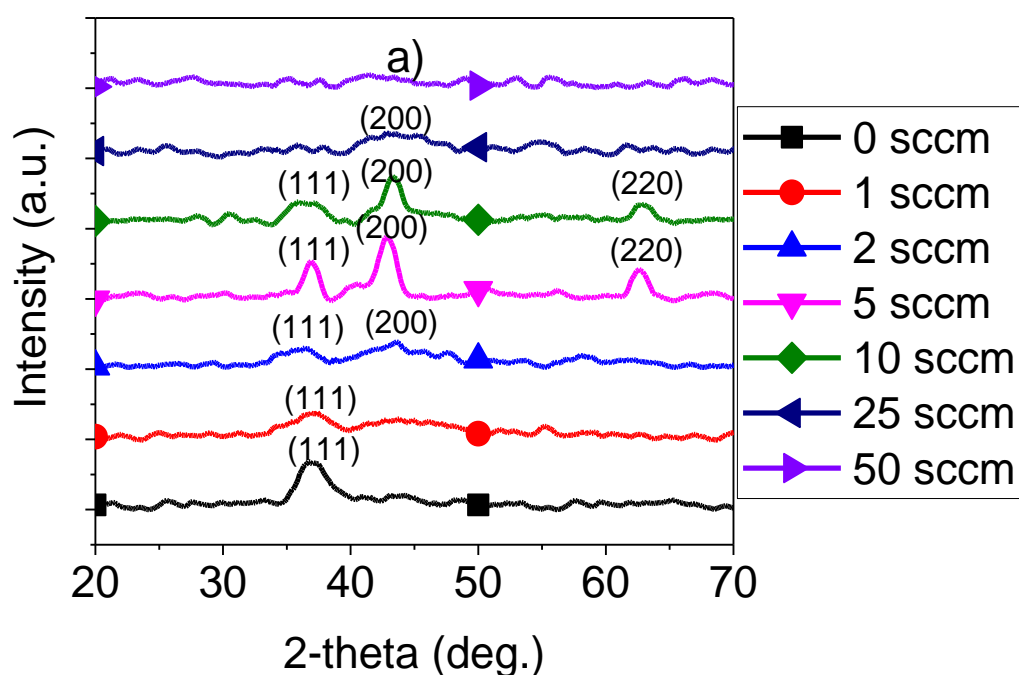


Figure 5.1. X-ray diffraction patterns of titanium monoxide thin films a) as deposited, and b) vacuum heat treated (A and R denote anatase and rutile phases of titanium dioxide, respectively).

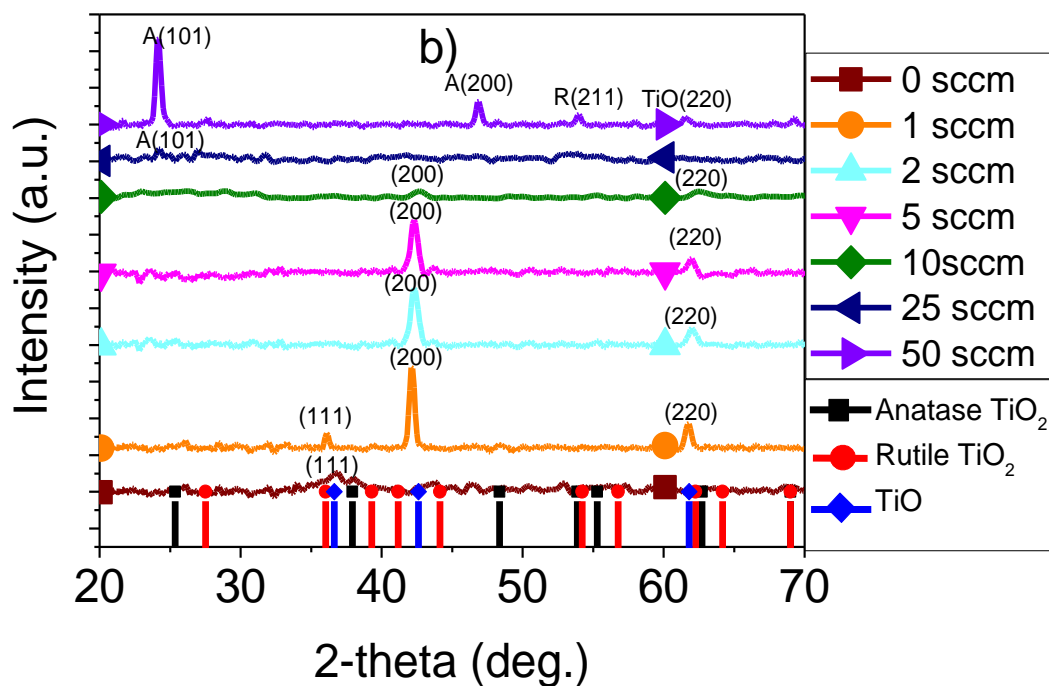
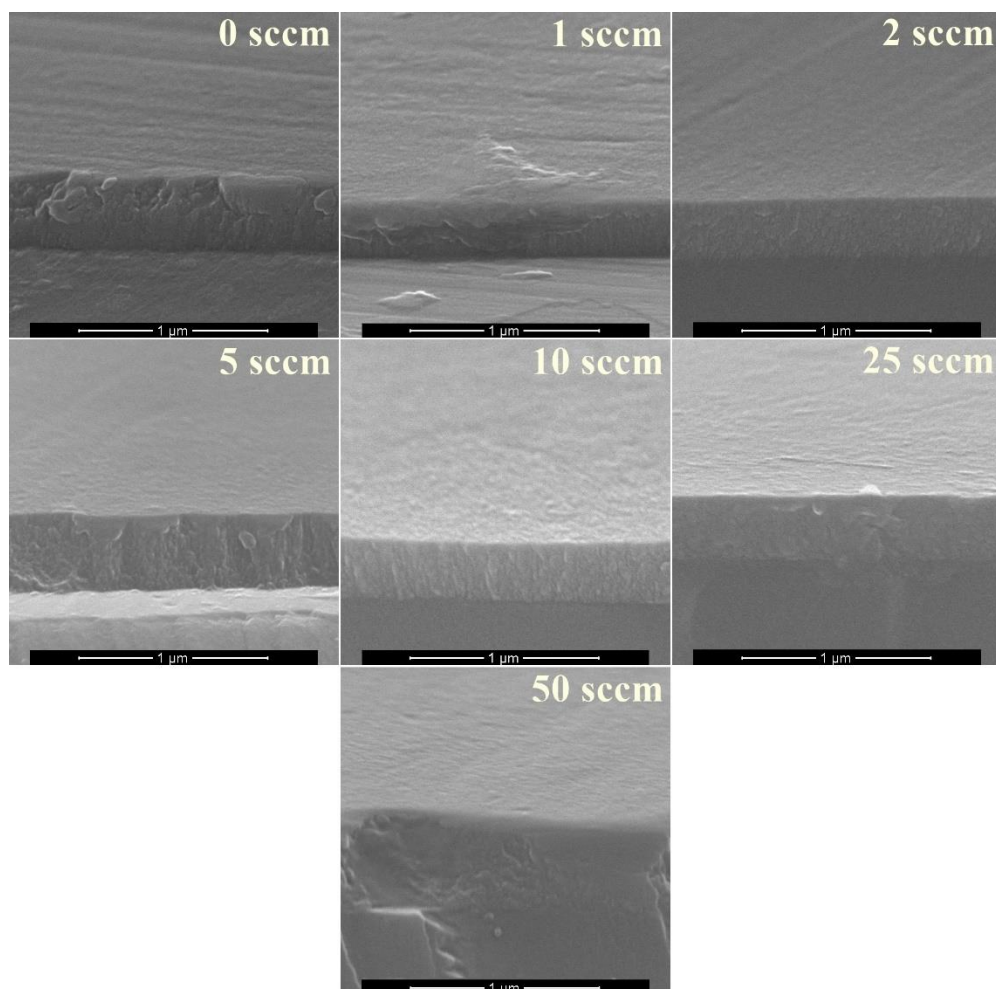


Figure 5.1 (Continued)

Figure 5.2 shows cross sectional images of the titanium monoxide thin films grown at a thickness of 300 nm. It is observed that thin films are grown yielding a combination of columnar and spherical parts. According to the study of Villarroel et al, TiO thin films are grown strongly at columnar structure, possibly due to the magnetron sputtering deposition technique [37]. Electron beam evaporation is a less energetic method compared to the magnetron sputtering, therefore film growth is realized at lower substrate temperatures. Substrate heating in sputtering can assist for the formation of columnar region in Thornton zone model [38]. Some glassy structures are formed which also explain the amorphous nature of the films observed in XRD spectra. It is seen that films are crack and pinhole free. The ability of the e-beam evaporation technique to deposit dense films is the main reason for the formation of dense and continuous films prepared in this work. The pin hole free characteristic of the films is important for most opto-electronic applications where cracks and pinholes

lead to leakage or short circuit problems especially in electronic devices. Such pinholes and cracks also have negative effect on the optical properties of the coatings behaving like scattering centers and may lead to hazy films.



*Figure 5.2.* Cross sectional SEM images of titanium monoxide thin films deposited using different oxygen flow rates.

XPS analysis was carried out to find the oxidation state of titanium oxide thin films.  $Ti^{+2}$ ,  $Ti^{+3}$  and  $Ti^{+4}$  states correspond to  $TiO$ ,  $Ti_2O_3$  and  $TiO_2$ , respectively. Since titanium is an oxygen scavenger, formation of stable state of  $TiO_2$  is indispensable on the surface of the films. For this reason, surface is etched to remove this  $TiO_2$  layer

before conducting the measurements. Ti 2p core level makes two separate peaks as  $2p_{3/2}$  and  $2p_{1/2}$ .  $Ti^{+2}$ ,  $Ti^{+3}$  and  $Ti^{+4}$  states are formed at 455.1-460.8, 457.8-463.9 and 458.7-464.4 eV positions, respectively. Figure 5.3. shows the titanium (Figure 5.3a) and oxygen (Figure 5.3b) peaks, which are obtained from XPS analysis for the case of increase in oxygen flow rate. Titanium peaks shift to longer binding energies when the structure transforms from metallic titanium to titanium dioxide [6]. Only two peaks are present when deposition is carried out without oxygen. Peaks are observed at shorter binding energies compared to titanium monoxide. When oxygen is introduced into the system, exact titanium monoxide peaks appear at 1, 2 and 5 sccm oxygen flow rates. However, additional  $Ti^{3+}$  and  $Ti^{4+}$  peaks are formed and become more apparent when the oxygen flow rate increases as indicated by an upward arrow in Figure 5.3a. When the flow rate is over than 25 sccm, titanium monoxide peaks lose intensity and start to disappear as indicated by a downward arrows in Figure 5.3a. On the other hand, titanium dioxide peaks become more sharp and stronger when the oxygen flow rate is over 25 sccm. Oxygen peak is formed at 530.1 eV binding energy for metal oxides. In addition to the main peak, surface hydroxylation can create an additional peak at around 531.5 eV. As shown in Figure 5.3b, oxygen peaks for TiO indicate that the formation of  $OH^-$  and  $H_2O$  are not observed in all oxygen flow rates [39, 40]. On the other hand, main peak position is changed between 530.2 to 529.9 eV at different deposition conditions. The observed shift in the XPS spectrum of  $TiO_x$  films depending on the oxygen content of the films is a common situation in oxygen containing compounds with different oxygen amounts, not only in  $TiO_x$  films but in most oxides, for example tin dioxide particles [41] and Al doped ZnO particles [42]. Although argon etching performed before XPS measurements can generate preferential etching of one of the elements in the compound, however we relate the observed shift in the XPS spectrum to the chemical environmental effects for each of the Ti ions in the films because argon etching was conducted on all of the substrates for equal durations and the observed peaks are consistent with the previous literature reports [43, 44].

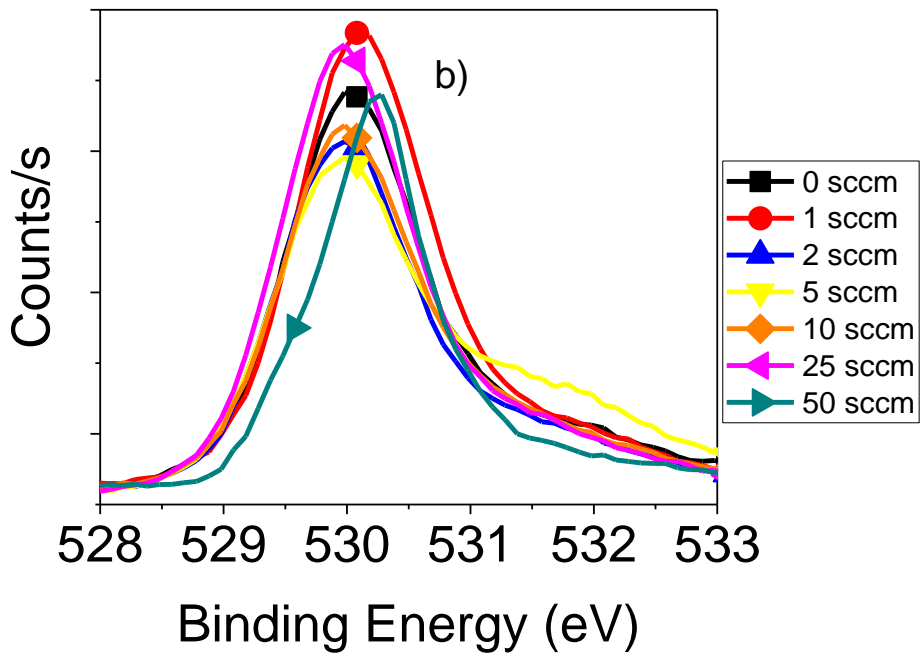
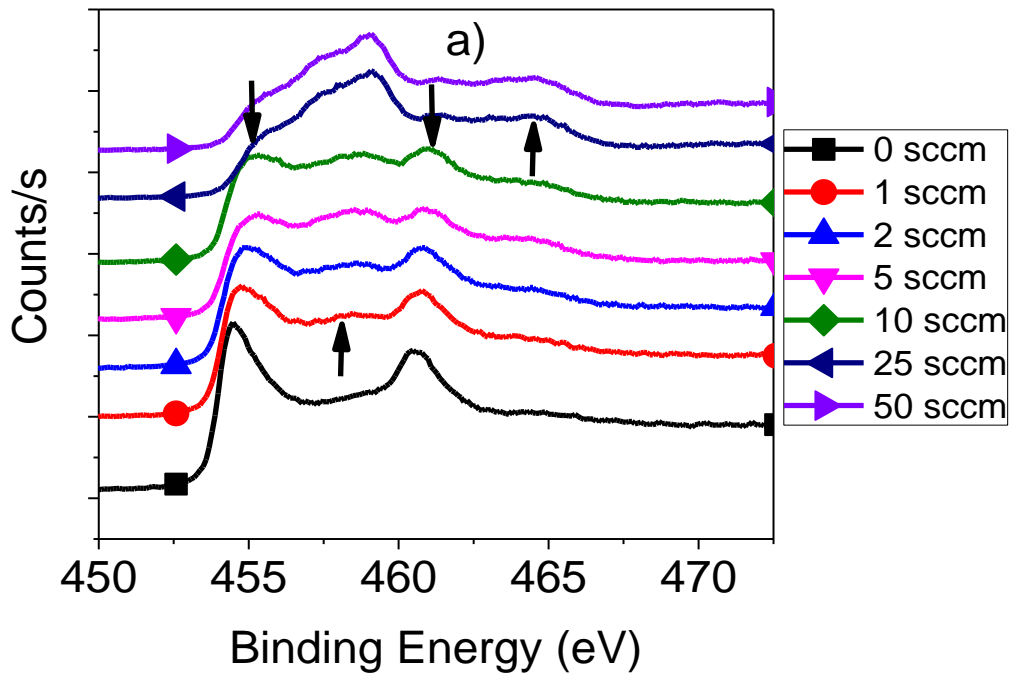


Figure 5.3. XPS analysis of TiO thin films for a) titanium and b) oxygen.

Titanium monoxide thin films were also investigated for the determination of their optical properties. Figure 5.4 shows the transmittance measurements of the titanium monoxide thin films. Due to the large difference in transmittance percentage, graphs are drawn in separate figures. Firstly transmission measurements were carried out. It was observed that there is no transparency for the samples deposited for 0 and 1 sccm oxygen flow rates and very low transparency is observed for oxygen flow rates of 2 to 10 sccm (Figure 5.4a). No transparency, which means highly absorbing nature, creates metallic color. This condition was also discussed in XRD section and is consistent with those results. When oxygen flow rate is over than 25 sccm, structure mostly transforms to titanium dioxide and interference fringes are formed in transmittance measurements (Figure 5.4b). This result matches well with XRD and XPS results. However, both of the samples have some absorption due to the presence of  $Ti^{+2}$  state in these thin films.

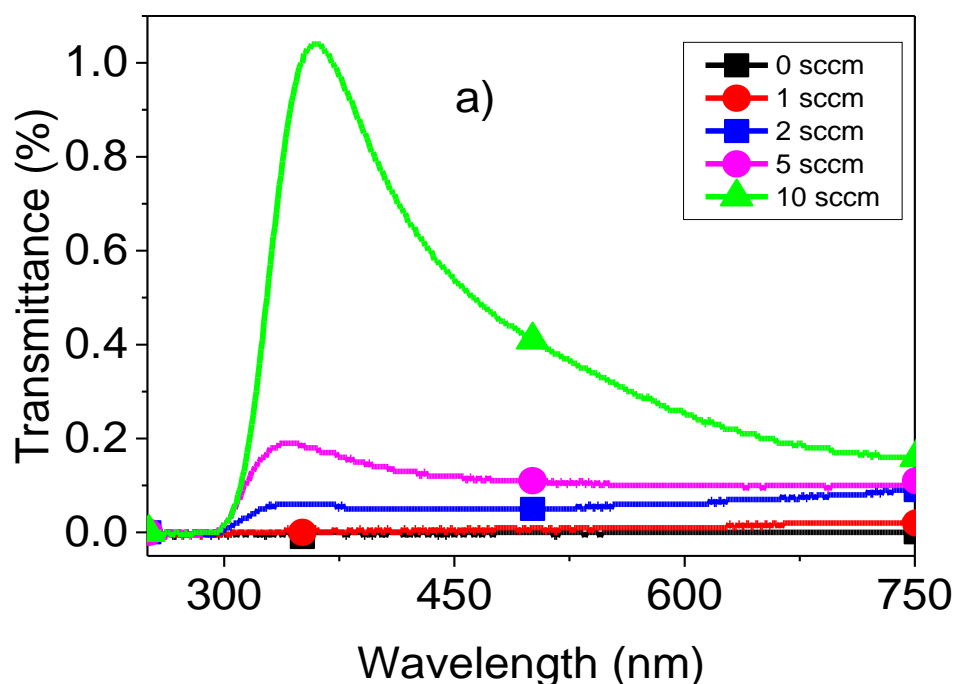


Figure 5.4. Transmission measurements of thin films deposited a) at 0, 1, 2, 5 and 10 and b) at 25 and 50 sccm oxygen flow rates.

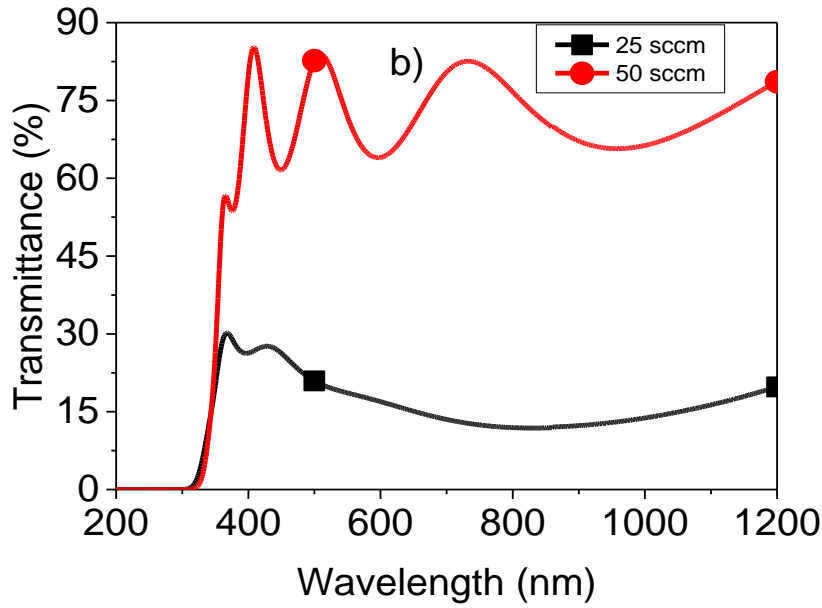


Figure 5.4 (Continued)

Both direct [31, 45, 46] and indirect band gap [9, 46] nature of titanium monoxide and titanium dioxide thin films can be observed in literature. The value of band gap is varying between 3.2-3.35 eV [46] for indirect and 3.6-3.8 eV [46] for direct band gap titanium dioxide thin films. Likewise for titanium monoxide thin films, direct band gap calculations yield 3.4 eV [33] and indirect band gap values are given as 2.9 eV [9]. In our study, calculations resulted in better fits when direct band gap is selected instead of indirect band gap, therefore, Tauc plots are drawn  $(\alpha h\nu)^2$  versus  $h\nu$  (Figure 5.5) and  $\alpha$  is calculated using Equation 5.1 where  $d$  is the physical thickness of the films and  $T$  defines the optical transmittance of thin films. Some of the studies in the literature emphasize the p-type conductivity of titanium monoxide where the value of band gap is strongly affected by the defect amounts and it shows a large range of variation [7]. Calculated values can be seen in Table 5.1 and they are in the same vicinity with the results which were published in literature [3, 9, 33].

$$\alpha = \frac{1}{d} \ln\left(\frac{1}{T}\right) \quad \text{Eq. [5.1]}$$

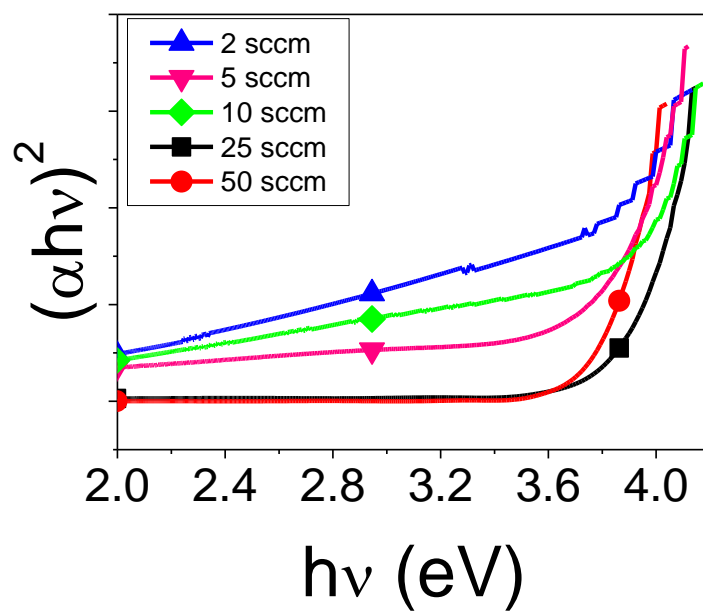


Figure 5.5. The variation of  $(h\nu\alpha)^2$  as a function of  $h\nu$  for titanium monoxide thin films deposited at 2, 5, 10, 25 and 50 sccm oxygen flow rates.

Table 5.1. Band gap values of titanium monoxide thin films.

Oxygen Flow Rate (sccm)	Band Gap (eV)
0	3.30
1	3.00
2	3.60
5	3.70
10	3.75
25	3.80
50	3.80

For the thin films showing no transparency, reflectance measurements are carried out to calculate the band gap of these thin films. Due to the absorbing nature of these films, their band gaps are calculated using Kubelka-Munk method. In this method,  $(f(R)*hv)^2$  are drawn against  $hv$ . Kubelka-Munk function ( $f(R)$ ), where  $R$  denotes reflection of the films, are calculated using Equation 5.2. Titanium oxide thin films are again accepted as direct band gap. Figure 5.6 demonstrates both reflectance and Kubelka-Munk function graphs. Linear region is extrapolated and intersection point with x axis gives the band gap value [45]. In the literature, TiO is reported to have 2.9 eV band gap value [9]. Band gap shows a decrease firstly when the oxygen flow rate increases for these absorbing thin films as given in Table 5.1. Higher band gap value obtained when deposition is carried without additional oxygen flow compared to the 1sccm oxygen flow rate condition. This decrease is due to the Moss-Burstein effect. For the heavily defective semiconductors, fermi level goes into valence band and band gap becomes the difference between Fermi energy level and conduction band minimum instead of valence band maximum and conduction band minimum. Therefore, addition of small oxygen decreases the defects in the films which is also consistent with Hall effect measurements yielding lower conductivity [47]. Small amount of oxygen doping yields similar results with literature regarding the band gap. The increase in the band gap values from 1 to 50 sccm oxygen flow rates is likely due to the presence of additional  $Ti^{+3}$  and  $Ti^{+4}$  states in the films as can be seen from XRD and XPS analysis. At 1 sccm oxygen flow rate, structure exhibits most likely TiO phase and band gap value is close to the actual band gap value of TiO. However, further increase in the oxygen flow rate results in a structure which is a mixture of TiO,  $TiO_2$  or compounds containing  $Ti^{+3}$  like  $Ti_2O_3$ . At high oxygen flow rates, structure converts to mostly  $TiO_2$  and calculated band gaps are around the band gap of pure  $TiO_2$ . Optical characterizations are consistent with the results of XRD and XPS analysis and confirmed that TiO structure is obtained at low oxygen flow rates and for oxygen flow rates over 25 sccm, mostly  $TiO_2$  films are deposited under the conditions used in this work.

$$F(R) = \frac{(1-R)^2}{2R} \quad \text{Eq. [5.2]}$$

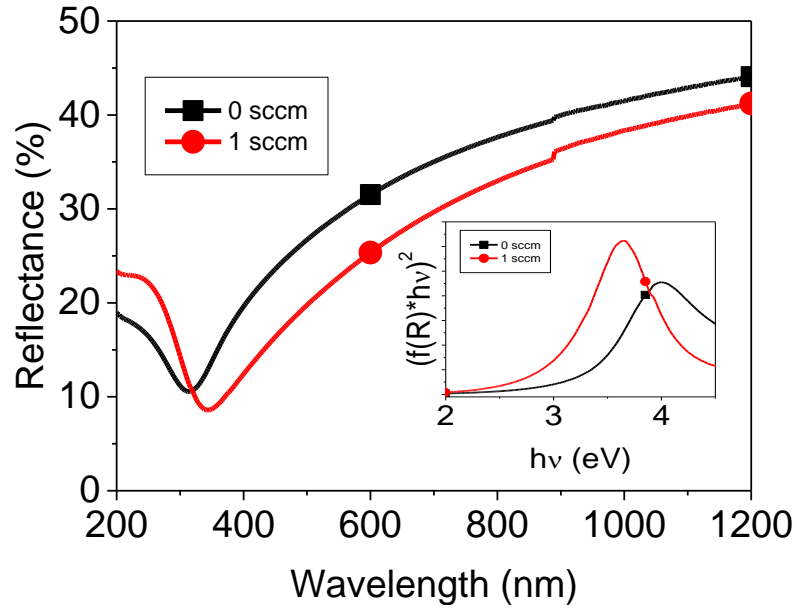


Figure 5.6. Reflectance and Kubelka-Munk function analysis (in the inset) of TiO thin films deposited at 0 and 1 sccm oxygen flow rates.

Electrical properties of titanium monoxide thin films were analyzed using Hall Effect measurements and the results are summarized in Table 5.2. It was seen that carrier type changes from p to n when the oxygen flow rate is over 25 sccm. Intrinsic TiO is a p-type material which preserves this behavior even  $Ti^{2+}$  based structure is doped with  $Ti^{3+}$  or  $Ti^{4+}$ . When structure is transformed to titanium dioxide, charge carriers originate from oxygen vacancies which result in n-type semiconducting behavior [7]. Change in defect source from oxygen vacancy to doped  $Ti^{3+}$  or  $Ti^{4+}$  ions into  $Ti^{2+}$  based crystal increases sheet carrier density of TiO films and conductivity shows an increase with decreasing amount of oxygen addition to deposition chamber. Also, with increase in oxygen flow rate, structure transforms to a more stable phase with a low amount of defect concentration. Additionally, in the study of Fan et al., increase in

resistivity with increase in oxygen amount is correlated with enhancing of disordering of atoms and carrier localization [36]. Lowest resistivity, which is  $1.7 \times 10^{-4}$  ohm.cm, is obtained when deposition is carried out under oxygen free condition. Mobility of the films remains almost the same when carrier type is maintained as p-type. However, when the carrier type changes to n-type, mobility values start to increase. It firstly rises to  $0.9 \text{ cm}^2/(\text{Vs})$  for 25 sccm oxygen flow rate, then mobility value increases to  $34.3 \text{ cm}^2/(\text{Vs})$  for 50 sccm oxygen flow rate condition. However, a sharp decrease in sheet carrier density for these n-type thin films causes almost 104 times increase in electrical resistivity.

Table 5.2. Hall Effect measurements of titanium oxide thin films for different oxygen flow rates.

Oxygen Amount (sccm)	Carrier Type	Sheet Carrier Density [ $1/\text{cm}^2$ ]	Hall Mobility [ $\text{cm}^2/(\text{Vs})$ ]	Resistivity (ohm.cm)
0	p-type	$3.6 \times 10^{18}$	0.4	$1.7 \times 10^{-4}$
1	p-type	$1.5 \times 10^{18}$	0.2	$6.9 \times 10^{-4}$
2	p-type	$6.3 \times 10^{17}$	0.3	$1.1 \times 10^{-3}$
5	p-type	$4.8 \times 10^{17}$	0.3	$1.6 \times 10^{-3}$
10	p-type	$4.3 \times 10^{17}$	0.2	$2.7 \times 10^{-3}$
25	n-type	$1.9 \times 10^{14}$	0.9	$1.2 \times 10^0$
50	n-type	$2.7 \times 10^8$	34.3	$2.3 \times 10^4$

The Fermi energy levels and valence band maxima of thin films were obtained from UPS measurements. Figure 5.7. gives the UPS spectra of titanium monoxide thin films deposited at 0, 1, and 10 sccm oxygen flow rates. Electronic band structure of the

deposited films was evaluated by using the previously established standard procedures [48]. Fermi energy levels are calculated by the extraction of cut-off energy positions from He I emission (21.21 eV), which also represents the work function of the material. The difference between the Fermi energy level and valence band maximum is found from the onset energy which can be seen in Figure 5.7a. By subtracting this value from the Fermi level, top of the valence band or, in other terms, ionization potential of the films was calculated. Minima of conduction band edge positions or the electron affinity values are found by adding the optical band gap values to the valence band maxima energies, where calculated optical band gaps are given in Table 5.1. Band positions of titanium oxide thin films are represented in Figure 5.8 for different deposition conditions. For sample deposited at 0 sccm oxygen flow rate, onset point is obtained at a lower value than 0 eV binding energy which shows that structure is in degenerated semiconductor nature. This situation is also consistent with the decrease in band gap when 1 sccm oxygen flow rate is used compared to no oxygen flow. When the deposition is performed without oxygen, fermi energy level is found to be -3.8 eV. However, fermi energy level shifts to -4.2 eV and -4.3 eV when the depositions are carried out at 1 and 10 sccm oxygen flow rates. Fermi energy level is located at high density of states which explains the metallic character of TiO [31]. It is seen that p-type character of the films is confirmed because Fermi levels are close to the valence band and consistent with the Hall effect results. The energy difference between the Fermi energy and the top of the valence band is around 0.1 eV which explains the high conductivity and the carrier concentration of the films where thermal energy is sufficient enough to excite holes and increase the hole concentration in the films. This energy difference is increased with the oxygen flow rate and carrier concentration decreases in the same trend and conductivity also decreases as shown by the Hall effect studies. This tunability of the electrical properties of TiO thin films is advantageous for most electronic applications and can be tailored upon the requirement of each specific application in optoelectronic devices.

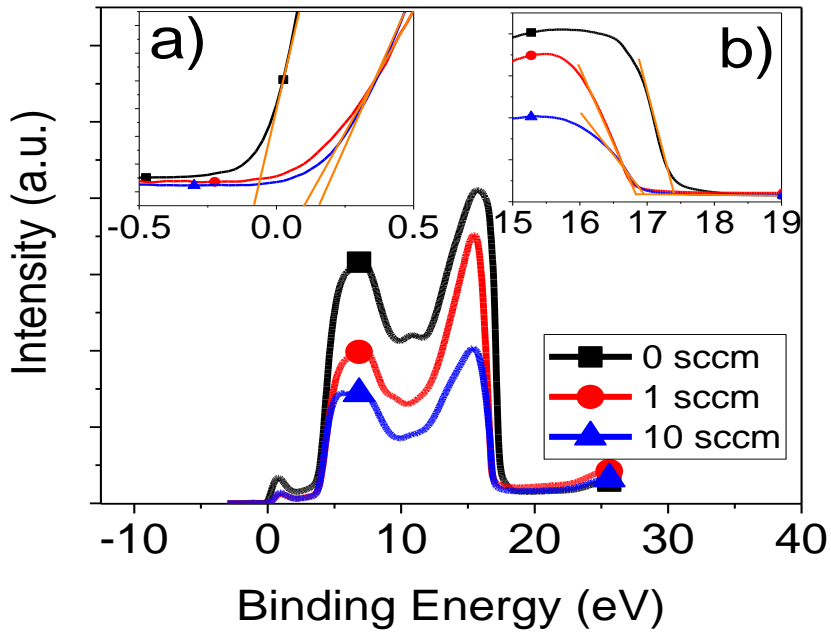


Figure 5.7. UPS spectra of titanium monoxide thin films deposited at 0, 1, and 10 sccm oxygen flow rates a) onset b) cut-off.

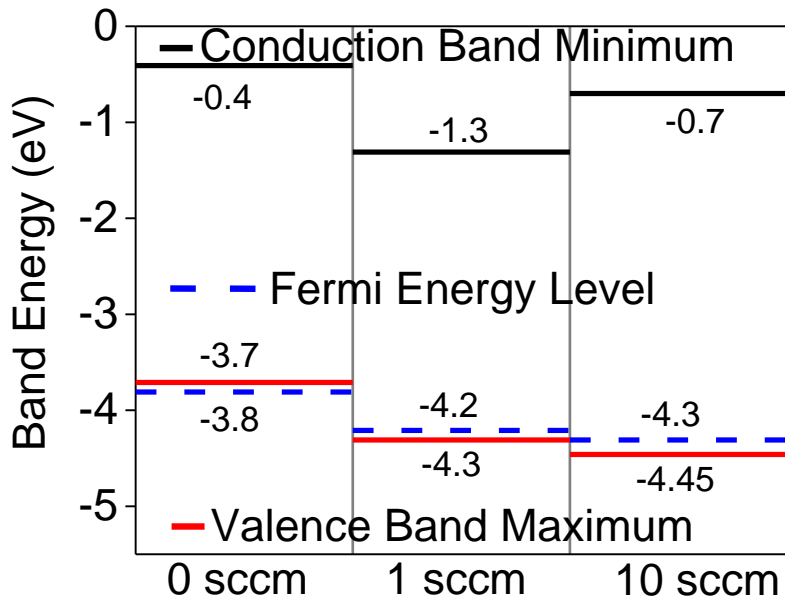


Figure 5.8. Energy band levels of titanium monoxide thin films deposited at 0, 1, and 10 sccm oxygen flow rates.

### **5.3. Conclusion**

In this work, TiO thin films were grown on glass substrates by e-beam evaporation technique under oxygen atmosphere at low temperatures. Films exhibit dense and homogeneous structure and well adhered to the substrate as confirmed by SEM analysis. According to XRD analysis, by adjusting the flow rate of oxygen, it is possible to deposit TiO films with different stoichiometry and as a result, films possess different optical and electrical properties. Deposited TiO films have high carrier concentration and high electrical conductivity and possess p-type characteristic. Such highly conductive p-type films are desirable for most optoelectronic applications and devices like MEMS and other integrated circuits. Properties of the films like mobility, carrier concentration, resistivity and optical transmission can easily be tuned over a wide range and can be employed in device engineering applications. Low temperature processability of the e-beam evaporated films makes it an excellent choice for many device applications, especially flexible electronics.



## REFERENCES

- [1] O. Banakh, P. Schmid, R. Sanjines, F. Levy, Electrical and optical properties of  $\text{TiO}_x$  thin films deposited by reactive magnetron sputtering, *Surface and Coatings Technology*, 151 (2002) 272-275.
- [2] A. Bally, P. Hones, R. Sanjinés, P. Schmid, F. Lévy, Mechanical and electrical properties of fcc  $\text{TiO}_{1+x}$  thin films prepared by rf reactive sputtering, *Surface and Coatings Technology*, 108 (1998) 166-170.
- [3] T.-T.-N. Nguyen, Y.-H. Chen, J.-L. He, Preparation of inkjet-printed titanium monoxide as p-type absorber layer for photovoltaic purposes, *Thin Solid Films*, 572 (2014) 8-14.
- [4] M. Kostenko, A. Lukoyanov, V. Zhukov, A. Rempel, Vacancies in ordered and disordered titanium monoxide: Mechanism of b1 structure stabilization, *Journal of Solid State Chemistry*, 204 (2013) 146-152.
- [5] R. A. Zárate, V. M. Fuenzalida, Titanium monoxide ultra-thin coatings evaporated onto polycrystalline copper films, *Vacuum*, 76 (2004) 13-17.
- [6] J. Yao, J. Shao, H. He, Z. Fan, Optical and electrical properties of  $\text{TiO}_x$  thin films deposited by electron beam evaporation, *Vacuum*, 81 (2007) 1023-1028.
- [7] W.C. Peng, Y.H. Chen, J.Y. Chen, J.L. He, D.S. Wu, High power impulse magnetron sputtered p-type  $\gamma$ -titanium monoxide films: Effects of substrate bias and post-annealing on microstructure characteristics and optoelectrical properties, *Materials Science in Semiconductor Processing*, 61 (2017) 85-92.
- [8] Z. G. Li, S. Miyake, M. Makino, Y. X. Wu, Microstructure and properties of nanocrystalline titanium monoxide films synthesized by inductively coupled plasma assisted reactive direct current magnetron sputtering, *Applied Surface Science*, 255 (2008) 2370-2374.
- [9] E. M. Assim, Optical constants of titanium monoxide  $\text{TiO}$  thin films, *Journal of Alloys and Compounds*, 465 (2008) 1-7.
- [10] S. Amano, D. Bogdanovski, H. Yamane, M. Terauchi, R. Dronskowski,  $\epsilon$ -tio, a novel stable polymorph of titanium monoxide, *Angewandte Chemie International Edition*, 55 (2016) 1652-1657.

- [11] M. G. Kostenko, A. V. Lukoyanov, A. A. Rempel, Electronic structure and stability of nonstoichiometric titanium monoxide  $\text{TiO}_y$  with structural vacancies in one of the sublattices, *Physics of the Solid State*, 55 (2013) 2108-2115.
- [12] A. A. Valeeva, A. A. Rempel, W. Sprengel, H. E. Schaefer, Vacancies on the Ti sublattice in titanium monoxide  $\text{TiO}_y$  studied using positron annihilation techniques, *Physical Review B*, 75 (2007)
- [13] W. Ouyang, F. Teng, X. Fang, High performance  $\text{BiOCl}$  nanosheets/ $\text{TiO}_2$  nanotube arrays heterojunction uv photodetector: The influences of self-induced inner electric fields in the  $\text{BiOCl}$  nanosheets, *Advanced Functional Materials*, 28 (2018) 1707178.
- [14] W.-C. Peng, Y.-C. Chen, J.-L. He, S.-L. Ou, R.-H. Horng, D.-S. Wu, Tunability of p- and n-channel  $\text{TiO}_x$  thin film transistors, *Scientific Reports*, 8 (2018) 9255.
- [15] L. Zheng, P. Yu, K. Hu, F. Teng, H. Chen, X. Fang, Scalable-production, self-powered  $\text{TiO}_2$  nanowell–organic hybrid uv photodetectors with tunable performances, *ACS Applied Materials & Interfaces*, 8 (2016) 33924-33932.
- [16] S. Han, Y.-C. Pu, L. Zheng, J. Z. Zhang, X. Fang, Shell-thickness dependent electron transfer and relaxation in type-ii core–shell  $\text{CdS}/\text{TiO}_2$  structures with optimized photoelectrochemical performance, *Journal of Materials Chemistry A*, 3 (2015) 22627-22635.
- [17] P. Yu, Z. Zhang, L. Zheng, F. Teng, L. Hu, X. Fang, A novel sustainable flour derived hierarchical nitrogen-doped porous carbon/polyaniline electrode for advanced asymmetric supercapacitors, *Advanced Energy Materials*, 6 (2016) 1601111.
- [18] L. Zheng, S. Han, H. Liu, P. Yu, X. Fang, Hierarchical  $\text{MoS}_2$  nanosheet@ $\text{TiO}_2$  nanotube array composites with enhanced photocatalytic and photocurrent performances, *Small*, 12 (2016) 1527-1536.
- [19] M.L. Tsai, M.Y. Li, J. R. D. Retamal, K.T. Lam, Y.C. Lin, K. Suenaga, L.J. Chen, G. Liang, L.J. Li, J.H. He, Single atomically sharp lateral monolayer p-n heterojunction solar cells with extraordinarily high power conversion efficiency, *Advanced Materials*, 29 (2017) 1701168.
- [20] S.-F. Leung, K.-T. Ho, P.-K. Kung, V. K. S. Hsiao, H. N. Alshareef, Z. L. Wang, J.-H. He, A self-powered and flexible organometallic halide perovskite photodetector with very high detectivity, *Advanced Materials*, 30 (2018) 1704611.

- [21] C.P. Lee, K.Y. Lai, C.A. Lin, C.T. Li, K.C. Ho, C.I. Wu, S.P. Lau, J.H. He, A paper-based electrode using a graphene dot/pedot:Pss composite for flexible solar cells, *Nano Energy*, 36 (2017) 260-267.
- [22] K.T. Ho, S.F. Leung, T.Y. Li, P. Maity, B. Cheng, H.C. Fu, O. F. Mohammed, J.-H. He, 2d layered perovskites: Surface effect on 2d hybrid perovskite crystals: Perovskites using an ethanolamine organic layer as an example, *Advanced Materials*, 30 (2018) 1870351.
- [23] A. R. Head, N. Johansson, Y. Niu, O. Snezhkova, S. Chaudhary, J. Schnadt, H. Bluhm, C. Chen, J. Avila, M.-C. Asensio, In situ characterization of the deposition of anatase TiO<sub>2</sub> on rutile TiO<sub>2</sub> (110), *Journal of Vacuum Science & Technology A*, 36 (2018) 02D405.
- [24] A. A. Valeeva, S. Z. Nazarova, A. A. Rempel, Influence of particle size, stoichiometry, and degree of long-range order on magnetic susceptibility of titanium monoxide, *Physics of the Solid State*, 58 (2016) 771-778.
- [25] B. Pabón, J. Beltrán, G. Sánchez-Santolino, I. Palacio, J. López-Sánchez, J. Rubio-Zuazo, J. Rojo, P. Ferrer, A. Mascaraque, M. Muñoz, Formation of titanium monoxide (001) single-crystalline thin film induced by ion bombardment of titanium dioxide (110), *Nature Communications*, 6 (2015) 6147.
- [26] H. Iwasaki, N. F. Bright, The stability of the polymorphs of titanium monoxide, *Journal of the Less Common Metals*, 21 (1970) 353-363.
- [27] Y. M. Wu, R. M. Nix, Growth of TiO<sub>x</sub> overlayers by chemical vapour deposition on a single-crystal copper substrate, *Journal of Materials Chemistry*, 4 (1994) 1403-1407.
- [28] T. Leichtweiss, R. A. Henning, J. Koettgen, R. M. TiO<sub>x</sub>. Schmidt, B. Holländer, M. Martin, M. Wuttig, J. Janek, Amorphous and highly nonstoichiometric titania (TiO<sub>x</sub>) thin films close to metal-like conductivity, *Journal of Materials Chemistry A*, 2 (2014) 6631-6640.
- [29] G. S. Chen, C. C. Lee, H. Niu, W. Huang, R. Jann, T. Schütte, Sputter deposition of titanium monoxide and dioxide thin films with controlled properties using optical emission spectroscopy, *Thin Solid Films*, 516 (2008) 8473-8478.
- [30] K. Grigorov, G. Grigorov, L. Drajeva, D. Bouchier, R. Sporcken, R. Caudano, Synthesis and characterization of conductive titanium monoxide films. Diffusion of silicon in titanium monoxide films, *Vacuum*, 51 (1998) 153-155.

- [31] T. Maeda, Y. Kobayashi, K. Kishi, Growth of ultra-thin titanium oxide on cu(100), fe/cu(100) and ordered ultra-thin iron oxide studied by low-energy electron diffraction and x-ray photoelectron spectroscopy, *Surface Science*, 436 (1999) 249-258.
- [32] V. M. Fuenzalida, C. R. Grahmann, C. Herrera, R. A. Zárate, C. Avila, M. E. Pilleux, Room-temperature uhv-deposited titanium monoxide films on oxidized polycrystalline copper, *MRS Proceedings*, 672 (2011)
- [33] M. Zribi, M. Kanzari, B. Rezig, Structural, morphological and optical properties of thermal annealed tio thin films, *Thin Solid Films*, 516 (2008) 1476-1479.
- [34] R. Wasielewski, P. Mazur, M. Grodzicki, A. Ciszewski, TiO thin films on gan(0001), *physica status solidi (b)*, 252 (2015) 1001-1005.
- [35] A. Pazidis, R. Reineke-Koch, Magnetron sputtered tiox layers: Structural, electrical, optical and thermochromic aspects, *Thin Solid Films*, 649 (2018) 43-50.
- [36] Y. J. Fan, C. Ma, T. Y. Wang, C. Zhang, Q. L. Chen, X. Liu, Z. Q. Wang, Q. Li, Y. W. Yin, X. G. Li, Quantum superconductor-insulator transition in titanium monoxide thin films with a wide range of oxygen contents, *Physical Review B*, 98 (2018) 064501.
- [37] R. Villarroel, R. Espinoza-González, J. Lisoni, G. González-Moraga, Influence of the oxygen consumption on the crystalline structure of titanium oxides thin films prepared by dc reactive magnetron sputtering, *Vacuum*, 154 (2018) 52-57.
- [38] K. S. Sree Harsha, Chapter 9 - nucleation and growth of films, in: K.S. Sree Harsha (Ed.) *Principles of vapor deposition of thin films*, Elsevier, Oxford, (2006), 685-829.
- [39] S. Bartkowski, M. Neumann, E. Kurmaev, V. Fedorenko, S. Shamin, V. Cherkashenko, S. Nemnonov, A. Winiarski, D. Rubie, Electronic structure of titanium monoxide, *Physical Review B*, 56 (1997) 10656.
- [40] V. V. Atuchin, V. G. Kesler, N. V. Pervukhina, Z. Zhang, Ti 2p and o 1s core levels and chemical bonding in titanium-bearing oxides, *Journal of electron spectroscopy and related phenomena*, 152 (2006) 18-24.
- [41] F. Zhang, Y. Lian, M. Gu, J. Yu, T. B. Tang, J. Sun, W. Zhang, Nanocrystalline tin oxide: Possible origin of its weak ferromagnetism deduced from nuclear magnetic resonance and x-ray photoelectron spectroscopies, *Physics Letters A*, 380 (2016) 3138-3143.

- [42] A. Kelchtermans, K. Elen, K. Schellens, B. Conings, H. Damm, H.-G. Boyen, J. D'Haen, P. Adriaensens, A. Hardy, M. K. Van Bael, Relation between synthesis conditions, dopant position and charge carriers in aluminium-doped ZnO nanoparticles, *RSC Advances*, 3 (2013) 15254-15262.
- [43] Y. Wang, H. Sun, S. Tan, H. Feng, Z. Cheng, J. Zhao, A. Zhao, B. Wang, Y. Luo, J. Yang, J. G. Hou, Role of point defects on the reactivity of reconstructed anatase titanium dioxide (001) surface, *Nature Communications*, 4 (2013) 2214.
- [44] B. Bharti, S. Kumar, H.-N. Lee, R. Kumar, Formation of oxygen vacancies and Ti<sup>3+</sup> state in TiO<sub>2</sub> thin film and enhanced optical properties by air plasma treatment, *Scientific Reports*, 6 (2016) 32355.
- [45] Z. Chen, W. Zhong, Z. Liang, W. Li, G. He, Y. Wang, W. Li, Y. Xie, Q. He, Photocatalytic activity enhancement of anatase TiO<sub>2</sub> by using TiO, *Journal of Nanomaterials*, 2014 (2014)
- [46] Z. Wang, U. Helmersson, P.-O. Käll, Optical properties of anatase TiO<sub>2</sub> thin films prepared by aqueous sol–gel process at low temperature, *Thin Solid Films*, 405 (2002) 50-54.
- [47] N. R. Yogamalar, A. C. Bose, Burstein–moss shift and room temperature near-band-edge luminescence in lithium-doped zinc oxide, *Applied Physics A*, 103 (2011) 33-42.
- [48] D. Cahen, A. Kahn, Electron energetics at surfaces and interfaces: Concepts and experiments, *Advanced Materials*, 15 (2003) 271-277.



## CHAPTER 6

### **ELECTRON BEAM EVAPORATED NiO AND TiO HOLE TRANSPORT LAYERS IN n-i-p CONFIGURED PEROVSKITE SOLAR CELL**

Perovskite absorber layers are quite unique materials due to their extraordinary properties. Addition to absorbing nature, perovskite layer has the capability for electron and hole transfer. Therefore, perovskite solar cells can be produced without using hole transport or electron transport layers, if the efficiency is not the primary factor. Spiro-OMeOTAD is crucial to obtain high efficiency perovskite solar cells. Up to now, there is no competitive hole transport layer material compared to spiro-OMeOTAD regarding the cell performance. However, spiro-OMeOTAD is a quite expensive material and due to its organic nature, stability is always questionable. This condition is ended up with studies on alternative oxide materials for hole transport layer (HTL) [1, 2].

Copper based inorganic HTL's are the first studied materials such as CuI and CuSCN due to their wide band gap, good transparency and good conductivity nature. These materials can be deposited using solution process techniques under low temperature conditions [1]. Also, oxide materials are widely used in the production of perovskite solar cells. NiO [3], CuO [4], V<sub>2</sub>O<sub>5</sub> [5] and MoO<sub>3</sub> [6] are the examples of some of the oxides used as HTL: these materials have primarily matched band edges and also they have good conductivity, good transparency and tunable band positions. There is limited study in the literature for the deposition of oxide HTL's on top of perovskite layer due to the high temperature annealing requirement. Perovskite layer decomposes at high temperatures. Therefore, the first choice is the use of these materials in inverted configuration [7, 8]. However, PCBM is the material used for electron transport layer

in inverted configuration which means the inclusion of one organic component with high cost. Another drawback is the poor quality perovskite film formation on top of HTL in inverted designs [2, 9].

Physical vapor deposition methods are low temperature processes and also there is no need for post thermal treatment for crystallization of thin films. From this point of view, study aims to produce oxide thin films for HTL in normal architecture (n-i-p architecture) which is the deposition of HTL on top of perovskite absorber. Addition to low temperature nature, electronic band positions can easily be tuned for the optimization of parameters in e-beam evaporation. Therefore, well matched band optimization can be supplied. Additionally, electron beam evaporation is a less energetic deposition method compared to sputtering. Also, this method provides line of sight deposition; there is no risk to fill any undeposited regions in perovskite layer like chemical vapor deposition. As a final advantage, it supplies better uniformity and better surface coverage.

Optimized deposition condition for  $\text{TiO}_2$  compact layer firstly sustained in this study followed by the deposition of  $\text{NiO}_x$  and  $\text{TiO}_x$  thin films on top of perovskite layer due to the advantages of e-beam deposition technique.  $\text{NiO}_x$  thin films were deposited in different layer thicknesses, oxygen flow rates and deposition temperatures. Similarly,  $\text{TiO}_x$  HTL's were produced in different coating thicknesses and oxygen flow rates. Main purpose of this study is to create better deposition conditions for  $\text{NiO}_x$  and  $\text{TiO}_x$  HTL for efficient solar cells.

## **6.1. Experimental Studies**

In this study, perovskite solar cells were produced in mesoporous n-i-p configuration. Cells are created on top of FTO coated glasses which has 10 ohm/sq sheet resistance. Firstly, some regions of the FTO layer were etched to minimize the risk of short circuit between the electrodes. Etching was performed using zinc powder and 0.1 M HCl

followed by the cleaning of the substrates ultrasonically using deionized water, acetone and isopropanol, sequentially. TiO<sub>2</sub> thin films were deposited by electron beam evaporation technique as the compact layer. Depositions were performed in Tecport physical vapor deposition system. Ti<sub>3</sub>O<sub>5</sub> precursor material supplied by Materion was firstly pre-melted in a copper crucible. Previous to the deposition, surface of the substrate was etched using plasma source. When the base pressure is lower than 10<sup>-5</sup> torr, etching was done using 20 sccm argon flow at 70 V bias voltage for 2 min. When the base pressure becomes lower than 8x10<sup>-6</sup> torr, deposition process starts. Depositions were performed with plasma assistance using 115 V bias voltage and they were carried out at 80°C and 2Å/s deposition rate. To prepare a good compact layer, TiO<sub>2</sub> thin films were firstly deposited on top of Schott Bk7 glass at 350 nm coating thickness. During the deposition process, oxygen was introduced to the vacuum chamber at different flow rates of 5, 15, 25 sccm and one of the film was deposited without any oxygen addition. Produced films were heat treated using the same annealing conditions which were used for the mesoporous layer. Optimum deposition conditions were determined for TiO<sub>2</sub> thin film and they were fixed in the production of this compact layer. Compact layer thickness was fixed to 50 nm as an optimized value. On top of the compact layer, mesoporous TiO<sub>2</sub> was deposited using spin coating technique. The solution used for the spin coating was produced by the dilution of Dyesol NRT-18 titania commercial paste with ethanol in 1:3 ratio. This solution was then rotated at 2000 rpm for 5 s which produces 250 nm coating thickness. After the coating process, thin films were annealed at 500°C for 2 h and these layers were dipped into TiCl<sub>4</sub> solution of 0.2 mmol concentration at 90°C. Following this process, a second annealing was conducted again at 500°C for 2 h. Perovskite absorber layer is the next layer for the cell production which is obtained using adduct method. In this method, deposition solution was prepared by mixing of PbI<sub>2</sub>, CH<sub>3</sub>NH<sub>3</sub>I (MAI) and N,N-dimethyl sulfoxide (DMSO) into 40% weight of N,N-dimethylformamide (DMF). Prepared solution was deposited using spin coating technique at 4000 rpm for 30 s. Diethyl ether was dropped on the spinning substrate at the fifth second of the rotation. Diethyl ether treatment was applied to wash out

DMF solvent. This treatment provides better solvent evaporation which yields good surface coverage of perovskite layer. Produced films were heat treated at 100°C for 5 min.

HTL's were deposited using electron beam deposition using the same vacuum system. NiO<sub>x</sub> and TiO<sub>x</sub> were deposited in different deposition conditions which are given in Table 6.1. NiO and TiO precursors were used as starting materials and they were purchased from Materion. While TiO was used in premelted condition, NiO was deposited directly from its chunky form. The characterizations of these single layer depositions of TiO and NiO thin films were evaluated in the previous two chapters (Chapter 4 and 5). Deposition rates of these two materials were chosen as 2 Å/s. As a final process, back contact gold layer was deposited on HTLs. Gold deposition was carried out by sputtering of gold target. Nanovak sputtering system was used in this process. Sputtering was performed at room temperature with DC power supply at corresponding voltage to provide 1 Å/s deposition rate.

Optical characterization of single layer deposited compact TiO<sub>2</sub> thin films were conducted using Perkin Elmer Lambda 950 UV-VIS-near-IR spectrophotometer. The resulting transmittance graphs were used to calculate refractive index. "Optilayer" optical thin film calculation software was used in the mathematical calculation of refractive index. Single layers were characterized morphologically and structurally using FEI, Nova NanoSEM 430 Scanning Electron Microscopy (SEM), PANalytical X-ray diffractometer (XRD) using Cu K $\alpha$  radiation (1.54 Å) at 3° grazing incidence and Thermo K-Alpha X-ray photoelectron spectroscopy (XPS). Perovskite layer was also characterized using XRD and SEM techniques. Finally produced cells were subjected to current-voltage analyses using Newport solar simulator 67005 at AM 1.5 conditions using Yokogawa GS610 source measure unit.

Table 6.1. Deposition conditions for NiO and TiO HTLs in the perovskite solar cell production.

	HTM	Deposition Temperature (°C)	Oxygen Flow Rate (sccm)	Thickness (nm)		
PSC1	NiO	80	0	50		
PSC2			10			
PSC3			25			
PSC4			50			
PSC5		30	25	10		
PSC6		170				
PSC7		80			25	25
PSC8						75
PSC9						100
PSC10						
PSC11	TiO	80	1	10		
PSC12			1	50		
PSC13			1	75		
PSC14			1	100		
PSC15			0	25		
PSC16			1			
PSC17			2			
PSC18			5			
PSC19			10			

## 6.2. Results and Discussions

### 6.2.1. Characterization of Single Layer TiO<sub>2</sub> Thin Films

Deposited and annealed TiO<sub>2</sub> thin films were characterized structurally and optically to determine suitable deposition conditions for TiO<sub>2</sub> compact layer. Firstly, produced thin films were investigated in their morphology and film structure using scanning electron microscope. Figure 6.1 shows both cross-sectional and surface images of compact layer. It is seen that thin films were deposited in good adherence to the substrate. Films are formed without any defective regions between film and the substrate. Also, surface of the film is rather smooth and surface is free from cracks.

Compact layer should be defect free for an efficient electron transfer. Any defective site can result with recombination which dramatically decreases the cell performance.

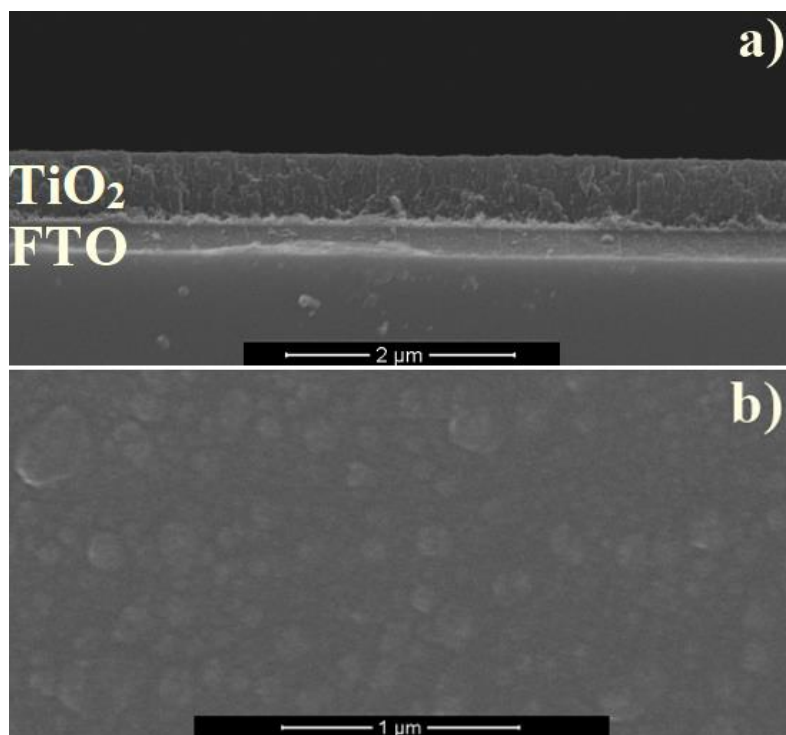


Figure 6.1. a) Cross-sectional image of TiO<sub>2</sub> compact layer b) Surface of the compact layer.

XRD measurements were carried out to understand the crystal structure of the TiO<sub>2</sub> compact layers. Measurements were conducted using both as deposited and annealed thin films. Measurements were performed at 3° grazing angle to annihilate the effect of the substrate. It is observed that crystallinity is not formed without heat treatment and all the coating layers have amorphous structure. Figure 6.2 shows the x-ray diffraction patterns of the as deposited and annealed thin films. As deposited TiO<sub>2</sub> thin film is corresponding to the condition of having no oxygen flow. After heat treatment, crystallinity is formed for all the conditions where oxygen flow is employed. There are two main phases of titanium dioxide: anatase and rutile. Their corresponding JCPDS card numbers are JCPDS card no: 21-1272 for the anatase phase and JCPDS

card no: 82-0514 for the rutile phase. Green labels on the horizontal axis in figure 6.2 show the diffraction positions for anatase (A) phase. Observed peak positions correspond to 25.3° to A (101), 36.9° to A(103), 37.9° to A(004), 48.1° to A(200) 53.8° to A(105), 55.3° to A(211), 64.2° to A(204), 69.0° to A(116), 70.2° to A(220) and 75.4° to A(215). Dominant orientation is (101) for all deposition conditions. At higher oxygen flow rates, intensities of the peaks become stronger. The number of the observed peaks is also lowered with higher flow rates.

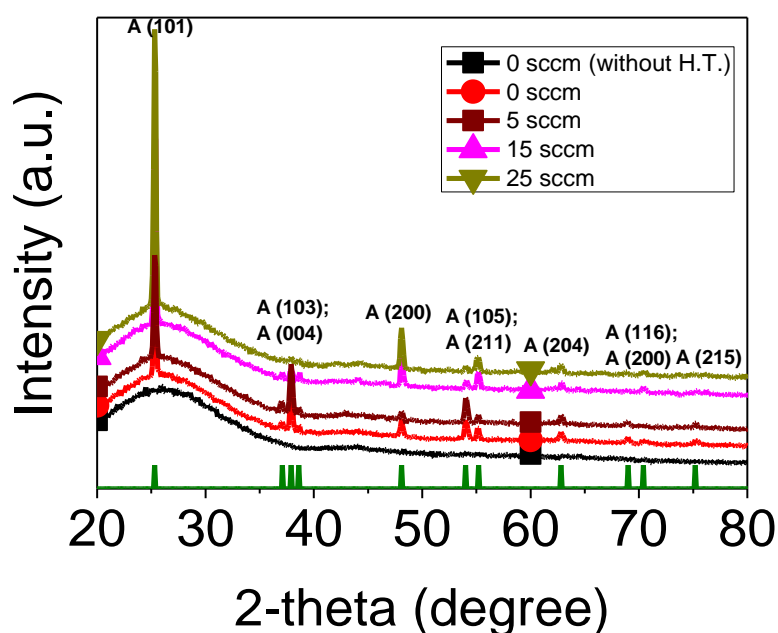


Figure 6.2. XRD patterns of TiO<sub>2</sub> compact layer for as deposited condition (0 sccm oxygen flow) and heat treated conditions using different oxygen flow rates as 0 sccm, 5 sccm, 15 sccm and 25 sccm.

As a final structural analysis, XPS measurements were carried out to understand the stoichiometry of the produced films. In other words, XPS can give information about oxygen deficiency of oxide based thin films. Thin films are firstly etched by argon to clean surface contaminants. Etching was applied at very low voltage not to create any preferential etching of Ti and O atoms. Ti 2p core level makes two separate peaks as 2p<sub>3/2</sub> and 2p<sub>1/2</sub>. Ti<sup>4+</sup> state is formed at 458.7-464.4 eV binding energy. XPS spectra

for Ti and O can be seen in Figure 6.3. After the heat treatment, stoichiometry of TiO<sub>2</sub> is nearly sustained for the all deposition conditions. However, exact position is obtained when 25 sccm oxygen flow rate is used. This means that annealing is not sufficient to provide the stoichiometric thin film formation. Binding energy for O 1s is formed at 530.1 eV for the metal oxide thin films. In each deposition condition, oxygen peak is formed near the expected value. Sometimes additional oxygen can be formed at 531.5 eV due to the presence of surface hydroxyls which are not formed in this study.

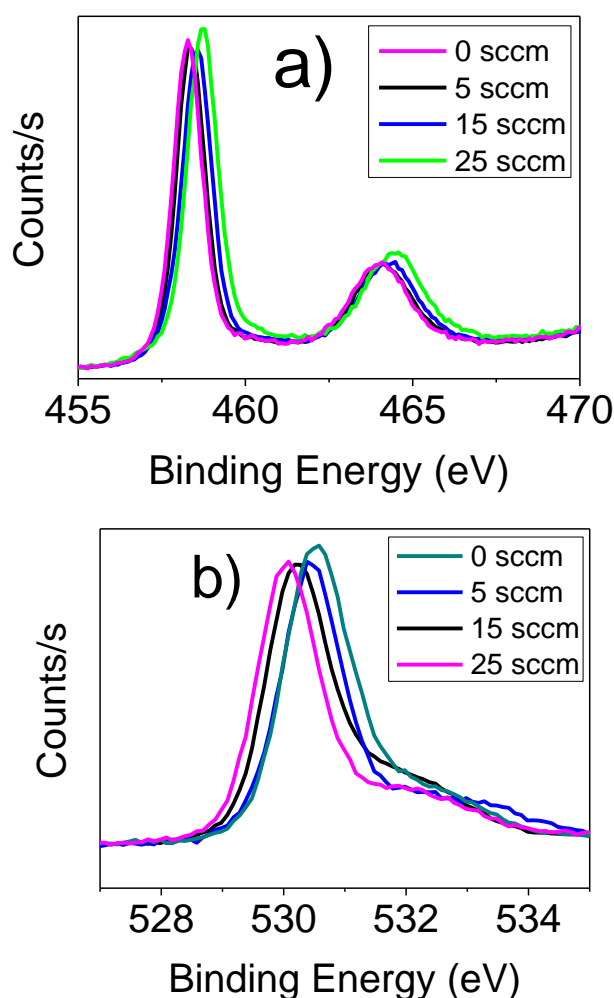


Figure 6.3. XPS spectra of a) Ti<sup>4+</sup> 2p level and b) O 1s level.

Titanium dioxide thin films were also evaluated regarding to their optical properties. Transmittance measurements were conducted between 400-1600 nm wavelength range. Figure 6.4 shows the transmittance spectrum for different deposition conditions. In this figure, measurements are compared with the bare substrate. Heat treatment fills oxygen deficient sites to supply a stoichiometric structure. Also, titanium is an oxygen sensitive element and its stable structure is  $\text{TiO}_2$ . Therefore, all the thin films show a similar transparency spectrum after annealing. However, less absorption is obtained when deposition was performed at 25 sccm oxygen flow rate. When higher refractive index material is coated on top of glass substrate (1.52), an interference pattern in lower transmittance was obtained compared to the substrate. When the coating does not create an optical path difference, it should have the same transparency with that of the substrate. If the film has an absorbing nature, a difference between the substrate and thin film at those points is resulted. Higher oxygen flow rates produce less absorbing films. Refractive index is calculated for thin films using Optilayer thin film characterization software (Figure 6.5). Higher refractive index is provided when higher oxygen flow rates are used in deposition. Denser films create higher refractive indices; because, there are many pores in low density films which are filled with water or air molecules. These molecules have lower refractive index than the thin film which yields a lower refractive index.

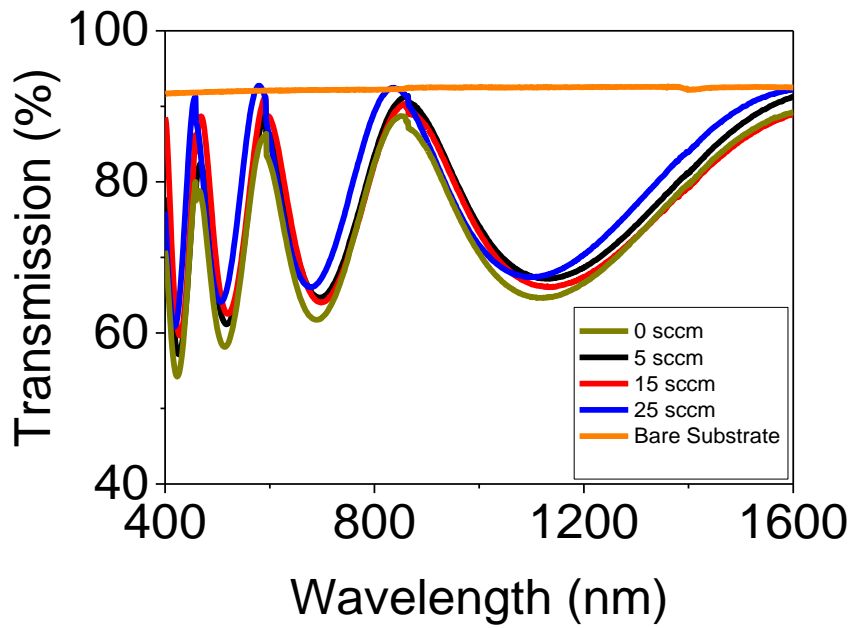


Figure 6.4. Optical transmittance spectrum of TiO<sub>2</sub> thin films which were deposited at 0, 5, 15, and 25 sccm oxygen flow rates.

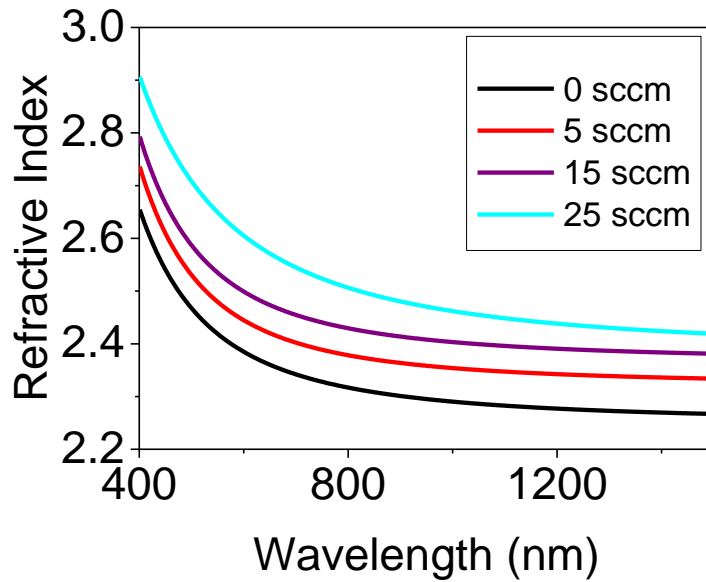


Figure 6.5. Refractive index dispersion for TiO<sub>2</sub> thin films which were deposited at 0, 5, 15, and 25 sccm oxygen flow rates.

### 6.2.2. Characterization of Perovskite Thin Films

In this study, perovskite absorber layers were deposited using adduct method which provides smooth, uniform, dense and large grained films. These positive effects yield enhancement of the cell performance [10]. Compared to adduct method, one step and two step deposition techniques depend on the deposition parameters and atmosphere. Figure 6.6 shows SEM images of perovskite thin films. Defect and crack free perovskite film formation can be seen in Figure 6.6a. The same figure also shows fully covered smooth surfaces. Dense and porosity free perovskite film formation can be seen in Figure 6.6b which shows the cross-section of the deposited compact electron transport layer and perovskite layer. These figures show that perovskite layer was formed at high quality and this is a parameter which is necessary for a high perovskite cell performance.

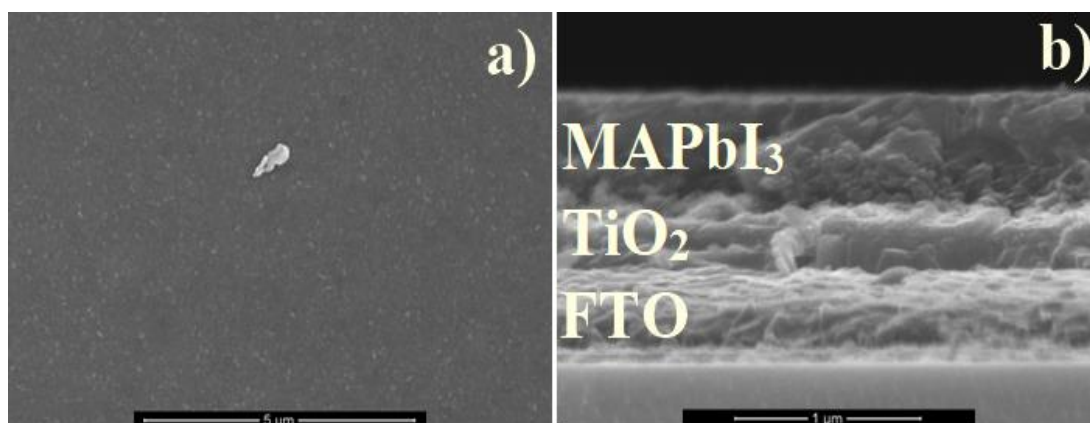


Figure 6.6. SEM images of perovskite thin film a) surface and b) cross-section.

Perovskite thin film analyses were made regarding to crystal orientation to determine the phases present. XRD measurements were carried out between 10 to 50 two theta degrees. Figure 6.7 gives the XRD pattern of MAPbI<sub>3</sub>. This diffraction pattern is well matched with the tetragonal phase of CN<sub>3</sub>NH<sub>3</sub>PbI<sub>3</sub> [11]. Also, no secondary phases

are observed in perovskite thin film. Crystallinity and pure structure of MAPbI<sub>3</sub> are the crucial properties to obtain a high performance from perovskite solar cell. In some studies, due to the partial reaction between MAI and PbI<sub>2</sub>, some diffraction peaks of PbI<sub>2</sub> can be observed. These unreacted molecules deteriorate the performance of the cell [12]. In this study, pure MAPbI<sub>3</sub> phase is obtained.

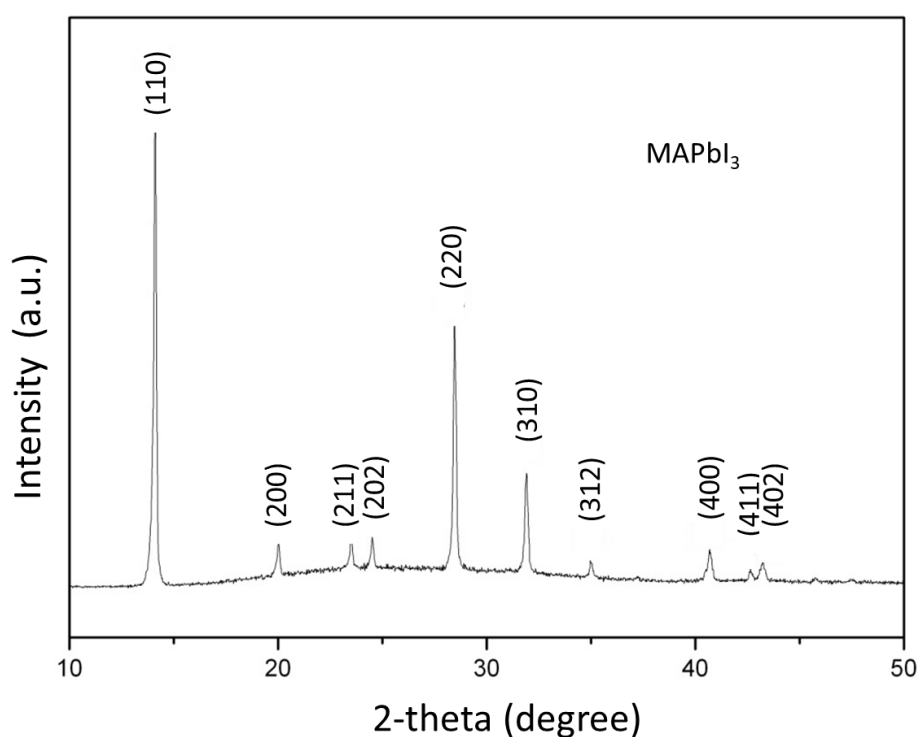


Figure 6.7. XRD pattern of CH<sub>3</sub>NH<sub>3</sub>PbI<sub>3</sub> perovskite thin film.

### 6.2.3. Characterization of Perovskite Solar Cells

As a final study, NiO and TiO thin films were used as hole transport layer. Structural, optical and electrical properties of NiO and TiO single layers were evaluated in the previous two chapters. In those chapters, NiO were deposited at different oxygen flow rates, deposition rate, deposition temperatures, and plasma assistance. Single layer analysis of NiO thin films helped to define important parameters for NiO HTL

deposition such as oxygen flow rate and deposition temperature. Plasma assistance can be effective; however, due to the damage probability risk of the perovskite layer, it was not applied during the production of perovskite solar cell. Also effects of layer thickness were evaluated using the production of the cell at different coating thicknesses. As a first study, NiO HTL's were deposited at 50 nm coating thickness and 80°C deposition temperature to evaluate the effect of the oxygen flow rate for 0, 10, 25 and 50 sccm. Figure 6.8 gives the J-V curves and Table 6.2 gives the results of the cell parameters. It was detected that 0 and 50 sccm oxygen flow rates result with low cell performance. Best cell performance was obtained when 25 sccm oxygen flow rate was used. Primary reason of the enhancement of the cell performance is the increase of the electrical conductivity of the layers with an increase in the oxygen flow rate. In chapter 4, it was detected that amount of oxygen was higher when a higher oxygen flow rate was used. Excess oxygen creates Ni<sup>2+</sup> vacancy sites. These vacant sites are replaced by two Ni<sup>3+</sup> ions with one hole donation to the valence band. However, when oxygen flow rate equals to 50 sccm, cell performance decreases. This condition is related to the band matching with the perovskite layer. Increase of the oxygen flow rate yields a higher band gap. When the valence band of HTL moves away from the HOMO level of the perovskite layer, it is difficult to transfer the holes from HOMO level of the perovskite to the valence band of HTL. Also, it was decided that mainly current density plays role on the performance of the cell. Results provide that better film formation was obtained when 25 sccm oxygen flow rate is used. Because, number of spherical particles was increased and size of needle particles was decreased with an increase in oxygen flow rate which can be seen in Chapter 4.

Table 6.2. Cell parameters of the devices produced with NiO HTL deposited at different oxygen flow rates of 0, 10, 25 and 50 sccm.

HTL Material	Sample	Oxygen Flow Rate (sccm)	Voc (V)	Jsc (mA/cm <sup>2</sup> )	Fill Factor (%)	Efficiency (%)
NiO	PSC1	0	0.39	8.16	21.59	0.69
	PSC2	10	0.51	16.15	29.99	2.47
	PSC3	25	0.77	18.06	30.87	4.29
	PSC4	50	0.51	7.86	26.97	1.08

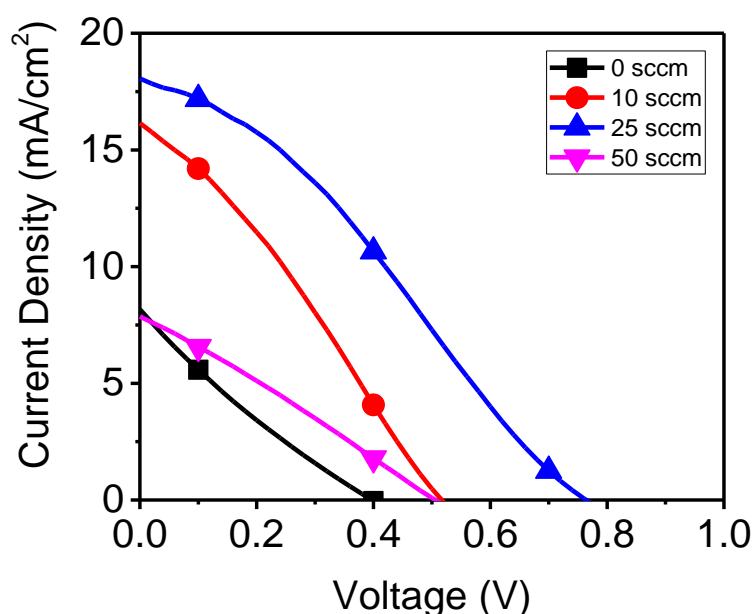


Figure 6.8. J-V curves for perovskite solar cells produced with NiO HTL deposited at different oxygen flow rates of 0, 10, 25 and 50 sccm.

Then, perovskite solar cells were produced using NiO HTL which was deposited at different deposition temperatures. In these cells, oxygen flow rate was kept constant at 25 sccm and again 50 nm coating thicknesses were used. Addition to 80°C, 30°C and 170°C deposition temperatures were used in the deposition of NiO HTL. Figure 6.9 and Table 6.3 give the results of the cell performances for these cells. At low and high deposition temperatures, performance of the cells was degraded. In both of these

conditions, lower voltage and current density were obtained compared to the base 80°C deposition temperature. At low deposition temperature, although fully spherical particle formation and low amount of Ni content were observed, its low band gap, high resistivity and small grain size suppress the cell performance. For the case of high deposition temperature, main reason of the low cell performance is the formation of cuboidal structures.

Table 6.3. Cell parameters of the devices produced with NiO HTL deposited at different deposition temperatures: 30, 80, and 170 °C.

HTL Material	Sample	Deposition Temperature (°C)	Voc (V)	Jsc (mA/cm <sup>2</sup> )	Fill Factor (%)	Efficiency (%)
NiO	PSC5	30	0.53	12.15	35.13	2.26
	PSC3	80	0.77	18.06	30.87	4.29
	PSC6	170	0.67	12.96	36.22	3.14

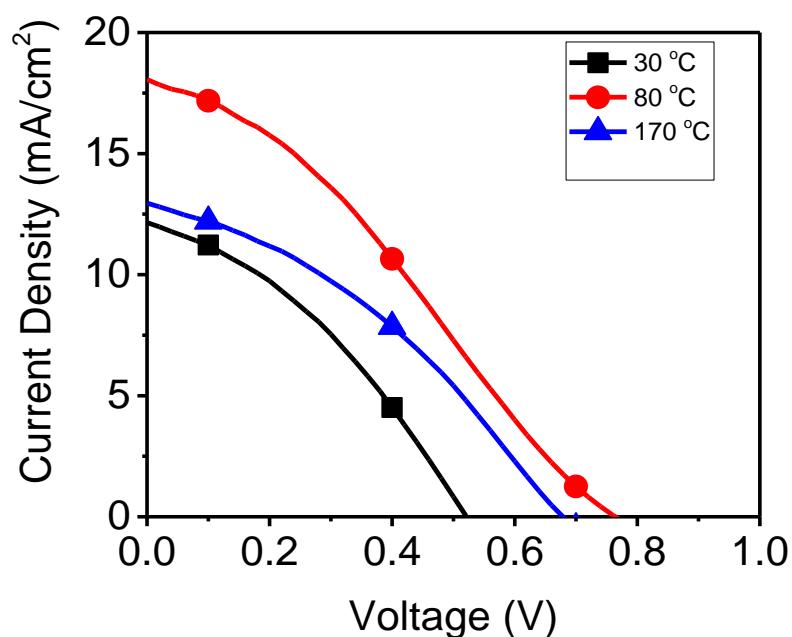


Figure 6.9. J-V curves for perovskite solar cells produced with NiO HTL deposited at different deposition temperatures: 30, 80, and 170 °C.

For the final study of NiO HTL, different layer thicknesses were evaluated. Oxygen flow rate and deposition temperature were taken as 25 sccm and 80°C. HTL's were deposited at 10, 25, 50, 75, and 100 nm thickness values. Results are given in Figure 6.10 and Table 6.4. It is found that 75 nm HTL provides the best cell efficiency which is 6.13 %. Although, this layer shows similar open circuit voltage with 50 nm layer, 75 nm coating thickness enhances both photo current and fill factor. This means that 75 nm coating thickness offers lower recombination and better charge extraction. This is possibly due to the defect and pin hole free layer formation at higher thicknesses. However, when the coating thickness is 100 nm, charge transfer is negatively affected and this causes a dramatic decrease in cell performance.

Table 6.4. Cell parameters of the devices produced with NiO HTL deposited at different layer thicknesses: 10, 25, 50, 75 and 100 nm.

HTL Material	Sample	HTL Thickness (nm)	Voc (V)	Jsc (mA/cm <sup>2</sup> )	Fill Factor (%)	Efficiency (%)
NiO	PSC7	10	0.37	18.48	31.63	2.16
	PSC8	25	0.49	14.88	42.35	3.09
	PSC3	50	0.77	18.06	30.87	4.29
	PSC9	75	0.77	18.93	42.03	6.13
	PSC10	100	0.55	16.66	42.29	3.87

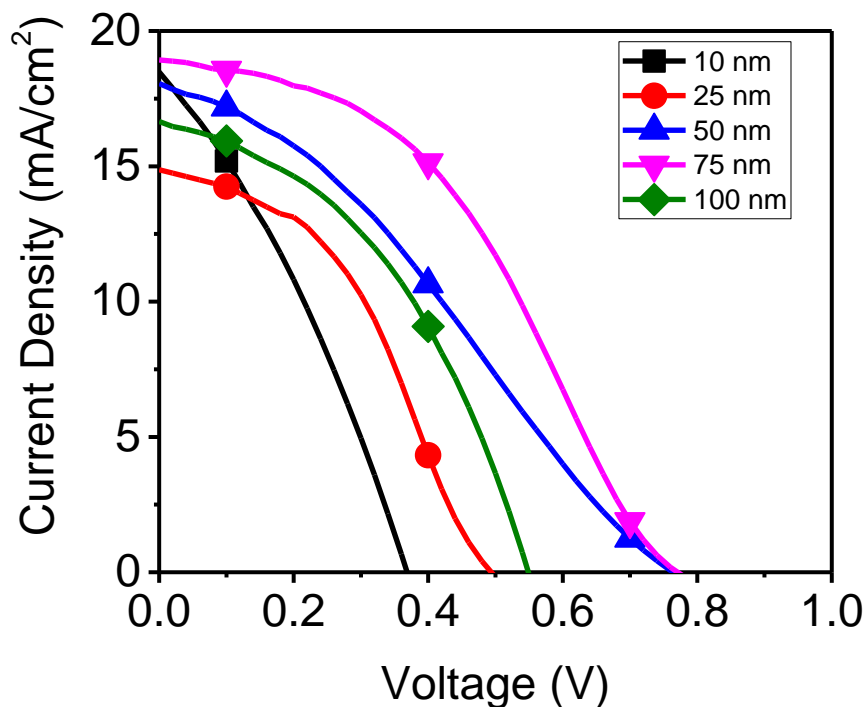


Figure 6.10. J-V curves for perovskite solar cells produced with NiO HTL deposited at different layer thicknesses: 10, 25, 50, 75 and 100 nm.

In the second study, TiO HTL was evaluated by studying different deposition conditions to obtain the best cell parameters. For this purpose, different layer thicknesses and different oxygen flow rates were employed in the production of perovskite solar cell. Effect of oxygen flow rate in the production of TiO single layers was explained in Chapter 5. The data given in that chapter is used in this study for the production of perovskite cells with TiO HTL. Firstly, TiO HTL was deposited at different thicknesses. In this study, oxygen flow rate was fixed to 1 sccm and deposition temperature was 80°C. Figure 6.11 and Table 6.5 give the performance of the cells. Best cell efficiency is obtained when 25 nm TiO HTL was deposited. Although, it yields a lower photocurrent compared to other cells, it offers very high open circuit voltage as 0.85 V. This means that 25 nm layer thickness is sufficient to produce defect free HTL. Open circuit voltage dramatically decreases when the layer

thickness increases due to the charge extraction problem. However, their high film quality provides a higher photocurrent density for thicker layers.

Table 6.5. Cell parameters of the devices produced with TiO HTL deposited at different layer thicknesses: 10, 25, 50, 75 and 100 nm.

HTL Material	Sample	HTL Thickness (nm)	Voc (V)	Jsc (mA/cm <sup>2</sup> )	Fill Factor (%)	Efficiency (%)
TiO	PSC11	10	0.57	6.88	22.75	0.89
	PSC16	25	0.85	14.54	35.35	4.37
	PSC12	50	0.61	18.80	35.72	4.10
	PSC13	75	0.65	15.45	39.28	3.95
	PSC14	100	0.49	14.86	42.37	3.09

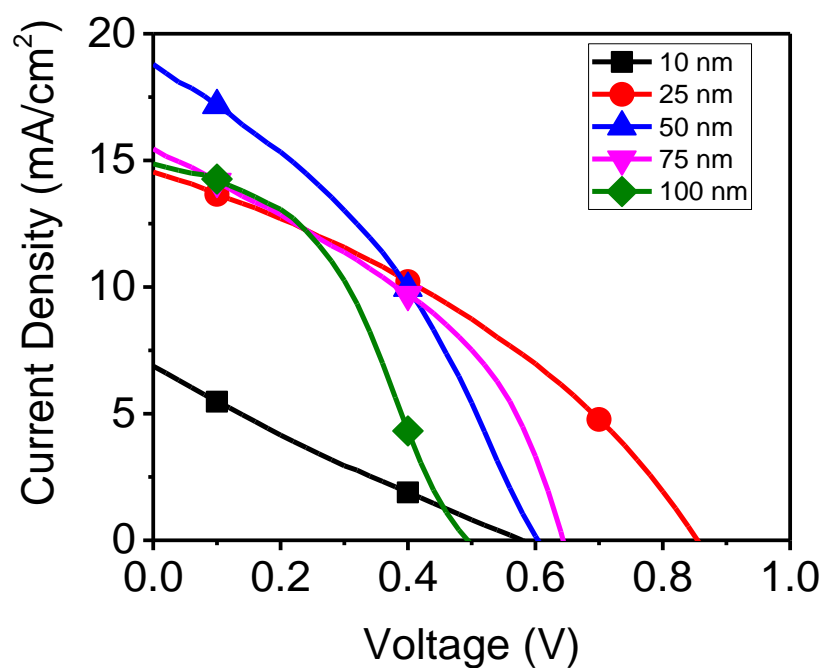


Figure 6.11. J-V curves for perovskite solar cells produced with TiO HTL deposited at different layer thicknesses: 10, 25, 50, 75 and 100 nm.

In the second study of TiO HTL's, perovskite cells were produced using TiO HTL which were deposited under different oxygen flow rates. 25 nm layer thickness and 80°C deposition temperature were used in this study. Oxygen flow rates were introduced to the vacuum chamber at 1, 2, 5, and 10 sccm and also one cell was produced without any oxygen addition. Performance of the cells can be seen in Figure 6.12 and Table 6.6. Open circuit voltage, which is lowered with the increase in oxygen flow rate, is maximized for 1 sccm oxygen flow rate. This is directly related to the band edge leveling with the perovskite layer and higher electrical conductivity. However, photocurrent density and fill factor dominantly change the cell performance and 2 sccm oxygen flow rate provides the best cell efficiency as 5.72 %. This is resulted due to the amount of free titanium. With an increase in the amount of oxygen, defect amount is minimized and therefore a better photocurrent density and fill factor were obtained.

Table 6.6. Cell parameters of the devices produced with TiO HTL deposited at different oxygen flow rates of 0, 1, 2, 5 and 10 sccm.

HTL Material	Sample	Oxygen Flow Rate (sccm)	Voc (V)	Jsc (mA/cm <sup>2</sup> )	Fill Factor (%)	Efficiency (%)
TiO	PSC15	0	0.65	14.08	25.87	2.37
	PSC16	1	0.85	14.54	35.35	4.37
	PSC17	2	0.79	17.96	40.29	5.72
	PSC18	5	0.73	16.57	41.40	5.01
	PSC19	10	0.49	10.21	11.71	0.59

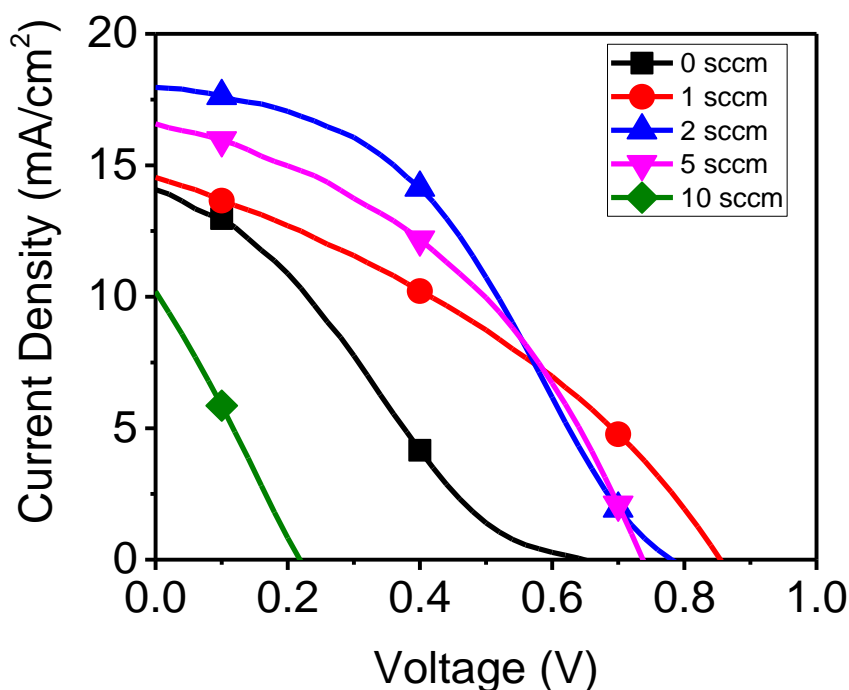


Figure 6.12. J-V curves for perovskite solar cells produced with TiO HTL deposited at different oxygen flow rates of 0, 1, 2, 5 and 10 sccm.

### 6.3. Conclusion

Titanium dioxide compact electron transport layer and nickel oxide and titanium monoxide hole transport layers were deposited using electron beam evaporation technique. These layers were used in the production of perovskite solar cells in n-i-p configuration. The deposition temperature of 80°C which is determined to be the optimum deposition temperature makes the application of this study possible on flexible substrates. TiO<sub>2</sub> compact layer was evaluated for its structural and optical properties and it was found that 25 sccm oxygen flow rate provides a high quality compact layer. Produced perovskite layer was also examined structurally, and it is shown that perovskite layer can be produced in highly crystalline and defect free conditions. NiO and TiO layers, which were fully characterized in the previous two chapters, were deposited on top of the perovskite layer as HTL. When the deposition

conditions are 80°C deposition temperature, 25 sccm oxygen flow rate and 75 nm layer thickness, best cell performance for NiO HTL was obtained as 6.13 %. Best cell for TiO HTL is obtained using 2 sccm oxygen flow rate and 25 nm coating thickness which yields 5.72 % photo-conversion efficiency.



## REFERENCES

- [1] M.H. Li, P.S. Shen, K-C. Wang, T.F. Guo, P. Chen, Inorganic p-type contact materials for perovskite-based solar cells, *Journal of Materials Chemistry A*, 3 (2015) 9011-9019.
- [2] B. Abdollahi Nejang, V. Ahmadi, H. R. Shahverdi, New physical deposition approach for low cost inorganic hole transport layer in normal architecture of durable perovskite solar cells, *ACS Applied Materials & Interfaces*, 7 (2015) 21807-21818.
- [3] S. Seo, I. J. Park, M. Kim, S. Lee, C. Bae, H. S. Jung, N.-G. Park, J. Y. Kim, H. Shin, An ultra-thin, un-doped NiO hole transporting layer of highly efficient (16.4%) organic–inorganic hybrid perovskite solar cells, *Nanoscale*, 8 (2016) 11403-11412.
- [4] C. Zuo, L. Ding, Solution-processed Cu<sub>2</sub>O and CuO as hole transport materials for efficient perovskite solar cells, *Small*, 11 (2015) 5528-5532.
- [5] L. Zhang, C. Jiang, C. Wu, H. Ju, G. Jiang, W. Liu, C. Zhu, T. Chen, V<sub>2</sub>O<sub>5</sub> as hole transporting material for efficient all inorganic Sb<sub>2</sub>S<sub>3</sub> solar cells, *ACS Applied Materials & Interfaces*, 10 (2018) 27098-27105.
- [6] B.-S. Kim, T.-M. Kim, M.-S. Choi, H.-S. Shim, J.-J. Kim, Fully vacuum-processed perovskite solar cells with high open circuit voltage using MoO<sub>3</sub>/npb as hole extraction layers, *Organic Electronics*, 17 (2015) 102-106.
- [7] S. S. Mali, H. Kim, S. E. Shim, C. K. Hong, A solution processed nanostructured p-type NiO electrode for efficient inverted perovskite solar cells, *Nanoscale*, 8 (2016) 19189-19194.
- [8] X. Yin, Z. Yao, Q. Luo, X. Dai, Y. Zhou, Y. Zhang, Y. Zhou, S. Luo, J. Li, N. Wang, H. Lin, High efficiency inverted planar perovskite solar cells with solution-processed NiO<sub>x</sub> hole contact, *ACS Applied Materials & Interfaces*, 9 (2017) 2439-2448.
- [9] S. Ye, W. Sun, Y. Li, W. Yan, H. Peng, Z. Bian, Z. Liu, C. Huang, CuSCN-based inverted planar perovskite solar cell with an average pce of 15.6%, *Nano Letters*, 15 (2015) 3723-3728.
- [10] M. S. Jamal, M. S. Bashar, A. K. M. Hasan, Z. A. Almutairi, H. F. Alharbi, N. H. Alharthi, M. R. Karim, H. Misran, N. Amin, K. B. Sopian, M. Akhtaruzzaman, Fabrication techniques and morphological analysis of perovskite absorber layer for

high-efficiency perovskite solar cell: A review, *Renewable and Sustainable Energy Reviews*, 98 (2018) 469-488.

[11] S. A. Shojaee, T. A. Harriman, G. S. Han, J. K. Lee, D. A. Lucca, Substrate effects on photoluminescence and low temperature phase transition of methylammonium lead iodide hybrid perovskite thin films, *Applied Physics Letters*, 111 (2017) 023902.

[12] Q. Guo, C. Li, W. Qiao, S. Ma, F. Wang, B. Zhang, L. Hu, S. Dai, Z. a. Tan, The growth of a  $\text{CH}_3\text{NH}_3\text{PbI}_3$  thin film using simplified close space sublimation for efficient and large dimensional perovskite solar cells, *Energy & Environmental Science*, 9 (2016) 1486-1494.

## CHAPTER 7

### **TUNING THE ELECTRON BEAM EVAPORATION PARAMETERS FOR THE PRODUCTION OF NIOBIUM PENTOXIDE COMPACT LAYERS FOR PEROVSKITE SOLAR CELLS**

Lead halide perovskite structure is firstly used in 2009 by Miyasaka group for dye sensitized solar cells; however cell performance remained at 3.8 % due to easily corroded perovskite structure by liquid electrolyte [1]. Reliability and importance of perovskite structure were understood by the work which was carried by Kim et al. in 2012. In this study, corrosive electrolyte was changed by a solid state hole transport layer [2]. Nowadays, best efficiency is reached to 22.7 % [3]. Enhancement of cell performance depends on the evolving of all individual layers and interfaces.

Perovskite solar cells have great potential to be used as commercially due to their ease of preparation, low cost, and high efficiencies. Interest in organo lead halide perovskites ( $\text{CH}_3\text{NH}_3\text{PbX}_3$ , X=I, Br, and Cl) is originated from their optimal band gap, large absorption coefficient, long carrier life time and high charge mobilities [4, 5]. Perovskite solar cells are built up on top of transparent conductive oxide (TCO) coated glass or plastic substrates. Cells are commonly formed by sequential deposition of four basic layers over the TCO layer which has a conventional n-i-p device configuration. These layers are electron transport layer (ETL), perovskite absorber, hole transport layer (HTL) and metal contact layer [4, 6].

ETL has an important role for electron extraction and hole blocking. Ideal layer should be deposited as a pinhole free layer and should possess high electrical conductivity. According to ETL, perovskite solar cells can be categorized as planar or mesoporous. In planar design, ETL is formed just as a thin n-type wide band gap semiconductor

film. This layer is also named as compact layer and main advantage of compact layer is the avoidance of charge recombination between electrons at TCO and holes at valence band of perovskite absorber [6, 7]. Additionally, mesoporous layer can be coated on compact layer for mesoporous design. Mesoporous layer supplies larger surface area which lowers the contact resistance, enhances electron transfer with increased photo conversion efficiency and also mesoporous layer is used as template for perovskite layer [8, 9]. Mesoporous layer also increases photon absorption due to light scattering [10].

Compact layer can be deposited by solution processing or vacuum coating techniques. Solution based techniques are cost effective and scalable, however in solution based deposited films without heat treatment, increased oxygen vacancy concentration is observed on the surface. Due to the oxygen vacancy sites, electron extraction slows down and charge recombination rate directly increases [11, 12]. High temperature post treatment is also crucial for solution based depositions due to the removal of organics or additives and it enhances crystallization together with interconnection. Also, for the efficient hole blocking compact layer, deposition should be done without cracks and pinholes. When we combine all these requirements, vacuum based deposition methods become reliable, industrial and highly reproducible techniques compared to solution based processes.

Most preferred material for compact ETL is  $\text{TiO}_2$  due to its environmentally friendly nature, wide band gap, high electron mobility, and good stability. However, there are also some studies using doped  $\text{TiO}_2$  [13],  $\text{ZnO}$  [14],  $\text{Cs}_2\text{CO}_3$  [15],  $\text{SnO}_2$  [16],  $\text{WO}_3$  [17] and  $\text{Nb}_2\text{O}_5$  [18]. Main aim is the reduction in interfacial resistance between TCO/compact layer and enhancement of charge collection in the use of alternative materials and deposition conditions [19]. Zinc oxide has a disadvantage due to the enhanced decomposition of perovskite layer [14, 20].  $\text{Nb}_2\text{O}_5$  is seen as a very good alternative ETL material due to its high carrier mobility, low hysteresis and suitable conduction band edge position [18, 21]. Also,  $\text{Nb}_2\text{O}_5$  is transparent, air and water

stable and band position can easily be tuned by changing stoichiometry or crystalline structure [22].

Potential use of Nb<sub>2</sub>O<sub>5</sub> thin films as a compact layer for perovskite solar cell was demonstrated in the previous studies [18, 21]. Advantages in electron beam evaporation technique motivate this study to provide the production of dense and defect free Nb<sub>2</sub>O<sub>5</sub> compact layers. However, quality of compact layer is directly related with the deposition conditions of oxygen flow rate and plasma assistance. In this study, effect of electron beam deposition parameters of Nb<sub>2</sub>O<sub>5</sub> compact layer on perovskite solar cell was explained using results of optical and structural analysis of single Nb<sub>2</sub>O<sub>5</sub> layer. All the depositions are performed at low temperatures to investigate the potential use in heat sensitive substrates. Also, these layers are subjected to the post annealing to observe the effect of high temperature in the production of compact layer for planar perovskite solar cells. Finally, potential use of Nb<sub>2</sub>O<sub>5</sub> compact layer together with TiO<sub>2</sub> mesoporous layer was investigated in this study.

## **7.1. Experimental Studies**

### **7.1.1. Deposition of Single Nb<sub>2</sub>O<sub>5</sub> Thin Films and Their Characterizations**

Nb<sub>2</sub>O<sub>5</sub> thin films were deposited using Tecport plasma assisted physical vapor deposition (PAPVD) system. Nb<sub>2</sub>O<sub>5</sub> deposition materials were supplied from LTS chemicals with 99.999% purity which is pre-melted in copper crucible before deposition. Depositions started when the pressure value was lower than  $8 \times 10^{-6}$  mbar. Thin films were deposited on Schott Bk7 glasses which were cleaned by wiping in acetone and etching in argon in the deposition system. Depositions were performed at different oxygen flow rates with or without the plasma assistance. Deposition parameters are given in Table 7.1. For characterization purposes, Nb<sub>2</sub>O<sub>5</sub> thin films

were deposited around 250 nm thickness at 0.2 nm/s deposition rate. Due to the different deposition conditions, actual coating thickness is generally different from the expected values. Depositions were performed at 80 °C deposition temperature which is quite advantageous for heat sensitive substrates. Jeol cold plasma source was used for plasma assistance and substrate etching. Applied bias voltage was 70 V during etching and 90 V during deposition. All the samples were exposed to 500°C heat treatment for 2 h which is the same with the treatment step for mesoporous layer in the cell production.

Single layer Nb<sub>2</sub>O<sub>5</sub> thin films were firstly analyzed for the optical properties. Reflectance and transmittance measurements were carried out using Perkin Elmer Lambda 950 UV-VIS-near-IR spectrophotometer. The refractive index and approximate layer thicknesses were calculated using the “Optilayer” optical thin film calculation software via mathematical approximation. Band gap values were obtained from the transmission cut-off point using Tauc plots. Layers were characterized morphologically and structurally using FEI, Nova Nano SEM 430 Scanning Electron Microscopy (SEM), PANalytical X-ray diffractometer (XRD) using Cu K $\alpha$  radiation (1.54 Å) at 1° grazing incidence to lower the substrate effect and Thermo K-Alpha X-ray photoelectron spectroscopy (XPS).

### **7.1.2. Perovskite Solar Cell Production and Their Characterizations**

Perovskite solar cells were constructed in planar and mesoporous structure on FTO coated glasses with 10 ohm/sq sheet resistance, supplied from Pilkington. Zinc powder and 2M HCl etching solution were used for patterning of FTO-coated glass substrates. FTO glasses were cleaned with deionized water, ethanol, acetone, and deionized water sequentially. Cleaned FTO glasses were coated by compact Nb<sub>2</sub>O<sub>5</sub> thin films at 60 nm coating thicknesses using e-beam vacuum deposition method. Coating parameters were the same with single layer deposition of Nb<sub>2</sub>O<sub>5</sub> thin films. Perovskite cells were

produced at two different architecture; these are planar and mesoporous. Also, planar cells were fabricated at as deposited and heat treated forms. Prepared cells are given in Table 7.1 and they are notified as C code.

Table 7.1. Deposition parameters for single layer  $Nb_2O_5$  thin films and cell configuration for these deposition conditions.

	Plasma Assistance	Oxygen Flow Rate (sccm)		Cell Configuration
R1	Yes	0	C1.1	Planar
			C1.2	Planar Heat Treated
			C1.3	Mesoporous
R2	Yes	10	C2.1	Planar
			C2.2	Planar Heat Treated
			C2.3	Mesoporous
R3	Yes	25	C3.1	Planar
			C3.2	Planar Heat Treated
			C3.3	Mesoporous
R4	Yes	50	C4.1	Planar
			C4.2	Planar Heat Treated
			C4.3	Mesoporous
R5	No	0	C5.1	Planar
			C5.2	Planar Heat Treated
			C5.3	Mesoporous
R6	No	10	C6.1	Planar
			C6.2	Planar Heat Treated
			C6.3	Mesoporous
R7	No	25	C7.1	Planar
			C7.2	Planar Heat Treated
			C7.3	Mesoporous
R8	No	50	C8.1	Planar
			C8.2	Planar Heat Treated
			C8.3	Mesoporous

For mesoporous cell design, TiO<sub>2</sub> was deposited by spin coating method. Solution for the spin coating was prepared by dissolving titania paste (Dyesol NRT-18) in ethanol at 1:3 weight ratio. Solution is spin coated on compact Nb<sub>2</sub>O<sub>5</sub> layer at 2000 rpm for 10 s. Optimized coating thickness was determined to be around 200 nm for mesoporous layer. Mesoporous layers were dried firstly at 125°C for 5 min. and heat treatment was conducted at 500°C for 2 h. Also, planar Nb<sub>2</sub>O<sub>5</sub> cells were heat treated at the same conditions for comparison of planar perovskite solar cell with and without heat treatment. Mesoporous cells were also post treated using 0.02 M TiCl<sub>4</sub> aqueous solution at 90°C for 10 min. After TiCl<sub>4</sub> treatment, cells were fired secondly again at 500°C for 2 h. Then, perovskite layers were deposited using one step anti-solvent dripping technique [23]. Perovskite solution was prepared by mixing 461 mg of PbI<sub>2</sub> (99%, Aldrich), 159 mg of CH<sub>3</sub>NH<sub>3</sub>I (Dyesol), and 78 mg of dimethyl sulfoxide (99.5%, Aldrich) (molar ratio 1:1:1) and 600 mg of N,N-dimethylformamide (99.8% anhydrous, Aldrich) solution was added into mixed solution at room temperature and finally it was stirred for 1 h. Dissolved solution was spin-coated on mesoporous and planar ETL's at 4000 rpm for 25 s. After 5 s of rotation in the spinning process, 0.5 ml of diethyl ether (99.5%, Aldrich) was slowly dripped on the surface of the substrate. Transparent films were heated to 100°C for 5 min to obtain a dense film [24]. Using these coating parameters, 200 nm perovskite layer was obtained which is suitable for both photon absorption and charge transfer. Spiro-OMeOTAD thin films were used as HTL. To prepare spiro-OMeOTAD solution, 72.3 mg spiro-OMeOTAD, 28.8 µl of 4-tert-butyl pyridine and 17.5 µl of lithium bis(trifluoromethanesulfonyl)imide (Li-TFSI) solution (520 mg Li-TFSI in 1 ml acetonitrile) were mixed in 1 ml of chlorobenzene. Then, solution was spin coated on perovskite layer at 3000 rpm for 30 s. Mesoporous, perovskite and hole transport layers were deposited at atmospheric conditions, however, ambient humidity was kept around 30-40%. Finally, 150 nm thick gold film was sputtered for back contact layer. Gold depositions were performed using metal masking and active cell areas were around 0.05 cm<sup>2</sup>.

Current-voltage analyses were performed using Yokogawa GS610 source measure unit under simulated AM 1.5 conditions using Newport solar simulator 67005. Electrochemical impedance spectroscopy was performed using Gamry reference 3000. Samples were illuminated with white LED light ( $60 \text{ mW/cm}^2$ ) and the obtained graphs were fitted using Echem analyst software.

## **7.2. Results and Discussions**

### **7.2.1. Optical Characterization of Single Layer Nb<sub>2</sub>O<sub>5</sub> Thin Films**

Single layer Nb<sub>2</sub>O<sub>5</sub> thin films were firstly characterized regarding optical properties. Transmittance measurements were carried out using spectrophotometer. Figure 7.1 shows the transmittance spectrum of the Nb<sub>2</sub>O<sub>5</sub> thin films indicating their absorptive nature. Difference between the maximum transmission points and bare substrate defines the absorption. Thin films coated without oxygen addition show strong absorption. When plasma assistance is used in the deposition, thin films can be produced closer to real stoichiometry. Plasma power enhances the mobility of charge carriers which reduces the free carrier absorption. Even if low amount of oxygen flow rate is used, absorption is dramatically lowered. However, more oxygen is required to decrease the absorption for non-assisted deposition (Figure 7.1b). High transparency is crucial for the ETL layer to maximize the number of photons reaching the perovskite absorbing layer. Therefore, oxygen addition is critical during the deposition of Nb<sub>2</sub>O<sub>5</sub> thin films. Transmittance spectrum of thin films are similar after heat treatment except the spectra for non-plasma assisted and oxygen free conditions because heat treatment in open atmosphere results in oxidation of low oxygen containing samples, which in turn greatly affects the absorption behavior. It was concluded that high optical transmission is only possible for sufficiently oxidized films, which can be obtained by either introducing oxygen into the deposition chamber or by heat treating the films in open atmosphere after deposition.

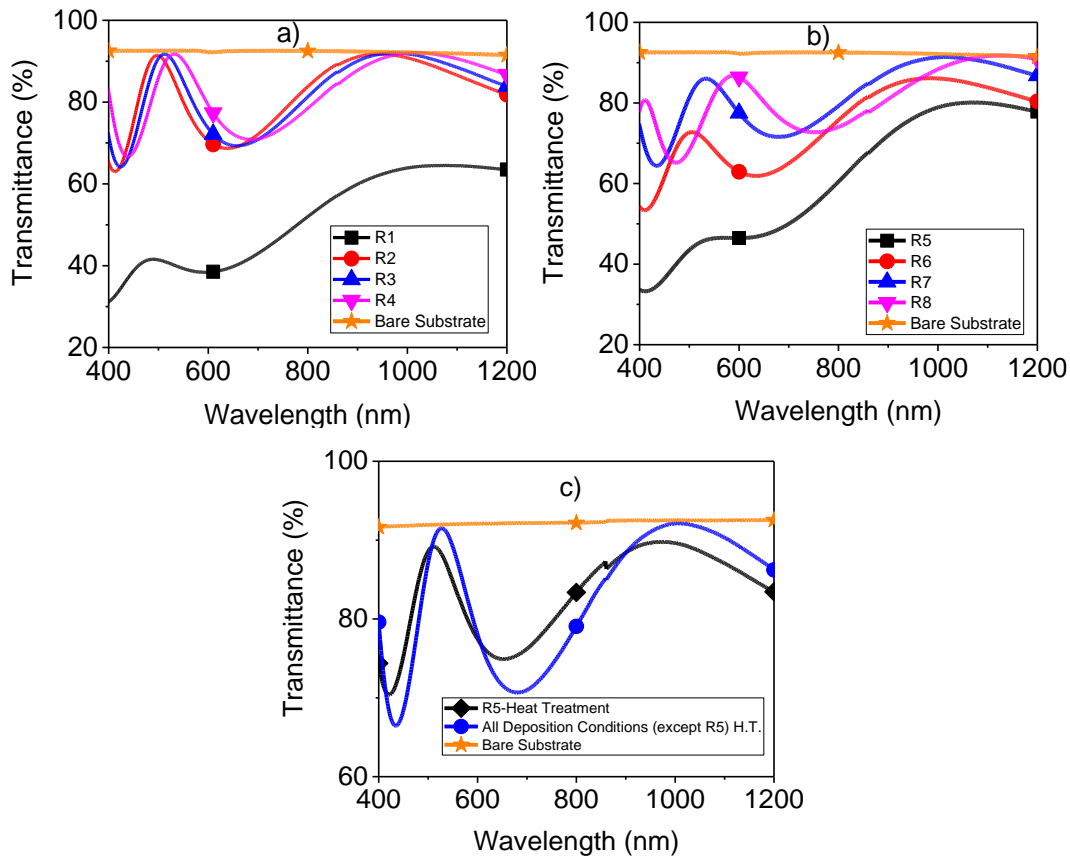


Figure 7.1. Transmission spectrum of Nb<sub>2</sub>O<sub>5</sub> thin films a) Plasma assisted deposition b) Non-plasma assisted deposition, c) After the heat treatment process.

Actual thicknesses of thin films were calculated by Optilayer thin film coating design software using mathematical models. Calculated values can be seen in Table 7.2. Plasma assistance yields thinner actual thicknesses. Thicker film formation is observed when deposition is performed under higher oxygen flow rate. Actual coating thicknesses were calculated using transmission spectra, therefore, calculated thicknesses for the heat treated samples are close into each other. Similar transmission spectra and coating thicknesses can be explained by rapid oxygen acceptance of films at the annealing temperature in ambient atmosphere.

Table 7.2. Actual thickness and band gap values for single layer Nb<sub>2</sub>O<sub>5</sub> thin films for as deposited and heat treated conditions.

	Actual thickness (nm)	Actual thickness (nm) (After heat treatment)	Band gap (eV)	Band gap (eV) (After heat treatment)
R1	197	241	3.45	3.70
R2	214	243	3.50	3.70
R3	223	238	3.55	3.70
R4	238	240	3.60	3.70
R5	220	235	3.55	3.68
R6	221	246	3.60	3.68
R7	241	238	3.60	3.68
R8	266	254	3.65	3.68

Refractive indexes of thin films were calculated using the fitting algorithms in Optilayer thin film coating design software. Transmittance and reflectance results were used together for better material characterization during the calculations. Change of refractive index with wavelength is given in Figure 7.2. Increase in oxygen flow rate resulted in decrease in the refractive index of thin films. Refractive index is a good indicator to infer density of thin films. Less dense films are possessing smaller refractive indexes. Because, water and air in atmosphere can easily be introduced to the porous regions of thin films, which decrease the refractive index. Increase in oxygen flow rate produces porous sites while growing on the substrate and creates lower refractive index where this phenomenon was also previously observed in some studies [25-27]. Plasma assistance helped in the formation of denser films compared to non-assisted deposition. Primary objective of the compact layer is efficient electron transfer to the FTO electrode. Thus, compact layer should be produced at denser and defect free conditions. High temperature firing of thin films increases the refractive index. Figure 7.2c and Figure 7.2d investigate the effect of heat treatment on plasma assisted and non-plasma assisted conditions. After the heat treatment, density of the samples, which is just the reverse compared to as deposited thin films, increases from low oxygen flow rate to high oxygen flow rate deposition condition.

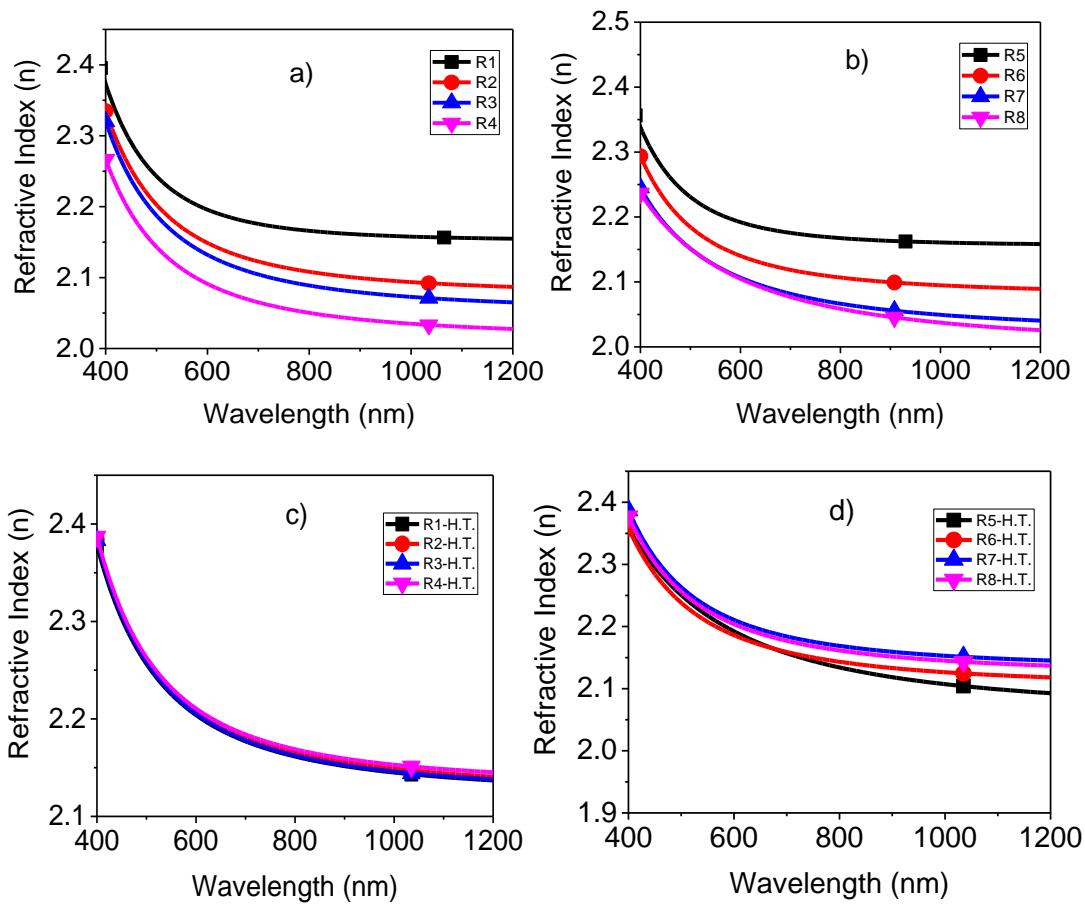


Figure 7.2. Refractive index spectrum of Nb<sub>2</sub>O<sub>5</sub> thin films a) Plasma assisted deposition, b) Non-plasma assisted deposition, c) Plasma assisted deposited samples after heat treatment, and d) Non-plasma assisted deposited samples after heat treatment.

Optical band gap is calculated using Tauc plot method which is obtained by plotting  $(h\nu\alpha)^m$  as a function of  $h\nu$ .  $m = 1/2$  is used for indirect band gap semiconductor materials like Nb<sub>2</sub>O<sub>5</sub>. When tangent line is drawn on flat side, intersecting point to  $h\nu$  gives the band gap which can be seen in Figure 7.3.  $1/d \cdot \ln(1/T)$  equation is used to calculate  $\alpha$ .  $d$  is the measure of thickness and transmittance is defined as  $T$ . Obtained band gap values are given in Table 7.2. Larger band gap formation is observed when depositions are performed at high oxygen flow rate conditions. At low oxygen deposition condition, amount of oxygen vacancy sites are high which increase the

concentration of localized states in band structure [28]. Therefore lower band gap formation is inevitable. Furthermore, amount of non-bridged oxygen atoms increases when deposition is carried out at low oxygen flow rates. This phenomenon increases the value of valence band edge and therefore band gap decreases. When plasma assistance is not used, obtained band gap is higher compared to plasma assisted depositions. Similar condition was seen for the RF sputtering studies. In that study, increase of RF power creates lower band gap  $\text{Nb}_2\text{O}_5$  thin films. This situation is explained by the formation of localized states around band edges. Mostly observed effect is the lowering of the conduction band edge [29]. Larger band gap provides lower recombination which leads to better cell efficiency. Heat treatment offers higher band gap with possible positive effect on cell performance. Increase of the carrier concentration is the main reason of the formation of larger band gap thin films.

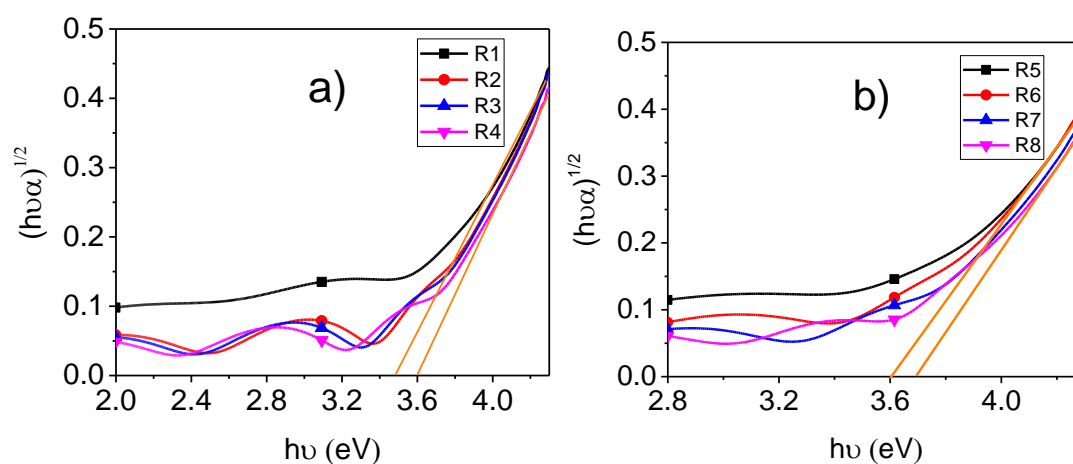


Figure 7.3. The variation of  $(h\nu\alpha)^{1/2}$  as a function of  $h\nu$  for  $\text{Nb}_2\text{O}_5$  thin films a) Plasma assisted depositions, and b) Non-plasma assisted depositions.

### 7.2.2. Structural Characterization of Single Layer Nb<sub>2</sub>O<sub>5</sub> Thin Films

To investigate the structural properties of electron beam deposited Nb<sub>2</sub>O<sub>5</sub> thin films, XRD, SEM and XPS measurements were carried out. XRD measurements were performed at 1° grazing incidence to eliminate the substrate effect, because thin films were deposited on top of amorphous glass substrates. All the deposition conditions generate amorphous structure; therefore only one deposition condition is shown in Figure 7.4. Also, it is detected that heat treatment does not cause any crystallinity. Heat treatment of thin films was performed around 500°C which is the same with firing temperature of mesoporous layer of perovskite solar cell. This condition is also observed in other studies [30-32]; crystallinity can be obtained only when the annealing temperature is over 600°C, which is higher than the softening point of glass substrates, so it was not performed in this study.

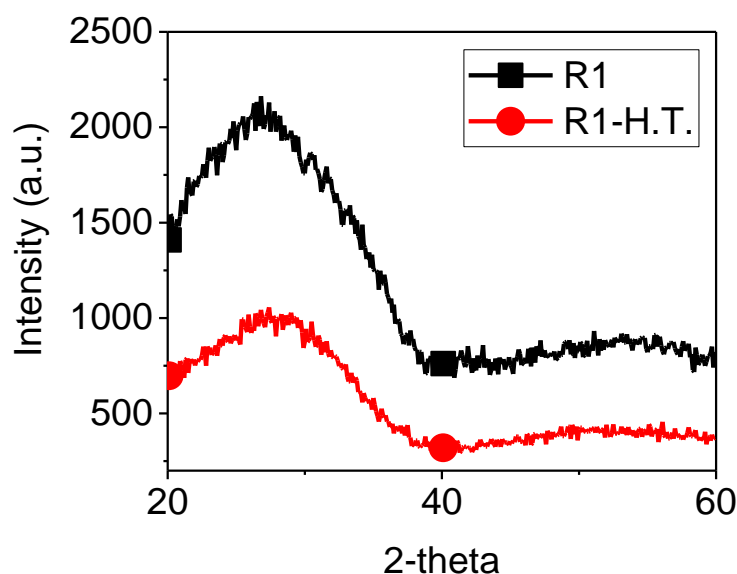


Figure 7.4. X-ray diffraction pattern of Nb<sub>2</sub>O<sub>5</sub> thin films.

Figure 7.5 shows cross sectional SEM images of Nb<sub>2</sub>O<sub>5</sub> thin films. Dense and defect free film formation is critical for efficient electron transport for the blocking layer. It

is seen that films have good adherence to the substrate surfaces. Also, all thin films show a dense appearance and pinhole formation is not observed. There is not a strong effect of deposition conditions on the morphology and topography of thin films due to the amorphous nature of the films.

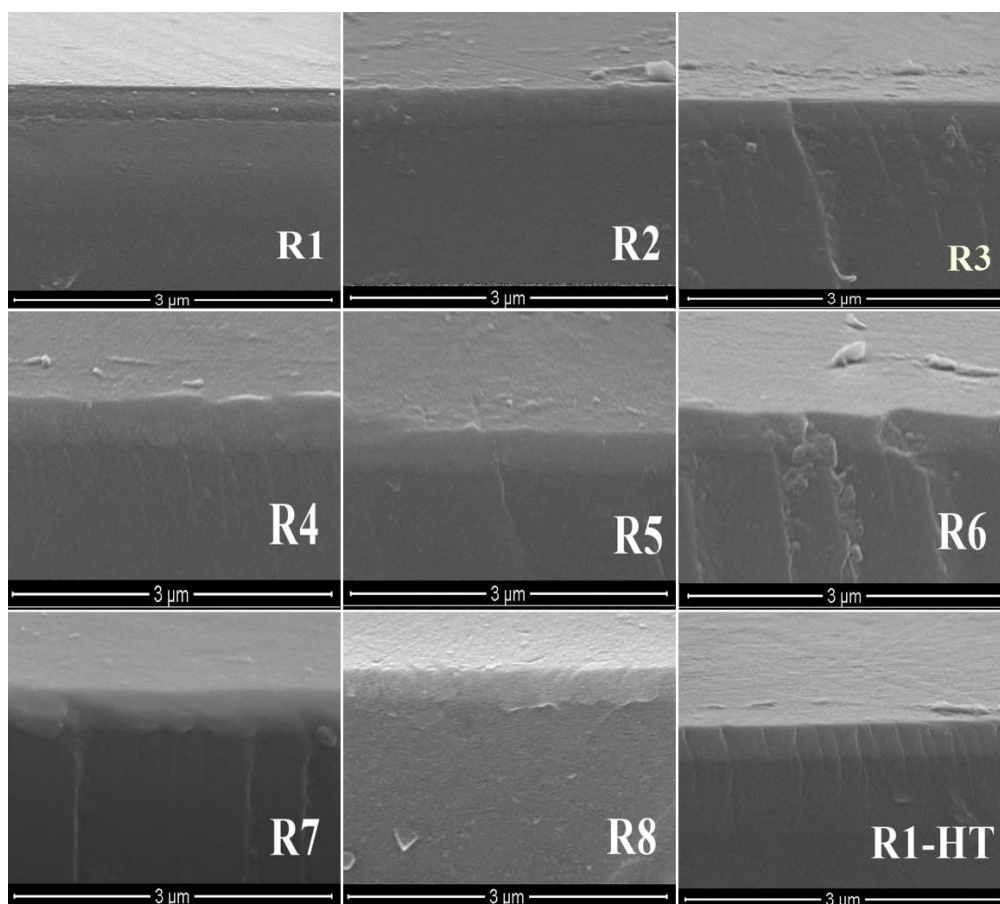


Figure 7.5. SEM images of Nb<sub>2</sub>O<sub>5</sub> thin films.

XPS analyses were carried out to understand the chemical composition of Nb<sub>2</sub>O<sub>5</sub> thin films. Figure 7.6 shows both 3d core level of niobium and 1s core level of oxygen peaks for plasma assisted and non-plasma assisted deposition conditions. Binding energies for niobium and oxygen were determined using the carbon shift procedure according to C1s peak at 284.8 eV. Core levels of Nb oxides are shown in doublet

peaks at  $3d_{5/2}$  and  $3d_{3/2}$  level. There are three possible oxide states of niobium which are +2, +3 and +5. Corresponding peaks are formed at 204.7, 206.1 and 207.6 eV binding energies for  $3d_{5/2}$  sequentially [33]. Without oxygen flow, thin films are formed with slightly less oxygen content compared to stoichiometric  $Nb_2O_5$  for both plasma assisted and non-plasma assisted conditions. When depositions are carried out under additional oxygen flow, stoichiometric form of  $Nb_2O_5$  has formed for 10 and 25 sccm oxygen flow rates for plasma assisted deposition.  $3d_{5/2}$  binding energies of Nb are observed at 207.2 eV and 207.3 eV for the above deposition conditions, respectively. However, 50 sccm oxygen flow rate produces slightly higher binding energy for Nb  $3d_{5/2}$  which is the evidence of higher oxygen entrance to the film possibly yielding lower conductivity and worse carrier transport. Oxygen addition is crucial to obtain stoichiometric  $Nb_2O_5$  for both plasma assisted and non-plasma assisted conditions. However, it is seen that 10 sccm oxygen flow rate is not sufficient for non-plasma assisted deposition, minimum 25 sccm oxygen flow rate should be supplied to the system to achieve stoichiometry. Figure 7.6c and Figure 7.6d show the oxygen spectra of niobium oxide thin films. Oxygen doublets can be observed in XPS spectra for oxide films. The major  $O^{2-}$  peak is found around 530.1 eV binding energy value for metal oxides. Other peak is the result of surface hydroxylation due to the absorption of  $OH^-$  and  $H_2O$  species which is generally observed around 531.5 eV [32]. Binding energy of the oxygen increases with the increase in oxygen flow rate for both plasma and non-plasma assisted conditions. Major peak is dominantly formed in all our samples and there is no evidence of the formation of surface adsorbed  $OH^-$  and  $H_2O$  molecules for  $Nb_2O_5$  thin films. XPS analysis was also carried out for the heat treated  $Nb_2O_5$  thin films. Both plasma assisted and non-plasma assisted samples were converged to the similar results (Figure 7.6e and 7.6f). Oxygen free deposition conditions provide best fitting to the stoichiometric form of +5 state of niobium oxide. When deposition includes oxygen addition, films have higher oxygen content than stoichiometric form which is understood by the shift in the peak of  $3d_{5/2}$  to higher values. This is not preferred for efficient electron transfer as explained above. Another input for this analysis is the production of thin films at higher oxygen content for non-

plasma assisted deposition compared to the plasma assisted condition after heat treatment. This is probably due to the higher amount of porous regions for the case of non-plasma assisted deposition where these regions can keep higher amount of oxygen during heat treatment process.

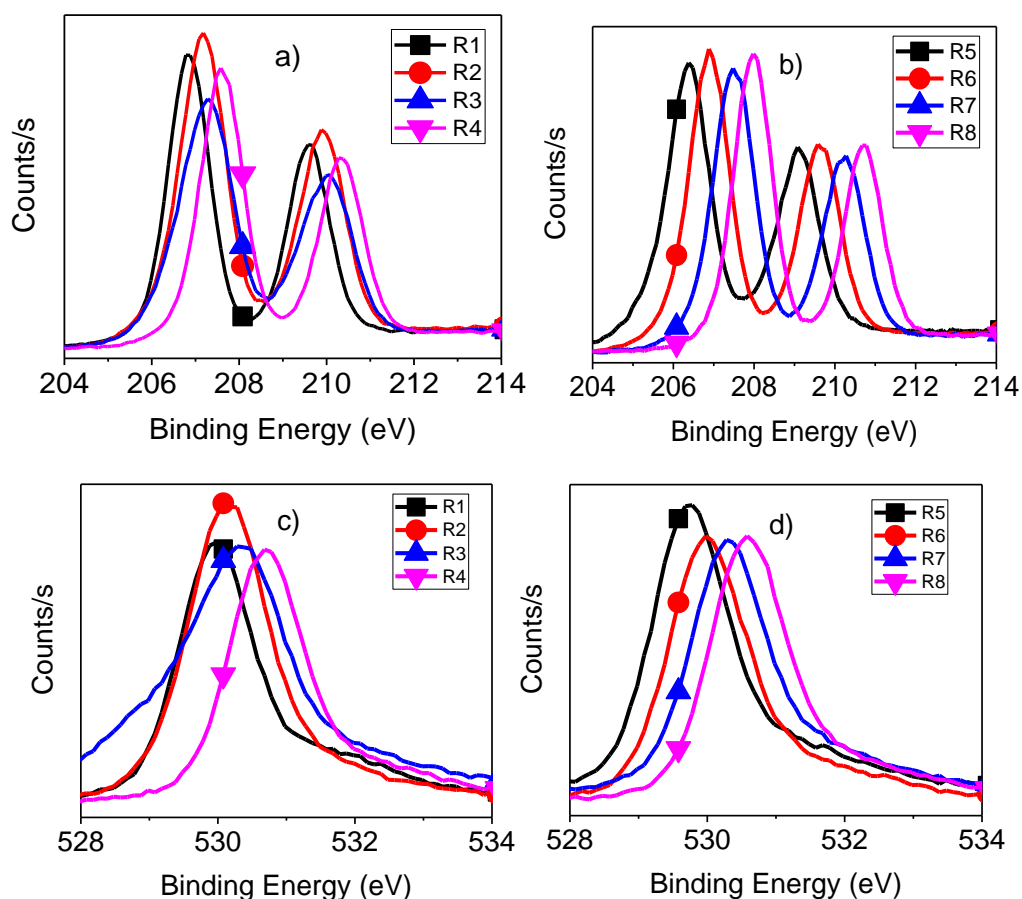


Figure 7.6. XPS analyses of  $\text{Nb}_2\text{O}_5$  thin films; a) Plasma assisted deposition condition for niobium, b) Non-plasma assisted deposition for niobium, c) Plasma assisted deposition condition for oxygen, d) Non-plasma assisted deposition for oxygen, e) Plasma assisted deposition condition for niobium (heat treated) and f) Non-plasma assisted deposition for niobium (heat treated).

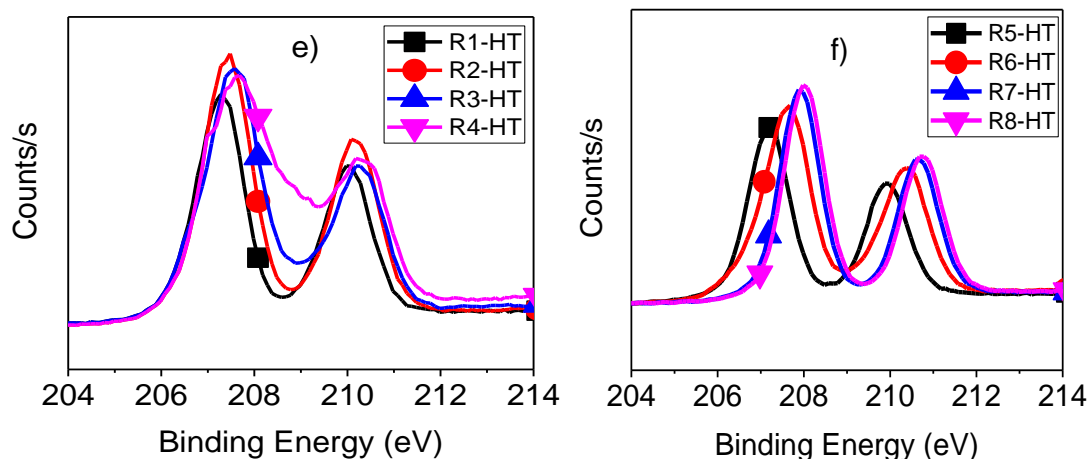


Figure 7.6 (Continued)

### 7.2.3. Characterization of Perovskite Solar Cells

Produced cells were firstly evaluated regarding interfaces between the layers. Figure 7.7 shows the SEM images of the intersection of both planar and mesoporous cells. The thickness of the compact layer was determined as 60 nm which is an optimized value for efficient electron transfer, hole blocking, and photonic transparency. It is seen that there are voids and discontinuities in the perovskite/ $\text{Nb}_2\text{O}_5$  blocking layer interface for planar architecture cells. Such an inhomogeneous perovskite layer is undesirable for solar cell applications because it hinders an efficient charge transfer between individual layers and possibly causing a decrease in the performance of the cell operation. Upon introduction of a mesoporous  $\text{TiO}_2$  layer on the blocking layer, a homogeneous void-free and continuous perovskite layer formation can be achieved. Such a mesoporous network can facilitate a proper wetting of the surface by the perovskite solution during spinning process and a more ideal structure can be formed.

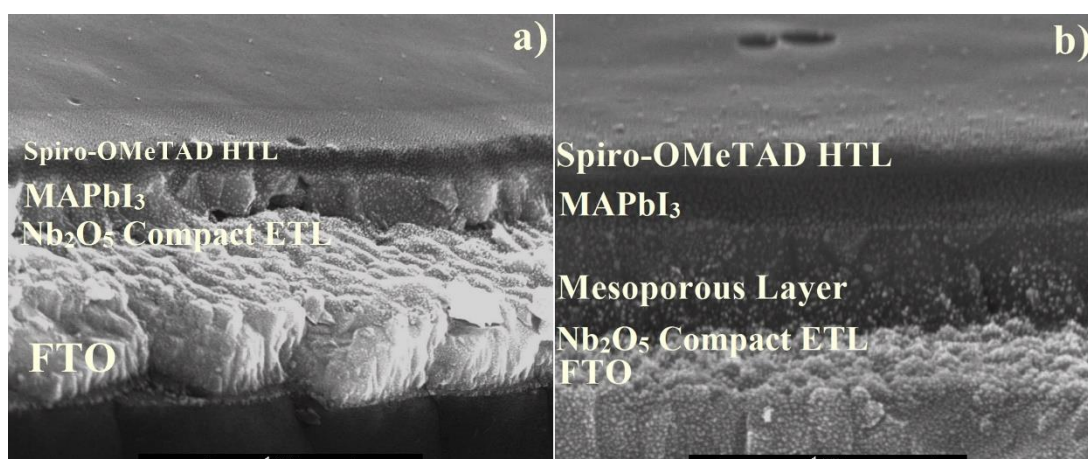


Figure 7.7. Cross sectional images of a) planar and b) mesoporous perovskite solar cells.

Secondly, cells were tested using current-voltage measurements under the illumination of simulated sunlight at  $100 \text{ mW/cm}^2$ . Planar, heat treated planar and mesoporous cell configurations were constructed and characterized. Firstly, as deposited compact  $\text{Nb}_2\text{O}_5$  layers were used in the planar cell configuration. Figure 7.8 shows current density-voltage characteristics of as deposited planar cells and measured photovoltaic parameters for all cell configurations are given in Table 7.3. In general, as deposited planar configured cells do not yield promising results. It is seen that plasma assistance leads to higher efficiency compared to non-plasma assisted films at high oxygen flow rate deposition conditions. Best cell in plasma assisted deposition condition is obtained at 25 sccm oxygen flow rate, however oxygen addition is detrimental for the non-plasma assisted conditions. Best as deposited planar cell yields 2.63 % conversion efficiency and it has 0.73 V  $V_{oc}$ ,  $9.41 \text{ mA/cm}^2$   $J_{sc}$  and 38.4 FF. Plasma assisted deposition produces denser films which can create positive effect for resistance to recombination. Also, it is sure that efficient electron transfer is strongly related to the band edge positions. Oxygen addition is required for better band matching for plasma assisted deposition; however, band matching is adversely affected from oxygen addition in non-plasma assisted deposition. Band gap values for different deposition conditions given in Table 7.2 show that these values for both

plasma assisted-25 sccm oxygen flow rate sample and non-plasma assisted-no oxygen sample produce the same 3.55 eV band gap. Although, larger band gap is advantageous to decrease recombination, band edge positions are negatively affected above 3.55 eV band gap. Therefore, the cell efficiencies are lowered at higher band gap compact Nb<sub>2</sub>O<sub>5</sub> layers.

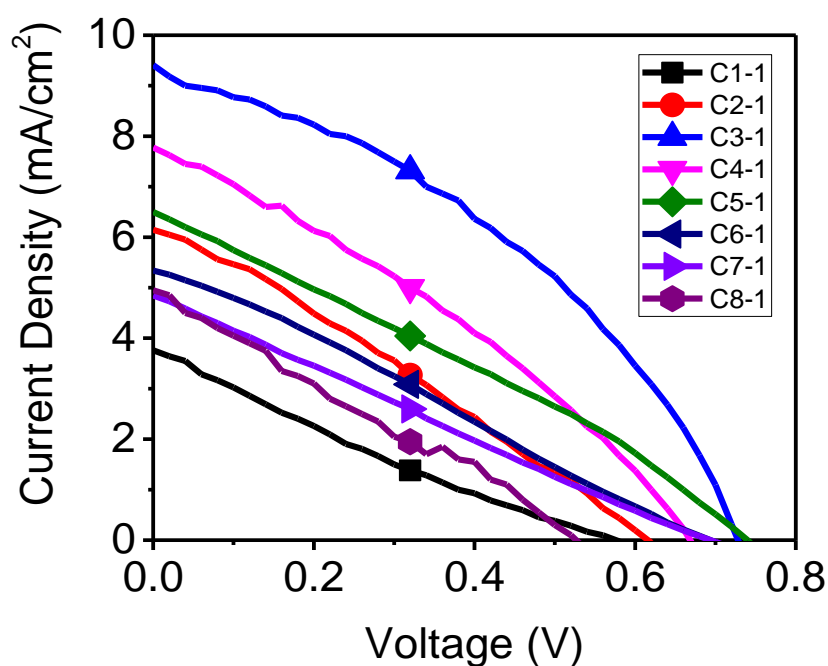


Figure 7.8. J-V graphs of as deposited Nb<sub>2</sub>O<sub>5</sub> compact layer used for perovskite solar cells of planar configuration.

Low performance of perovskite cell produced using as deposited Nb<sub>2</sub>O<sub>5</sub> compact layer forwards the study to working at high temperature annealing conditions. Due to the use of glass substrate, annealing process was performed at 500°C. Figure 7.9 gives the J-V graphs of the cells and results are given in Table 7.3. XRD result shows that crystallinity is not formed after the annealing process similar to the case of as deposited condition. Also, annealing yields larger band gap thin films compared to the as deposited forms. For the as deposited cells, it is found that there is a band gap

limitation for better cell performance. Due to the larger band gap nature, heat treatment heals the cell performance compared to as deposited condition. Denser structure of heat treated samples is observed using refractive index dispersion given in Figure 7.2c and Figure 7.2d. Denser films supply better charge transport with better cell performance. Also, obtained band gap and refractive index distributions are similar for all deposition conditions after heat treatment; however, there is a considerable difference in cell performances depending on deposition condition. This can be due to the conduction band edge position matching of compact layer and perovskite layer for efficient charge extraction. Another factor can be the structural consistence between the perovskite and compact layer. Highest efficiency is obtained when 25 sccm oxygen flow rate and plasma assisted deposition condition is used where photoconversion efficiency reaches to 5.33%. Open circuit voltage was obtained as 0.81 V which is 10% higher than the as deposited compact layer condition. Annealing also results in better fill factor, which increases from 38.4% to 48.7%. Especially shunt resistance becomes better compared to the as deposited condition which is realized by the removal of alternative pathways for the charge carriers. Short current density is not affected from heat treatment in a positive manner. Current density is directly related to the number of absorbed photons by the perovskite layer. In all deposition conditions, compact layer was produced with low absorption; therefore all the photons easily pass through the compact layer and can reach perovskite. However, differences in the current density values between different deposition conditions given in Table 7.3 can be related to the non-uniformity of perovskite layer on top of the compact layer where low efficiency values obtained from planar cells are mainly due to this interface problem as seen in cross-sectional SEM images in Figure 7.7. We believe that adduct method employed in this study, fails to generate a solid and continuous perovskite layer with the Nb<sub>2</sub>O<sub>5</sub> compact layers.

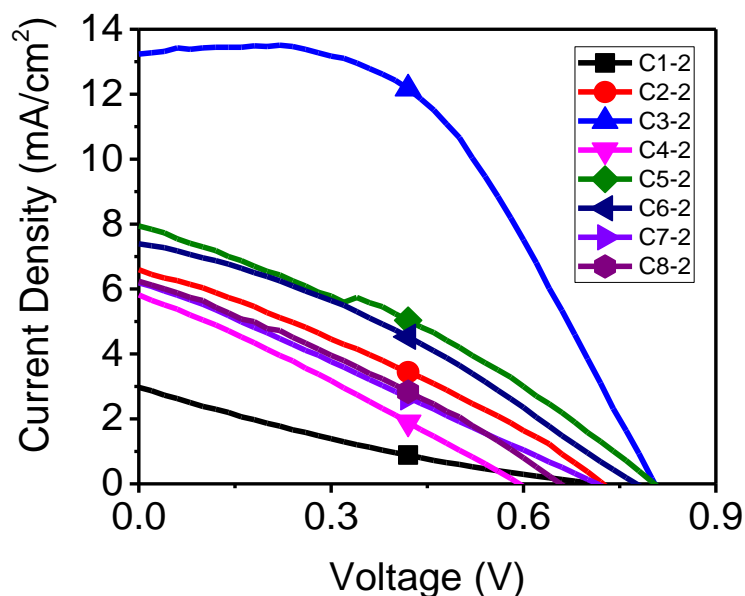


Figure 7.9. J-V graphs of heat treated Nb<sub>2</sub>O<sub>5</sub> compact layer used for the production of planar perovskite solar cells.

Mesoporous perovskite cells were constructed to observe the effect of addition of a mesoporous layer to provide a better host for perovskite formation. TiO<sub>2</sub> mesoporous layer was deposited on top of compact Nb<sub>2</sub>O<sub>5</sub> layer. Mesoporous layer can be used in active and passive situation regarding to electron transfer. Passive mesoporous layers are used for template purposes for the perovskite layer and they have insulator nature, also referred as scaffolding layer. Active mesoporous layer serves as both template and electron transfer layer. Planar cells, which are produced using as deposited and heat treated Nb<sub>2</sub>O<sub>5</sub> compact layer, suffered from uniformity problems between compact layer and perovskite layer. Therefore, the use of mesoporous layer becomes crucial. J-V curves of perovskite cells produced using mesoporous layer are given in Figure 7.10. Similar to planar cells, best cell is obtained when 25 sccm oxygen flow rate is used in plasma assisted deposition and also without oxygen addition for the non-plasma assisted deposition. The use of mesoporous layer doubles the cell efficiency compared to best cell in planar configuration. Photoconversion efficiency for plasma assisted and non-plasma assisted conditions reached to 13.87 % and 12.95

%, respectively. For all deposition conditions, better FF is obtained together with a lower series resistance and a higher shunt resistance compared to planar counterparts. Fill factor of the best cell becomes 69.6 %. The best cell for non-plasma assisted deposition condition provides 0.07 V higher open circuit voltage compared to the best cell produced with plasma assisted deposition. The cell with non-plasma assisted compact layer yields 0.2 eV lower band gap compared to the cell produced using plasma assisted compact layer. This difference probably provides a better conduction band matching with mesoporous TiO<sub>2</sub> layer which results in efficient electron transport. Whereas, plasma assisted deposition generates higher photocurrent density possibly due to the less defective nature of the compact layer. Employing Nb<sub>2</sub>O<sub>5</sub>/m-TiO<sub>2</sub> electron transport layer has some advantages over widely used c-TiO<sub>2</sub>/m-TiO<sub>2</sub> configuration. Nb<sub>2</sub>O<sub>5</sub>/m-TiO<sub>2</sub> bilayer offers better charge extraction due to its matched conduction band position. Nb<sub>2</sub>O<sub>5</sub> has lower valence band position which minimizes the possible recombination processes. Also, the use of Nb<sub>2</sub>O<sub>5</sub> lowers charge accumulation at the perovskite electron transport layer interface, which is also advantageous for enhanced cell performance.

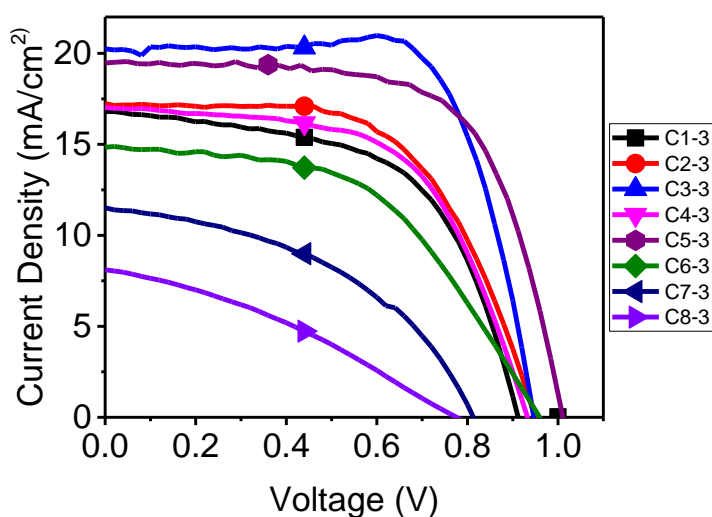


Figure 7.10. J-V graphs of perovskite cells produced using mesoporous TiO<sub>2</sub> layer and Nb<sub>2</sub>O<sub>5</sub> compact layer.

Table 7.3. Measured photovoltaic parameters for all cell configurations.

	Voc (V)	Jsc (mA/cm <sup>2</sup> )	Fill Factor (%)	Efficiency (%)
<b>Planar Configuration</b>				
C1-1	0.57	3.76	21.9	0.47
C2-1	0.61	6.15	28.5	1.07
C3-1	0.73	9.41	38.4	2.63
C4-1	0.67	7.78	31.9	1.66
C5-1	0.74	6.50	28.7	1.38
C6-1	0.69	5.34	26.8	0.99
C7-1	0.69	4.84	24.9	0.83
C8-1	0.53	4.95	25.4	0.67
<b>Heat Treated Planar Configuration</b>				
C1-2	0.71	2.97	19.7	0.42
C2-2	0.73	6.60	30.0	1.45
C3-2	0.81	13.51	48.7	5.33
C4-2	0.59	5.82	27.8	0.95
C5-2	0.81	7.94	33.3	2.14
C6-2	0.77	7.39	33.4	1.90
C7-2	0.71	6.19	26.3	1.16
C8-2	0.65	6.24	30.3	1.23
<b>Mesoporous Cell Configuration</b>				
C1-3	0.91	16.81	58.0	8.86
C2-3	0.95	17.25	59.3	9.71
C3-3	0.95	20.98	69.6	13.87
C4-3	0.93	17.02	59.1	9.35
C5-3	1.02	19.55	64.9	12.95
C6-3	0.95	14.89	51.8	7.33
C7-3	0.81	11.52	44.5	4.15
C8-3	0.77	8.11	33.4	2.09

In order to further investigate and understand the dynamics regarding the variations in the performances of different architectures, electrochemical impedance spectroscopy measurements were conducted on each type of cell architecture. Charge transfer ( $R_{ct}$ ) and recombination resistances ( $R_{rec}$ ) were extracted from the Nyquist plots of the cells using the equivalent circuit given in Figure 7.11 and the results are given in Table 7.4. There are two major semicircles which represent charge transfer resistances in the

high frequency region and recombination resistances in the middle frequency region. A third feature is observed for heat treated planar cells and mesoporous cells which is related to ionic motion. The capacitances were replaced with constant phase elements for a better fitting procedure due to the fact that individual layers may not be perfectly smooth and defect free. The electrochemical impedance measurements revealed that major contribution of the heat treatment of the planar cells is the improvement in the charge transfer resistance of the cells. Although heat treated Nb<sub>2</sub>O<sub>5</sub> layer based cells possess higher recombination resistances, the enhancement of the overall efficiency of the heat treated planar cells is related to the reduced charge transfer between individual layers, especially the Nb<sub>2</sub>O<sub>5</sub>/perovskite interface, which leads to enhanced charge collection inside the cells. However, heat treated Nb<sub>2</sub>O<sub>5</sub> based planar cells still suffer from high recombination rates. Introduction of the mesoporous TiO<sub>2</sub> layer greatly increases the recombination resistance of the cells up to 4 fold and is the main reason of the outstanding photovoltaic performance of the mesoporous cells compared to the planar cells. Reduced recombination rate manifests itself as an improvement especially in the open circuit voltage and fill factor values as expected. Voltages up to 1.02 V and fill factor of 0.7 could be achieved by reducing the recombination rates combined with a low charge transfer resistance and efficiencies up to 13% could be obtained.

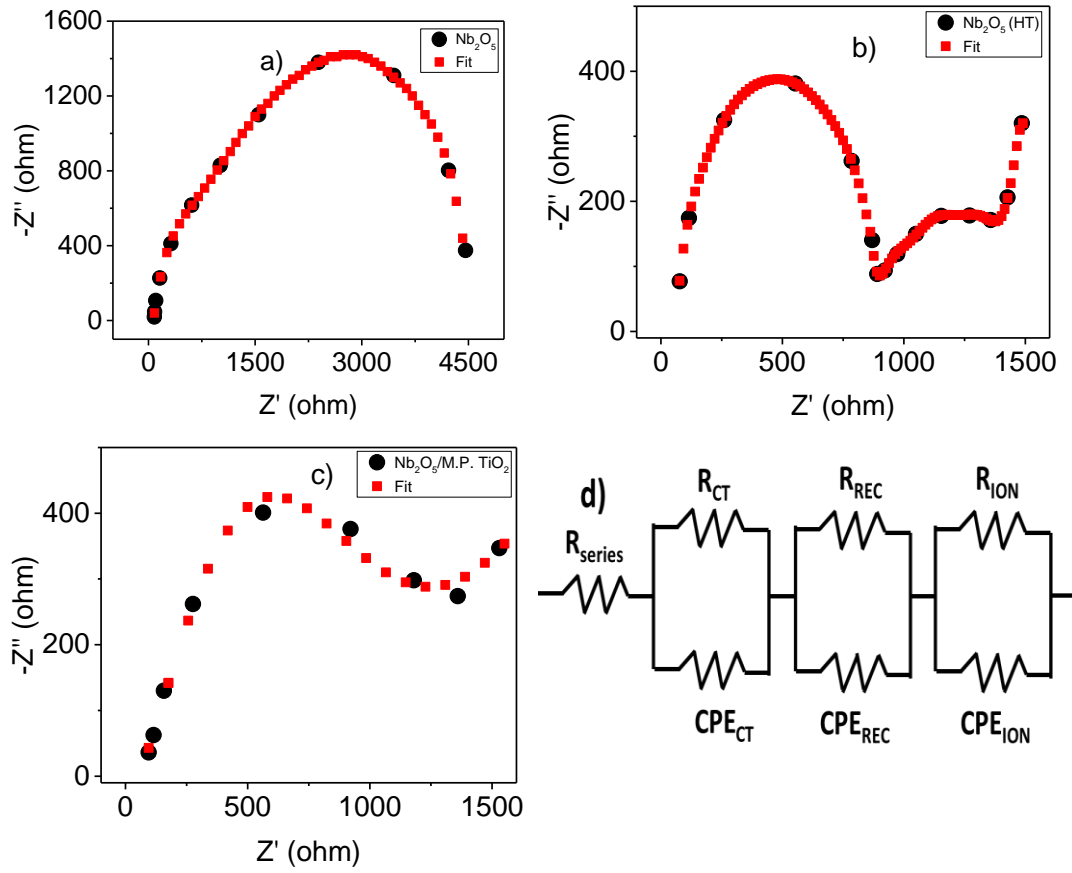


Figure 7.11. Nyquist plots of the cells produced using a) Planar Nb<sub>2</sub>O<sub>5</sub>, b) Planar heat treated Nb<sub>2</sub>O<sub>5</sub>, c) Nb<sub>2</sub>O<sub>5</sub> compact layer and mesoporous TiO<sub>2</sub> and d) Equivalent circuit model used to fit the impedance data.

Table 7.4. Charge transfer (*R<sub>ct</sub>*) and recombination (*R<sub>rec</sub>*) resistances of the cells.

	<i>R<sub>ct</sub></i> (ohm.cm <sup>2</sup> )	<i>R<sub>rec</sub></i> (ohm.cm <sup>2</sup> )
Nb <sub>2</sub> O <sub>5</sub> planar	3168	3911
Nb <sub>2</sub> O <sub>5</sub> planar (H.T.)	880	966
Nb <sub>2</sub> O <sub>5</sub> / M.P. TiO <sub>2</sub>	1362	4036

### 7.3. Conclusion

$\text{Nb}_2\text{O}_5$  compact layer was used in the production of perovskite solar cell instead of widely used  $\text{TiO}_2$  compact layer.  $\text{Nb}_2\text{O}_5$  compact layers were deposited by means of electron beam evaporation method which is a highly reproducible and defect free technique. In order to tune the possible effects of deposition parameters, single layer  $\text{Nb}_2\text{O}_5$  thin films were produced at different oxygen flow rate and plasma assistance conditions. Compact layers used in solar cells should be highly transparent to the incoming photons for efficient light harvesting. It was seen that films indicated a highly absorbing nature when no oxygen addition was used in the depositions. Plasma assistance leads to the formation of stoichiometric films with minimized absorption. However, heat treatments minimize the absorption for all deposition conditions. Low oxygen flow rate and plasma assistance provide low porosity with high refractive index. High oxygen flow rates yielded higher band gap values due to reduced oxygen vacancy sites. Plasma assistance lowers the band gap because of localized state formation which results in lower conduction band edge and heat treatment increases the band gap due to the enhancement in carrier concentration. XRD studies and SEM images show that compact layers were produced in amorphous nature, defect free and well adherence conditions. XPS results indicate that oxygen addition is crucial to obtain stoichiometric form of compact layer. Although 10 sccm is enough for plasma assisted deposition condition, whereas 25 sccm oxygen flow rate should be supplied for non-plasma assisted deposition. SEM images showed some interface problems when cells were produced in planar configurations. However, mesoporous layer serves as a host for a more homogeneous perovskite layer formation. Mesoporous cells dramatically increase cell efficiencies compared to the planar and heat treated planar cell configurations. Oxygen additions yield improved cell efficiencies for the plasma assisted deposition condition; however, oxygen addition decreases the cell performance for non-plasma assisted deposition. We relate this decrease to the movement of band edge and suppressed charge transfer between the perovskite and the  $\text{Nb}_2\text{O}_5$  layer. Best cell performances are 13.87 % and 12.95 % for plasma assisted

and non-plasma assisted conditions, respectively. EIS measurements revealed that main reason is the enhancement of charge transfer for the heat treated planar cells compared to the as deposited films. Suppressed recombination is the main reason of enhancement for the mesoporous cell configuration due to improved interface characteristics compared to the planar architecture.

## REFERENCES

- [1] A. Kojima, K. Teshima, Y. Shirai, T. Miyasaka, Organometal halide perovskites as visible-light sensitizers for photovoltaic cells, *Journal of the American Chemical Society*, 131 (2009) 6050-6051.
- [2] H.-S. Kim, C.-R. Lee, J.-H. Im, K.-B. Lee, T. Moehl, A. Marchioro, S.-J. Moon, R. Humphry-Baker, J.-H. Yum, J. E. Moser, M. Grätzel, N.-G. Park, Lead iodide perovskite sensitized all-solid-state submicron thin film mesoscopic solar cell with efficiency exceeding 9%, *Scientific reports*, 2 (2012) 591.
- [3] <https://www.Nrel.Gov/pv/assets/images/efficiency-chart.Png>, in, 2019.
- [4] Z. Guo, L. Gao, C. Zhang, Z. Xu, T. Ma, Low-temperature processed non-TiO<sub>2</sub> electron selective layers for perovskite solar cells, *Journal of Materials Chemistry A*, 6 (2018) 4572-4589.
- [5] R. Ranjan, A. Prakash, A. Singh, A. Singh, A. Garg, R. K. Gupta, Effect of tantalum doping in a TiO<sub>2</sub> compact layer on the performance of planar spiro-ometad free perovskite solar cells, *Journal of Materials Chemistry A*, 6 (2018) 1037-1047.
- [6] M. F. M. Noh, C. H. Teh, R. Daik, E. L. Lim, C. C. Yap, M. A. Ibrahim, N. A. Ludin, A. R. bin Mohd Yusoff, J. Jang, M. A. M. Teridi, The architecture of the electron transport layer for a perovskite solar cell, *Journal of Materials Chemistry C*, (2018)
- [7] T. Ye, J. Xing, M. Petrović, S. Chen, V. Chellappan, G. S. Subramanian, T. C. Sum, B. Liu, Q. Xiong, S. Ramakrishna, Temperature effect of the compact TiO<sub>2</sub> layer in planar perovskite solar cells: An interfacial electrical, optical and carrier mobility study, *Solar Energy Materials and Solar Cells*, 163 (2017) 242-249.
- [8] H. J. Snaith, A. Abate, J. M. Ball, G. E. Eperon, T. Leijtens, N. K. Noel, S. D. Stranks, J. T.-W. Wang, K. Wojciechowski, W. Zhang, Anomalous hysteresis in perovskite solar cells, *The journal of physical chemistry letters*, 5 (2014) 1511-1515.
- [9] J. H. Heo, H. J. Han, D. Kim, T. K. Ahn, S. H. Im, Hysteresis-less inverted CH<sub>3</sub>NH<sub>3</sub>PbI<sub>3</sub> planar perovskite hybrid solar cells with 18.1% power conversion efficiency, *Energy & Environmental Science*, 8 (2015) 1602-1608.
- [10] Z. Song, S. C. Watthage, A. B. Phillips, M. J. Heben, Pathways toward high-performance perovskite solar cells: Review of recent advances in organo-metal halide

perovskites for photovoltaic applications, *Journal of Photonics for Energy*, 6 (2016) 022001.

[11] X. Zhang, H. Tian, X. Wang, G. Xue, Z. Tian, J. Zhang, S. Yuan, T. Yu, Z. Zou, The role of oxygen vacancy-Ti<sup>3+</sup> states on TiO<sub>2</sub> nanotubes' surface in dye-sensitized solar cells, *Materials Letters*, 100 (2013) 51-53.

[12] T. Su, Y. Yang, Y. Na, R. Fan, L. Li, L. Wei, B. Yang, W. Cao, An insight into the role of oxygen vacancy in hydrogenated TiO<sub>2</sub> nanocrystals in the performance of dye-sensitized solar cells, *ACS applied materials & interfaces*, 7 (2015) 3754-3763.

[13] J. Song, S. Li, Y. Zhao, J. Yuan, Y. Zhu, Y. Fang, L. Zhu, X. Gu, Y. Qiang, Performance enhancement of perovskite solar cells by doping TiO<sub>2</sub> blocking layer with group vb elements, *Journal of Alloys and Compounds*, 694 (2017) 1232-1238.

[14] J. Yang, B. D. Siempelkamp, E. Mosconi, F. De Angelis, T. L. Kelly, Origin of the thermal instability in CH<sub>3</sub>NH<sub>3</sub>PbI<sub>3</sub> thin films deposited on zno, *Chemistry of Materials*, 27 (2015) 4229-4236.

[15] Q. Hu, J. Wu, C. Jiang, T. Liu, X. Que, R. Zhu, Q. Gong, Engineering of electron-selective contact for perovskite solar cells with efficiency exceeding 15%, *ACS nano*, 8 (2014) 10161-10167.

[16] W. Ke, G. Fang, Q. Liu, L. Xiong, P. Qin, H. Tao, J. Wang, H. Lei, B. Li, J. Wan, Low-temperature solution-processed tin oxide as an alternative electron transporting layer for efficient perovskite solar cells, *Journal of the American Chemical Society*, 137 (2015) 6730-6733.

[17] K. Wang, Y. Shi, Q. Dong, Y. Li, S. Wang, X. Yu, M. Wu, T. Ma, Low-temperature and solution-processed amorphous WO<sub>x</sub> as electron-selective layer for perovskite solar cells, *The journal of physical chemistry letters*, 6 (2015) 755-759.

[18] J. Feng, Z. Yang, D. Yang, X. Ren, X. Zhu, Z. Jin, W. Zi, Q. Wei, S. F. Liu, E-beam evaporated Nb<sub>2</sub>O<sub>5</sub> as an effective electron transport layer for large flexible perovskite solar cells, *Nano Energy*, 36 (2017) 1-8.

[19] A. K. Chilvery, A. K. Batra, B. Yang, K. Xiao, P. Guggilla, M. D. Aggarwal, R. Surabhi, R. B. Lal, J. R. Currie, B. G. Penn, Perovskites: Transforming photovoltaics, a mini-review, *Journal of Photonics for Energy*, 5 (2015) 057402.

[20] H. Si, Q. Liao, Z. Zhang, Y. Li, X. Yang, G. Zhang, Z. Kang, Y. Zhang, An innovative design of perovskite solar cells with Al<sub>2</sub>O<sub>3</sub> inserting at zno/perovskite interface for improving the performance and stability, *Nano Energy*, 22 (2016) 223-231.

- [21] S. L. Fernandes, A. C. Véron, N. F. Neto, F. A. Nüesch, J. H. D. da Silva, M. A. Zaghete, F. d. O. Carlos, Nb<sub>2</sub>O<sub>5</sub> hole blocking layer for hysteresis-free perovskite solar cells, *Materials Letters*, 181 (2016) 103-107.
- [22] R. A. Rani, A. S. Zoolfakar, A. P. O'Mullane, M. W. Austin, K. Kalantar-Zadeh, Thin films and nanostructures of niobium pentoxide: Fundamental properties, synthesis methods and applications, *Journal of Materials Chemistry A*, 2 (2014) 15683-15703.
- [23] M. S. Jamal, M. S. Bashar, A. K. M. Hasan, Z. A. Almutairi, H. F. Alharbi, N. H. Alharthi, M. R. Karim, H. Misran, N. Amin, K. B. Sopian, M. Akhtaruzzaman, Fabrication techniques and morphological analysis of perovskite absorber layer for high-efficiency perovskite solar cell: A review, *Renewable and Sustainable Energy Reviews*, 98 (2018) 469-488.
- [24] N. Ahn, D.-Y. Son, I.-H. Jang, S. M. Kang, M. Choi, N.-G. Park, Highly reproducible perovskite solar cells with average efficiency of 18.3% and best efficiency of 19.7% fabricated via lewis base adduct of lead(ii) iodide, *Journal of the American Chemical Society*, 137 (2015) 8696-8699.
- [25] N. R. Murphy, L. Sun, J. T. Grant, J. G. Jones, R. Jakubiak, Molybdenum oxides deposited by modulated pulse power magnetron sputtering: Stoichiometry as a function of process parameters, *Journal of Electronic Materials*, 44 (2015) 3677-3686.
- [26] P.-k. Chiu, Y.-T. Liao, H.-Y. Tsai, D. Chiang, Effect of electron-beam deposition process variables on the film characteristics of the CrO<sub>x</sub> films, *AIP Advances*, 8 (2018) 025016.
- [27] M. B. Cosar, K. C. Icli, M. Ozenbas, Plasma assisted low temperature electron beam deposited NiO thin films for electro-optic applications, *Journal of Vacuum Science & Technology A*, 36 (2018) 031501.
- [28] Y.-C. Ji, H.-X. Zhang, X.-H. Zhang, Z.-Q. Li, Structures, optical properties, and electrical transport processes of SnO<sub>2</sub> films with oxygen deficiencies, *physica status solidi (b)*, 250 (2013) 2145-2152.
- [29] N. Usha, R. Sivakumar, C. Sanjeeviraja, M. Arivanandhan, Niobium pentoxide (Nb<sub>2</sub>O<sub>5</sub>) thin films: Rf power and substrate temperature induced changes in physical properties, *Optik - International Journal for Light and Electron Optics*, 126 (2015) 1945-1950.

- [30] X. Xiao, G. Dong, C. Xu, H. He, H. Qi, Z. Fan, J. Shao, Structure and optical properties of Nb<sub>2</sub>O<sub>5</sub> sculptured thin films by glancing angle deposition, *Applied Surface Science*, 255 (2008) 2192-2195.
- [31] R. Lorenz, M. O'Sullivan, A. Fian, D. Sprenger, B. Lang, C. Mitterer, Effects of bias pulse frequencies on reactively sputter deposited NbO<sub>x</sub> films, *Thin Solid Films*, 660 (2018) 335-342.
- [32] Ö. D. Coşkun, S. Demirel, G. Atak, The effects of heat treatment on optical, structural, electrochromic and bonding properties of Nb<sub>2</sub>O<sub>5</sub> thin films, *Journal of Alloys and Compounds*, 648 (2015) 994-1004.
- [33] A. Mozalev, R. M. Vázquez, C. Bittencourt, D. Cossement, F. Gispert-Guirado, E. Llobet, H. Habazaki, Formation–structure–properties of niobium-oxide nanocolumn arrays via self-organized anodization of sputter-deposited aluminum-on-niobium layers, *Journal of Materials Chemistry C*, 2 (2014) 4847-4860.

## CHAPTER 8

### SUMMARY, CONCLUSIONS AND SUGGESTIONS

Electron beam evaporation is an important production technique for thin films. This method yields high quality, uniform, dense materials and a reliable production technique for thin films. There are some studies in literature to produce thin film layers of the perovskite solar cells using this method. This study focuses on the use of this method for the development of charge transport layers. Charge transport layers can be produced in different structural, optical and electrical properties depending on the parameters which are used in electron beam evaporation process. Oxide based thin films were used as charge transport layers and these thin films are formed in oxygen deficient nature. Therefore, oxygen flow ratio was determined as primary parameter. Additionally, plasma assistance, deposition temperature and deposition rate are the other evaluated process parameters. During the development period of thin films, they were studied in single layer form which was deposited using above defined process parameters at different values.

The use of inorganic alternative materials instead of spiro-OMeTAD hole transport layer (HTL) is a popular topic for perovskite solar cells. NiO is the most pronounced alternative of these materials due to its suitable band edges with perovskite absorber and good optical and electrical properties. There are studies in literature for the use of NiO as HTL which are mostly based on p-i-n (inverted) cell architecture due to the production difficulties encountered in the formation of n-i-p architecture. Electron beam evaporation provides an option to deposit oxide materials without the requirement of further post processing. This idea is used as a motivation in this study and for the deposition of NiO HTL in n-i-p (normal) architecture on perovskite absorbers. Addition to NiO, this thesis also evaluates the possible usage of TiO as

HTL. TiO is a very interesting material due to its metallically conducting nature and it also shows a p-type conductivity. This condition makes it a possible candidate for hole conduction. Like in NiO, normal n-i-p architecture in cell design is applied for TiO HTL. For both of the materials, structural, optical and electrical properties strictly depend on the deposition condition. For this reason, single layers of these materials were evaluated firstly and the results were used to understand their effects on perovskite solar cells. In the final study, the use of Nb<sub>2</sub>O<sub>5</sub> was evaluated for electron conducting purposes. This material was also deposited using electron beam evaporation and similarly, best deposition condition was searched for the Nb<sub>2</sub>O<sub>5</sub> thin films. In the following, performed studies will be summarized.

- NiO thin films were deposited at a thickness of 250 nm on top of glass substrates using electron beam evaporation technique. Deposition was performed by the sublimation of chunky particles. Single layer thin films of NiO were produced at different values of oxygen flow rates, deposition temperatures, deposition rates and plasma assistance as process parameters. The first observation is the morphology dependence of the NiO thin film on the deposition temperature. For low deposition temperature dominant morphology is spherical, it becomes firstly needle and later transforms to cuboidal with the increase in deposition temperature. According to XRD analysis, NiO was formed in cubic crystal structure with (111) plane as the dominant plane. The (111) diffraction peak was used to calculate the grain size and lattice parameter of NiO thin films. Calculated results showed that there is a tendency to have larger grain size and lattice size with the increase in oxygen flow rate. NiO thin films were obtained at minimized absorption where the deposition conditions used are higher oxygen flow rate or higher deposition temperature or lower deposition rate. Calculated refractive index values using the reflectance results are good indicators for the density of thin films. Denser films were deposited when the deposition conditions set to low oxygen flow rate or high deposition temperature or low deposition rate. Lowest resistivity

is measured as  $1.5 \times 10^2$  ( $\Omega \cdot \text{cm}$ ) when the deposition was carried out without oxygen addition and under plasma assistance. Although this sample has low mobility, carrier concentration was too high. This condition is directly related to denser films with higher crystallinity. Also, tunability of the band positions with deposition conditions was presented. The valence band edge of NiO films varies between -5.12 and -5.50 eV, which is quite suitable for most organic and metalorganic perovskite based solar devices.

- TiO thin films are suitable for many interesting applications due to their superior properties in hardness, decorative coloring, thermoelectric properties, gas sensing and electrical conductivity. These unique properties are related with the structural vacancy concentration. Also, titanium monoxide provides p-type conductivity which makes it possible candidate for hole transportation in perovskite solar cells. Titanium monoxide thin films were deposited at a thickness of 300 nm using electron beam evaporation technique. Additional oxygen was introduced to vacuum chamber at different amounts during the deposition. Deposition temperature was kept at around  $80^\circ\text{C}$  which is also suitable for sensitive substrates. TiO thin films yield crystallinity without high temperature heat treatment requirements. XPS and XRD analyses provide consistent results that transformation from TiO to  $\text{TiO}_2$  was realized at oxygen flow rates higher than 25 sccm. Additional oxygen firstly creates partial +3 state and +4 state becomes dominant when oxygen flow rate is 50 sccm. Produced thin films exhibit dense and homogeneous structure and they were well adhered to the substrate as confirmed by SEM analysis. Thin films which were produced at 0 and 1 sccm oxygen flow rates yield completely non-transparent films. Thin films become transparent with increase in oxygen amount. The results of band gap and UPS analysis show consistency such that band gap is firstly lowered with the addition of 1 sccm oxygen flow rate compared to oxygen free deposition conditions and following increase in oxygen flow rates increase the band gap of thin films. First decrease is due to

the Moss-Burstein effect in which Fermi energy level is formed under the valence band which provides a higher band gap for oxygen free deposition condition compared to 1 sccm oxygen flow rate condition. Deposited TiO films have high carrier concentration and high electrical conductivity and possess p-type characteristic.

- These NiO and TiO thin films were used in the production of perovskite solar cells as hole transport layer. Cells were produced in n-i-p configuration using TiO<sub>2</sub> compact, TiO<sub>2</sub> mesoporous layer and CH<sub>3</sub>NH<sub>3</sub>PbI<sub>3</sub> perovskite layer. This study consists of three sub studies. As a first study, suitable deposition conditions were evaluated for titanium dioxide compact layer. Defect free compact layer formation was presented by SEM images. It is obtained that crystallinity was obtained after the heat treatment process, opposite to the formation of amorphous structure in as deposited condition. Also, higher oxygen flow rate minimizes the absorption and produces more stoichiometric structure; for this reason, 25 sccm oxygen flow rate deposition condition was used in the production of TiO<sub>2</sub> compact layer. Secondly, perovskite thin films were examined regarding to their crystal structure and morphology. Perovskite absorbers were obtained at high quality due to the formation of perovskite absorber in fully dense and the presence of only CH<sub>3</sub>NH<sub>3</sub>PbI<sub>3</sub> phase. Finally, optimized electron beam deposition condition check was carried out for NiO and TiO HTLs. Controlled deposition parameters were selected as different deposition temperature, oxygen flow rate and layer thicknesses for the deposition of NiO HTL. Oxygen flow rate and coating thickness are the changing parameters for the use of TiO HTL. Photoconversion efficiency of perovskite solar cells heals with increase in oxygen flow rate during the deposition of NiO HTL. Main reason of the performance healing is the enhancement of conductivity with increase in oxygen flow rate. Performance healing no longer continues at 50 sccm oxygen flow rate due to the fact that too much increase in band gap yields damaging of the band levelling. Best cell

performance was obtained when the deposition temperature is 80°C. The decrease in the cell performance is due to the low conductivity at lower deposition temperatures and formation of cuboidal structure at higher deposition temperatures. 75 nm HTL thickness maximizes the cell efficiency as 6.13 %. This cell provides a high current density and fill factor due to the good coverage of the film on the perovskite layer. TiO HTLs were firstly deposited using different coating thicknesses in perovskite solar cells. Highest performance was obtained when the thickness of the TiO layer is 25 nm. This thickness of the TiO thin film yields a good coverage of the substrate surface together with a high charge extraction. Study was followed by the production of TiO at different oxygen flow rates. Highest open circuit voltage was obtained when the deposition was carried out at 1 sccm oxygen flow rate. While oxygen free deposition condition creates metallic TiO, small amount of oxygen provides p-type conductivity. However, more addition of oxygen dramatically decreases the conductivity of TiO thin film. Best cell performance was obtained as 5.72 % efficiency when 2 sccm oxygen flow rate is used due to the high photocurrent and fill factor values of the cell.

- Final study evaluates the use of electron beam evaporated Nb<sub>2</sub>O<sub>5</sub> thin films as compact electron transport layer instead of widely used counterpart of TiO<sub>2</sub> for the production of perovskite solar cells. Nb<sub>2</sub>O<sub>5</sub> thin films were deposited in single layer form using the deposition parameters of different oxygen flow rate and plasma assistance conditions. As a first inference, thin films yield an absorbing nature when the deposition is carried out without any oxygen addition. This absorbing character lowers the transmittance and it is an unwanted condition for efficient light harvesting. Additionally, the increase in oxygen flow rate and plasma assisted deposition minimize the absorption providing stoichiometry of thin films. Thin films were formed at higher band gap when higher oxygen flow rate was used due to the reduced oxygen vacancy sites. Plasma assistance provides lower band gap because of the localized state

formation. Thin films were created in good adherence to the substrate with defect free and amorphous nature. Oxygen addition is an important parameter which controls stoichiometry. Compared to non-plasma assisted deposition, stoichiometric Nb<sub>2</sub>O<sub>5</sub> thin films were sustained at lower oxygen flow rates. Electron transport layer was used in the forms of Nb<sub>2</sub>O<sub>5</sub> compact layer, heat treated Nb<sub>2</sub>O<sub>5</sub> compact layer and Nb<sub>2</sub>O<sub>5</sub> compact – TiO<sub>2</sub> mesoporous bilayer. Perovskite absorber was not well-spread on the Nb<sub>2</sub>O<sub>5</sub> compact layer and interface problems were observed. Introduction of the mesoporous layer provides a good host for the homogenous deposition of perovskite layer. Mesoporous cells dramatically increase cell efficiencies compared to the planar and heat treated planar cell configurations. Oxygen additions yield improved cell efficiencies for the plasma assisted deposition condition; however, oxygen addition decreases the cell performance for non-plasma assisted deposition. Band edges of Nb<sub>2</sub>O<sub>5</sub> thin films can be tuned by controlling the oxygen flow rate and this condition supplies better charge transport. Best cell performances are 13.87 % and 12.95 % for plasma assisted and non-plasma assisted conditions, respectively. Resistance to recombination was obtained at higher value in mesoporous cell configuration compared to planar configuration in electrochemical impedance measurements due to the improved interface characteristics.

This thesis aimed the production of perovskite solar cells based on inorganic ETLs and HTLs which were produced using electron beam evaporation. Also, produced perovskite solar cells were evaluated using the knowledge which was obtained from the single layer deposition of inorganic charge transport layers. Performed studies in this thesis provided a new approach for the deposition of inorganic HTLs in normal (n-i-p) configuration. Although there are a few studies using of NiO as HTL, this is the first study which uses TiO as HTL. Also, this study presented the importance of Nb<sub>2</sub>O<sub>5</sub> as ETL. Also, all the layers were deposited at around 80°C which showed the performance of these coating on flexible polymeric substrates.

Photo conversion efficiencies of the cells do not provide a sufficient performance for the replacement of these materials as the alternative materials; however, obtained cell performances are promising for the future studies.

Some of the possible future studies can be described as below:

- Thickness optimization for perovskite absorber should be studied for better charge transfer process between the absorber and inorganic charge transport layers.
- Alternative perovskite absorbers should be studied to provide better band edge matching with inorganic charge transport layers.
- Electron beam evaporation technique can be compared with the sputtered deposition of inorganic charge transport layers.
- Hole transport layers can be deposited on the tilted substrates to provide better coverage of perovskite absorber.
- Studies performed in this thesis can be applied on flexible polymeric substrates.
- Lower deposition rates can be used for hole transport layers to provide a time for a better localization and good coverage without damaging the perovskite absorber.
- Nb<sub>2</sub>O<sub>5</sub> compact layers can be exposed to post processes such as etching, cleaning or using chemical agents to provide better host for perovskite absorber.
- Thickness optimization can be carried out for Nb<sub>2</sub>O<sub>5</sub> compact layers which can minimize the interface problems.
- Alternative deposition techniques and alternative perovskite absorbers can be studied together with Nb<sub>2</sub>O<sub>5</sub> compact layer.



## CURRICULUM VITAE

### PERSONAL INFORMATION

Surname, Name : Coşar, Mustafa Burak  
Nationality : Turkish (TC)  
Date and Place of Birth : 10 June 1987, Zonguldak  
Phone : +90 505 410 03 65  
E-mail : e150149@metu.edu.tr

### EDUCATION s

Degree	Institution	Year of Graduation
PhD	METU, Metallurgical and Materials Engineering	2019
MS	METU, Metallurgical and Materials Engineering	2013
BS	METU, Metallurgical and Materials Engineering	2010

### WORK EXPERIENCE

Year	Place	Enrollment
2012-Present	ASELSAN	R&D Engineer
2010-2012	METU, Metallurgical and Materials Engineering	Research Assistant

### FOREIGN LANGUAGES

Advanced English

## PUBLICATIONS

- [1] M. B. Cosar, K. C. Icli, M. Ozenbas, Effect of oxygen flow rate on the low temperature deposition of titanium monoxide thin films via electron beam evaporation, *Journal of Vacuum Science & Technology A*, 37 (2019) 031505.
- [2] Y. Çat, V. Baran, G. Afacan, M. B. Coşar, S. Özçelik, Investigation of electromagnetic interference shielding effectiveness of cz grown Ge optical windows, *Crystal Research and Technology*, 53 (2018) 1800069.
- [3] M. B. Cosar, K. C. Icli, M. Ozenbas, Plasma assisted low temperature electron beam deposited NiO thin films for electro-optic applications, *Journal of Vacuum Science & Technology A*, 36 (2018) 031501.
- [4] M. B. Cosar, G. H. Aydogdu, H. Batman, A. E. S. Ozhan, A solution to adhesion problem of oxide thin films on zinc selenide optical substrates, *Surface and Coatings Technology*, 314 (2017) 118-124.
- [5] M. B. Cosar, A. E. S. Ozhan, G. H. Aydogdu, Improving the laser damage resistance of oxide thin films and multilayers via tailoring ion beam sputtering parameters, *Applied Surface Science*, 336 (2015) 34-38.
- [6] B. Cosar, K. C. Icli, H. I. Yavuz, M. Ozenbas, Photovoltaic performance of bifacial dye sensitized solar cell using chemically healed binary ionic liquid electrolyte solidified with SiO<sub>2</sub> nanoparticles, *Electrochimica Acta*, 87 (2013) 425-431.
- [7] M. Ghaffari, M. B. Cosar, H. I. Yavuz, M. Ozenbas, A. K. Okyay, Effect of au nano-particles on TiO<sub>2</sub> nanorod electrode in dye-sensitized solar cells, *Electrochimica Acta*, 76 (2012) 446-452.